MESOPHASE-BASED APPROACHES FOR ON-CHIP MEMBRANE PROTEIN CRYSTALLIZATION AND STRUCTURE DETERMINATION

BY

DARIA SERGEYEVNA KHVOSTICHENKO

DISSERTATION

Submitted in partial fulfillment of the requirements
for the degree of Doctor of Philosophy in Chemical Engineering
in the Graduate College of the
University of Illinois at Urbana-Champaign, 2012

Urbana, Illinois

Doctoral Committee:

Professor Paul J.A. Kenis, Chair
Professor Stephen G. Sligar
Professor Charles F. Zukoski
Assistant Professor Brendan A. Harley
Assistant Professor Charles M. Schroeder

Abstract

Transmembrane proteins traverse the lipid bilayers of cell membranes and play a highly important role in many processes *in vivo*. Malfunctions of membrane proteins have been shown to cause a variety of disease states, for example, cystic fibrosis, hereditary hearing loss, and hypothyroidism. Furthermore, membrane proteins are targets of over 60% of all drugs available on the market. Thus, information on membrane protein function is of immense importance for the understanding of processes associated with disease states and for the development of new and improved therapeutics.

Detailed spatial structures of proteins are typically obtained from crystal X-ray diffraction data. Crystallizing membrane proteins, however, is extremely difficult due to their amphiphilic properties that affect their stability in aqueous solutions. The trial-and-error nature of the crystallization process requires large-scale screening efforts, which is often hampered by the limited availability of membrane protein samples.

In meso crystallization is a powerful alternative to the traditional crystallization of membrane proteins directly from aqueous solutions. The method involves reconstitution of the proteins into so-called lipidic mesophases that are comprised of lipid bilayers, providing a native-like environment for the proteins. Lipidic mesophases form spontaneously upon mixing of the aqueous solution of a protein with a lipid. The microstructural properties of the mesophase play a highly important role in crystallogenesis *in meso* and depend on the composition of the overall mixture in a complex manner. Understanding the effect of mesophase microstructure on the outcome of crystallization trials is necessary for improving the success rate of the process. Mesophases, however, are difficult to handle due to their high viscosity, and require special mixing and dispensing tools both for protein crystallization and for microstructural studies. The properties of lipidic mesophases also hampered miniaturization using microfluidic technologies, commonly used for screening of protein crystallization from solutions.

Microfluidic platforms developed in this dissertation are the only examples of microfluidic devices that combine mesophase-handling capabilities and X-ray transparency as required for *in situ* analysis of mesophases and of protein crystals. The platforms provide a route to reduce the preparative scale, automate sample formulation, and eliminate manual handling in two distinct aspects of mesophase-based technologies: (i) screening of the structure/composition

relationships of the properties of lipidic mesophases, and (ii) *in meso* crystallization of membrane proteins.

Macroscale studies of the phase behavior of lipidic mesophases with additives typically present in membrane protein crystallization highlight the complexity of structure/composition relationships in these systems, as discussed in Chapter 2. These studies are highly laborious and require the preparation of a large number of samples with systematically varying compositions. Microfluidic platforms developed and validated in Chapters 3 and 4 allow for automated simultaneous formulation of multiple samples and scale down the amount of material per sample at least 300-fold compared to the standard macroscale method. X-ray transparency of the platforms enables small-angle X-ray scattering analysis on-chip, as required to establish the microstructure of the mesophases. The platforms address two types of structural studies of mesophases. The microfluidic system presented in Chapter 3 is designed for the studies of the effect of additives on the microstructure of mesophases in multicomponent crystallization mixtures. The chip developed in Chapter 4 is applicable for studies of phase behavior in binary lipid/water mixtures, which is necessary for the understanding of fundamental principles of self-assembly in lipidic systems and for assessing suitability of novel lipids for *in meso* crystallization.

Chapter 5 describes a microfluidic platform for *in meso* crystallization of membrane proteins. The platform reduces the amount of material per trial 7-fold compared to similar macroscale methods. Platform architecture has been validated by crystallizing a membrane protein Photosynthetic Reaction Center (RC) from *Rhodobacter Sphaeroides*. Furthermore, crystal structure of RC was solved using X-ray diffraction data collected on-chip. Thus, the platform fully eliminates manual crystal harvesting and is a highly promising tool for structural biology. The platform is uniquely positioned for the simultaneous analysis of the protein crystals and the surrounding mesophase, which is not possible with existing macroscale approaches. This information is invaluable for unraveling the factors defining the outcome of crystallization trials and for improving the success rate in membrane protein crystallization.

Acknowledgments

I am grateful for the support of many people who helped me along the way. First and foremost, my family and friends made this experience a lot easier and much more pleasurable than it would have been otherwise.

I have been fortunate to have Prof. Paul Kenis as my advisor. He has been infinitely supportive of all my pursuits and ideas, and with his encouragement and advice I was able to get through some of the very challenging projects described in this thesis.

Being a part of the Kenis group has been a great experience. My work would have been much more difficult without the expertise of my labmates, in particular, Dr. Sarah Perry, Dr. Amit Desai, Dr. Joshua Tice, Sudipto Guha, Sachit Goyal, Dr. Ashtamurthy (Ash) Pawate, and Jeremy Schieferstein. Some of the best ideas that pushed the project forward originated in conversations with them. Several of Kenis group members deserve special credit for their contributions to this work. Sarah initiated many of the directions developed in this dissertation. Trips to Argonne National Lab would have been unimaginable without the help of Ash and Sudipto. The work on the crystallization platform and protein crystallography was largely a mutual effort between me, Jeremy, and Ash. I also appreciate the help of undergraduate students who worked with me on various projects. Johnathan Ng contributed a lot to the studies of the phase behavior of lipidic mesophases, Monisha Menon was involved in the phase behavior studies as well as the development of the X-ray transparent SlipChip, and Danial Soorty was instrumental in the early stages of the development of the crystallization platform.

I am absolutely indebted to Dr. Elena Kondrashkina, Dr. Keith Brister, and Jay Von Osinski from the Life Sciences Collaborative Access Team (LS-CAT) at the Advanced Photon Source, Argonne National Lab, for the development of the setup for small-angle X-ray data collection. Most of the results presented in this dissertation would have been impossible without that instrument. Protein crystallography work was aided by Dr. Joseph Brunzelle from LS-CAT. Dr. Danielle Gray and Dr. Amy Fuller from the George L. Clark X-Ray Facility have provided a lot of help in X-ray data collection and analysis. Mike Harland and Rob Brown from the machine shop at the School of Chemical Sciences patiently converted my scribbles into functional parts. Dr. Philip Laible from Argonne National Lab generously provided photosynthetic reaction center for protein crystallization trials.

This project was funded by the NIH Common Fund Structural Biology Program (grant R01 GM86727). Use of the Advanced Photon Source was supported by the U. S. Department of Energy, Office of Science, Office of Basic Energy Sciences, under Contract No. DE-AC02-06CH11357. Use of the LS-CAT Sector 21 was supported by the University of Illinois, Michigan Economic Development Corporation and the Michigan Technology Tri-Corridor (Grant 085P1000817).

Table of Contents

Chapter 1.
Lipidic mesophases and *in meso* crystallization of membrane proteins

1.1 Introduction

Transmembrane proteins play a pivotal role in many cellular processes, for example, in transport of components across cell membranes, signaling between cells and subcellular domains, and biochemical pathway regulation. Normal function of membrane proteins is paramount for health, and malfunctions have been linked to conditions as diverse as polycystic kidney disease, Alzheimer's disease, and cystic fibrosis.[1] Because of their biological importance, membrane proteins account for over 60% of drug targets.[2] Detailed information on the structure of membrane proteins and on the mechanisms of their action is invaluable for the understanding of their function, as required for the developments of new and improved treatments. However, high-resolution structures of membrane proteins are only scarcely available. The bottleneck here is the difficulty of obtaining sufficiently large, diffraction-quality membrane protein crystals for X-ray diffraction analysis, the primary source of structural information. As of October 2012, only ~1100 crystal structures of membrane proteins are currently available, of which only 400 are unique,[3] compared to >80000 structures of soluble proteins.[4]

The two most common crystallization methods for membrane proteins are *in surfo* and *in meso*,[5] although crystallization from detergent-stabilized solutions in apolar solvents[6] and from bicelle-stabilized solutions has also been reported.[7] Most approaches for membrane protein crystallization require that a protein initially be transferred from the native cell membrane into an aqueous solution. The difficulties in the crystallization of membrane proteins are conferred by their intrinsically amphiphilic structure, *i.e.*, presence of hydrophilic and hydrophobic domains within the protein molecule (Figure 1.1A). To prevent denaturing of hydrophobic domains upon exposure to the hostile aqueous environment, membrane proteins are solubilized in detergent micelles that form a protective shield around the part of the molecule that originally resided in the interior of the cell membrane (Figure 1.1B). In the *in surfo* method a precipitant is added directly to a solution detergent-solubilized protein to induce crystallization and crystals grow

from a solution.[5] In the *in meso* method pioneered by Landau and Rosenbusch[8] the solution of detergent-stabilized protein is mixed with a lipid to form a mesophase (Figure 1.1C), a self-assembled nanoscale structure composed of lipid bilayers with embedded protein molecules. Precipitant is then added to the protein-containing mesophase (Figure 1.1D), with subsequent protein crystal growth taking place within the mesophase (Figure 1.1E). The lipid bilayers of the mesophase create a membrane-like environment for the protein and are thought to maintain it in the native conformation. The *in meso* method has been credited with a number of breakthroughs human membrane protein structures, such as β2 adrenergic receptor[9] and κ-opioid receptor,[10] targets of many common drugs.

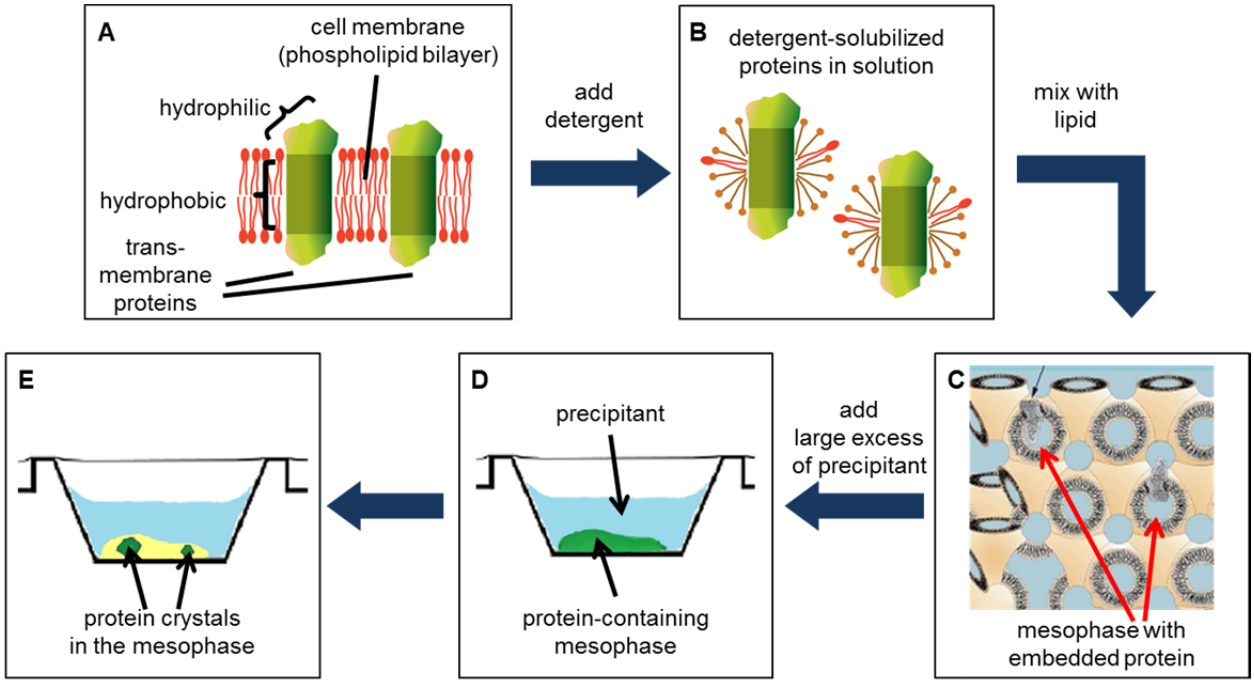

Figure 1.1. A cartoon representation of the *in meso* crystallization approach.[5,6,7] Red arrows in panel C point at depictions of protein molecules embedded in the bilayers of a mesophase of lipid monoolein. Protein purification and concentrating steps in-between A, B, and C are not shown. (Parts of the figure are reprinted from M. Caffrey, Current Opinion in Structural Biology, 2000, 10(4), 486-497, with permission from Elsevier, and from P. Nollert, Journal of Applied Crystallography, 2002, 35(5), 637-640, with permission of the International Union of Crystallography, http://dx.doi.org/10.1107/S0021889802012001.)

In Chapter 1.2.1 and 1.2.2 we describe the properties of relevant mesophases and the current mechanistic understanding of the in crystallogenesis *in meso*, Chapter 1.2.4 describes reported implementations of the *in meso* method, and Chapter 1.2.5 focuses on the challenges associated with the method. Structure and properties of lipidic mesophases are discussed in detail in Chapter 1.3.1-1.3.3. Chapter 1.4.1-1.4.3 focus on the challenges associated with *in meso* crystallization of membrane proteins and studies of the phase behavior of lipidic mesophases and

with related miniaturization strategies. For brevity, solutions of membrane proteins will be referred to as "protein solutions" throughout the dissertation.

1.2 Crystallization of membrane proteins in lipidic mesophases

1.2.1 Lipidic mesophases for *in meso* crystallization

This section briefly summarizes the aspects of structure and properties of lipidic mesophases relevant for *in meso* crystallization. Lipidic mesophases are described in detail Chapter 1.2.1 and 1.2.2.

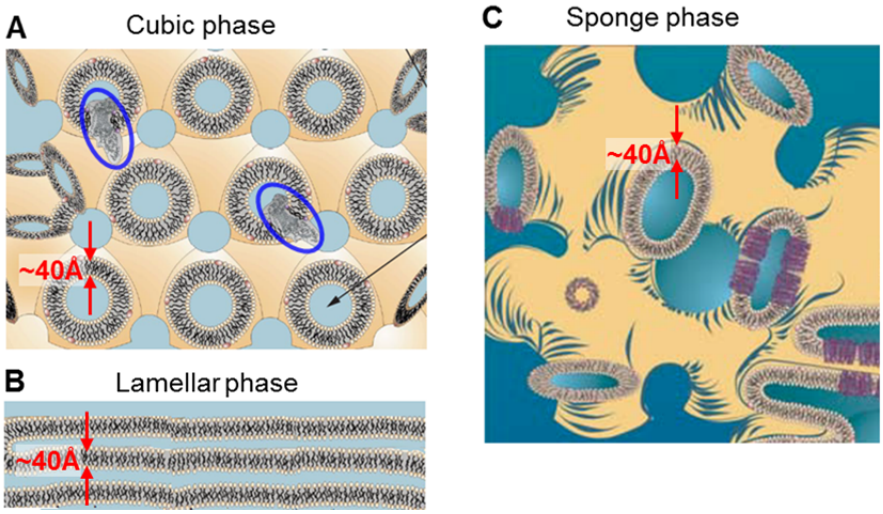

Figure 1.2. Cartoon representations of mesophase types. Lipid bilayers are shown in brown and yellow, aqueous compartments are shown in blue. As much as possible, the dimensions of lipid monolein (light brown), membrane proteins (grey or purple), thicknesses of lipid bilayer and dimensions of aqueous compartments have been drawn to scale. In case of lipid monoolein, lipid bilayer thickness in all lipidic phases is approximately 40 Å at room temperature and is indicated with red arrows. **(A)** Curved lipid bilayers of the lipidic cubic mesophase of *Pn3m* type with reconstituted membrane proteins encircled in blue ovals for clarity. **(B)** Lamellar mesophase. (Reprinted from M. Caffrey, Current Opinion in Structural Biology, 2000, 10(4), 486-497, with permission from Elsevier.) **(C)** Sponge phase with reconstituted membrane proteins (purple). (Reprinted from V. Cherezov, J. Clogston, M.Z. Papiz, M. Caffrey, Journal of Molecular Biology, 2006, vol. 357(5), 1605-1618, with permission from Elsevier.)

Lipidic mesophases consist of highly ordered lipid bilayers interspersed with aqueous channels and self-assemble spontaneously when certain lipids are mixed with water or aqueous solutions.[11] The two classes of mesophases most relevant in the *in meso* crystallization are lamellar and cubic. The lamellar phase is comprised of stacks of flat lipid bilayers, whereas in the cubic phase the bilayers are highly curved and are saddle-shaped at every point in the mesophase (Figure 1.2).[12] The distinguishing property of cubic mesophases is the 3D-continuous structure of the bilayers as well as of the aqueous channels.

Cubic phases are prerequisite for crystallogenesis *in meso*,[13] presumably due to the bicontinuous structure of both lipidic and aqueous compartments that allows for 3D diffusion of proteins within the mesophase. On the contrary, in lamellar phases protein molecules are constrained to moving along a single lamella. The aqueous channels of cubic mesophases are sufficiently large to incorporate hydrophilic domains of membrane protein molecules, whereas the size of the aqueous compartments in lamellar phases is likely too small, causing the proteins to separate from the mesophase.[14] Because the microstructure of lipidic mesophases is sensitive to temperature and composition of the crystallization mixture, compatibility of a given set of crystallization conditions with cubic phase formation must be assessed experimentally.[15-18]

Formation of mesophases has been reported in many synthetic and naturally occurring lipids. The lipid most commonly used for *in meso* crystallization is monoolein[8,15] (Figure 1.3), a monoacylglycerol with 18 atoms in the hydrocarbon chain of the lipid tail. Other homologues of monoacylglycerols have also been tested as matrices for *in meso* crystallization,[19-22] and in a recent report a new family of isoprenoid lipids suitable for *in meso* crystallization has also been demonstrated.[23,24] The structure of the lipid molecule defines the properties of cubic mesophases, such as the thickness and curvature of lipid bilayers, the size of aqueous channels within the mesophase, and stability of cubic phases, as discussed in Chapter 1.3. These properties have important implications for protein crystallogenesis *in meso*.

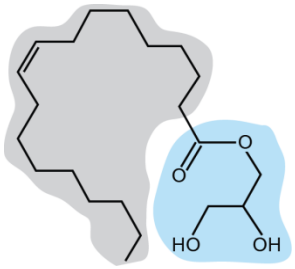

Figure 1.3 Structure of lipid monoolein with the polar head group shaded in blue and the hydrocarbon tail shaded in grey.

1.2.2 Mechanism of *in meso* crystallization

Phase transformations and properties of the mesophase itself have been shown to play a highly important role in the outcome of crystallization trials *in meso*.[13,25-28] All membrane protein crystals grown *in meso* are of type 1,[29] with protein molecules packed in ordered sheets.[30] In the case of membrane protein bacteriorhodopsin, crystal formation *in meso* was observed as long as the bilayer curvature in the mesophase was within a certain range.[28] Although a bulk cubic phase was required for crystal growth,[13] atomic force microscopy measurements showed that crystal nucleation occurs with a local cubic-to-lamellar rearrangement.[31] Existence of a lamellar phase surrounding a membrane protein crystals grown *in meso* was also confirmed optically[13] and in

SAXS studies.[26] Based on these findings, mechanistic description of crystallogenesis focused on the concepts of bending elasticity and topology of lipid bilayers.[13,25-27]

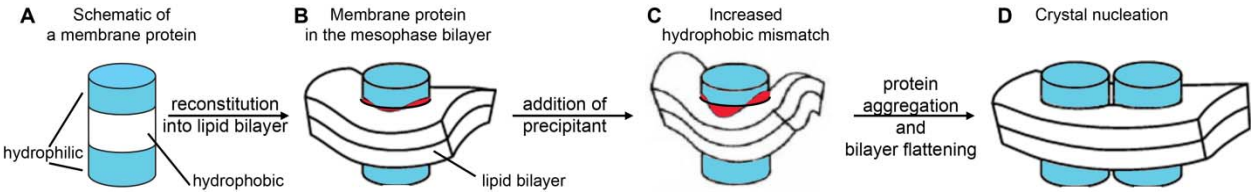

Figure 1.4. Hydrophobic matching at the protein–membrane interface in membranous media with diverse curvatures. Membrane proteins are shown schematically as cylinders. Lipid bilayers are depicted as planar or curved structures. **(A)** Schematic depiction of hydrophobic (white) and hydrophilic (blue) domains of a membrane protein. **(B, C)** Protein cylinder interacting with a curved bilayer of a cubic lipidic mesophase (B) before and (C) after precipitant addition. Mismatch between the two hydrophobic surfaces is shown in red. (D) Two membrane protein in a flattened bilayer of the mesophase; hydrophobic mismatch is relieved. (Parts of the figure are reprinted from P. Nollert, H. Qiu, M. Caffrey, J. P. Rosenbusch and E. M. Landau, Federation of Europian Biochemical Societies Letters, 2001, 504, 179-186, with permission from Elsevier.)

The driving force of protein crystal nucleation is believed to be the geometric mismatch between the saddle-shaped bilayers of the cubic phase and the hydrophobic domains of proteins adapted to planar cell membranes (Figure 1.4).[13,27] For the optimal coverage of the hydrophobic domains of protein molecules, the lipid bilayers must adopt a strained, locally flattened geometry (Figure 1.4B).[13,27] The free energy cost of bilayer flattening becomes higher upon addition of precipitants that cause the intrinsic bilayer curvature to increase (Figure 1.4C).[21,28,32-34] Moving another protein molecule into the already flattened bilayer region from elsewhere in the mesophase, however, is energetically favorable because it reduces the cumulative bilayer bending stress in the system. This provides the driving force for crystal nucleation, which occurs with locally flattened (lamellar) bilayers surrounding protein clusters (Figure 1.4D), eventually driving phase separation of a protein crystal from the surrounding mesophase,[13,27] in agreement with experimental observations.

While high mean bilayer curvature favors MP crystal nucleation *in meso*, it may arrest protein diffusion required for crystal growth. Bilayer curvature is not uniform throughout the mesophase, and protein molecules are believed to reside in bilayer regions with low local curvature and to traverse bilayer regions with locally high curvature at a high energy cost during diffusion.[27] Successful *in meso* crystallization trials have been correlated with conditions that correspond to a high protein mobile fraction and a fast diffusion rate.[35,36] Thus, MP crystal formation *in meso* relies on a delicate balance of conflicting requirements for crystal nucleation and growth.

1.2.3 Optimization of *in meso* crystallization

The efforts to engineer mesophase properties to improve success rate of crystallization trials relied heavily on the mechanistic understanding of crystallogenesis and its relation to the microstructure of mesophases.

Of primary importance for *in meso* crystallization is the presence of a cubic phase in the crystallization system. Here, compatibility of crystallization screens with cubic phase formation has been tested[16,37,38] and suitable precipitant kits are commercially available, for example, the Cubic^{TM} Screen from Emerald Biosystems. To address poor low-temperature stability of MO cubic phases (Chapter 1.2.3), monoacylglycerols[39] and isoprenoid lipids[23,24] with a cubic phase stable at temperatures lower than that of MO have been developed and successfully used for membrane protein crystallization.[24,39] The isoprenoid lipids, due to their branched structure, were also shown to stabilize protein-protein contacts in the crystal, potentially facilitating crystallization.[24]

The importance of hosting lipid is highlighted in the studies of monoacylglycerol homologues of with lipid tail lengths of 14, 15, and 16 carbon atoms and different positions of the double bond within the chain as matrices for the crystallization of an outer membrane sugar transporter OprB.[22] Only one of the three 15-atom homologues tested in that work produced diffraction-quality crystals of OprB, although small crystals formed in 15- and 16-carbon monoacylglycerols, as well as in monoolein.

Lipidic sponge phases have been reported as suitable crystallization matrices for membrane proteins with sizeable hydrophilic domains that are too large to be accommodated by the aqueous channels of highly structured cubic phases.[25] Sponge phases (Figure 1.2C) are isotropic liquids that consist of disordered lipid bilayers suitable for membrane protein reconstitution and sufficiently flexible to conform to the size of hydrophilic domains. Sponge phase formation can be induced by various additives in the precipitant addition step, such as low-molecular weight polyethyleneglycols, Jeffamine, and alcohols.[25,40] Because of the flexibility of lipid bilayers in the sponge phases, the mechanism of crystallization is likely different from that in highly structured lipidic mesophases. Here, the formation of favorable contacts between hydrophilic domains of membrane proteins may be expected to play a major role. A set of sponge phase-inducing precipitants has been reported[40] and is available in a commercial crystallization kit from Molecular Dimensions.

A number of high-throughput methods for assessing successful crystallization conditions have been reported, such as testing the compatibility of precipitants with the cubic mesophase formation,[37,38] and deducing optimal crystallization conditions based on the rate of protein diffusion.[36] Host lipid screens are used in state of the art crystallization protocols.[41]

1.2.4 Implementations of the *in meso* method

The very first *in meso* crystallization protocol relied on the introduction of salt crystals into protein-laden mesophase in order to induce crystal growth.[8] The approach currently used in structural biology relies on a modification[42] of the original protocol with solutions of precipitants, instead of solid salts, added to the mesophase (Figure 1.1). Three distinct implementations of this method have been reported.[15,43,44] Although all implementations rely on the same sequence of steps, the protocols for mesophase formulation and incubation with precipitant, as well as relative amounts of lipid, protein solution, and precipitant, differ between the methods.

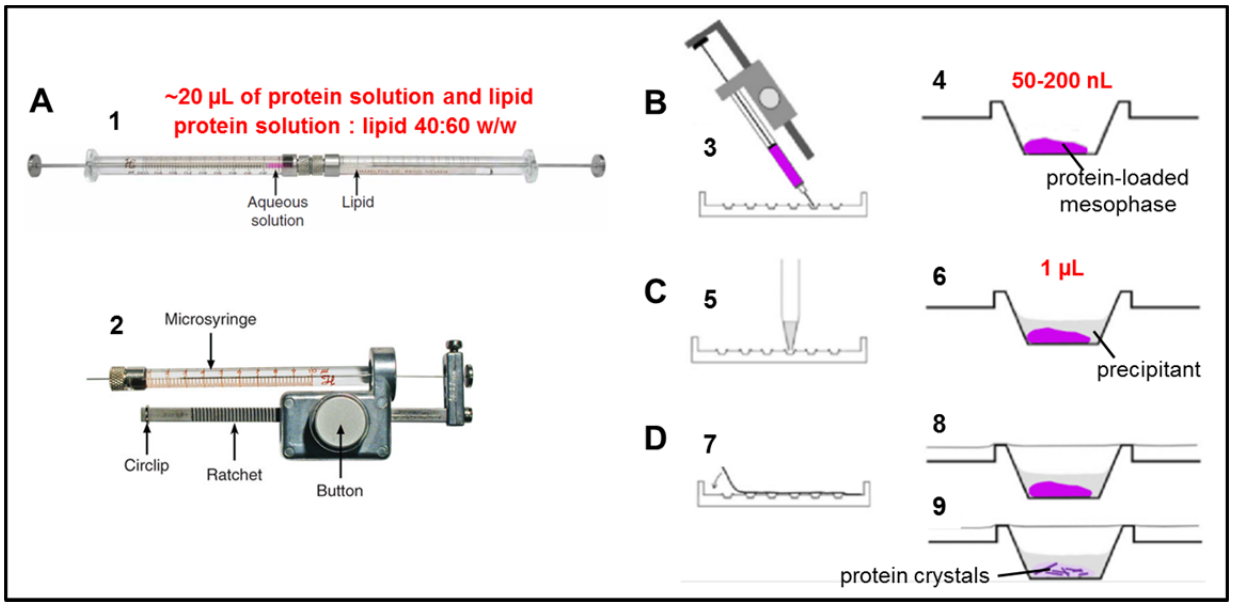

Figure 1.5. Workflow in the standard protocol for in meso crystallization. **(A)** (1) Protein-loaded mesophase is initially formed by coupling two syringes (one filled with 60% monoolein and the other with 40% protein solution) and by mixing of the two components with repetitive cycling of the entire combined volume from one barrel to the other. (2) The mesophase-filled syringe is attached to a ratchet dispenser. **(B)** The mesophase is dispensed into each microwell with the ratchet dispenser (3, 4). (Reprinted by permission from Macmillan Publishers Ltd: Nature Protocols (M. Caffrey, V. Cherezov, Nature Protocols, 2009, 4(5), 706-731), © 2009.) **(C)** Precipitant solutions fill the wells of a crystallization tray (5), a single well also shown (6). **(D)** The wells are sealed with clear transparent tape (7) and stored (8). The protein-containing mesophase is stable in an excess of overlaying liquid (6-9). Crystals appear only within the lipid matrix (9). Even though less than 200 nL of material is required per crystallization well, at 5-20 µL of the protein solution is necessary for mesophase preparation. (Reprinted by permission from E. Wallace, D. Dranow, P. D. Laible, J. Christensen and P. Nollert, Public Library of Science ONE, 2011, 6, e24488, © 2011.)

The most widely used variant of the method[15] (Figure 1.5) relies on the preparation of a uniformly mixed mesophase with homogeneous protein loading. Monoolein is typically mixed with the protein solution in the ratio of 60:40 w/w (v/v). Due to the extremely high viscosity of lipidic mesophases a coupled syringe mixer (Figure 1.5A) is typically used in this step. The mixer consists of two syringes connected with an airtight coupler, with one syringe containing the protein solution, and the other syringe with a molten lipid. Mixing is achieved by pushing the contents back and forth between the syringes. A small amount of the mesophase (20-100 nL) is dispensed into a crystallization well and a large excess of precipitant (microliters) is added directly on top of the mesophase. Again, due to the high viscosity of the mesophase, accurate dispensing requires either a crystallization robot[45] or a ratchet dispenser[46] (Figure 1.5), and may be challenging even with these tools.

The protocol described above has been used in almost all reported *in meso* crystallization trials to date. The most common crystallization setup for this approach is the microbatch format (Figure 1.6A), although the method is amenable to other trial formats typical for crystallization from solutions (Figure 1.6). The major drawback of the method is the large amount (at least several μL) of the protein solution required for the mesophase preparation in the coupled syringe mixer, although only nanoliter or even picoliter[47] amounts of the sample are required for the crystallization. This limits the flexibility of the method and imposes constraints when working with scarcely available protein samples.

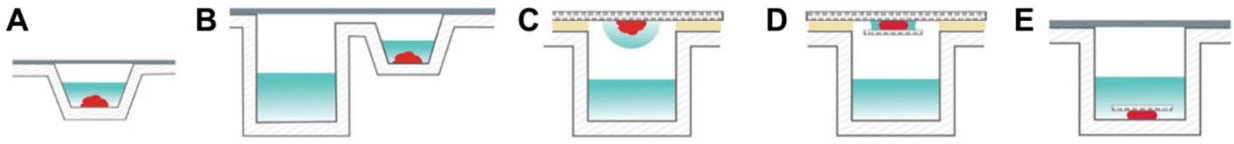

Figure 1.6. Types of *in meso* crystallization experiments that can be performed with commercially available plates and pre-mixed protein-loaded mesophase. The types of plates used include (**A**) microbatch, (**B**) sitting drop and (**C**,**D**) hanging drop. In **D** and **E**, a sandwich is made of the mesophase (red) by placing a small glass coverslip (hatched) (**D**) below or (**E**) above the bolus. The precipitant solution is colored a shaded pale blue, the vacuum grease is yellow and the sealing tape is gray. (Reprinted by permission from Macmillan Publishers Ltd: Nature Protocols (M. Caffrey, V. Cherezov, Nature Protocols, 2009, 4(5), 706-731), © 2009.)

A recently reported protocol[43] (Figure 1.7), termed post lipidic cubic phase formation incorporation (PLI), omitted mesophase formulation with homogenous protein loading. Instead, a lipid/water mesophase was prepared in coupled syringes and dispensed into crystallization wells (Figure 1.7A). A protein solution was added to this pre-formed mesophase, and the protein was found to spontaneously partition into the mesophase upon incubation, which took up to 12

hours (Figure 1.7B, C). Crystallization was then carried out in the sitting drop format (Figure 1.6B, Figure 1.7D), with the precipitant solution added on top of the mesophase in the well, and incubated against a reservoir with the same precipitant. Under favorable conditions protein crystal growth was observed within the mesophase (Figure 1.7E). The protein solution/mesophase (or monoolein) ratio was maintained at 2:1 v/v, different from that typically used with homogeneous mesophase formulation. Remarkably, the protocol was efficient even upon incubating the protein solution with dry monoolein. In this case the mesophase must form spontaneously due to diffusion of water into monoolein, which happens significantly faster than diffusion of the protein into the mesophase due to the very large differences in molecular sizes.

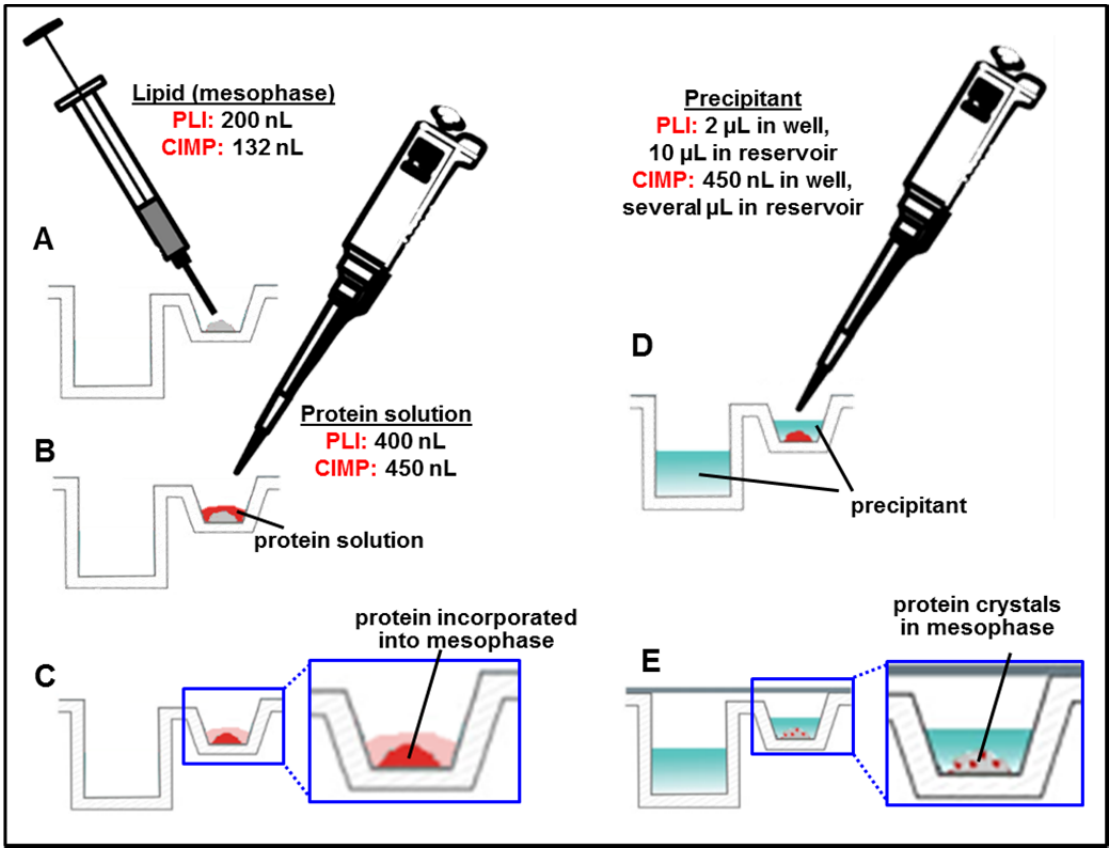

Figure 1.7. Workflow in the PLI[43] and CIMP[44] protocols for *in meso* crystallization. **(A)** In the PLI protocol the mesophase or molten MO (grey) is dispensed into microwells using airtight syringes. In the CIMP approach a well-plate pre-coated with MO (Quiagen) is used. **(B)** A solution of membrane protein (red) is dispensed into the well by conventional pipetting and is incubated with lipidic material for several hours, resulting in **(C)** protein incorporation into the mesophase. **(D)** Precipitating reagents (pale blue) are added. In the PLI approach identical solutions are used in the well and the reservoir. In the CIMP approach a diluted precipitant is added in the well and a concentrated precipitant is used in the reservoir. **(E)** The wells are sealed and stored. Crystals only appear within the lipid matrix. Amounts of material required per crystallization well in the two methods are indicated for steps 1, 2, and 4. (Parts of the figure are reprinted by permission from Macmillan Publishers Ltd: Nature Protocols (M. Caffrey, V. Cherezov, Nature Protocols, 2009, 4(5), 706-731), © 2009, and from E. Wallace, D. Dranow, P. D. Laible, J. Christensen and P. Nollert, Public Library of Science ONE, 2011, 6, e24488, © 2011.)

The advantages of the PLI protocol include the elimination of the cumbersome mesophase mixing and dispensing steps (in the case when dry monoolein is used) and, unlike in the standard *in meso* protocol shown in Figure 1.5, the ability to carry out crystallization trials with proteins available in amounts insufficient for the coupled-syringe mixer. However, the PLI method has only been used to produce crystals of three highly similar membrane proteins,[43,48] and applicability of this method for a wide range of membrane proteins remains to be tested. Some of the potential problems associated with the method are (1) the long incubation time required for protein incorporation in the mesophase, which may be suboptimal due to the possibility of protein denaturation, and (2) the lack of control over protein transport into the mesophase in crystallization well with implications for reproducibility of crystallization trials. On the other hand, passive mixing for mesophase formulation may be advantageous because the proteins are not subjected to substantial and potentially damaging shear forces in the mixing step.

A slightly different protocol,[44] termed controlled *in meso* phase crystallization (CIMP), combines the PLI approach with vapor diffusion commonly used in the crystallization from solutions. The protocol involves two steps: (i) the protein solution is incubated with dry monoolein; and (ii) precipitant solution is added to the mesophase and the reservoir well. Precipitant solutions in the crystallization well and the equilibration reservoir have different concentrations, providing a way to probe a larger parameter space than in the PLI method. The CIMP method has been tested with two previously crystallized membrane proteins and also used to obtain diffraction-quality crystals of a novel protein.[44]

1.2.5 Microfluidic platforms for *in meso* crystallization

Sophisticated microfluidic devices routinely automate fluid handling and formulation of samples on the nanoliter scale for screening of a large number of experimental conditions in a wide range of applications.[49-54] These systems typically rely on the well-developed methods of multilayer soft lithography to fabricate complex microfluidic networks with channel heights and widths on the order of tens to hundreds of micrometers.[55,56] Multilayer devices fabricated in elastomeric material polydimethylsiloxane (PDMS) provide fluid routing capabilities via pneumatic valve actuation (Figure 1.8), where a thin elastomeric membrane deflects under a pressure gradient to close or open the fluid channel of the other fluidic layer.[55]

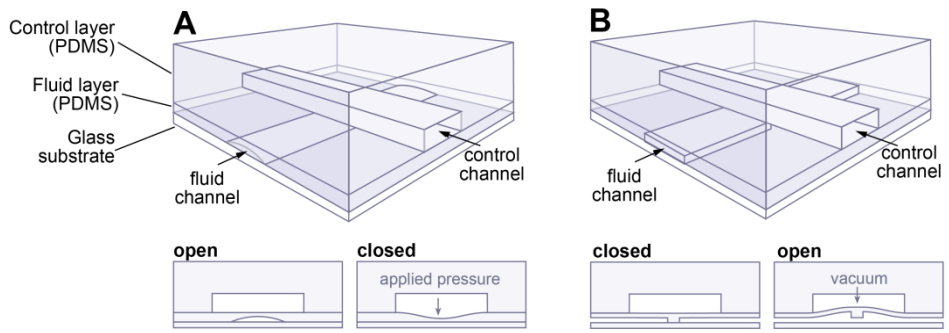

Figure 1.8. Operation of valves in multilayer microfluidic devices fabricated in polydimethylsiloxane (PDMS).[55,56] **(A)** Normally open valves.[55] **(B)** Normally closed valves.[57-60] Image courtesy of Dr. J. Tice, University of Illinois.

Various microfluidic approaches to microfluidic screening of crystallization conditions of soluble proteins in aqueous solutions have been demonstrated, as summarized in a recent review article.[61] However, only two microfluidic platforms have addressed the *in meso* crystallization protocol,[48,62] the main difficulties arising from handling viscous mesophases on the microscale. The plug-based system developed by Li et *al.*[48] emulates the PLI method described in Chapter 1.2.4. The platform automates mesophase-precipitant formulation for *in meso* crystallization trials with ~80 nL of mesophase per trial, but the mesophase, with or without the protein, must be prepared on the microliter scale in coupled syringes off-chip.

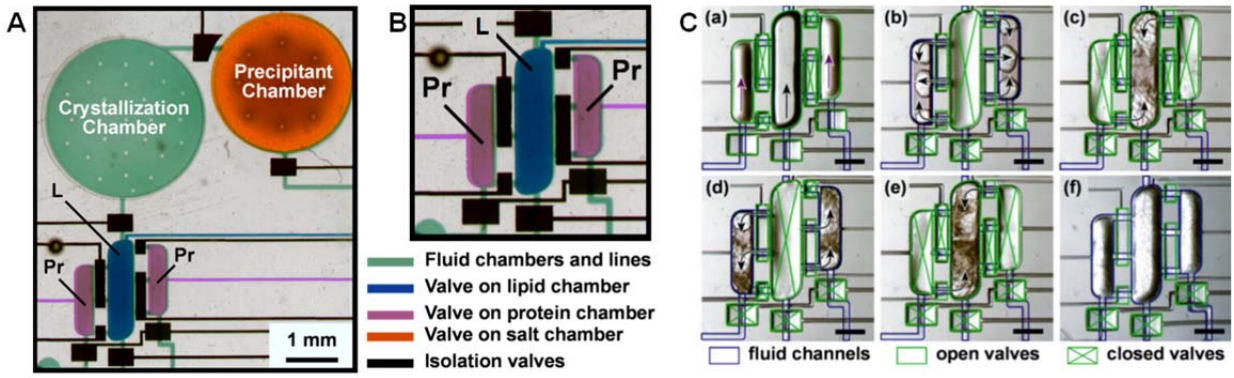

Figure 1.9. Optical micrograph of a microfluidic platform for *in meso* protein crystallization. **A.** A complete platform. After mixing the lipid (L) with protein solution (Pr) in the lipidic mixer (blue, purple), the resulting mesophase is transferred to the crystallization chamber, and combined with the precipitant from the precipitant chamber. Fluid manipulation is achieved by pneumatic actuation of isolation valves (black) and injection valves located on top of every fluid chamber. **B.** A magnified image of the lipidic mixer configuration from panel A. **C.** Optical micrographs of 9.95 mg/mL solution of membrane protein bacteriorhodopsin mixing with monoolein in a microfluidic chip (observed through partially crossed polarizers). Blue lines delineate the edges of the fluidic channels. **(a)** Filling of chambers with protein solution and lipid (arrows); **(b)** Straight-line injection of lipid into the side chambers containing protein; **(c-e)** Chamber-to-chamber injection of the fluid mixture through different sets of inlets to create a circulating motion. The cycle repeats starting at **(b)**. **(f)** The slightly birefringent mixture after mixing. Scale bar: 500 µm. (Reprinted with permission from S. L. Perry, G. W. Roberts, J. D. Tice, R. B. Gennis, P. J. A. Kenis, Crystal Growth and Design, 2009, 9, 2566-2569, © 2009 American Chemical Society.)

The only reported platform that truly scales down the amount of sample required for mesophase formulation is the lipidic mixer developed in by Kenis *et al.*[62] The individual mesophase samples can be prepared at a scale of ~20 nL (Figure 1.9A, B). Mixing is achieved by

a sequence of actuations of valves located over each compartment of the mixer (Figure 1.9C).

1.3 Lipidic mesophases

This section describes structure and properties of lipidic mesophases, with the focus on types of phases relevant for this work. In Chapter 1.3.1 reported types of lipidic mesophases and their topology are reviewed. Mathematical relationships between molecular structure of amphiphiles, mesophase type, and mesophase composition are summarized in Chapter 1.3.2. Properties of monoolein/water mesophases and are described in Chapter 1.3.3 along with the effects of salts and detergents, the two common additives in the *in meso* protein crystallization.

1.3.1 Types and topological properties of lipidic mesophases

Lipidic mesophases are self-assembled soft materials with long-range order that form upon mixing water or aqueous solutions with certain lipids, either synthetic or naturally occurring.[11,17] Lipid molecules are amphiphilic, with small polar head groups and long apolar hydrocarbon tails.

The distinguishing feature of lipidic mesophases is their structure comprised of ordered lipid bilayers. Mesophases can form with different arrangements of bilayers referred to as phase types,[63-65] which are established from small-angle X-ray scattering (SAXS) data[15,63,66,67] through a procedure described in detail in Appendix A. Several types of mesophases have been discovered so far in lipid-containing systems:[11,17] 1D-ordered lamellar mesophases, 2D-ordered inverse hexagonal H_{II}, and 3D-ordered cubic mesophases of different morphologies (Figure 1.10).

Cubic mesophases belong to a fascinating class of bicontinuous amphiphilic systems, where both lipid bilayers and aqueous channels are continuous throughout the mesophase (Figure 1.10). All types of bicontinuous cubic mesophases discovered so far have a rigorous geometrical definition:[29,68] the midplanes of lipid bilayers form infinite periodic minimal surfaces (IPMS) that are saddle-shaped at every point in such a manner that the sum of principal curvatures is zero. Cubic mesophases with IPMS of gyroid (G), primitive cubic (P) and double diamond (D) types have been discovered in various lipidic systems.[11,17] These symmetries correspond to crystallographic cubic space groups *Ia3d* (Q^{230}), *Im3m* (Q^{229}), and *Pn3m* (Q^{224}). All three

notations, *i.e.*, the IPMS symmetry, the crystallographic space group name, and the crystallographic space group number, are used interchangeably in literature.

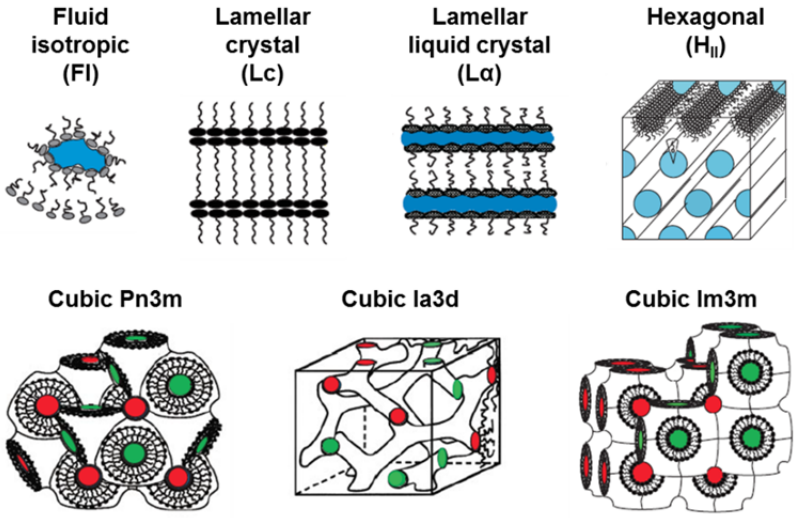

Figure 1.10. Lipid phases. Cartoon representations of the various liquid (fluid isotropic phase, FI), solid (lamellar crystal phase, *Lc*), mesophase states (lamellar liquid-crystal phase, *Lα*; cubic *Pn3m* phase [Q^{224}]; cubic *Ia3d* phase [Q^{230}]; cubic Im3m phase [Q^{229}]; and inverted hexagonal phase, *HII*) adopted by lipids. Individual lipids are shown as lollipop figures, with the pop and stick parts representing the polar headgroup and the apolar acyl chain, respectively. The blue, green and red colored regions represent water. (Reprinted from M. Caffrey, Current Opinion in Structural Biology, 2000, 10(4), 486-497, with permission from Elsevier.)

In addition to the lattice type, ordered phases are characterized by the lattice parameter, *i.e.*, the size of the smallest repeating unit of the periodic lattice,[2] which is also established from SAXS data. The unit cells of cubic mesophases are of cubic symmetry according to the crystallographic classification,[69] and only one value is required to characterize all three dimensions of the 3D cell. The procedure for lattice parameter determination of cubic phases is described in Appendix A.

The *Lα* phase consists of stacks of monoolein lipid bilayers separated with layers of water[1] and is only ordered in one dimension. Here the lattice parameter refers to the distance between the midplanes of bilayers because it is the only regular repeat parameter for this arrangement of bilayers.

The hexagonal H_{II} phase is comprised of aqueous cylinders of infinite length with lipid headgroups packed on cylinder surfaces (Figure 1.10). The cylinders are packed in a hexagonal honey-comb like arrangement, placing this phase type accordingly in the family of hexagonal symmetry. The repeat distance for this phase may be represented as either the center-to-center

distance between the cylinders or the length of the side of the hexagon circumscribing the cylinder. The two are mathematically related to each other through simple trigonometry.

1.3.2 Structure-composition relationships for cubic lipidic mesophases

Below we review relationships between molecular shape, mesophase microstructure, and mesophase composition relevant for this work. A wider range of relationships and mesophase types is covered in a detailed review by Kulkarni et *al.*[67] Table 1.1 lists notations used in this section and in other chapters of this dissertation to describe mesophase geometry and composition.

Table 1.1 Notations used to describe mesophase geometry and composition

Notation	Variable
γ_p	Amphiphile packing parameter[70] (Equation 1.1)
vl	Volume of the amphiphile tail
l	Length of the amphiphile tail
$ahead$	Headgroup area per amphiphile
fl	Volume fraction of the lipid in the mesophase
faq	Volume fraction of the aqueous compartments in the mesophase
d	Lattice parameter of the mesophase
r_w	Radius of the aqueous channels of the mesophase
σ, χ	Geometrical parameters of cubic mesophases (Table 2)

Lipid mesophases of interest here are of the inverse type (type *II*, Figure 1.11), *i.e.*, the area occupied by the heads of the amphiphiles is smaller than the area occupied by amphiphile tails. Seminal work by Israelachvili *et al.*[70] related the general types of structures formed by amphiphiles to their molecular shape, which is represented in terms of the packing parameter γ_p:

$$\gamma_p = \frac{v_l}{a_{head} l} \qquad \text{Equation 1.1}$$

where v_l is the volume occupied by the hydrocarbon tail, l is the length of the tail, and a_{head} is the optimal headgroup area of the amphiphile polar head. Schematic representations of different molecular shapes and corresponding values of packing parameters are shown in Figure 1.11. Inverse assemblies require that the amphiphile have a cone-like shape with a relatively small hydrophilic head and a voluminous hydrophobic tail (Figure 1.11). The concepts of the amphiphile molecular shape and the packing parameter have been successfully used to explain multiple types of self-assembled structures formed by amphiphiles. For monoolein mesophases, these concepts have also been invoked to rationalize the effects of various additives on the microstructure of the mesophase, as discussed in Chapter 1.3.3.

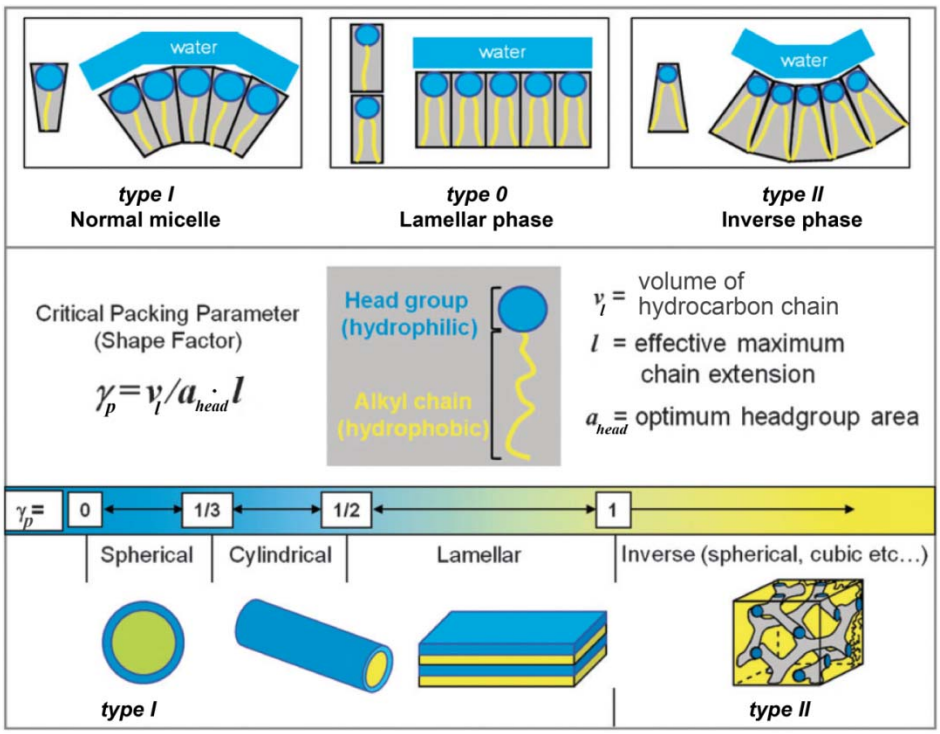

Figure 1.11. Relationship between molecular shape and types of self-assembled amphiphilic structures. Depending on the molecular shape of an amphiphile, type 0, I or II micelles are formed. The geometry of an aggregate or self-assembly is determined by the dimensionless critical packing parameters *(γ_p)* based on the theory by Israelachvili et al.[70] Double headed arrows indicate the range of most preferred geometries: spherical (γ_p = 0–1/3), cylindrical (γ_p = 1/3–1/2), lamellar (γ_p = 1/2–1) and inverse (type *II*) micelles (γ_p > 1). Increasing yellow color towards right indicates an increase in the hydrophobic character of an amphiphile. (Reproduced from C. V. Kulkarni, W. Wachter, G. Iglesias-Salto, S. Engelskirchen and S. Ahualli. Physical Chemistry Chemical Physics, 2011, 13, 3004-3021, with permission from the Royal Society of Chemistry.)

The molecular structure of amphiphiles can be linked to the composition of the mesophase through relationships established for IMPS structures based on their topology:[64]

$$\phi_l = 2\sigma\left(\frac{l}{d}\right) + \frac{4}{3}\pi\chi\left(\frac{l}{d}\right)^3 \qquad \text{Equation 1.2}$$

and

$$a_{head} = 2v_l \frac{\sigma d^2 + 2\pi\chi l^2}{\phi_l d^3} \qquad \text{Equation 1.3}$$

where φ_l is the volume fraction of the lipidic compartments, d is the lattice parameter of the cubic phase, and σ and χ are geometric characteristics of a given cubic phase (Table 1.2). The lipid bilayer thickness is twice the value of l. The volume fractions of the lipidic compartments φ_l and of the aqueous compartments φ_{aq} add up to unity: $\varphi_l + \varphi_{aq} = 1$.

Another important aspect of cubic mesophase geometry is the radius of the aqueous channels, which can be calculated using two different approaches.[71,72] Based on the topological

properties of the IPMS surfaces, the radius of the aqueous channels r_w is calculated simply as[72]

$$r_w = d\sqrt{-\frac{\sigma}{2\pi\chi}} - l \qquad \text{Equation 1.4.}$$

The amphiphile length l can be calculated from equation 1.2 based on the composition φ_l and the lattice parameter d.

Table 1.2. Values of parameters used in structure-composition relationships for cubic mesophases.

Phase type	σ[65]	χ[65]	λ[71]	k_v[71]
Pn3m	1.919	-2	$\sqrt{3}/2$	0.780
Ia3d	3.091	-8	$1/\sqrt{8}$	0.491
Im3m	2.345	-4		

In another approach the aqueous compartments of mesophase are represented as a network of cylindrical rods with junction points. The volume is of each rod is[71]

$$v_{rod} = \pi r_w^2 \cdot \lambda d \cdot \left(1 - k_v r_w / (\lambda d)\right) \qquad \text{Equation 1.5}$$

where l and k_v are constants for a given phase type. Rod volume is related to the volumetric composition of the mixture:

$$\varphi_{aq} = \frac{n v_{rod}}{d^3} \qquad \text{Equation 1.6}$$

where n is the number of rods per unit cell. The radius of the channels r_w is calculated by simultaneously solving equations 1.5 and 1.6. The values of l, k_v, and n for *Pn3m* and *Ia3d* phases are listed in Table 1.2. As demonstrated by Briggs *et al.*,[72] for monoolein/water mesophases the radii calculated using the two approaches differed by less than 1 Å for a wide range of temperatures.

Finally, the surface-averaged values of mean curvature (sum of the two principal curvatures) and Gaussian curvature (product of the two principal curvatures) at the distance l from the bilayer midplanes are calculated as

mean curvature[65] $\langle H \rangle = -\frac{2\pi\chi l}{\sigma d^2 + 2\pi\chi l^2}$ Equation 1.7

and Gaussian curvature[64] $\langle K \rangle = -\frac{2\pi\chi}{\sigma d^2}$ Equation 1.8.

Equation 1.7 indicates that mean bilayer curvature increases with decreasing lattice parameter, and decreases with decreasing lipid tail length. Equation 1.8 shows that for a given mesophase type Gaussian curvature depends only on the lattice parameter.

We note that all relationships above rely on the assumption of the additivity of volumes. Thus, for the binary lipid/water system the volume fractions of aqueous and lipidic compartments are calculated simply based on the gravimetric composition of the sample and densities of lipid and water, although true volumetric relationships between the two compartments may deviate from the nominal ones due to non-zero volumes of mixing. Another standard assumption used in all equations listed above is that the lipid tail length, and, consequently, the bilayer thickness, is constant throughout the mesophase. For monoolein mesophases the variation in the lipid tail length and volume are believed to be associated with significant unfavorable free energy contributions,[73] justifying the assumption of their constant values.

1.3.3 Phase behavior of monoolein mesophases

Phase behavior monoolein/water mesophases. Monoolein, the lipid most commonly used for *in meso* crystallization, exhibits rich thermotropic and lyotropic phase behavior when mixed with water. Monoolein forms as many as six different phase types,[70,72] of which four are ordered, including two[63] cubic phases, as shown in the temperature-composition phase diagram in Figure 1.12. Some properties of monoolein mesophases are summarized in Table 1.3. All mesophases formed in monoolein/water systems are of the inverse type (type *II*, Figure 1.11), due to the "conical" amphiphile shape brought about by the *trans* double bond in the hydrophilic tail (Figure 1.2).

Monoolein and other monoacylglycerols have a propensity to form persistent undercooled metastable cubic phases,[74] and its observed phase behavior between 0 and 20 °C is differed depending on whether data were collected by heating (stable, Figure 1.12A) or cooling (metastable, Figure 1.12B) the samples. Remarkably, the undercooled metastable phases showed a series of reproducible phase transitions that obeyed the phase rule, mimicking equilibrium phase behavior and complicating the studies of phase transitions for monoolein and other monoacylglycerols.[72,74] To escape the metastable zone and to resume stable behavior upon heating in that temperature range, sample cooling to -13 °C was required.[74] The persistent metastable behavior has been attributed to small free energy differences between different types of mesophases and the high energy barrier for scission of the lipid bilayers as necessary for cubic-to-lamellar phase transition.[74] Note that most *in meso* crystallization protocols with

uniformly mixed protein-loaded mesophases rely on molten monoolein for mesophase formulation, and thus are likely to result in the metastable regime if incubation with precipitant is carried out below 20 °C.

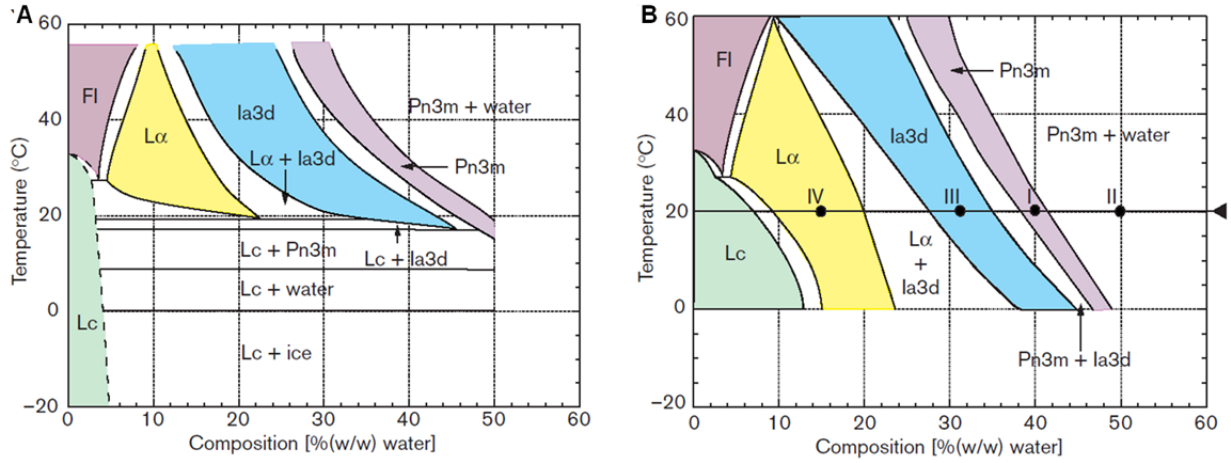

Figure 1.12. Temperature/composition phase diagram for the monoolein/water system. **(A)** Equilibrium phase diagram[74] and **(B)** metastable phase diagram.[72] Points I, II, and IV along the 20 °C isotherm correspond to single-phase regions with *Pn3m*, *Ia3d*, and *Lα* phases, respectively. Point II corresponds to a two-phase system where the *Pn3m* phase coexists with excess aqueous phase. (Reprinted from M. Caffrey, Current Opinion in Structural Biology, 2000, 10(4), 486-497, with permission from Elsevier.)

Table 1.3. Selected properties of various phases found in monoolein/water mixtures; adapted from references 74, 63, 75, and 66.

Notation	*Lc*	*Fl*	*Lα*	H_{II}	*Pn3m*	*Ia3d*
Phase type	Lamellar crystal	Fluid isotropic	Lamellar	Inverse hexagonal	Cubic	Cubic
Physical state	Solid	Fluid	Fluid	Fluid	Fluid	Fluid
Molecular ordering	1D-ordered	Disordered	1D-ordered	2D-ordered	3D-ordered	3D-ordered
Continuity	-	- (Homogenous solution of water in lipid)	-	Hydrophobic layers are continuous for small molecules	Bicontinous	Bicontinuous
Optical properties	Birefringent	Non-birefringent	Birefringent	Birefringent	Non-birefringent	Non-birefringent
Apparent viscosity,[66] relative to viscosity of water	N/A	30 x	10^4 x		10^7 x	10^7 x
Lipid bilayers	Flat	-	Flat	Curved	Curved	Curved

Overall, the studies of the phase behavior and, especially, of the microstructure of monoolein mesophases are complicated due to closely spaced phase transitions in the temperature range of interest (20-25 °C) and batch-to-batch variation of monoolein. Samples with nominally identical compositions were found to belong to different phase types, and lattice parameters of samples with identical composition depended on the batch of monoolein.[76]

In the range of temperatures of interest in this work, 20-25 °C, monoolein/water mesophases show stable behavior regardless of their thermal history. Monoolein proceeds through the following sequence of phases upon increasing hydration level (Figure 1.12):[72,74] lamellar crystal *Lc*, lamellar liquid crystal *Lα*, cubic *Ia3d*, and cubic *Pn3m*, with regions of two-phase coexistence in-between. The latter phase can only contain up to 40-43 wt% of water in this range of temperatures,[74,76] and a bulk aqueous phase separates from the water-saturated (fully hydrated) *Pn3m* mesophase if the overall water content of the sample is above that value.

Lattice parameters of monoolein mesophases shrink with increasing temperature due to the decrease in both the radius of the aqueous channels and the thickness of lipid bilayers (Equation 1.4). Briggs *et al.*[72] established a correlation for the length of the monoolein lipid tail as a function of temperature based on Equation 1.2 and SAXS data on lattice parameters as a function of sample composition:

$$l = 18e^{(-0.0019T)} \qquad \text{Equation 1.9}$$

where T is sample temperature in °C, and *l* is in Å.

Effect of salts on the microstructure of monoolein mesophases. Salts are the most common components in precipitant cocktails used for protein crystallization, but data on the effect on individual salts on the phase behavior of monoolein mesophases are extremely scarce.[32-34] Typically, the studies are carried out for monoolein coexisting with excess salt solution at a single temperature.

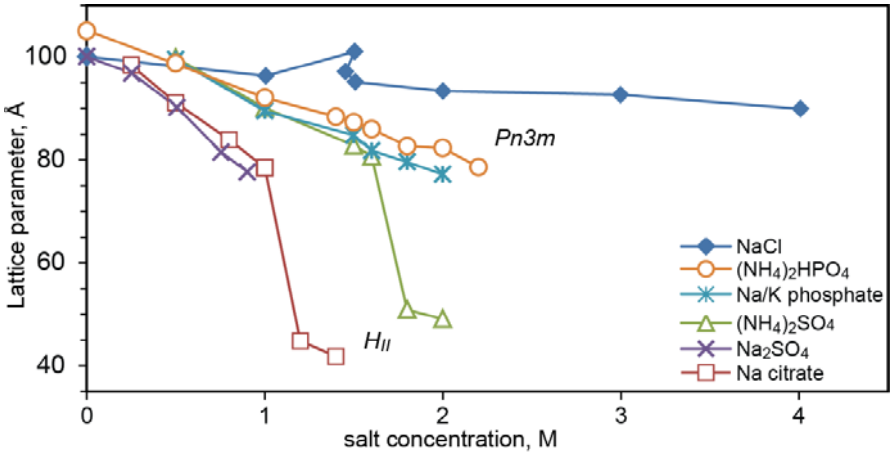

Figure 1.13. Effect of kosmotropic salts on the lattice parameter of fully hydrated mesophases of monoolein.[33,34]

The effect of salts on the phase behavior of monoolein mesophases and on their microstructure correlates with the Hofmeister series. Kosmotropic salts[33,34] (Figure 1.13) cause

the lattice parameter of the *Pn3m* phase to decrease compared to monoolein/water systems and in several cases result in the *Pn3m* – H_{II} transition as the salt concentration in solution increases. Interestingly, at a given pH the *Pn3m* – H_{II} transition for different salts, in spite of different salt concentrations, appeared to take place in a very narrow range of *Pn3m* lattice parameters, 77-81Å, suggesting a common curvature-driven mechanism of the phase transition. Chaotropic salts and urea,[25,34] on the contrary, cause the lattice parameters to increase (Figure 1.14) and may drive a *Pn3m* – sponge phase transition in these systems.

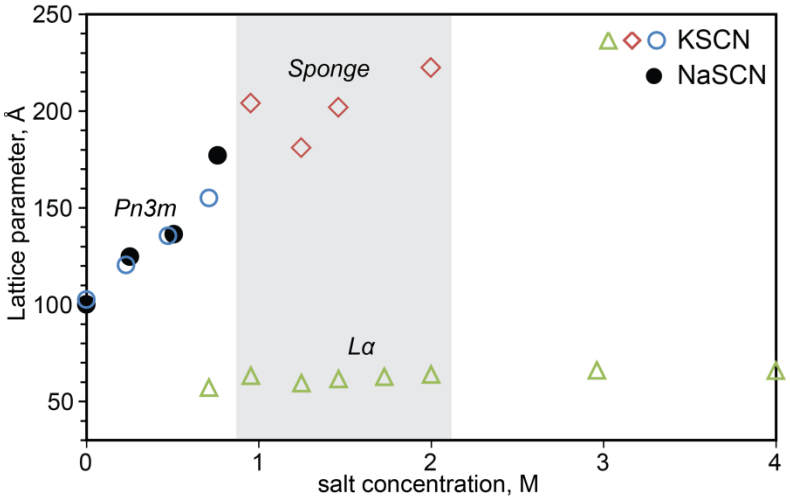

Figure 1.14. Comparison of the effect of chaotropic salts KSCN[25] and NaSCN[34] on the phase behavior of monoolein mesophases at 20 °C. Mixtures with KSCN were prepared using 60 wt% of monoolein and 40 wt% of the KSCN solution. Mixtures with NaSCN were prepared with an unspecified excess of the NaSCN solution.

Larger or smaller lattice parameters in monoolein/salt solution systems have been attributed to the effect of respective salts on the area of the lipid/water interface within the mesophase, with kosmotropes causing the area to shrink and chaotropes causing it to increase.[67,77,78] The length and volume of the lipid tail are usually assumed to vary little at a given temperature.[73] Combined, these assumptions indicate that the lipid bilayers become more curved in mixtures with kosmotropic salts and flattened in mixtures with chaotropic salts (Equations 1.4, 1.7, and 1.8). The lipid headgroup area a_{head} must vary accordingly to meet structure-composition relationships, becoming smaller in mixtures with kosmotropic salts and larger in mixtures with chaotropic salts. However, convincing explanations of the mechanism underlying these changes have not been put forward so far.

Two studies of similar chaotropic salts, KSCN and NaSCN,[25,34] allow for a comparison of the phase behavior under different compositional conditions at 20 °C (Figure 1.14). Mixtures

with KSCN were prepared using 40 wt% of salt solution and 60 wt% of monoolein,[25] whereas mixtures with NaSCN were formulated with a large excess of salt solution.[34] Interestingly, coexisting *Pn3m* and *Lα* phases were observed in the former set above KSCN concentration of 0.5 M, whereas in the set with NaSCN only pure *Pn3m* phases are observed. Although these observations may be related to an insufficiently wide range of NaSCN concentrations, they may also reflect the differences in the water contents of the two sets of samples. We note that based on our data presented in Chapter 2, potassium and sodium have almost identical effects on the lattice parameter and are not expected to cause the differences of the observed magnitude.

Effect of detergents on the microstructure of monoolein mesophases. Detergents are introduced into *in meso* crystallization mixtures as a necessary component of the membrane protein solutions (Chapter 1.1, Figure 1.1). Early reports indicated that detergents promote formation of lamellar phases unfavorable for crystallization, and their effect on the phase behavior of lipidic mesophases has been studied in a number of works to assess compatibility of detergents with the *in meso* method. Below we focus on the properties of monoolein mesophases with detergent β-octylglucoside (βOG),[14,76,79-84] one of the most common detergents for membrane protein solubilization. Other members of the alkylglucopyranoside family of detergents[76,79,80] show trends similar to those for βOG, as expected based on the similarity of their structures.

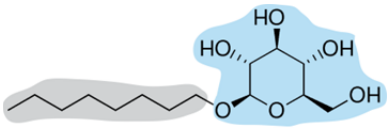

Figure 1.15 Structure of βOG with the polar head group shaded in blue and the hydrocarbon tail shaded in grey.

Due to their amphiphilic properties, detergents are incorporated in the lipid bilayers of the mesophase, and their effect on the microstructure of monoolein mesophases has been rationalized in terms of molecular shape.[13,76,80] In particular, βOG (Figure 1.15) has a larger polar glucoside headgroup and a significantly less voluminous 8-carbon tail chain hydrophobic tail compared to monoolein. These structural differences result in lowering of the average amphiphile packing parameter (Equation 1.1) in mixed bilayers and favor mesophases with less curved bilayers (Figure 1.11). The flattened bilayers in cubic mesophases can accommodate aqueous channels of larger radii, producing mesophases with larger lattice parameters. However, despite the different tail lengths of the amphiphiles, the thickness of the lipid bilayers in the *Pn3m* mesophase was found to remain almost constant upon mixing of monoolein with detergent solutions containing up to 10 wt% (0.34M) βOG.[85]

The effect of detergents has been studied almost exclusively using mixtures of monoolein with detergent solutions prepared in the 60:40 w/w ratio,[76,79,80] presumably to mimic the first step of the original protocol for *in meso* crystallization. In these systems, as the detergent concentration in solution increased, the detergent/monoolein ratio in the final mixture increased as well, whereas the water/monoolein ratio decreased. Only a few datasets are available for other types of mesophase formulations,[14,76,79] with a notable exception of a very detailed ternary phase diagram for the monoolein/βOG/water system.[81-83]

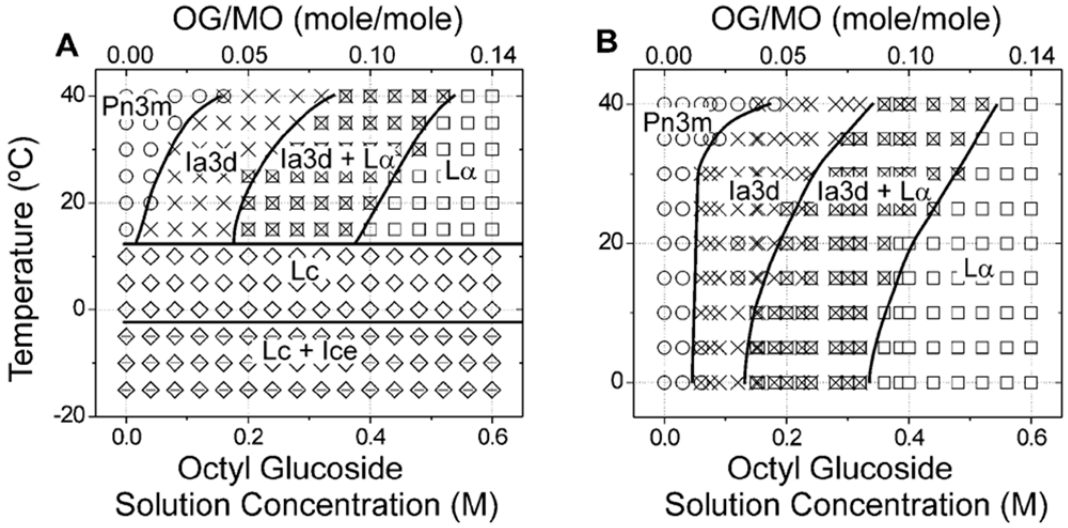

Figure 1.16. The identity and location in temperature-composition space of the various phases present in the monoolein/βOG/water system determined by x-ray diffraction. Samples were prepared with 60% (w/w) monoolein (MO) and a 40% (w/w) aqueous solution of βOG. **(A)** Measurements made in the heating direction from -15 °C to 40 °C. The identity of each of the phases is as follows: (-) *Lc*, (□) *Lα*, (◊) ice, (×) cubic-*Ia3d*, and (○) cubic-*Pn3m*. **(B)** Measurements made in the cooling direction from 30 °C to -15 °C, and in the heating direction from 25 °C to 40 °C. The identity of each of the phases is as follows: (□) *Lα*, (×) cubic-*Ia3d*, and (○) cubic-*Pn3m*. The samples were incubated at each temperature for a minimum of 4 h. The solid lines represent phase boundaries and are drawn to guide the eye. (Reprinted from Y. Misquitta and M. Caffrey, Biophysical Jounal, 2003, 85, 3084-3096, with permission from Elsevier.)

In mixtures of monoolein with solutions of βOG in water prepared using the 60/40 monoolein:solution weight ratio, the mesophase types changed in a highly systematic fashion as the detergent concentration in solution increased (Figure 1.16 A, B),[79] and the sequence of phase transformations matched that for monoolein/water mixtures upon dehydration (Figure 1.12). Lattice parameters of cubic phases, however, were significantly larger than those established in monoolein/water mesophases at the same temperature, as anticipated based on the larger preferred radii of aqueous channels and constant bilayer thickness (Equation 1.4). Metastability, characteristic of monoolein/water mesophases, was also observed in monoolein/βOG/water mixtures: phase behavior in the 0-12 °C range depended on the thermal history of the sample

(Figure 1.16 A, B). In another report[80] metastability was observed upon mesophase cooling to as low as -25 °C for a number of detergents, including βOG.

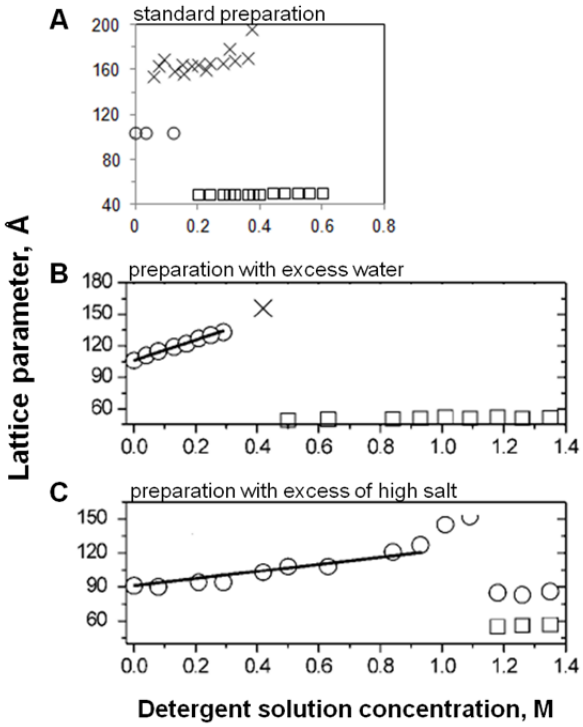

Figure 1.17. Dependence of monoolein phase behavior on detergent concentration at 20 °C in mixtures initially prepared with 60 wt% of monoolein and 40 wt% of βOG solutions **(A)** without further manipulation, **(B)** upon addition of excess water to the mixtures, or **(C)** upon addition of an excess of 2 M Na/K phosphate, pH 5.6. The βOG concentration on the X-axis refers to that in the initial preparation. The identity of each of the phases is as follows: (□) Lα, (×) cubic-*Ia3d*, and (○) cubic-*Pn3m*. The solid lines superimposed on the cubic-*Pn3m* phase data represent a linear fit of form: $d = 96.4\ M + 106$ in B, and $d = 33.4\ M + 91$ in C, where d is the lattice parameter of the cubic-*Pn3m* phase (in Å) and M is the molar concentration of the βOG solution. The linear fit in C was from 0 to 0.93 M βOG solution. The last two data points at 1.01 and 1.09 M βOG solution were not included because the corresponding diffraction patterns consisted of a few relatively broad low-angle reflections and therefore their lattice parameters could not be accurately determined. (Reprinted from Y. Misquitta and M. Caffrey, Biophysical Jounal, 2003, 85, 3084-3096, with permission from Elsevier.)

Figure 1.17B shows the types and lattice parameters of monoolein/βOG/water mesophases that contained an excess of water,[79] with notable differences in the phase behavior compared to mesophases with a limited amount of water at the same detergent concentration in solution (Figure 1.17A). These findings suggest that the samples in Figure 1.17A are significantly water-stressed, and the mesophases could accommodate larger amounts of water at a given βOG/monoolein ratio. Datasets for mesophases under both water-stressed and excess water conditions are in excellent agreement with the full ternary diagram for monoolein/βOG/water mixtures at 20 °C mapped using NMR techniques.[81-83] Compared to their water-stressed counterparts, fully hydrated mesophases with mixed βOG/monoolein bilayers may be more suitable proxies for assessing the phase behavior of the system in crystallization trials that always take place under excess aqueous solution conditions. Indeed, in monoolein/βOG mesophases prepared with excess of 2M K/Na phosphate (Figure 1.17C), the cubic phase persisted at even higher detergent loadings than in fully hydrated mixtures with water shown in Figure 1.17B, which would be almost impossible to infer from data on partially hydrated systems in Figure 1.17A. Overall, these comparisons highlight the difficulties in

inferring the phase behavior of complex multicomponent systems in a wide range of compositions from a limited set of data. Nevertheless, data on water-stressed mixtures may be useful for assessing the suitability of the mesophase for protein stabilization in the first step of the protocol before precipitant addition because membrane proteins are known to be unstable in lamellar phases.[14]

1.4 Key challenges

1.4.1 Crystallization of membrane proteins in lipidic mesophases

As in any protein crystallization method, crystallization *in meso* is achieved in a trial-and-error manner and requires sampling of a large number of conditions. For example, over 15000 crystallization trials were set up to obtain a few diffraction-quality crystals of β2 adrenergic receptor.[15] This approach presents the typical challenges, such as the large amount of protein sample required for crystallization efforts on that scale, and manually intensive set up of crystallization trials. Liquid-handling robots are expensive and may be beyond reach of many structural biology labs.

In addition to those challenges, the *in meso* method is perceived as difficult in the structural biology community, not least due to the special tools required for almost every step of the standard protocol (Figure 1.5), such as the coupled syringe mixer and the ratchet dispenser. Because of the non-uniform appearance of bulk mesophases, the *in meso* method also requires special glass sandwich well plates[86] to facilitate observation of protein crystals. These plates are not suitable for the relatively user-friendly variants of the in meso method, such as PLI[43] and CIMP[44] (Figure 1.6).

The last and possibly the most important challenge is the manual harvesting of fragile protein crystals for crystal X-ray diffraction, which may also be detrimental for crystal quality. The high viscosity of the mesophase, coupled with the typically small size of membrane protein crystals (5-50 μm), make this step difficult, yet several hundred crystals may need to be harvested in order to obtain quality X-ray diffraction data.

1.4.2 Phase behavior of lipidic mesophases

Precipitants used to induce crystallization are complex mixtures of multiple components, such as polyethyleneglycols (PEGs) of various molecular weights, organic and inorganic salts, and small organic molecules such as short-chain saturated alcohols and cholesterol.[16] In addition to these components, protein-solubilizing detergents are also incorporated into the mesophase along with the proteins.[13,14,76,79-83] All these components are known to affect the phase behavior of monoolein, as summarized in Chapter 1.3.3.[14,32-34,76,79-84] An *in meso* crystallization system contains at least two phases, the aqueous precipitant solution and the viscous mesophase with embedded protein (Figure 1.1D). The enormous complexity of such multiphase multicomponent systems precludes *a priori* predictions of the phase behavior under crystallization conditions. Thus, extensive experimental phase behavior studies are required to ensure that the components are compatible with the formation of the cubic phase.

Detailed information about phase transformations in real, highly complex multi-component multi-phase crystallization mixtures is necessary to improve the understanding of the mechanism of *in meso* crystallization. Monoolein/water systems exhibit rich mesomorphism and intricate phase behavior at temperatures relevant for protein crystallization, with *Pn3m*, *Ia3d* or *Lα* mesophases forming depending on the hydration level and the thermal history of the sample.[72,74] Although multiple studies showed that both detergents[14,76,79-81,84] and salts[32-34] affect the phase behavior of monoolein (Chapter 1.3.3), their combined effects have rarely been investigated. Furthermore, few studies[14,76,79] mimic crystallization systems by independently controlling the monoolein/detergent ratio and the amount of aqueous phase, as determined by the two steps of the crystallization process. The distributions of components between the phases in the two-phase system, and, in turn, the properties of the mesophase, are likely to depend on relative amounts of the mesophase and the solution. However, only little information is available about the location of the hydration boundary in crystallization-like systems and about actual conditions experienced by the protein within the mesophase during crystallization.

Phase behavior studies require the preparation of a large number of samples with different compositions to obtain a detailed map. For example, the phase diagram of the binary monoolein/water system in Figure 1.12A is based on data from 25 samples.[72] Over 200 samples had to be prepared to assess compatibility of commercial protein crystallization screens with the formation of the cubic phase.[16] State-of-the-art procedure[15] involves mixing lipids and aqueous

solutions in the coupled syringe mixer (Figure 1.5) followed by dispensing the mesophase into thin-walled glass capillaries for SAXS analysis. Mixing in the coupled syringe mixer requires 5-20 μL (mg) of both lipid and the aqueous solution. The overall procedure is highly laborious, repetitive, sample-consuming, and not easily amenable for automation, which all impediment for studies to unravel the phase behavior of lipidic mesophases as necessary for the optimization of *in meso* crystallization and for the fundamental studies in soft matter.

1.4.3 X-ray-compatible microfluidic platforms for mesophase formulation and *in meso* crystallization

Microfluidic approaches offer great potential for providing inexpensive tools for *in meso* crystallization and studies of the phase behavior of lipidic mesophases by automating sample formulation and reducing the amount of materials. The main challenges in both applications are (1) on-chip handling of the viscous mesophases and (2) development of an X-ray transparent chip architecture. The latter is a requirement for *in situ* mesophase analysis by SAXS, and is highly desirable for *in situ* protein crystal X-ray diffraction analysis to eliminate cumbersome and damaging crystal harvesting steps.

Development of X-ray compatible platforms capable of mesophase handling is a non-trivial task and platforms of this type have not been reported to date. Available platforms for both protein crystallization and phase behavior studies are mostly limited to handling of low-viscosity aqueous solutions, with the exception of the two systems described in Chapter 1.2.5. Established methods of rapid prototyping[56,87] and fabrication of microfluidic devices with integrated fluid handling capabilities[55] produce devices with mm-thick layers of PDMS on a glass substrate (Chapter 1.2.5) and are unsuitable for *in situ* X-ray analysis due to X-ray attenuation by the chip materials.[88]

Microfluidic systems for phase behavior studies typically rely on phase transitions driven by composition changes due to diffusion of solutes,[89-94] evaporation of water,[95-99] and osmotic stress.[91,100] These platforms are unsuitable for the formulation of viscous mesophases with strict pre-set ratios of volume or weight of components. In addition to those limitations, X-ray compatible chip architectures for phase behavior studies have not been reported so far.

Only a few X-ray transparent microfluidic chips have been reported for protein crystallography, mainly for on-chip crystallization and *in situ* crystal X-ray diffraction of soluble

proteins.[88,101-110] The chips, with a single exception,[110] are fabricated in rigid polymeric materials and are thus incapable of fluid valving and routing necessary for formulating complex arrays of multicomponent mixtures on-chip in an automated fashion.

As discussed in Chapter 1.2.2, the microstructure of the mesophase is of key importance for the outcome of crystallization trials. The ability to study both protein crystals and mesophase properties in X-ray transparent microfluidic platforms would be invaluable for further elucidating the mechanism of *in meso* crystallization and engineering crystallization systems to improve the success rate of the crystallization process.

1.5 References

1 A. W. Partridge, A. G. Therien and C. M. Deber. Polar mutations in membrane proteins as a biophysical basis for disease. *Peptide Sci.*, 2002, **66**, 350-358.

2 J. P. Overington, B. Al-Lazikani and A. L. Hopkins. How many drug targets are there? *Nat. Rev. Drug Discov.*, 2006, **5**, 993-996.

3 P. Raman, V. Cherezov and M. Caffrey. The membrane protein data bank. *Cell. Mol. Life Sci.*, 2006, **63**, 36-51.

4 H. M. Berman, J. Westbrook, Z. Feng, G. Gilliland, T. N. Bhat, H. Weissig, I. N. Shindyalov and P. E. Bourne. The protein data bank. *Nucleic Acids Res.*, 2000, **28**, 235-242. http://www.pdb.org.

5 C. Hunte, G. von Jagow and H. Schagger, eds., *Membrane protein purification and crystallization: A practical guide, 2nd edition*, Academic Press, San Diego, 2003.

6 J. P. Rosenbusch, A. Lustig, M. Grabo, M. Zulauf and M. Regenass. Approaches to determining membrane protein structures to high resolution: Do selections of subpopulations occur? *Micron*, 2001, **32**, 75-90.

7 R. Ujwal and J. U. Bowie. Crystallizing membrane proteins using lipidic bicelles. *Methods*, 2011, **55**, 337-341.

8 E. M. Landau and J. P. Rosenbusch. Lipidic cubic phases: A novel concept for the crystallization of membrane proteins. *Proc. Natl. Acad. Sci. USA*, 1996, **93**, 14532-14535.

9 V. Cherezov, D. M. Rosenbaum, M. A. Hanson, S. G. F. Rasmussen, F. S. Thian, T. S. Kobilka, H.-J. Choi, P. Kuhn, W. I. Weis, B. K. Kobilka and R. C. Stevens. High-resolution crystal structure of an engineered human β_2-adrenergic G-protein coupled receptor. *Science*, 2007, **318**, 1258-1265.

10 H. Wu, D. Wacker, M. Mileni, V. Katritch, G. W. Han, E. Vardy, W. Liu, A. A. Thompson, X.-P. Huang, F. I. Carroll, S. W. Mascarella, R. B. Westkaemper, P. D. Mosier, B. L. Roth, V. Cherezov and R. C. Stevens. Structure of the human κ-opioid receptor in complex with jdtic. *Nature*, 2012, **425**, 327-332.

11 M. L. Lynch and P. T. Spicer, eds., *Bicontinuous liquid crystals*, CRC Press, 2005.

12 D. M. Anderson, H. T. Davis, L. E. Scriven and J. C. C. Nitsche. Periodic surfaces of prescribed mean curvature. *Advances in Chemical Physics*, 2007, 337-396.

13 P. Nollert, H. Qiu, M. Caffrey, J. P. Rosenbusch and E. M. Landau. Molecular mechanism for the crystallization of bacteriorhodopsin in lipidic cubic phases. *FEBS Lett.*, 2001, **504**, 179-186.
14 E. Sparr, P. Wadsten, V. Kocherbitov and S. Engström. The effect of bacteriorhodopsin, detergent and hydration on the cubic-to-lamellar phase transition in the monoolein–distearoyl phosphatidyl glycerol–water system. *Biochim. Biophys. Acta - Biomembr.*, 2004, **1665**, 156-166.
15 M. Caffrey and V. Cherezov. Crystallizing membrane proteins using lipidic mesophases. *Nat. Protocols*, 2009, **4**, 706-731.
16 V. Cherezov, H. Fersi and M. Caffrey. Crystallization screens: Compatibility with the lipidic cubic phase for in meso crystallization of membrane proteins. *Biophys. J.*, 2001, **81**, 225-242.
17 K. Fontell. Cubic phases in surfactant and surfactant-like lipid systems. *Colloid Polymer Sci.*, 1990, **268**, 264-285.
18 B. Alberts, D. Bray, J. Lewis, M. Raff, K. Roberts and J. D. Watson, *Molecular biology of the cell*, Garland Science, New York, 1994.
19 M. Caffrey, J. Lyons, T. Smyth and D. J. Hart, in *Current topics in membranes*, ed. D. Larry, Academic Press, 2009, vol. 63, ch. 4, pp. 83-108.
20 V. Cherezov. Lipidic cubic phase technologies for membrane protein structural studies. *Curr. Opin. Struct. Biol.*, 2011, **21**, 559-566.
21 L. V. Misquitta, Y. Misquitta, V. Cherezov, O. Slattery, J. M. Mohan, D. Hart, M. Zhalnina, W. A. Cramer and M. Caffrey. Membrane protein crystallization in lipidic mesophases with tailored bilayers. *Structure*, 2004, **12**, 2113-2124.
22 D. Li, J. Lee and M. Caffrey. Crystallizing membrane proteins in lipidic mesophases. A host lipid screen. *Cryst. Growth Design*, 2011, **11**, 530-537.
23 J. Yamashita, M. Shiono and M. Hato. New lipid family that forms inverted cubic phases in equilibrium with excess water: Molecular structure − aqueous phase structure relationship for lipids with 5,9,13,17-tetramethyloctadecyl and 5,9,13,17-tetramethyloctadecanoyl chains. *J. Phys. Chem. B*, 2008, **112**, 12286-12296.
24 V. Borshchevskiy, E. Moiseeva, A. Kuklin, G. Büldt, M. Hato and V. Gordeliy. Isoprenoid-chained lipid β-xyloc16+4—a novel molecule for *in meso* membrane protein crystallization. *J. Gryst. Growth*, 2010, **312**, 3326-3330.
25 V. Cherezov, J. Clogston, M. Z. Papiz and M. Caffrey. Room to move: Crystallizing membrane proteins in swollen lipidic mesophases. *J. Mol. Biol.*, 2006, **357**, 1605-1618.
26 V. Cherezov and M. Caffrey. Membrane protein crystallization in lipidic mesophases. A mechanism study using X-ray microdiffraction. *Faraday Discuss.*, 2007, **136**, 195-212.
27 M. Grabe, J. Neu, G. Oster and P. Nollert. Protein interactions and membrane geometry. *Biophys. J.*, 2003, **84**, 854-868.
28 R. Efremov, G. Shiryaeva, G. Bueldt, A. Islamov, A. Kuklin, L. Yaguzhinsky, G. Fragneto-Cusani and V. Gordeliy. SANS investigations of the lipidic cubic phase behaviour in course of bacteriorhodopsin crystallization. *J. Gryst. Growth*, 2005, **275**, e1453-e1459.
29 H. Michel and J. Deisenhofer. Nobel lecture. The photosynthetic reaction centre from the purple bacterium rhodopseudomonas viridis. *EMBO J.*, 1989, **8**, 2149-2170.

30 M. Caffrey, D. Li and A. Dukkipati. Membrane protein structure determination using crystallography and lipidic mesophases: Recent advances and successes. *Biochemistry*, 2012, **51**, 6266-6288.
31 Y. Qutub, I. Reviakine, C. Maxwell, J. Navarro, E. M. Landau and P. G. Vekilov. Crystallization of transmembrane proteins *in cubo*: Mechanisms of crystal growth and defect formation. *J. Mol. Biol.*, 2004, **343**, 1243-1254.
32 M. Caffrey. Kinetics and mechanism of transitions involving the lamellar, cubic, inverted hexagonal and fluid isotropic phases of hydrated monoacylglycerides monitored by time-resolved x-ray diffraction. *Biochemistry*, 1987, **26**, 6349-6363.
33 R. Vargas, L. Mateu and A. Romero. The effect of increasing concentrations of precipitating salts used to crystallize proteins on the structure of the lipidic Q^{224} cubic phase. *Chem. Phys. Lipids*, 2004, **127**, 103-111.
34 H. Takahashi, A. Matsuo and I. Hatta. Effects of chaotropic and kosmotropic solutes on the structure of lipid cubic phase: Monoolein-water systems. *Mol. Cryst. Liquid Cryst. A*, 2000, **347**, 231-238.
35 V. Cherezov, J. Liu, M. Griffith, M. A. Hanson and R. C. Stevens. LCP-FRAP assay for pre-screening membrane proteins for in meso crystallization. *Cryst. Growth Design*, 2008, **8**, 4307-4315.
36 F. Xu, W. Liu, M. A. Hanson, R. C. Stevens and V. Cherezov. Development of an automated high throughput LCP-FRAP assay to guide membrane protein crystallization in lipid mesophases. *Cryst. Growth Design*, 2011, **11**, 1193-1201.
37 J. S. Joseph, W. Liu, J. Kunken, T. M. Weiss, H. Tsuruta and V. Cherezov. Characterization of lipid matrices for membrane protein crystallization by high-throughput small angle X-ray scattering. *Methods*, 2011, **55**, 342-349.
38 C. E. Conn, C. Darmanin, X. Mulet, S. Le Cann, N. Kirby and C. J. Drummond. High-throughput analysis of the structural evolution of the monoolein cubic phase *in situ* under crystallogenesis conditions. *Soft Matter*, 2012, **8**, 2310-2321.
39 Y. Misquitta, V. Cherezov, F. Havas, S. Patterson, J. M. Mohan, A. J. Wells, D. J. Hart and M. Caffrey. Rational design of lipid for membrane protein crystallization. *J. Struct. Biol.*, 2004, **148**, 169-175.
40 A. B. Wohri, L. C. Johansson, P. Wadsten-Hindrichsen, W. Y. Wahlgren, G. Fischer, R. Horsefield, G. Katona, M. Nyblom, F. Oberg, G. Young, R. J. Cogdell, N. J. Fraser, S. Engstrom and R. Neutze. A lipidic-sponge phase screen for membrane protein crystallization. *Structure*, 2008, **16**, 1003-1009.
41 V. Cherezov, E. Abola and R. C. Stevens. Recent progress in the structure determination of GPCRs, a membrane protein family with high potential as pharmaceutical targets. *Methods Mol. Biol.*, 2010, **654**, 141-168.
42 M. L. Chiu, P. Nollert, M. C. Loewen, H. Belrhali, E. Pebay-Peyroula, J. P. Rosenbusch and E. M. Landau. Crystallization in cubo: General applicability to membrane proteins. *Acta Crystallogr. D*, 2000, **56**, 781-784.
43 E. Wallace, D. Dranow, P. D. Laible, J. Christensen and P. Nollert. Monoolein lipid phases as incorporation and enrichment materials for membrane protein crystallization. *PLoS ONE*, 2011, **6**, e24488.
44 J. Kubicek, R. Schlesinger, C. Baeken, G. Büldt, F. Schäfer and J. Labahn. Controlled *in meso* phase crystallization – a method for the structural investigation of membrane proteins. *PLoS ONE*, 2012, **7**, e35458.

45 V. Cherezov, A. Peddi, L. Muthusubramaniam, Y. F. Zheng and M. Caffrey. A robotic system for crystallizing membrane and soluble proteins in lipidic mesophases. *Acta Crystallogr. D*, 2004, **60**, 1795-1807.
46 V. Cherezov and M. Caffrey. A simple and inexpensive nanoliter-volume dispenser for highly viscous materials used in membrane protein crystallization. *J. Appl. Crystallogr.*, 2005, **38**, 398-400.
47 V. Cherezov and M. Caffrey. Picolitre-scale crystallization of membrane proteins. *J. Appl. Crystallogr.*, 2006, **39**, 604-606.
48 L. Li, Q. Fu, C. Kors, L. Stewart, P. Nollert, P. Laible and R. Ismagilov. A plug-based microfluidic system for dispensing lipidic cubic phase (LCP) material validated by crystallizing membrane proteins in lipidic mesophases. *Microfluidics Nanofluidics*, 2010, **8**, 789-798.
49 J. Melin and S. R. Quake. Microfluidic large-scale integration: The evolution of design rules for biological automation. *Annu. Rev. Biophys. Biomol. Structure*, 2007, **36**, 213-231.
50 A. D. van der Meer, A. A. Poot, M. H. G. Duits, J. Feijen and I. Vermes. Microfluidic technology in vascular research. *J. Biomed. Biotechnol.*, 2009, **2009**.
51 S. J. Maerkl. Next generation microfluidic platforms for high-throughput protein biochemistry. *Curr. Opin. Biotechnol.*, 2011, **22**, 59-65.
52 P. Neuži, S. Giselbrecht, K. Länge, T. J. Huang and A. Manz. Revisiting lab-on-a-chip technology for drug discovery. *Nat. Rev. Drug Discov.*, 2012, **11**, 620-632.
53 D. Gao, H. Liu, Y. Jiang and J.-M. Lin. Recent developments in microfluidic devices for in vitro cell culture for cell-biology research. *Trends Anal. Chem.*, 2012, **35**, 150-164.
54 H. Yin and D. Marshall. Microfluidics for single cell analysis. *Curr. Opin. Biotechnol.*, 2012, **23**, 110-119.
55 M. A. Unger, H.-P. Chou, T. Thorsen, A. Scherer and S. R. Quake. Monolithic microfabricated valves and pumps by multilayer soft lithography. *Science*, 2000, **288**, 113-116.
56 Y. Xia and G. M. Whitesides. Soft lithography. *Angew. Chem. Int. Ed.*, 1998, **37**, 550-575.
57 K. Hosokawa and R. Maeda. A pneumatically-actuated three-way microvalve fabricated with polydimethylsiloxane using the membrane transfer technique. *J. Micromech. Microeng.*, 2000, **10**, 415.
58 G. A. Cooksey, C. G. Sip and A. Folch. A multi-purpose microfluidic perfusion system with combinatorial choice of inputs, mixtures, gradient patterns, and flow rates. *Lab Chip*, 2009, **9**, 417-426.
59 B. R. Schudel, M. Tanyeri, A. Mukherjee, C. M. Schroeder and P. J. A. Kenis. Multiplexed detection of nucleic acids in a combinatorial screening chip. *Lab Chip*, 2011, **11**, 1916-1923.
60 R. Mohan, B. R. Schudel, A. V. Desai, J. D. Yearsley, C. A. Apblett and P. J. A. Kenis. Design considerations for elastomeric normally closed microfluidic valves. *Sensors Actuators B*, 2011, **160**, 1216-1223.
61 L. Li and R. F. Ismagilov. Protein crystallization using microfluidic technologies based on valves, droplets, and SlipChip. *Annu. Rev. Biophys.*, 2010, **39**, 139-158.

62 S. L. Perry, G. W. Roberts, J. D. Tice, R. B. Gennis and P. J. A. Kenis. Microfluidic generation of lipidic mesophases for membrane protein crystallization. *Cryst. Growth Design*, 2009, **9**, 2566-2569.
63 K. Larsson. Two cubic phases in monoolein-water system. *Nature*, 1983, **304**, 664-664.
64 S. T. Hyde. Microstructure of bicontinuous surfactant aggregates. *J. Phys. Chem.*, 1989, **93**, 1458-1464.
65 D. C. Turner, Z.-G. Wang, S. M. Gruner, D. A. Mannock and R. N. McElhaney. Structural study of the inverted cubic phases of di-dodecyl alkyl-β-d-glucopyranosyl-rac-glycerol *J. Phys. II*, 1992, **2**, 2039-2063.
66 R. Mezzenga, C. Meyer, C. Servais, A. I. Romoscanu, L. Sagalowicz and R. C. Hayward. Shear rheology of lyotropic liquid crystals: A case study. *Langmuir*, 2005, **21**, 3322-3333.
67 C. V. Kulkarni, W. Wachter, G. Iglesias-Salto, S. Engelskirchen and S. Ahualli. Monoolein: A magic lipid? *Phys. Chem. Chem. Phys.*, 2011, **13**, 3004-3021. A number of equations in the article contain typos, and it is best to consult original works referenced there.
68 P. Mariani, V. Luzzati and H. Delacroix. Cubic phases of lipid-containing systems. Structure analysis and biological implications. *J. Mol. Biol.*, 1988, **204**, 165-189.
69 D. E. Sands, *Introduction to crystallography*, W.A. Benjamin, Inc., New York, NY, 1969.
70 J. N. Israelachvili, D. J. Mitchell and B. W. Ninham. Theory of self-assembly of hydrocarbon amphiphiles into micelles and bilayers. *J. Chem. Soc. Faraday Trans. II*, 1976, **72**, 1525-1568.
71 A. Gulik, V. Luzzati, M. De Rosa and A. Gambacorta. Structure and polymorphism of bipolar isopranyl ether lipids from archaebacteria. *J. Mol. Biol.*, 1985, **182**, 131-149.
72 J. Briggs, H. Chung and M. Caffrey. The temperature-composition phase diagram and mesophase structure characterization of the monoolein/water system. *J. Phys. II*, 1996, 723-751.
73 G. C. Shearman, O. Ces and R. H. Templer. Towards an understanding of phase transitions between inverse bicontinuous cubic lyotropic liquid crystalline phases. *Soft Matter*, 2010, **6**, 256-262.
74 H. Qiu and M. Caffrey. The phase diagram of the monoolein/water system: Metastability and equilibrium aspects. *Biomaterials*, 2000, **21**, 223-234.
75 W. Longley and T. J. McIntosh. A bicontinuous tetrahedral structure in a liquid-crystalline lipid. *Nature*, 1983, **303**, 612-614.
76 X. Ai and M. Caffrey. Membrane protein crystallization in lipidic mesophases: Detergent effects. *Biophys. J.*, 2000, **79**, 394-405.
77 M. Caffrey. A lipid's eye view of membrane protein crystallization in mesophases. *Curr. Opin. Struct. Biol.*, 2000, **10**, 486-497.
78 M. Caffrey. Membrane protein crystallization. *J. Struct. Biol.*, 2003, **142**, 108-132.
79 Y. Misquitta and M. Caffrey. Detergents destabilize the cubic phase of monoolein: Implications for membrane protein crystallization. *Biophys. J.*, 2003, **85**, 3084-3096.
80 C. Sennoga, A. Heron, J. M. Seddon, R. H. Templer and B. Hankamer. Membrane-protein crystallization in cubo: Temperature-dependent phase behaviour of monoolein-detergent mixtures. *Acta Crystallogr. D*, 2003, **59**, 239-246.

81 G. Persson, H. Edlund, H. Amenitsch, P. Laggner and G. Lindblom. The 1-monooleoyl-*rac*-glycerol/*n*-octyl-β-d-glucoside/water system. Phase diagram and phase structures determined by NMR and X-ray diffraction. *Langmuir*, 2003, **19**, 5813-5822.

82 G. Persson, H. Edlund and G. Lindblom. Thermal behaviour of cubic phases rich in 1-monooleoyl-*rac*-glycerol in the ternary system 1-monooleoyl-*rac*-glycerol/*n*-octyl-β-d-glucoside/water. *Eur. J. Biochem.*, 2003, **270**, 56-65.

83 G. Persson, H. Edlund and G. Lindblom. Phase behaviour of the 1-monooleoyl-*rac*-glycerol /*n*-octyl-β-d-glucoside/water system. *Progr. Colloid Polym. Sci.*, 2004, **123**, 36-39.

84 B. Angelov, M. Ollivon and A. Angelova. X-ray diffraction study of the effect of the detergent octyl glucoside on the structure of lamellar and nonlamellar lipid/water phases of use for membrane protein reconstitution. *Langmuir*, 1999, **15**, 8225-8234.

85 B. Angelov, A. Angelova, M. Ollivon, C. Bourgaux and A. Campitelli. Diamond-type lipid cubic phase with large water channels. *J. Am. Chem. Soc.*, 2003, **125**, 7188-7189.

86 V. Cherezov and M. Caffrey. Nano-volume plates with excellent optical properties for fast, inexpensive crystallization screening of membrane proteins. *J. Appl. Crystallogr.*, 2003, **36**, 1372-1377.

87 D. C. Duffy, J. C. McDonald, O. J. A. Schueller and G. M. Whitesides. Rapid prototyping of microfluidic systems in poly(dimethylsiloxane). *Anal. Chem.*, 1998, **70**, 4974-4984.

88 K. Dhouib, C. Khan Malek, W. Pfleging, B. Gauthier-Manuel, R. Duffait, G. Thuillier, R. Ferrigno, L. Jacquamet, J. Ohana, J.-L. Ferrer, A. Theobald-Dietrich, R. Giege, B. Lorber and C. Sauter. Microfluidic chips for the crystallization of biomacromolecules by counter-diffusion and on-chip crystal X-ray analysis. *Lab Chip*, 2009, **9**, 1412-1421.

89 F. Shi, Z. Han, J. Li, B. Zheng and C. Wu. Mapping polymer phase diagram in nanoliter droplets. *Macromolecules*, 2012, **44**, 686-689.

90 S. Park, P. A. L. Wijethunga, H. Moon and B. Han. On-chip characterization of cryoprotective agent mixtures using an ewod-based digital microfluidic device. *Lab Chip*, 2011, **11**, 2212-2221.

91 J. U. Shim, G. Cristobal, D. R. Link, T. Thorsen, Y. W. Jia, K. Piattelli and S. Fraden. Control and measurement of the phase behavior of aqueous solutions using microfluidics. *J. Am. Chem. Soc.*, 2007, **129**, 8825-8835.

92 M. J. Anderson, C. L. Hansen and S. R. Quake. Phase knowledge enables rational screens for protein crystallization. *Proc. Natl. Acad. Sci. USA*, 2006, **103**, 16746-16751.

93 M. O. A. Sommer and S. Larsen. Crystallizing proteins on the basis of their precipitation diagram determined using a microfluidic formulator. *J. Synchrotron Rad.*, 2005, **12**, 779-785.

94 C. L. Hansen, M. O. A. Sommer and S. R. Quake. Systematic investigation of protein phase behavior with a microfluidic formulator. *Proc. Natl. Acad. Sci. USA*, 2004, **101**, 14431-14436.

95 P. Moreau, J. Dehmoune, J. B. Salmon and J. Leng. Microevaporators with accumulators for the screening of phase diagrams of aqueous solutions. *Appl. Phys. Lett.*, 2009, **95**, 033108.

96 J.-B. Salmon and J. Leng. Microfluidics for kinetic inspection of phase diagrams. *Compt. Rend. Chim.*, 2009, **12**, 258-269.

97 J. Leng, M. Joanicot and A. Ajdari. Microfluidic exploration of the phase diagram of a surfactant/water binary system. *Langmuir*, 2007, **23**, 2315-2317.
98 J. Leng, B. Lonetti, P. Tabeling, M. Joanicot and A. Ajdari. Microevaporators for kinetic exploration of phase diagrams. *Phys. Rev. Lett.*, 2006, **96**, 084503.
99 X. Zhou, J. Li, C. Wu and B. Zheng. Constructing the phase diagram of an aqueous solution of poly(n-isopropyl acrylamide) by controlled microevaporation in a nanoliter microchamber. *Macromol. Rapid Comm.*, 2008, **29**, 1363-1367.
100 S. Selimovic, F. Gobeaux and S. Fraden. Mapping and manipulating temperature-concentration phase diagrams using microfluidics. *Lab Chip*, 2010, **10**, 1696-1699.
101 G. Kisselman, W. Qiu, V. Romanov, C. M. Thompson, R. Lam, K. P. Battaile, E. F. Pai and N. Y. Chirgadze. X-chip: An integrated platform for high-throughput protein crystallization and on-the-chip X-ray diffraction data collection. *Acta Crystallogr. D*, 2011, **67**, 533-539.
102 B. Zheng, J. D. Tice, L. S. Roach and R. F. Ismagilov. A droplet-based, composite PDMS/glass capillary microfluidic system for evaluating protein crystallization conditions by microbatch and vapor-diffusion methods with on-chip x-ray diffraction. *Angew. Chem. Int. Ed.*, 2004, **43**, 2508-2511.
103 C. J. Gerdts, M. Elliott, S. Lovell, M. B. Mixon, A. J. Napuli, B. L. Staker, P. Nollert and L. Stewart. The plug-based nanovolume microcapillary protein crystallization system (mpcs). *Acta Crystallogr. D*, 2008, **64**, 1116-1122.
104 C. P. Steinert, J. Mueller-Dieckmann, M. Weiss, M. Roessle, R. Zengerle and P. Koltay, Miniaturized and highly parallel protein crystallization on a microfluidic disc, 20th IEEE Intl. Conf. on Micro Electro Mechanical Systems (MEMS 2007), Hyogo, Japan, 2007.
105 J. D. Ng, P. J. Clark, R. C. Stevens and P. Kuhn. In situ X-ray analysis of protein crystals in low-birefringent and X-ray transmissive plastic microchannels. *Acta Crystallogr. D*, 2008, **64**, 189-197.
106 C. L. Hansen, S. Classen, J. M. Berger and S. R. Quake. A microfluidic device for kinetic optimization of protein crystallization and in situ structure determination. *J. Am. Chem. Soc.*, 2006, **128**, 3142-3143.
107 C. Sauter, K. Dhouib and B. Lorber. From macrofluidics to microfluidics for the crystallization of biological macromolecules *Cryst. Growth Design*, 2007, **7**, 2247-2250.
108 E. D. Greaves and A. Manz. Toward on-chip X-ray analysis. *Lab Chip*, 2005, **5**, 382-391.
109 R. Barrett, M. Faucon, J. Lopez, G. Cristobal, F. Destremaut, A. Dodge, P. Guillot, P. Laval, C. Masselon and J.-B. Salmon. X-ray microfocussing combined with microfluidics for on-chip X-ray scattering measurements. *Lab Chip*, 2006, **6**, 494-499.
110 S. Guha, S. L. Perry, A. S. Pawate and P. J. A. Kenis. Fabrication of X-ray compatible microfluidic platforms for protein crystallization. *Sensors Actuators B*, 2012, **174**, 1-9.

Chapter 2.

Phase behavior of monoolein mesophases with detergent β-octyglucoside and phosphate salt solutions

Abstract

This chapter summarizes the results of the studies of phase behavior of mesophases of monoolein (MO) mixed with additives frequently used in the *in meso* membrane protein crystallization, namely, sodium and potassium phosphate salts and the detergent β-octylglucoside (βOG), in a wide range of compositions relevant for *in meso* crystallization of membrane proteins. Two types of systems were studied: (1) mixtures of MO with salt solutions above the hydration boundary, and (2) mixtures of MO with βOG and salt solutions in a wide range of hydration conditions. In the latter case, series of samples with constant values of βOG/MO ratios ($R_{\beta OG/MO}$) were analyzed. At a given value of $R_{\beta OG/MO}$, the salt solution content in the samples varied from 10 to 80 wt%, covering a range of conditions below and above the hydration boundary. We discuss the implications of our findings for the investigation of the mechanism of membrane protein crystallization in lipidic mesophases and for the studies of the suitability of precipitants for *in meso* crystallization.

2.1 Introduction

As discussed in Chapter 1.2.2, phase transformations and properties of lipidic mesophases themselves have been shown to play a highly important role in the *in meso* crystallization process.[1-7] However, in spite of the advances in mechanistic studies, *in meso* crystallization remains a trial-and-error process, and detailed information about phase transformations in real, highly complex multi-component multi-phase crystallization mixtures would enhance the understanding of the mechanism. Mixtures of monoolein (MO) and water exhibit rich mesomorphism and intricate phase behavior at temperatures relevant for protein crystallization, with *Pn3m*, *Ia3d* or *Lα* mesophases forming depending on the hydration level and the thermal history of the sample (Chapter 1.3.3).[8,9] Multiple studies showed that both detergents[10-16] and salts,[17-19] the two major non-protein components in crystallization mixtures, affect the phase behavior of MO, but their combined effects have rarely been investigated.[10] Furthermore, few studies[10-13,16] mimic crystallization systems by independently controlling the MO/detergent ratio and the amount of aqueous phase, as determined by the two steps of the crystallization process (Section 1.2.4). The distribution of components between the phases in the two-phase system, and, in turn, the properties of the mesophase, are likely to depend on relative amounts of the mesophase and the solution. Consequently, little information is available about the actual conditions experienced by the protein within the mesophase during crystallization.

Here we report a study of the phase behavior of MO mesophases with detergent β-octylglucoside (βOG) and sodium or potassium dihydrophosphate solutions, which are often used as precipitants in the crystallization of membrane protein bacteriorhodopsin. We investigated two types of systems: (1) MO mixed with salt solutions above the hydration boundary, and (2) MO mixed with βOG and salt solutions in a wide range of hydration conditions. In the latter case, we analyzed series of samples with constant values of βOG/MO ratios ($R_{\beta OG/MO}$). At a given value of $R_{\beta OG/MO}$, the salt solution content in the samples varied from 10 wt% to 80 wt%, covering a range of conditions below and above the hydration boundary. Phase types and lattice parameters of all samples were determined by SAXS. To the best of our knowledge, no data of this type for crystallization-like systems are available for a wide range of conditions. We discuss the trends in phase behavior and component distribution and implications for membrane protein crystallization.

2.2 Materials and methods

Sample preparation. Homogeneous solid mixtures with fixed ratios of MO and βOG were prepared gravimetrically as follows. Target amounts of MO (Sigma Aldrich, 99%) and βOG (Anatrace, Anagrade) were weighed in a glass vial and dissolved in chloroform (Sigma Aldrich, ≥99.8%). The solvent was removed under a stream on nitrogen gas. Solid samples were dried in a desiccator under vacuum at room temperature (21-23 °C) overnight.

Solutions of potassium dihydrophosphate (Sigma-Aldrich) and sodium dihydrophosphate (EMD Chemicals) were pH-adjusted to pH of 5.50.

Mesophase samples containing solid MO or solid βOG/MO mixtures (lipidic part) and salt solutions (aqueous part) were formulated gravimetrically in a coupled-syringe mixer[20] at 21-23 °C. The total mass of each sample in the composition range of 50-90 wt % of the lipidic part was approximately 40 mg. Samples containing 10-40 wt % of the lipidic part were prepared with approximately 15 mg of the lipidic part.

After mixing the samples were dispensed into 2 to 4 borosilicate glass capillaries (0.9 mm, Charles Supper Company), depending on the amount of sample available. Capillaries were sealed with Critoseal (Leica Microsystems) and Quick-set epoxy (Henkel) to minimize water loss. Samples were stored at –12 °C in the dark for at least 12 hrs between sample preparation and data collection.

SAXS data collection. Prior to SAXS data collection the samples were equilibrated for at least 3 hrs at the data collection temperature. For series prepared with 1.3M NaH_2PO_4 and studied at two temperatures, 20 and 25 °C, the samples were kept at 20 °C overnight and further maintained at 25 °C for 4 hours prior to SAXS data collection. Although freezing is known to affect the phase behavior of mesophases at low temperatures by triggering the transition from a metastable to a thermodynamically stable sequence of phases, metastability was not observed for MO/detergent mixtures in the temperature range of interest here,[12] 20-25 °C, and is not expected to be an issue in this work.

For samples prepared with sodium dihydrophosphate solutions SAXS data were collected in a helium chamber using a Bruker M18XHF rotating anode generator supplying a Cu Kα (λ = 1.541838 Å) radiation beam that was collimated using a pinhole collimator. Kβ radiation was

filtered out with a Ni filter. A Highstar multiwire detector was used to collect the data. Samples were mounted in the He chamber on an automated goniometer at sample to detector distance of 63.2 cm and calibrated using silver behenate as the standard.[21] To prevent X-ray scattering by air, the chamber was continuously purged with helium gas during data collection. Temperature was maintained using a custom-built temperature-controlled sample holder.

Diffractograms were convolved and integrated in Bruker-SAXS 4.0 software. Phase assignment was carried out based on the presence of characteristic sets of reflections of lipidic mesophases as described in Appendix A. Phase assignments were done in *DIFFRAC^{plus} Topas 3* (Bruker AXS GmbH, Karlsruhe, Germany, 2005) based on whole powder pattern decomposition[22,23] for cubic phases, as implemented in the software, with added individual peaks for lamellar phases if necessary. Lattice parameters of cubic phases were calculated automatically during the phase assignment. Lamellar phases are only ordered in one dimension and cannot be automatically handled by *DIFFRAC^{plus} Topas 3*. For lamellar phases, lattice parameters were calculated directly from Bragg's law based on fitted peak positions of the highest-intensity reflection (Appendix A).

SAXS data for samples prepared with potassium dihydrophosphate solutions were collected on protein crystallography beamline LS-CAT 21-ID-D at the Advanced Photon Source (APS), Argonne National Lab. A detailed description of the setup is available elsewhere.[24] For SAXS measurements, a vacuum flight tube and an adjustable beam stop with an incorporated pin-diode were installed between the sample and the CCD detector (Rayonix MX300). The beamline was equipped with a microdiffractometer (MAATEL MD2) consisting of a goniometer, XYZ micropositioner and an on-axis video microscope. The latter was used to monitor the position of the sample in the X-ray beam. The size of the X-ray beam was 20 μm. The beam energy was 8 keV. Attenuation of the incident X-ray beam and exposure time were adjusted to avoid radiation damage.[25]

Raw diffractograms were integrated in Fit2D software (v. 12.077, A. P. Hammersley, ESRF, 1994). Integrated diffractograms were processed in MATLAB (R2008a, v. 7.6.0.324, The MathWorks Inc., Natick, MA). Publicly available MATLAB code (findpeaks.m, T. C. O'Haver, v2, revised Oct 27, 2006) was used for locate peak center positions. A series of MATLAB scripts was developed for baseline correction, and phase assignment for integrated diffractograms. Accuracy of all phase assignments was verified manually. For phase assignment, diffraction

angles were converted into *d*-spacings using Bragg's law. Mesophases were identified based on characteristic sets of reflections and lattice parameters were calculated using the peak position of the highest-intensity reflection (Appendix A). In this approach full fitting of the intensity profile and simultaneous fitting of multiple peaks was not performed in the lattice parameter calculations. The accuracy of lattice parameters calculated with Matlab was verified by performing whole powder pattern decomposition[22,23] in *DIFFRAC^{plus} Topas 3* for several samples. The difference between the lattice parameters calculated using the two methods was found to be within 0.5 Å, smaller than the difference in multiple measurements for identical samples.

Validation of mixed βOG/MO samples. To verify that solid βOG/MO mixtures did not deteriorate during the formulation of homogeneous detergent/lipid mixtures, mesophase samples with identical overall compositions were prepared with (i) solid βOG/MO mixtures and phosphate buffer solution (25 mM NaH_2PO_4, pH 5.5), and (ii) solid MO mixed with a solution of βOG in the same phosphate buffer. For the latter case, 5%, 10%, and 15% w/v solutions of βOG in phosphate buffer (25 mM NaH_2PO_4, pH 5.5) were used. Phases identified in samples of identical compositions prepared by the two methods were identical. The lattice parameters of cubic phases and lamellar phases differed by less than 3 and 2 Å, respectively. The differences in the lattice parameters may be attributed to inevitable slight deviations in sample composition.

2.3 Results

Findings on the effect of sodium and potassium phosphate salts and detergent β-octylglucoside on the phase behavior of MO mesophases are presented below. In the first part we investigated the effect of salt concentration in solution on the lattice parameter of MO mesophases above full hydration and discuss plausible mechanisms underlying our observations. In the second part we studied combined effects of phosphate salts and detergents on the phase behavior of MO mesophases in a wide range of hydration levels. We conclude by discussing the implications of our findings for the studies of membrane protein crystallization systems as well as for the studies of crystallogenesis *in meso* in Chapter 2.4.

Because of the complex composition of systems discussed below and the presence of multiple phases within a single sample, a number of variables are required to for detailed description. The concentration of salt in solutions used for sample formulation is denoted as c_{salt}, and the *overall* weight fraction of salt solution in the sample is denoted as w_{aq}. In contrast, volume fraction of salt solution φ_{aq} refers strictly to the combined volume fraction of water and salt *only within the mesophase*, rather than to the overall composition of the multiphase mixture. Because salt ions are unlikely to partition into non-polar lipid bilayers, φ_{aq} reflects the volume fraction of the aqueous compartments of the mesophase.

2.3.1 Mesophases of monoolein and phosphate salt solutions under conditions of full hydration

Figure 2.1 shows lattice parameters of monoolein mesophases prepared with K and Na phosphate salt solutions of 0.7 - 2.0 M and containing 40-80 wt% of the respective salt solution. All mesophases in these systems were of the *Pn3m* type and all samples contained excess aqueous phase. Both K and Na salts showed similar effects and caused the lattice parameter of the mesophase to decrease as the salt concentration increases, in quantitative agreement with available data.[18] The lattice parameters in all salt-containing systems studied here, 76-96 Å, were noticeably smaller than in water-saturated monoolein mesophases, ~108 Å at 25 °C. At the same molarity of the salt solution (c_{salt}) and overall sample composition (w_{aq}) the lattice parameters in K and Na salts differed, on average, by 1 Å. This result is not unexpected because the magnitude of the effect of ions on the lattice parameter is known to correlate with the position of ions in

Hofmeister series,[26] where K and Na are located immediately next to each other. Due to the small differences in the values of relevant lattice parameters and the slightly different temperatures at which K- and Na-containing samples were measured we did not further compare the results obtained with, respectively, the K and Na salts.

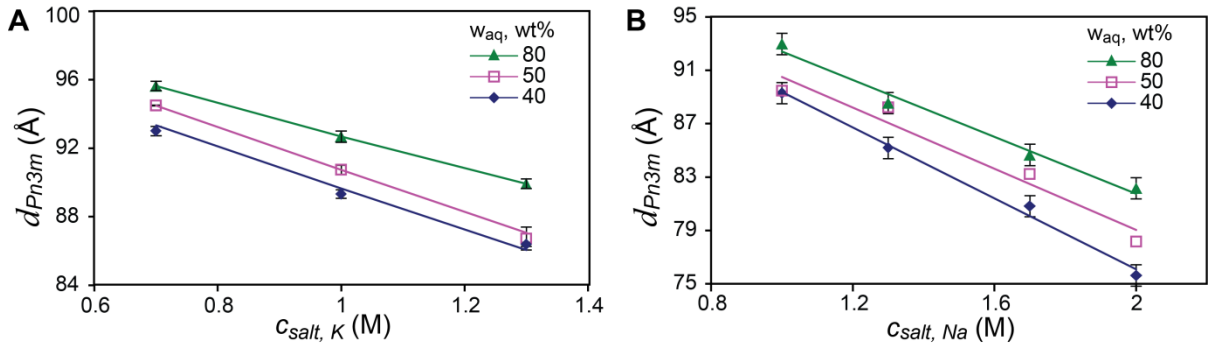

Figure 2.1. Lattice parameters of mesophases obtained upon mixing of MO with phosphate salt solutions as a function of salt concentration in solution (K or Na) and salt solution content (w_{aq} = 40, 50, or 80 wt%) in the sample: samples prepared with solutions of **(A)** KH_2PO_4 and **(B)** NaH_2PO_4. Error bars correspond to one standard deviation (N = 3 or 4). Lines are linear fits to data.

Detailed inspection of samples and of lattice parameter values revealed several interesting trends: (i) all samples had lattice parameters lower than in MO/water mesophases and contained excess aqueous phase in addition to the mesophase, whereas MO/water mesophases contain ~43% of water at the onset of bulk aqueous phase separation;[12] (ii) values of lattice parameters for the *Pn3m* phases were not only smaller than in fully hydrated MO/water mixtures, but were also lower than those accessible in MO/water systems before the *Pn3m-Ia3d* transition,[8,9] as reported previously for monoolein with various small solutes;[12,17-19,27,28] and (iii) the lattice parameter of the mesophase depended not only on the concentration of salt in the system, but also on the amount of excess aqueous phase (salt solution/monoolein ratio).

Phase transitions in lipidic mesophases are typically explained on the basis of curvature elastic free energy of bilayer bending.[29-31] However, clear explanations of the origins of the effect of small solutes on bilayer bending have not been put forward so far. Below we argue that our findings can be explained by considering a complementary free energy contribution, the interfacial tension (IFT) between the hydrocarbon part of the bilayer and the aqueous channels of the mesophase, as done in the classical theory of self-assembly of amphiphiles.[32] IFT is known to be important in the micellization of non-ionic surfactants,[33,34] and may serve as a complementary contribution to the curvature elastic free energy of bilayer bending typically used

to explain phase transitions in lipidic mesophases.[29-31] Although IFT has not yet been included in models for phase behavior of lipidic mesophases, presumably due to their mathematical complexity, it may provide a general way to explain the effect of small solutes on the curvature of lipid bilayers observed experimentally.

Although data on the effect of phosphate salts on the IFT at the hydrocarbon/aqueous solution interface are not available, the IFT is likely to increase upon the addition of phosphate salts. In the Hofmeister series phosphates are located between chloride and sulfate anions,[35] both of which are known to increase the IFT[36] compared to systems with pure water. Because ions of sodium and potassium phosphate salts are sufficiently small to enter the aqueous channels of the mesophase, they are likely to have the same effect on the bilayer/channel IFT in the mesophase. Under this assumption, to reduce the energy penalty of interface formation, the area per MO headgroup a_{head} is expected to decrease compared to mesophases prepared with pure water. Changes in the other two packing parameters, the lipid tail length l and the hydrocarbon chain volume v_l, are believed to be associated with significant unfavorable contributions to the free energy,[31] and variations of these two parameters are usually assumed to be minimal at a given temperature. We also note that because MO headgroups are uncharged, electrostatic screening effects, important for ionic amphiphiles, are unlikely to account for the observed trends.

The phase behavior observed in MO mixtures with salt solutions is fundamentally different from that caused by a purely osmotic effect upon decrease of the activity of water in the bulk aqueous phase coexisting with the mesophase,[37] as was noted previously.[12,17-19,27,28] In the latter case the sequence of phase transformations and of values of lattice parameters would be the same as in partially dehydrated MO/water mesophases. Purely osmotic effects were observed, for example, in the presence of polyethylene glycols of high molecular weight[37] that are excluded from the mesophase due to steric constraints.

Lattice parameters and hydration boundary in MO/salt solution mixtures. Although exact location of hydration boundaries in salt-containing systems is not known, a crude estimate for φ_{aq} yielded a range, albeit rather wide, of 26-39% v/v at full hydration in MO mixed with salt solutions, lower than the 43% in MO/water systems. The estimate of the hydration boundary is based on the following observations: phase separation was observed at 40 wt% salt solution in all systems studied here, providing the upper limit. Mixtures of MO with 2M NaH_2PO_4 at 30 wt% of the solution resulted in homogeneous mesophases (Chapter 2.3.2), indicating the lower limit for

the hydration boundary. Because the density of salt solutions is higher than that of MO, 40% w/w translates into 39% v/v at most, and 30% w/w into 26% v/v at the least. We also note that the exact location of the hydration boundary likely depends on the concentration of salt in aqueous solutions used for the mesophase preparation.

The hydration boundary in the first approximation is determined by the accessible values of packing parameters (Equation 1.1) of lipid molecules in the mesophase. The observed shift to lower φ_{aq} values, as well as lower values of lattice parameters, are consistent with the smaller allowed headgroup area in mesophases prepared with salt solutions. The dependence of φ_{aq} on a_{head} can be intuitively explained as follows: the inverse mesophases can be very crudely represented as lipid monolayers draped over cylindrical aqueous channels with polar lipid heads packed on the surface of the channel.[38] Provided that the phase type does not change, the radii of aqueous channels in the mesophase must shrink compared to systems with pure water for a_{head} to decrease. Smaller radii of aqueous channels lead to a lower ratio of the aqueous volume to the lipidic volume in the mesophase (Equation 1.4), *i.e.*, lower accessible values of φ_{aq}. Although precise measurements were not carried out, we expect that the hydration boundary will shift to lower φ_{aq} values as the phosphate salt concentration increases since the area per headgroup likely decreases with increasing salt concentration.

Figure 2.2 shows the subset of calculated accessible values of the lipid headgroup area and tail length given the values of *Pn3m* lattice parameter and the range of φ_{aq} values at the hydration boundary established here. Calculations were based on equations 1.2 and 1.3 and the standard assumption of the additivity of volumes of MO and the aqueous solution upon mesophase formation. The point corresponding to fully hydrated MO with pure water is also shown in Figure 2.2. The optimal value of the lipid tail length, l_{opt} = 17.2 Å, was selected as the average for 22.5 °C and 25 °C based on the correlation by Briggs *et al.*[8] (Equation 1.9). As can be seen in Figure 2.2, if the lipid tail length is maintained at l_{opt}, the smallest accessible value of the lattice parameter of the *Pn3m* mesophase within the range of hydration boundaries is ~80 Å, with a concomitant decrease in the headgroup area compared to the MO/water system. However, the values of lattice parameters of *Pn3m* mesophases in MO/salt solution systems measured here were as low as 76 Å, requiring that the length of the MO tail become smaller than l_{opt} to remain within the plausible range of hydration boundaries. Therefore, local packing of MO in salt-containing mesophases likely involves changes in the packing of hydrocarbon tails in addition to

the decrease in the headgroup area. The magnitude of this effect is difficult to assess precisely because of the uncertainty in the exact location of the hydration boundary and the assumptions made in the calculations.

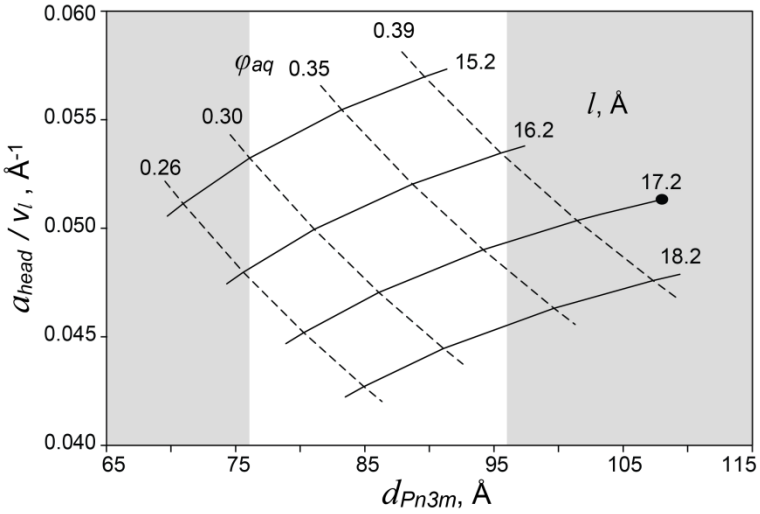

Figure 2.2. Relationship between headgroup area per lipid molecule a_{head} and lipid tail length l in *Pn3m* mesophases, the lattice parameter of the mesophase d_{Pn3m}, and the volume fraction of the aqueous component φ_{aq} based on equations 1.2 and 1.3 (Chapter 1). Solid lines correspond to constant values of tail length l; dashed lines correspond to constant values of φ_{aq}. The black dot corresponds to the fully hydrated *Pn3m* mesophase in the MO/water system at 25 °C. Values of the lattice parameters for MO mixed with salt solutions measured in this work are located between the areas shaded in grey.

Available data on other systems appear to lend support to our hypothesis about the effect of the bilayer/channel IFT on the lattice parameter of MO mesophases at full hydration for solutes that do not partition into the lipid bilayer. For example, in MO mesophases prepared with solutions of sodium iodide that decrease the IFT,[36] lattice parameters were reported to increase as the salt concentration increased.[19] The aqueous solution content in mesophases at full hydration is expected to change accordingly in those systems.

Lattice parameters of MO/salt solution mesophases are not accessible in MO/water systems. The lattice parameters of the *Pn3m* phases established here and in other reports under similar conditions are in the range of 79 - 96 Å. In MO/water mesophases, on the other hand, the *Pn3m*-*Ia3d* transition occurs as the lattice parameter of the *Pn3m* falls below 100-102 Å. The main driving force of this phase transition is believed to be the curvature free energy of lipid bilayers.[29-31]

Persistence of *Pn3m* phases in salt-containing systems can potentially be explained by the smaller headgroup area compared to *Ia3d* phases under otherwise identical conditions (Figure 2.3). The energy penalty of the lipid bilayer/aqueous channel interface formation would be

reduced in this case, offsetting the suboptimal free energy of the bilayer bending associated with forming *Pn3m* phases with a small lattice parameter. Figure 2.3 shows that the difference in the headgroup areas between the two types of mesophases increases as φ_{aq} decreases, making the associated free energy contribution more pronounced in MO/salt solution mesophases than in MO/water mesophases. Incidentally, consideration of the IFT contribution may also explain formation of *Pn3m* phases in water-saturated systems, lifting the energetic degeneracy of *Pn3m* and *Ia3d* phases predicted by curvature-only models that assume constant bilayer thickness.[29,30] We note however, that other effects, such as the free energy of bilayer compression,[31] must also play an important role in the prevalence of the *Pn3m* phase over the *Im3m* phase in MO systems because the latter has the lowest a_{head} values of the three cubic mesophases.

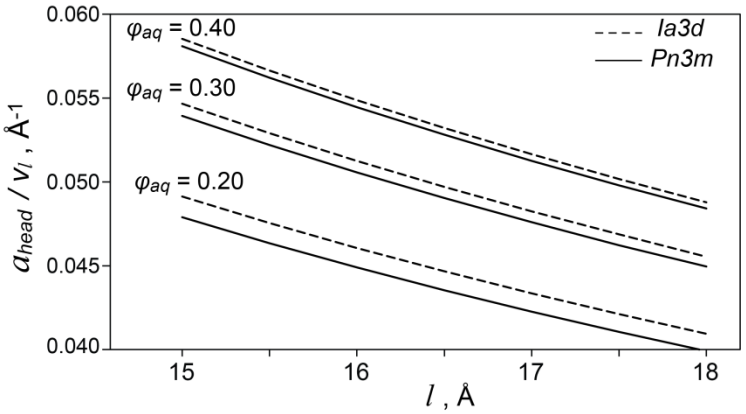

Figure 2.3. Headgroup area per lipid molecule a_{head} as a function of lipid tail length l and the volume fraction of the aqueous component φ_{aq} in *Pn3m* and *Ia3d* mesophases calculated using equations 1.2 and 1.3 (Chapter 1).

Dependence of lattice parameters on the amount of excess salt solution. At the same value of c_{salt}, in solution, lattice parameters of mesophases were found to increase as the overall amount of solution in the mixture w_{aq} increased (Figure 2.1). Because all mixtures studied here contained excess bulk aqueous phase, this effect could not be attributed to swelling of the mesophase to accommodate ever increasing amounts of the aqueous phase. Using φ_{aq} = 0.35 as a crude estimate of the hydration boundary based on our observations, the volume of excess aqueous phase varied from ~0 in mixtures formulated with 40 wt% of salt solutions, to approximately three times that of the mesophase in mixtures with 80 wt% of salt solutions. To the best of our knowledge, dependence of lattice parameters on the amount of excess solution has not been reported previously in MO mesophases mixed with solutions of salts, presumably due to the lack of studies with varied amounts of the excess aqueous phase.

The variation in the lattice parameters at a given temperature is not possible without changes in the internal composition of the mesophase, and is not observed in binary MO/water systems above the hydration boundary, in agreement with the phase rule. In the ternary MO/water/salt systems studied here, compositional changes likely originated from the re-distribution of salt between the aqueous compartments of the *Pn3m* phase and the coexisting bulk aqueous phase. The increasing values of lattice parameters indicate that c_{salt} in the aqueous channels of the mesophase decreased relative to the nominal value of c_{salt} in the solution used for sample preparation. This trend appears more prominent as the amount of excess aqueous phase increases, as expected for a system where one component distributes between two immiscible phases. The change in the composition of the mesophase may be quite significant. For example, the lattice parameter of the mesophase prepared with 80 wt% (3-fold excess) of 1.3M KH_2PO_4 solution corresponds to ~0.8M on the 40 wt% trendline (Figure 2.1A). The lattice parameters at 40 wt% of the salt solution provide the closest estimate for the true value of c_{salt} in the aqueous compartments of the mesophase because those samples are closest to the onset of the bulk aqueous phase separation.

Different concentrations of salt within the aqueous compartments of the mesophase and the coexisting bulk aqueous phase must result in osmotic stress that must be offset by other free energy contributions. As the unit cells of the mesophase become larger, some sources of strain relief may be: (i) curvature elastic free energy is reduced as curvature of lipid bilayers decreases and becomes closer to the spontaneous curvature;[37] (ii) chain compression stress[31] of the hydrocarbon tails decreases because tail lengths closer to the optimal value l_{opt} become attainable (Figure 2.2); and (ii) steric repulsion between MO headgroups[32] decreases as the area per headgroup becomes larger.

2.3.2 Mesophases of monoolein and 2M NaH_2PO_4 in a wide range of hydration conditions

Figure 2.4 shows the sequence of phases observed in MO mixed with 10-80 wt% of 2M NaH_2PO_4 at 22.5 °C for two different batches (indicated as the vendor batch number on the MO container). The sequence of phase types in a wider range of conditions upon increasing w_{aq} (Figure 2.4A) followed that of the MO/water system, with one notable exception: at 30 and 35 wt% of salt solution either an *Ia3d* or an H_{II} phase was observed. In the second batch of MO only an H_{II} phase was observed in mixtures with 30 and 40 wt% of salt solution. The lattice

parameters of cubic mesophases were lower than those in the MO/water systems, in agreement with our findings discussed in Chapter 2.3.1 and with previously published reports (Chapter 1.3.3).[17-19] Although the fully hydrated *Pn3m* aqueous phase appeared at slightly different values of w_{aq} for the two MO batches, its lattice parameter increased consistently as the amount of aqueous phase increased, as discussed in detail in Section 2.3.1. Batch-to-batch variations for MO mesophases have been observed previously.[12]

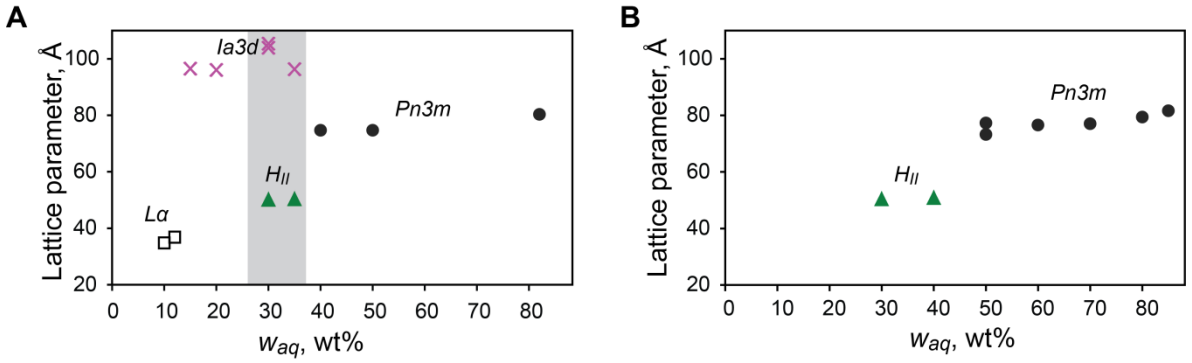

Figure 2.4. Types of mesophases identified in SAXS analysis of MO mixed with solutions of 2M NaH_2PO_4, pH 5.5 for two different batches **(A, B)** of MO. Each data point represents an independently prepared sample. Mesophases are denoted as follows: *Pn3m* (circles), *Ia3d* (crosses), *Lα* (squares), and H_{II} (triangles). **A.** Intermittent formation of *Ia3d* and H_{II} phases was observed at 30 and 35 wt% of solution (area shaded in grey), depending on the sample. Coexisting *Ia3d* and H_{II} phases were not observed within a single sample. Lattice parameters of mesophases were calculated as described in Appendix A.

The appearance of the H_{II} phase in our samples was remarkable because this phase does not consistently form in MO/water mesophases at temperatures below 90 °C (Figure 1.12) and has not been observed in mixtures with 2 M phosphate salts at ambient temperature under full hydration conditions (Chapter 2.3.1 and Figure 1.14 in Chapter 1.1.3). While the H_{II} phase has the values of a_{head} lower than that in any cubic phase at a given composition, it has the highest curvature at the lipid/aqueous channel interface and is also known to require significant packing frustrations of lipidic chains.[39]

Another interesting feature is the intermittent appearance of H_{II} and *Ia3d* phases at a given value of w_{aq} (Figure 2.4A). We emphasize that coexisting H_{II} and *Ia3d* phases were not observed in our samples, and the two phases shown at the same sample compositions in Figure 2.3A represent two different independently prepared samples. We attempted to establish whether metastable behavior of MO mesophases[9,10,15] may account for the observed differences by preparing a large amount of sample with w_{aq} = 30% followed by dispensing into several capillaries, maintaining the capillaries at -12 °C or -80 °C overnight, and then at 22.5 °C prior to data collection at the same temperature. Samples in all capillaries were of the H_{II} type,

suggesting that metastability did not account for our observations of intermittent *Ia3d* and H_{II} phase appearance. Therefore, our observations may have been caused by the slight differences in sample compositions in different preparations.

Overall, our data for MO/salt solution systems demonstrate the complex nature of phenomena governing phase behavior and microstructure of mesophases even upon addition of relatively simple additives that affect bilayer geometry through dispersion interactions rather than through direct incorporation into the bilayer. These phenomena are significantly more complex than pure osmotically-driven MO/water phase transformations[37] that match simple dehydration behavior.

2.3.3 β-Octylglucoside/monoolein/phosphate salt solution systems

Here series of samples with constant βOG/MO ratios were analyzed. At a given $R_{\beta OG/MO}$, salt solution content in the samples varied from 10 wt% to 80 wt%, covering a range of conditions below and above the hydration boundary. The conditions were chosen to reflect the compositions of mixtures typical in crystallization trials of membrane protein bacteriorhodopsin, where a protein solution containing up to 15% of βOG is mixed with monoolein in a 60:40 v/v ratio,[10] and crystallization is induced by the subsequent addition of a concentrated salt solution. Thus, the βOG/MO ratio remains fixed throughout the trial and is independent of the amount of the aqueous phase and its salt concentration. Samples with three βOG/MO weight ratios, 0.033, 0.066, and 0.099 w/w were used, which correspond to the βOG concentrations of 5, 10, and 15%, respectively, in the 60:40 MO:detergent solution mixture. Concentrations of salt c_{salt} in solutions used here, 0.7-1.3 M KH_2PO_4 and 1.3-2.0 M NaH_2PO_4, are also within the range used for crystallization of bacteriorhodopsin.[3,10] The range of salt concentrations for KH_2PO_4 was limited by its solubility in water at ambient temperature, slightly above 1.3 M.

The location of phase boundaries and the values of lattice parameters found in this work were accounted for by the interplay between competing effects of detergents and phosphate salts on the microstructure of lipidic mesophases. As discussed in the previous section, phosphate salts favor mesophases with higher bilayer curvature, smaller lipid headgroup area, and smaller radii of aqueous channels, and extend the range of the *Pn3m* phase formation to lower hydration levels compared to MO/water mesophases. Detergent additives are known to have the opposite

effect, favoring microstructures with less curved bilayers: cubic phases form with larger lattice parameters, extending the range of the *Lα* phase formation higher hydration levels.[10-16] Incorporation of βOG in MO bilayers and subsequent changes in molecular packing due to the differences in the molecular shapes of lipid and detergent molecules provide a rationale for this behavior.[10,14,32,40] Indeed, a significantly bulkier headgroup of βOG compared to that of MO and, consequently, a larger average area per amphiphile headgroup in mixed MO/βOG bilayers, should lead to observed changes in the microstructure based on the relationship between molecular parameters and mesophase composition (Equations 1.2 and 1.3). The differences in the hydrocarbon tail length of the two molecules are likely to be less important in defining the microstructure: incorporation of βOG in MO mesophases was found to have little effect on the thickness of the bilayers.[41]

Trends in the phase behavior and values of lattice parameters. Figure 2.5 shows the types of mesophases found in the mixtures as a function of βOG and salt solution content and sample temperature, along with approximate locations of hydration boundaries established based on the appearance of the sample.

Remarkably, despite the complexity of the quaternary mixtures, the sequence of phases in each series was highly regular and was identical to that in MO/water mesophases at similar temperatures.[8,9] The lamellar *Lα* phase formed in the "dry" end of the phase diagram. As the amount of the aqueous phase in the mix increased, the *Lα* -*Ia3d* transition, followed by the *Ia3d*-*Pn3m* transition took place, and at full hydration all mesophases were exclusively of the *Pn3m* type. At a given salt solution content w_{aq}, lattice parameters were found to increase with increasing detergent loading, and to decrease with increasing salt concentration c_{salt} in solution. Some of the latter decrease could be attributed to the lower water content in the system and a smaller volume of solutions used because of the higher density at higher salt concentrations. However, identical trends for systems with a large excess of solutions coexisting with the *Pn3m* mesophase indicated that the changes in the salt concentration in solutions used for sample preparation were the defining factor for the values of the lattice parameters.

The regularity in the sequence of phases likely stemmed from the mutually mitigating effects of βOG and phosphate salts on the curvature of the lipid bilayers, as discussed above, as well as from the relatively low detergent loading and salt concentrations in solutions. Previous reports provided evidence that phase behavior of MO with additives does not necessarily

replicate that of MO/water mesophases. For example, certain βOG/MO ratios and mesophase hydration levels give rise to phenomena not found in MO/water mesophases both with[10] and without[13,16,42] significant amounts of salt in the system, such as the coexistence of *Pn3m* and *Lα* phases, although regular sequences of mesophases similar to those in MO/water systems have also been observed.[10] We also note that coexisting *Pn3m* and *Lα* phases discovered in crystallization systems in the vicinity of protein crystals were not found anywhere in the entire phase space tested here. In only one sample in this work coexisting *Pn3m*, *Ia3d*, and *Lα* mesophases were observed, but the lattice parameter of the lamellar phase was 44 Å, significantly lower than 50-55 Å of the lamellar mesophase surrounding protein crystals.[4] At the same time, the lattice parameters of *Pn3m* phases found here are in agreement with values of 85-97 Å in crystallization mixtures with protein crystals.[4] These findings provide additional evidence that the combination of coexisting *Pn3m* and *Lα* phases is brought about by the crystals, presumably due to elastic constrains on the bilayers in proximity of membrane protein molecules packed in sheets within the crystal.

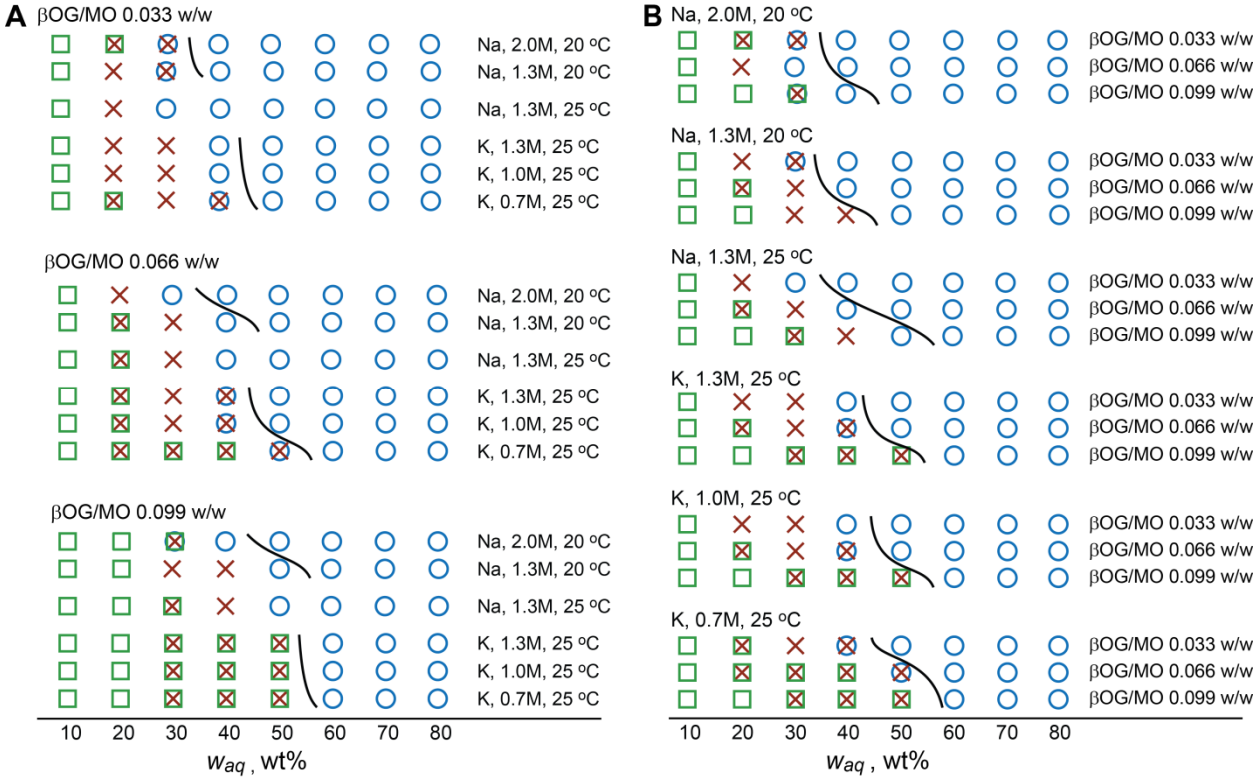

Figure 2.5. Phase diagrams of MO/βOG/salt solution mixtures as a function of weight fraction of salt solution w_{aq} at **(A)** constant βOG/MO ratios and **(B)** constant salt concentrations. K and Na denote KH_2PO_4 and NaH_2PO_4, respectively. Mesophases are denoted as follows: (□) *Lα,* (×) *Ia3d*, (○) *Pn3m.* Mesophase identity was established by SAXS. The solid curves indicate approximate locations of hydration boundaries based on the appearance of samples and are drawn to guide the eye.

The range of mixture compositions in which specific types of mesophases appeared varied as expected based on the known effects of detergents and phosphate salts. Specific trends are discussed below.

Dependence of phase behavior on salt concentration at constant βOG/MO ratio. As the salt concentration increased, boundaries of all phases (*Lα*, *Ia3d*, and *Pn3m*) shifted towards the lower content of the salt solution in the mixture (Figure 2.5A). This change was not unexpected and agreed with the anticipated effect of phosphate salts that extend the range of cubic phase formation and promote mesophases with higher bilayer curvature and smaller values of lattice parameters. For example, in the mixtures with the $R_{\beta OG/MO}$ of 0.066 w/w, the *Ia3d* phase was observed at up to 50 wt% of the salt solution at the salt concentration of 0.7 M KH_2PO_4, but only at up to 40 wt% of solution at 1.0 and 1.3 M KH_2PO_4. At the same time, the interval of lamellar phase existence decreased from 10-40% of the salt solution at 0.7 M KH_2PO_4 to 10-20% with 1.0 and 1.3 M KH_2PO_4.

Systems with other βOG/MO ratios prepared with solutions of KH_2PO_4 followed similar trends, as did mixtures containing NaH_2PO_4 solutions of 1.3 M and 2.0 M concentrations at 20 °C. An exception among the samples with NaH_2PO_4 was the series with the $R_{\beta OG/MO}$ of 0.033, the lowest one studied here. At the aqueous solution loading of 20 wt% in this series the trend was seemingly reversed compared to other systems: a lamellar phase is observed in the mesophase samples with 2.0 M NaH_2PO_4, but not with 1.3 M NaH_2PO_4. The series with 2.0 M NaH_2PO_4 also deviated if trends with respect to varying βOG/MO ratio at a given salt solution concentration are considered, as described in the following section. A number of factors may account for this behavior, for example, a noticeably lower *volume* fraction of solution in mixtures with the higher salt concentration, as well as a significantly lower water/salt ratio as the 2.0 M NaH_2PO_4 solution contains 25 wt% of the salt. These factors could lead to unattainable constraints on the packing parameters in the bilayer or significant effects of specific interactions between the solution and the hydrophilic heads of MO and βOG. Highly curved bilayers caused by 2.0 M NaH_2PO_4 could lead to phase separation of a detergent-rich phase, with insufficient detergent at $R_{\beta OG/MO} = 0.033$ to counteract the curvature induced by the high salt concentration, unlike in series with higher detergent loadings. We note that pure MO mixed with a 2.0 M NaH_2PO_4 solution below full hydration also exhibited highly unusual behavior, forming either an *Ia3d* phase or a hexagonal H_{II} phase at the salt solution content of 30 wt% at 22.5 °C (Chapter

2.3.2). For comparison, MO only forms hexagonal mesophases at temperatures above approximately 90 °C when mixed with water.[8] Hexagonal phase formation in MO/excess salt solution systems at ambient temperature requires a significantly higher concentration of salt in solution.[17]

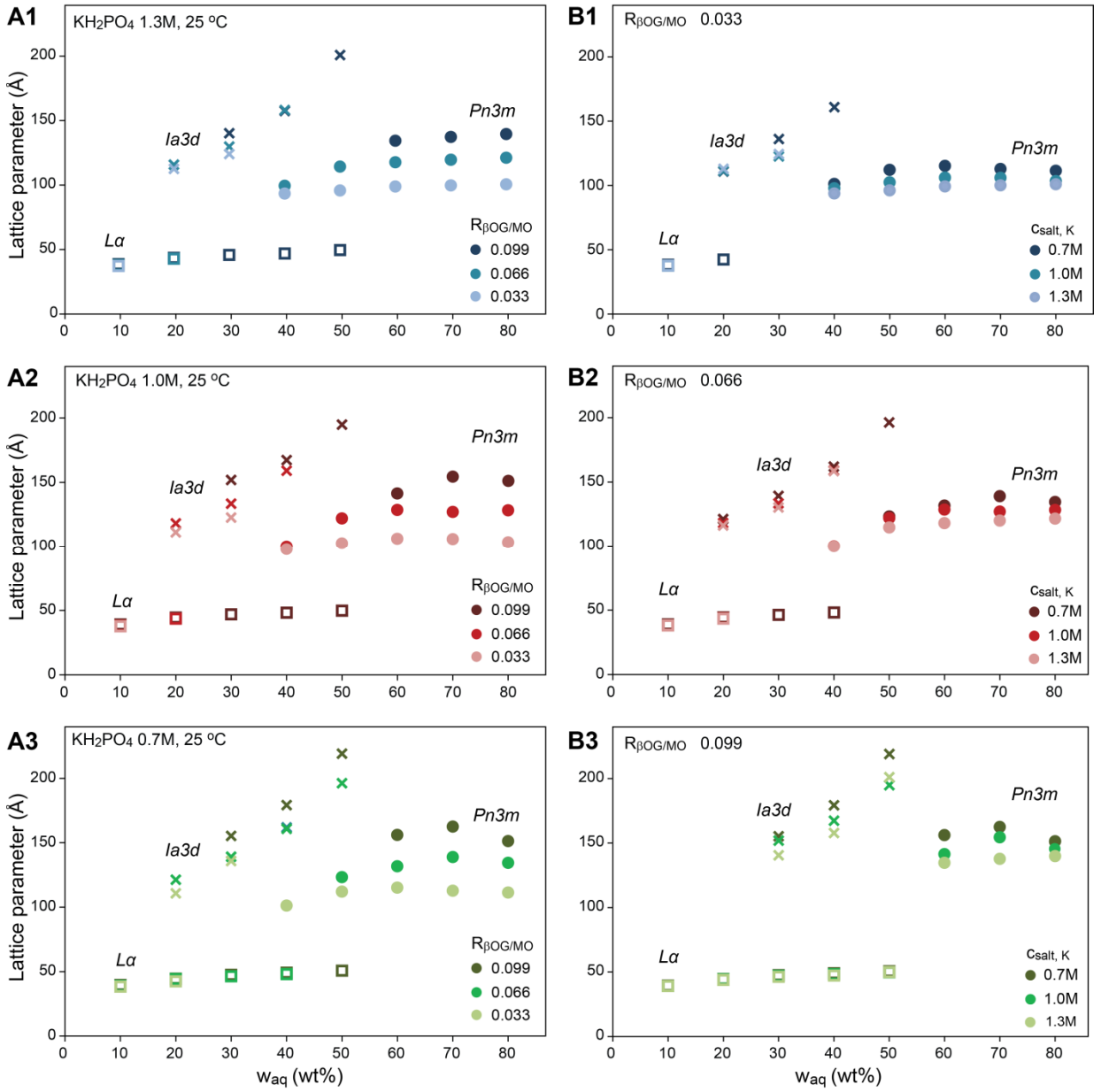

Figure 2.6. Lattice parameters of MO/βOG/salt solution mesophases prepared with KH_2PO_4 as a function of weight fraction of salt solution w_{aq} at three different salt concentrations c_{salt} and three different βOG/MO ratios. **(A1-A3)** Each panel represents samples formulated with constant c_{salt} at different βOG/MO ratios. **(B1-B3)** Each panel represents samples formulated with a constant βOG/MO at different c_{salt} values. Mesophases are denoted as follows: (□) *Lα,* (×) *Ia3d*, (○) *Pn3m*. Mesophase microstructure was established by SAXS.

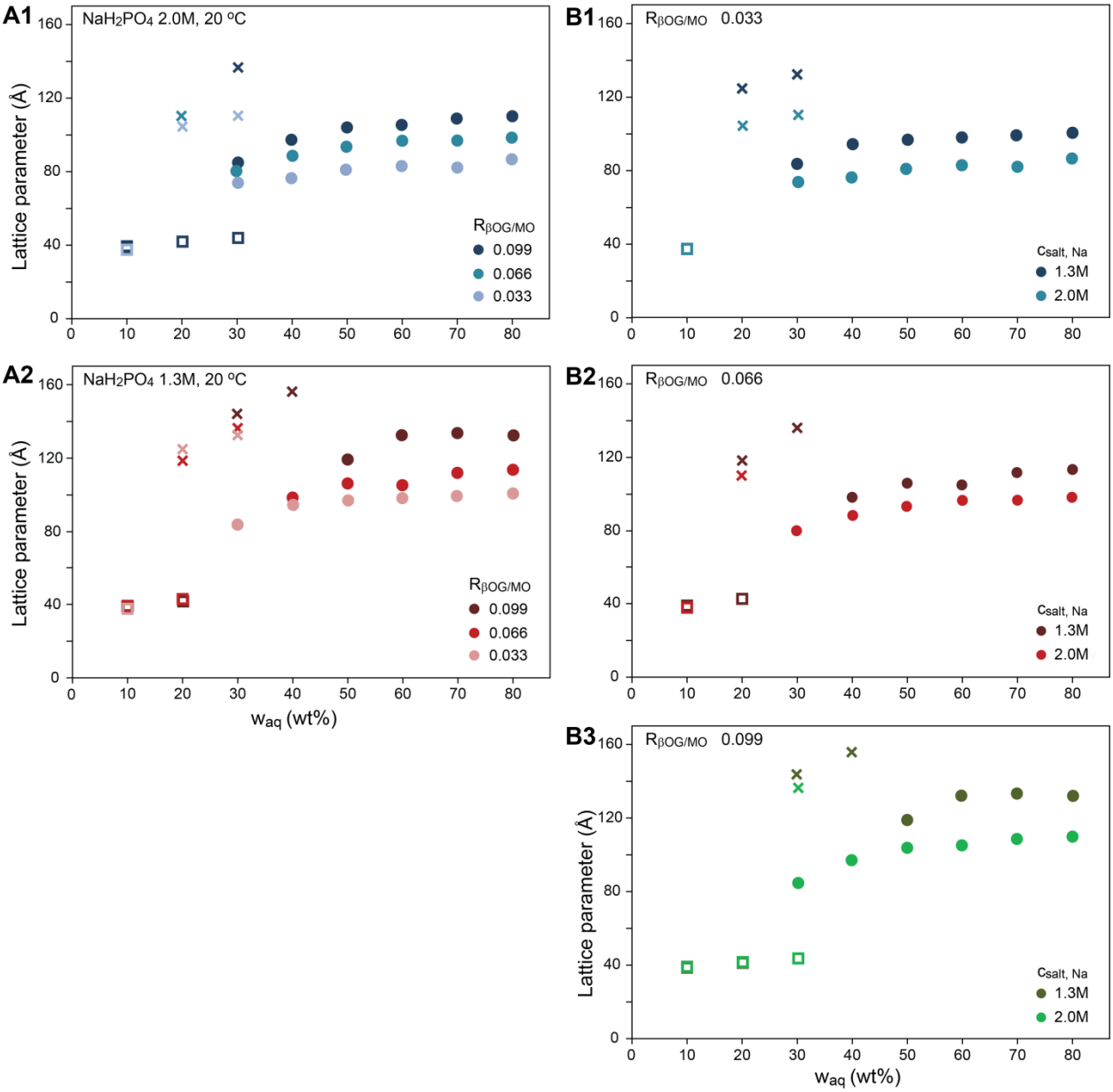

Figure 2.7. Lattice parameters of MO/βOG/salt solution mesophases prepared with NaH_2PO_4 as a function of weight fraction of salt solution w_{aq} at two different salt concentrations c_{salt} and three different βOG/MO ratios. **(A1, A2)** Each panel represents samples formulated with constant c_{salt} at different βOG/MO ratios. **(B1-B3)** Each panel represents samples formulated with a constant βOG/MO ratio at different c_{salt} values. Mesophases are denoted as follows: (□) *Lα,* (×) *Ia3d*, (○) *Pn3m*. Mesophase microstructure was established by SAXS.

Dependence of phase behavior on βOG/MO ratio at constant salt concentration. At the same salt concentration, the boundaries for all phases tended to shift in the direction of higher salt solution content in the mixture as the βOG/MO ratio increases (Figure 2.5B). These shifts were consistent with the effect of βOG on the average molecular packing parameters[32] in the

bilayers of the mesophase, resulting in the formation of mesophases with lower bilayer curvature and larger values of lattice parameters (Figures 2.6 and 2.7). As an example, in mixtures prepared with 1.0 M KH_2PO_4 salt solutions the boundary for pure *Pn3m* phase formation shifted from 40 wt% of the salt solution to 60 wt% as the $R_{\beta OG/MO}$ ratio increased from 0.033 to 0.099 w/w. The *Lα* phase range extended from 10 wt% to 50 wt% of the salt solution. Similar trends take place for mixtures with NaH_2PO_4 solutions. The series with the βOG/MO ratio of 0.033 and the salt concentration of 2.0 M appeared to be an outlier again, as the *Lα* phase and the *Ia3d* phase persist to higher salt solution contents at the βOG/MO ratio of 0.033 than at 0.066.

Comparison with MO/water mesophases. Interestingly, the trends in phase behavior observed upon increased detergent loading or decreased salt concentration were very similar to those in MO/water mesophases at decreasing temperatures (Figure 1.12),[8,9] although exact locations of phase boundaries were different in the two classes of systems. The major changes, based on data for systems with KH_2PO_4, were: (i) the shift of the hydration boundary to the higher aqueous loading, as discussed above; (ii) widening of the *Lα* + *Ia3d* coexistence region at the expense of (iii) narrowing of the pure *Ia3d* phase region of the phase diagram; and (iv) larger values of lattice parameters. At the same time, the pure *Pn3m* phase region near the hydration boundary in quaternary systems appeared to remain narrow, similar to the behavior observed in the binary MO/water system. The *Pn3m* + *Ia3d* coexistence was only observed in a few samples, making related trends difficult to infer unambiguously.

The trends in the phase behavior outlined above were likely brought about by the similarly changing packing of amphiphiles in the bilayers. In MO/water systems at lower temperatures,[8,9] as well as in MO/βOG/salt solution mesophases at higher βOG loadings or lower salt concentrations, the bilayer curvature tends to decrease. Therefore, the minimal values of lattice parameters attainable in cubic phases become higher. Because the values of lattice parameters also decrease as the aqueous loading in the mesophase decreases, the *Ia3d* - *Lα* phase separation occurs at larger values of w_{aq} to maintain preferred molecular packing in the bilayer becomes larger as the bilayers become flatter, causing observed changes. Preferred hydration levels of lamellar phases did not appear to vary significantly in the systems studied here.

Effects of different salts on the phase behavior. Two of the series of samples had identical temperature of 25°C and salt concentration of 1.3M, and the only difference was the cation, Na or K, of the phosphate salt. Figure 2.5A and B show that Na had a stronger cubic

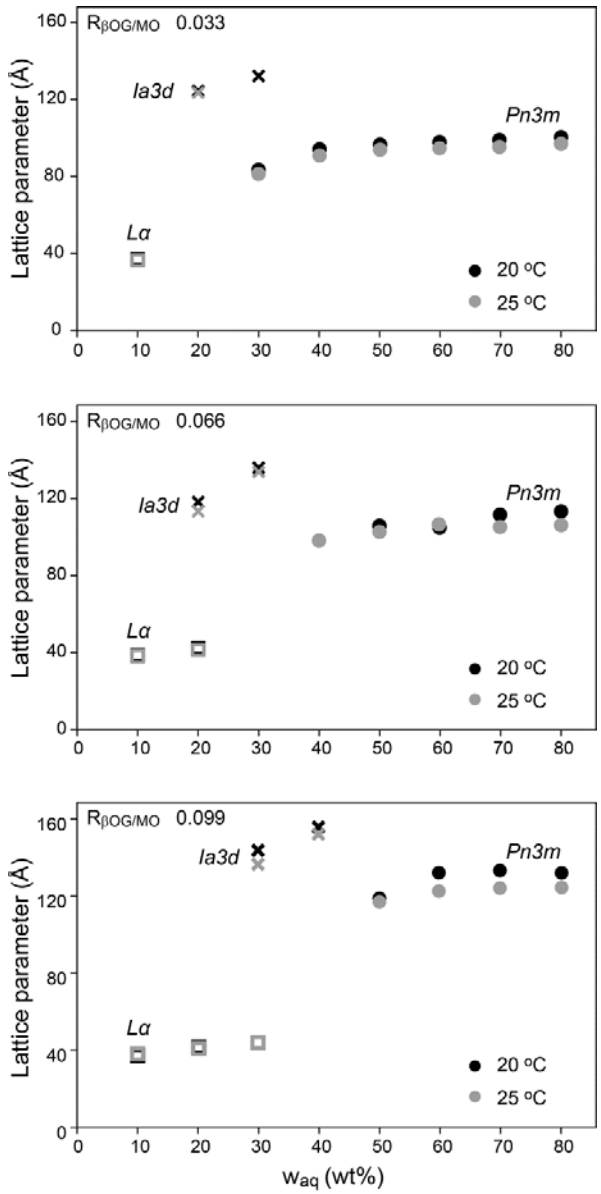

Figure 2.8. Lattice parameters of MO/βOG/salt solution mesophases as a function of temperature at different weight fractions of salt solution w_{aq} and βOG/MO ratios. All samples were prepared with 1.3M NaH_2PO_4. Mesophases are denoted as follows: *Pn3m* (circles), *Ia3d* (crosses), *Lα* (squares). Mesophase identity was established based on SAXS data.

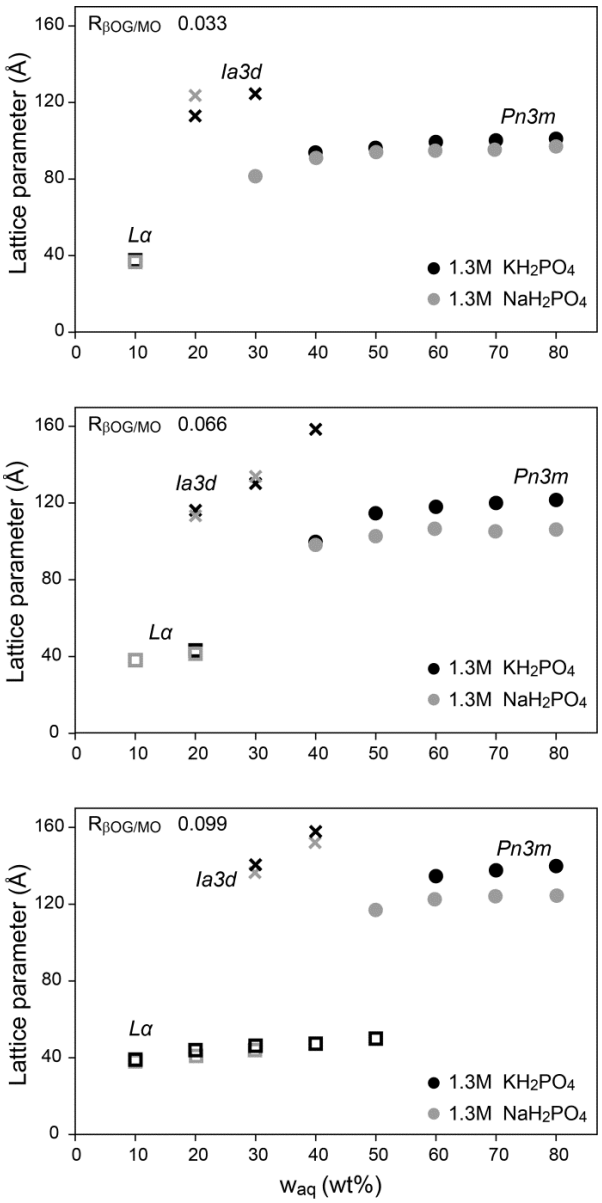

Figure 2.9. Effect of the cation on lattice parameters of MO/βOG/salt solution mesophases at different weight fractions of salt solution w_{aq} and βOG/MO ratios and the salt concentration of 1.3M. Mesophases are denoted as follows: *Pn3m* (circles), *Ia3d* (crosses), *Lα* (squares). Mesophase identity was established based on SAXS data.

phase-promoting effect than did K, which is evident in the persistence of the *Pn3m* phase to lower values of w_{aq} in mixtures with the sodium salt than in otherwise identical mixtures with the potassium salt. Also, lattice parameters of mesophases prepared with NaH_2PO_4 were lower than of those prepared with KH_2PO_4 under otherwise identical conditions (Figure 2.9). This finding was somewhat unexpected as the effects of cations on uncharged lipidic mesophases are believed to correlate with their position in the Hofmeister series, where Na and K are found immediately

next to each other. The lower water/salt ratio, 35:1 mol/mol in 1.3M NaH_2PO_4 solutions, *vs.* 41:1 mol/mol in KH_2PO_4 solutions, and the resulting lower water/amphiphile molar ratio under seemingly identical conditions may have played a role in the observed differences.

Lattice parameters of mesophases below full hydration. Lattice parameters of mesophases below the hydration boundary (Figures 2.6-2.9) changed as anticipated based on the effects of βOG and phosphate salts on the packing parameters and curvature of lipid bilayers, as well as on the effect of hydration level w_{aq} on the lattice parameters. An increase in the βOG/MO ratio caused the lattice parameters to decrease, and an increase in c_{salt} caused the lattice parameters to decrease at a given value of w_{aq}, with a few outliers possibly resulting from imperfectly formulated samples. Lattice parameters of mesophases consistently grew larger as w_{aq} increased in single-phase as well as in coexisting-phase regions. The latter indicated that the compositions of coexisting phases varied with the overall composition in the quaternary systems studied in this work, unlike in the binary MO/water mixtures. In binary systems the phase rule requires that compositions, and, consequently, lattice parameters of coexisting phases be invariant at a given temperature regardless of the overall composition of the mixture. The changing lattice parameters in coexisting phases in the quaternary systems could result from increasing hydration levels in both coexisting phases, from the redistribution of detergent between the phases, and from redistribution of salt between the aqueous compartments, and were likely a combination of all these factors. Thus, the βOG/MO ratios and salt concentrations in the aqueous compartments of the coexisting phases must be different from the nominal ones used for sample preparation, making the regular trends in the phase behavior observed here ever more remarkable.

Closer inspection of data revealed noticeable quantitative differences in the trends for lattice parameters of mesophases above and below full hydration. Above full hydration changes in salt concentration, βOG/MO ratio, and sample temperature caused significant variations in the values of a_{Pn3m} at a given value of w_{aq}, as discussed below. On the contrary, below full hydration, where mostly *Ia3d* and *Lα* phases formed, the hydration level w_{aq} had the prevailing effect on the lattice parameters. At fixed values of w_{aq}, lattice parameters of *Ia3d* phases varied little compared to lattice parameters of *Pn3m* mesophases above full hydration upon identical changes in c_{salt}, $R_{\beta OG/MO}$, and sample temperature in almost all sets of samples (Figures 2.6 and 2.7). Lattice parameters of lamellar phases were defined almost exclusively by the values of w_{aq} and

followed a linear trend $a_{L\alpha} = 0.36w_{aq} + 35.6$ regardless of the presence of *Ia3d* phase and the range of the lamellar phase existence. At a given w_{aq} the values of $a_{L\alpha}$ did not differ by more than 3.5 Å among all samples regardless of all other parameters. Another interesting feature in the series where the *Ia3d* phase formed in a wide composition range was the near-constant slope da_{Ia3d}/dw_{aq} at a given βOG/MO ratio (Figures 2.6 and 2.7). The slope was practically independent of the salt concentration and of the presence of coexisting phases of other types. The specific type of coexisting phase also did not appear to affect the trend for the lattice parameters of *Ia3d* phases, as highlighted by data for samples with $R_{\beta OG/MO} = 0.066$, where values of a_{Ia3d} for pure *Ia3d*, *Ia3d* + *Lα*, and *Ia3d* + *Pn3m* samples fell on the same linear trend. These observations may indicate that lattice parameters below full hydration were largely defined by geometry constraints related to the relatively small volume of the aqueous sub-compartments of the mesophase. These constraints force the amphiphiles to pack with suboptimal values of tail lengths and headgroup areas, with phase separation providing a route for re-distribution of components and formation of bilayers with more favorable packing. On the other hand, in fully hydrated systems the amount of aqueous solution within the mesophase and the lattice parameters of the mesophase are likely determined by optimal packing parameters, resulting in noticeable changes when these parameters change.

Effect of additives on the hydration boundary and lattice parameters at full hydration. All mesophases coexisting with excess aqueous phase were of the *Pn3m* type (Figure 2.5), suggesting that this was also the mesophase type adopted at the onset of aqueous phase separation, analogous to MO/water mesophases in a similar temperature range. The hydration boundaries shifted in the direction of higher aqueous solution content as the βOG/MO ratio increased or as the concentration of salt decreased (Figure 2.5A, B). The location of the hydration boundary appeared more sensitive to the βOG/MO ratio than to the concentration of salt in solution, as evidenced by more frequent observations of hydration boundary shifts in datasets with constant c_{salt} and varying $R_{\beta OG/MO}$ (Figure 2.5B) than in datasets with constant $R_{\beta OG/MO}$ ratio and varying c_{salt} (Figure 2.5A). As discussed in Chapter 2.3.1, the hydration boundary shifts to lower values of w_{aq} to satisfy geometry/composition relationships as the lattice parameters decrease, and, conversely, is expected to shift to higher values as the lattice parameters increase. In mixtures with KH_2PO_4 the lattice parameters of *Pn3m* mesophases at full hydration increased by ~6.5 Å if $R_{\beta OG/MO}$ in the sample increased by 0.01, whereas for salt

solutions the lattice parameter decreased by 3.3 Å if the salt concentration increased by 0.1M. Because the location of the hydration boundary was only established to within 10 wt% of salt solution in the sample, several ways of selecting data for the analysis were tested, yielding similar values in all cases (see Appendix B for details).

In this work $R_{\beta OG/MO}$ was varied in increments of 0.033, and, to offset the effect of βOG, salt concentration would have to increase by more than 0.6 M for every increment. This value is slightly larger than the range of concentrations of KH_2PO_4 used here and, coupled with the uncertainty in the determination of the hydration boundary, may explain our observations on the stronger effect of βOG compared to the effect of salt. Values in systems with NaH_2PO_4 were different from those in systems with KH_2PO_4 and appeared to depend on the detergent loading, further complicating the issue (see Appendix B for details). In series with NaH_2PO_4 containing 0.066 and 0.033 βOG/MO we estimated an increase of 2.6 Å per a $R_{\beta OG/MO}$ increase of 0.01 for the effect of βOG and 3.3 Å per an increase of 0.1M in the salt concentration. The series with $R_{\beta OG/MO}$ = 0.099 was an outlier in the dataset with NaH_2PO_4, with respective values of ~6 Å for the effect of βOG and 5.4 Å for the effect of salt.

Remarkably, the quantitative effect of additives on the values of lattice parameters of *Pn3m* mesophases in quaternary mixtures at full hydration was different from that calculated based on data for ternary MO/water/additive mixtures. Without detergent the lattice parameters decrease by only about 1.0-1.4 Å if either KH_2PO_4 or NaH_2PO_4 salt increases by 0.1M according to our own and previously published data.[18] Therefore, the introduction of detergent resulted in the enhancement in the effect of salt on the lattice parameter, where the decrease of at least 3.3 Å per 0.1M of salt concentration was observed. Although the origin of this effect is not clear, we speculate that shorter chains of βOG compared to MO may relieve chain packing frustrations upon bilayer bending, providing access to mesophases with smaller lattice parameters. Additionally, our data on mixtures with NaH_2PO_4 indicate that the effect of salt on the lattice parameter in hydrated mesophases may vary depending on the detergent loading. Similarly, the average effect of βOG on the lattice parameter appeared to vary as a function of c_{salt} and may differ from that in ternary systems under certain conditions, as illustrated by our findings for samples containing NaH_2PO_4. The correlation obtained by Misquitta and Caffrey for ternary βOG/MO/water systems[10] (Figure 1.17) produced the value of 5 Å for every 0.01 increase in $R_{\beta OG/MO}$. This value is similar to our estimates for quaternary βOG/MO/water/salt systems at all

KH_2PO_4 concentrations and $R_{\beta OG/MO}$ values, as well as at both NaH_2PO_4 concentrations and the $R_{\beta OG/MO}$ = 0.099. However, the respective effect of βOG on the lattice parameters in mixtures with NaH_2PO_4 and the βOG/MO ratios of 0.033 and 0.066 was significantly less pronounced at 3.4 Å, and the value deduced for mixtures with 2M Na/K phosphate[10] is even lower at 1.7 Å. Our data are based on at least four measurements for every data point, and the quantitative differences outlined above are unlikely to arise due to aberrant sample compositions.

Lattice parameters of mesophases beyond the hydration boundary. Although all mesophases coexisting with excess aqueous phase maintained *Pn3m* symmetry, their lattice parameters showed dependence on the amount of excess aqueous solution even if all other parameters (c_{salt}, $R_{\beta OG/MO}$, sample temperature) were constant, as shown in Figures 2.6-2.9. At low salt concentrations (0.7 and 1.0 M) a maximum in the values of lattice parameters was observed at w_{aq} of 60-70%. As the salt concentration increased, the maximum disappeared, and a steady increase in the values of lattice parameters beyond the hydration boundary took place (Figures 2.6 and 2.7). These trends may be explained by considering partition of salt and detergent between the mesophase and the coexisting bulk aqueous phase. Our findings for MO/salt solution systems strongly suggest that salt re-distributes between the aqueous channels of the mesophase and the bulk aqueous phase so that the effective salt concentration in the mesophase becomes lower, as discussed above. This phenomenon may account for the increasing values of lattice parameters observed here for MO/detergent/salt solution mesophases. On the other hand, the maxima and subsequently decreasing values of lattice parameters at relatively low salt concentrations could be explained by partition of βOG between the mesophase and the bulk aqueous phase, causing the effective βOG/MO ratio in the bilayers to decrease. Lower solubility of βOG at higher salt concentrations may explain the apparent lack of this trend in samples prepared with salt solution concentrations above 1.0 M, where partition of salt dominates likely the changes in the lattice parameters. These observations strongly suggest that the effective salt concentration in the aqueous channels of the mesophase, as well as the βOG/MO ratio in the bilayers, differ from the nominal values in mesophases beyond the hydration boundary.

2.4 Discussion

2.4.1 Implications for membrane protein crystallization

The outcome of a crystallization trial must be determined by the exact conditions experienced by the protein molecules within the mesophase. Certain mesophase properties, such as the diffraction pattern, the lattice type, and the lattice parameter of the mesophase are easily established and may provide information about the size of the aqueous channels within the mesophase,[43,44] important for protein diffusion and crystallogenesis.[45,46] At the same time, our data illustrate the difficulties in assessing the exact compositional makeup of the mesophase in crystallization systems and its effect on crystallization. Some of the parameters that are sensitive to βOG/MO ratio in bilayers and the salt concentration within the channels are the viscosity and elasticity of bilayers, and electrostatic screening between the hydrophilic domains of the protein. A better understanding of the effect of those variables could provide routes for optimizing crystallization protocols and improving the success rate of *in meso* crystallization.

2.4.2 Implications for assessment of compatibility of detergents and crystallization screens with *in meso* crystallization

Because mesophases of cubic type are required for membrane protein crystallogenesis *in meso*, compatibility of crystallization screens as well as detergents with cubic phase formation has been investigated in a number of reports.[5,47,48] However, only a single data set for MO combined with detergents and precipitants at crystallization-relevant concentrations is available.[10] Most studies focused on either MO mixed with detergent solutions in the 60:40 v/v ratio, as in the original protocol for *in meso* crystallization, or for MO mixed with excess, usually unspecified, of a multi-component precipitant solution (Section 1.3.3). Nevertheless, such data have been invaluable in assessing general trends on the effect of certain components on the microstructure of MO mesophases and the relative magnitude of this effect as, for example, in the data for series of *n*-alkyl-β-D-glucopyranoside detergents.[10,12,15]

Our results, however, highlight the difficulty of inferring the microstructure of the resultant mesophase in the crystallization trial from the information on the effect of individual additives on the phase behavior of MO under a limited range of conditions, as discussed in Chapter 1.3.3. For example, our samples with βOG/MO ratios of 0.033, 0.066, and 0.099

produced *Ia3d*, *Ia3d* + *Lα*, and *Lα* phases, respectively, when mixed with water to match the 60:40 MO:detergent solution ratio, yet all formed *Pn3m* cubic phases when mixed with an excess of a phosphate salt solution in a wide range of concentrations c_{salt}. These observations agree with previously reported data.[10] Information on detergent-containing mesophases at full hydration in absence of precipitant may provide a relevant starting point for assessing the phase behavior in crystallization systems, yet data for MO/detergent/water mesophases with hydration level varied independently of detergent loading are scarce[10-13,16] and typically cover a very limited range of phase space, although the ternary MO/βOG/system has been investigated in great detail.[10,11,13,16] Additionally, our results showed that quantitative effects of individual components on the lattice parameter of MO mesophases at and above full hydration are affected by the presence of other components in the systems. Thus, if fine-tuning of lattice parameters in crystallization systems is of interest, the analysis of the complete system including MO, detergents, and precipitants under conditions expected during a crystallization trial, would be necessary until reliable modeling approaches or correlations become available.

The systems studies here were relatively simple due to easily discernible compartmentalization of additives. One additive (salt) remained in the aqueous environment both within and outside of the mesophase, and the incorporation of the second additive (detergent) in the bilayers was determined by its amphiphilic properties, making qualitative prediction of trends relatively straightforward. If solely the resultant phase type and the plausible trend in the variation of the lattice parameters are of interest in such systems, partial data on the effect of individual components may suffice, especially for fully hydrated mesophases. Commercially available crystallization screens, however, contain components that may partition between the aqueous compartments and the bilayers of the mesophase, significantly complicating the phase behavior. Phase types and lattice parameters of lipidic mesophases in these systems may be expected to depend strongly on the amount of excess precipitant in the mixture, further necessitating experimental studies of the phase behavior to assess compatibility of crystallization screens.

2.5 Conclusions

We investigated the phase behavior of mesophases of MO mixed with additives frequently used for *in meso* membrane protein crystallization, namely, sodium and potassium phosphate salts and the detergent β-octylglucoside. The compositions of mixtures were selected to closely resemble conditions during membrane protein crystallization in meso: βOG/MO and salt/water ratios were kept constant, while varying the hydration level (the weight fraction of the salt solution in the mixture) in the mixture. MO mixtures with salt solutions without detergent under conditions of excess aqueous phase were also studied.

Quaternary MO/βOG/water/phosphate salt mesophases studied here exhibited a remarkably regular behavior with a sequence of phases tracing that of MO/water mesophases as a function of aqueous solution content. Locations of phase boundaries and values of lattice parameters both above and below the hydration boundary shifted in agreement with previously established effects of detergents and phosphate salts on the microstructure of MO mesophases. At the same time, quantitative effects of each additive (detergents or phosphate salts) on lattice parameters in fully hydrated mesophases in the quaternary systems differed from those estimated from data for ternary MO/water/additive systems, making *a priori* quantitative predictions of lattice parameters in crystallization mixtures difficult. Additionally, we found evidence of re-distribution of both types of additives between the mesophase and the aqueous solution, potentially causing significant changes in the compositional makeup of the mesophase, such as the βOG/MO ratio and the salt concentration in the aqueous channels within the mesophase.

In summary, our findings strongly suggest that compatibility of precipitants with cubic phase formation, a requirement for protein crystallogenesis *in meso*, must be probed under conditions of crystallization trials, *i.e.*, with detergent present in the mixture, and with a large amount of precipitant. Exact amount of precipitant in the mixture may be expected to be of special importance for precipitants containing small molecules that may partition between aqueous and lipidic environments. Even if the propensity of MO mesophases for the formation of persistent metastable phases is ignored, the multitude of detergents and precipitants available, as well as the lack of fine control over detergent concentrations in protein solutions used for crystallization, make the parameter space enormous. Recent developments[47,48] in the high-throughput SAXS analysis of lipidic mesophases may aid greatly in these studies.

2.6 References

1 P. Nollert, H. Qiu, M. Caffrey, J. P. Rosenbusch and E. M. Landau. Molecular mechanism for the crystallization of bacteriorhodopsin in lipidic cubic phases. *FEBS Lett.*, 2001, **504**, 179-186.

2 M. Grabe, J. Neu, G. Oster and P. Nollert. Protein interactions and membrane geometry. *Biophys. J.*, 2003, **84**, 854-868.

3 R. Efremov, G. Shiryaeva, G. Bueldt, A. Islamov, A. Kuklin, L. Yaguzhinsky, G. Fragneto-Cusani and V. Gordeliy. SANS investigations of the lipidic cubic phase behaviour in course of bacteriorhodopsin crystallization. *J. Cryst. Growth*, 2005, **275**, e1453-e1459.

4 V. Cherezov and M. Caffrey. Membrane protein crystallization in lipidic mesophases. A mechanism study using X-ray microdiffraction. *Faraday Discuss.*, 2007, **136**, 195-212.

5 V. Cherezov, H. Fersi and M. Caffrey. Crystallization screens: Compatibility with the lipidic cubic phase for in meso crystallization of membrane proteins. *Biophys. J.*, 2001, **81**, 225-242.

6 V. Cherezov, J. Clogston, Y. Misquitta, W. Abdel-Gawad and M. Caffrey. Membrane protein crystallization *in meso*: Lipid type-tailoring of the cubic phase. *Biophys. J.*, 2002, **83**, 3393-3407.

7 V. Cherezov, J. Clogston, M. Z. Papiz and M. Caffrey. Room to move: Crystallizing membrane proteins in swollen lipidic mesophases. *J. Mol. Biol.*, 2006, **357**, 1605-1618.

8 J. Briggs, H. Chung and M. Caffrey. The temperature-composition phase diagram and mesophase structure characterization of the monoolein/water system. *J. Phys. II*, 1996, 723-751.

9 H. Qiu and M. Caffrey. The phase diagram of the monoolein/water system: Metastability and equilibrium aspects. *Biomaterials*, 2000, **21**, 223-234.

10 Y. Misquitta and M. Caffrey. Detergents destabilize the cubic phase of monoolein: Implications for membrane protein crystallization. *Biophys. J.*, 2003, **85**, 3084-3096.

11 E. Sparr, P. Wadsten, V. Kocherbitov and S. Engström. The effect of bacteriorhodopsin, detergent and hydration on the cubic-to-lamellar phase transition in the monoolein–distearoyl phosphatidyl glycerol–water system. *Biochim. Biophys. Acta - Biomembr.*, 2004, **1665**, 156-166.

12 X. Ai and M. Caffrey. Membrane protein crystallization in lipidic mesophases: Detergent effects. *Biophys. J.*, 2000, **79**, 394-405.

13 G. Persson, H. Edlund, H. Amenitsch, P. Laggner and G. Lindblom. The 1-monooleoyl-*rac*-glycerol/*n*-octyl-β-d-glucoside/water system. Phase diagram and phase structures determined by NMR and X-ray diffraction. *Langmuir*, 2003, **19**, 5813-5822.

14 B. Angelov, M. Ollivon and A. Angelova. X-ray diffraction study of the effect of the detergent octyl glucoside on the structure of lamellar and nonlamellar lipid/water phases of use for membrane protein reconstitution. *Langmuir*, 1999, **15**, 8225-8234.

15 C. Sennoga, A. Heron, J. M. Seddon, R. H. Templer and B. Hankamer. Membrane-protein crystallization in cubo: Temperature-dependent phase behaviour of monoolein-detergent mixtures. *Acta Crystallogr. D*, 2003, **59**, 239-246.

16 G. Persson, H. Edlund and G. Lindblom. Phase behaviour of the 1-monooleoyl-*rac*-glycerol /*n*-octyl-β-d-glucoside/water system. *Progr. Colloid Polym. Sci.*, 2004, **123**, 36-39.

17 M. Caffrey. Kinetics and mechanism of transitions involving the lamellar, cubic, inverted hexagonal and fluid isotropic phases of hydrated monoacylglycerides monitored by time-resolved x-ray diffraction. *Biochemistry*, 1987, **26**, 6349-6363.
18 R. Vargas, L. Mateu and A. Romero. The effect of increasing concentrations of precipitating salts used to crystallize proteins on the structure of the lipidic Q^{224} cubic phase. *Chem. Phys. Lipids*, 2004, **127**, 103-111.
19 H. Takahashi, A. Matsuo and I. Hatta. Effects of chaotropic and kosmotropic solutes on the structure of lipid cubic phase: Monoolein-water systems. *Mol. Cryst. Liquid Cryst. A*, 2000, **347**, 231-238.
20 M. Caffrey and V. Cherezov. Crystallizing membrane proteins using lipidic mesophases. *Nat. Protocols*, 2009, **4**, 706-731.
21 T. C. Huang, H. Toraya, T. N. Blanton and Y. Wu. X-ray powder diffraction analysis of silver behenate, a possible low-angle diffraction standard. *J. Appl. Crystallogr.*, 1993, **26**, 180-184.
22 A. Le Bail, H. Duroy and J. L. Fourquet. Ab-initio structure determination of $lisbwo_6$ by X-ray powder diffraction. *Mater. Res. Bull.*, 1988, **23**, 447-452.
23 G. Pawley. Unit-cell refinement from powder diffraction scans. *J. Appl. Crystallogr.*, 1981, **14**, 357-361.
24 E. Kondrashkina, D.S. Khvostichenko, S.L. Perry, J. von Osinski, P.J.A. Kenis and K. Brister. Using macromolecular-crystallography beamline and microfluidic platform for small-angle diffraction studies of lipidic mesophases for membrane protein crystallization. *J. Phys. Conf. Ser.*, 2012, accepted.
25 V. Cherezov, K. M. Riedl and M. Caffrey. Too hot to handle? Synchrotron X-ray damage of lipid membranes and mesophases. *J. Synchrotron Rad.*, 2002, **9**, 333-341.
26 W. Kunz, J. Henle and B. W. Ninham. 'Zur lehre von der wirkung der salze' (about the science of the effect of salts): Franz hofmeister's historical papers. *Curr. Opin. Colloid Interface Sci.*, 2004, **9**, 19-37.
27 L. Saturni, F. Rustichelli, G. M. Di Gregorio, L. Cordone and P. Mariani. Sugar-induced stabilization of the monoolein pn3m bicontinuous cubic phase during dehydration. *Phys. Rev. E*, 2001, **64**, 040902.
28 P. Mariani, F. Rustichelli, L. Saturni and L. Cordone. Stabilization of the monoolein *Pn3m* cubic structure on trehalose glasses. *Eur. Biophys. J.*, 1999, **28**, 294-301.
29 D. C. Turner, Z.-G. Wang, S. M. Gruner, D. A. Mannock and R. N. McElhaney. Structural study of the inverted cubic phases of di-dodecyl alkyl-β-d-glucopyranosyl-rac-glycerol *J. Phys. II*, 1992, **2**, 2039-2063.
30 D. P. Siegel. Fourth-order curvature energy model for the stability of bicontinuous inverted cubic phases in amphiphile−water systems. *Langmuir*, 2010, **26**, 8673-8683.
31 G. C. Shearman, O. Ces and R. H. Templer. Towards an understanding of phase transitions between inverse bicontinuous cubic lyotropic liquid crystalline phases. *Soft Matter*, 2010, **6**, 256-262.
32 J. N. Israelachvili, D. J. Mitchell and B. W. Ninham. Theory of self-assembly of hydrocarbon amphiphiles into micelles and bilayers. *J. Chem. Soc. Faraday Trans. II*, 1976, **72**, 1525-1568.
33 T. R. Carale, Q. T. Pham and D. Blankschtein. Salt effects on intramicellar interactions and micellization of nonionic surfactants in aqueous solutions. *Langmuir*, 1994, **10**, 109-121.

34 P. Mukerjee and C. C. Chan. Effects of high salt concentrations on the micellization of octyl glucoside: Salting-out of monomers and electrolyte effects on the micelle − water interfacial tension. *Langmuir*, 2002, **18**, 5375-5381.
35 Y. Zhang and P. S. Cremer. Chemistry of Hofmeister anions and osmolytes. *Annu. Rev. Phys. Chem.*, 2010, **61**, 63-83.
36 R. Aveyard and S. M. Saleem. Interfacial tensions at alkane-aqueous electrolyte interfaces. *J. Chem. Soc. Faraday Trans. I*, 1976, **72**, 1609-1617.
37 H. Chung and M. Caffrey. The curvature elastic-energy function of the lipid-water cubic mesophase. *Nature*, 1994, **368**, 224-226.
38 A. Gulik, V. Luzzati, M. De Rosa and A. Gambacorta. Structure and polymorphism of bipolar isopranyl ether lipids from archaebacteria. *J. Mol. Biol.*, 1985, **182**, 131-149.
39 R. P. Rand, N. L. Fuller, S. M. Gruner and V. A. Parsegian. Membrane curvature, lipid segregation, and structural transitions for phospholipids under dual-solvent stress. *Biochemistry*, 1990, **29**, 76-87.
40 C. V. Kulkarni, W. Wachter, G. Iglesias-Salto, S. Engelskirchen and S. Ahualli. Monoolein: A magic lipid? *Phys. Chem. Chem. Phys.*, 2011, **13**, 3004-3021.
41 B. Angelov, A. Angelova, M. Ollivon, C. Bourgaux and A. Campitelli. Diamond-type lipid cubic phase with large water channels. *J. Am. Chem. Soc.*, 2003, **125**, 7188-7189.
42 D.S. Khvostichenko, E. Kondrashkina, S. L. Perry, K. Brister, P. J. A. Kenis. An X-ray transparent microfluidic platform for screening of the phase behavior of lipidic mesophases, 2012, submitted (Chapter 3).
43 P. Garstecki and R. Hołyst. Scattering patterns of self-assembled cubic phases. 1. The model. *Langmuir*, 2002, **18**, 2519-2528.
44 P. Garstecki and R. Hołyst. Scattering patterns of self-assembled cubic phases. 2. Analysis of the experimental spectra. *Langmuir*, 2002, **18**, 2529-2537.
45 V. Cherezov, J. Liu, M. Griffith, M. A. Hanson and R. C. Stevens. LCP-FRAP assay for pre-screening membrane proteins for *in meso* crystallization. *Cryst. Growth Design*, 2008, **8**, 4307-4315.
46 F. Xu, W. Liu, M. A. Hanson, R. C. Stevens and V. Cherezov. Development of an automated high throughput LCP-FRAP assay to guide membrane protein crystallization in lipid mesophases. *Cryst. Growth Design*, 2011, **11**, 1193-1201.
47 J. S. Joseph, W. Liu, J. Kunken, T. M. Weiss, H. Tsuruta and V. Cherezov. Characterization of lipid matrices for membrane protein crystallization by high-throughput small angle X-ray scattering. *Methods*, 2011, **55**, 342-349.
48 C. E. Conn, C. Darmanin, X. Mulet, S. Le Cann, N. Kirby and C. J. Drummond. High-throughput analysis of the structural evolution of the monoolein cubic phase in situ under crystallogenesis conditions. *Soft Matter*, 2012, **8**, 2310-2321.

Chapter 3.

An X-ray transparent microfluidic platform for screening of the phase behavior of lipidic mesophases[1]

Abstract

This chapter describes a microfluidic platform that enables the formulation of highly viscous lipidic mesophases and the subsequent probing of their phase behavior with small-angle X-ray scattering (SAXS). The X-ray compatible platform is comprised of thin polydimethylsiloxane (PDMS) layers sandwiched between cyclic olefin copolymer (COC) sheets for a total thickness of 220 μm. The mesophases are formulated on-chip by mixing lipid with aqueous solutions using less than 40 nL of each material per sample, which is a significant reduction from the microliter-scale necessary when using the current standard for sample preparation, a coupled-syringe mixer. To prepare uniform mesophases, an active on-chip mixing strategy is employed, coupled with periodic cooling of the sample to reduce the viscosity. The platform was validated by preparing and analyzing mesophases of lipid monoolein (MO) mixed with aqueous solutions of different concentrations of β-octylglucoside (βOG), a detergent frequently used in membrane protein crystallization. Four samples were prepared in parallel on chip, by first metering and automatically diluting βOG to obtain detergent solutions of different concentration, then metering MO, and then mixing by actuation of pneumatic valves. Integration of detergent dilution and subsequent mixing significantly reduces the number of manual steps needed for sample preparation. SAXS data revealed three different types of mesophases on-chip. Furthermore, identical samples formulated on different chips exhibited excellent agreement in microstructural parameters. Similarly, phase behavior observed on-chip corresponded well with that observed for 300-fold larger samples prepared via the traditional coupled-syringe method ("off-chip"), further validating the utility of the microfluidic platform for on-chip characterization of mesophase behavior.

[1] Part of the work presented in this chapter has been submitted for publication: D.S. Khvostichenko, E. Kondrashkina, S.L. Perry, A.S. Pawate, K. Brister, P.J.A. Kenis. "An X-ray transparent microfluidic platform for screening of the phase behavior of lipidic mesophases". D.S.K. designed and fabricated chips, formulated samples, collected and analyzed SAXS data. S.L.P. fabricated chips and collected SAXS data, A.S.P. collected SAXS data, E.K. and K.B. developed the setup for SAXS data collection. D.S.K. and P.J.A.K. wrote the manuscript. The figures shown here were created by D.S.K. with input from P.J.A.K.

3.1 Introduction

Certain lipids, when mixed with water or aqueous solutions, self-assemble into lipidic mesophases whose structure consists of highly ordered arrangements of continuous lipidic bilayers interpenetrated with aqueous channels.[1] The phase type, *i.e.*, the arrangement of lipid bilayers, is highly sensitive to the composition of the mixture as well as temperature, and can be reliably identified from small-angle X-ray scattering (SAXS) data.[2,3] Lipidic mesophases have been used in a number of applications such as drug delivery[4] and biosensing.[5] Most importantly, lipidic mesophases serve as matrices for stabilizing and crystallizing integral membrane proteins that are otherwise very difficult to handle, owing to their amphiphilic nature.[3,6] In the *in meso* crystallization approach, membrane proteins are reconstituted into the lipid bilayers of the mesophase, which prevents the protein from unfolding. Crystallization is triggered by adding a multi-component precipitant solution, with protein crystals growing within the lipidic mesophase in a successful crystallization trial. To date the *in meso* method accounts for ~10% of all structures of membrane proteins available in the public domain.[6] Among recent successes of the method are structures of the human β2 adrenergic receptor,[7] the dopamine D3 receptor, [8] and the κ-opioid receptor.[9]

The lipid most commonly used for *in meso* crystallization is monoolein (MO).[3] Under crystallization-relevant conditions it usually forms three types of mesophases: lamellar phase *Lα* and two cubic phases of different symmetries referred to as *Pn3m* and *Ia3d.*[10-15] The lamellar phase consists of stacks of lipid bilayers with one-dimensional spatial periodicity, whereas *Pn3m* and *Ia3d* phases contain curved lipid bilayers in complex geometries, are bicontinuous and periodic in three dimensions.[2,10,11,16,17]

The type of mesophase is crucial for the success of crystallization trials as protein crystal growth has only been reported from bulk cubic phases.[15,18] The components of the crystallization mixture affect phase behavior in a non-trivial way.[19] In particular, detergents used to stabilize the protein prior to its incorporation in the mesophase have a profound effect on the phase behavior and tend to promote the formation of lamellar mesophases which are unsuitable for crystallization.[13,14,20]

Exploration of phase diagrams to unravel trends in phase behavior requires preparation and analysis of a large number of samples, a highly arduous task. For lipidic mesophases the

situation is exacerbated by their high viscosity.[21] In the state of the art procedure, each mesophase sample is prepared by mixing the lipid with water in a coupled-syringe mixer on a milligram (microliter) scale.[3] The resulting mixture is then dispensed into a glass capillary for SAXS analysis.[3] Recently, mixing of lipid and an aqueous component was automated in a 96-well plate format,[22] but still 30 μL of MO and solution had to be metered manually for each sample. While only 50 nL of mesophase is required for analysis in another recently published approach for high-throughput SAXS analysis of lipidic mesophases,[23] the sample had to be formulated on a bulk scale in a coupled-syringe mixer and dispensed in small boluses using an expensive robotic system. Furthermore, the high-throughput SAXS methods reported to date[23,24] are limited to the formulation of lipidic mesophases in equilibrium with a large excess of aqueous solutions, excluding a large region of the phase space.

Microfluidics offers the potential to automate metering and simultaneous preparation of multiple samples, making it very attractive for the studies of the phase behavior. Previously, a microfluidic platform capable of preparing uniformly mixed mesophases on a ~20 nL scale was demonstrated. The platform relied on an active mixing strategy,[25] unlike a number of other microfluidic platforms reported for less challenging phase behavior studies.[26-39] The chip was validated by the *in meso* crystallization of membrane protein bacteriorhodopsin. Microfluidic systems developed to date for phase behavior studies are only applicable to low-viscosity solutions and typically rely on phase transitions driven by composition changes due to diffusion of solutes,[26,27,34-37] evaporation of water,[29-33], and osmotic stress.[38,39] Such platforms are not suitable for the formulation of viscous mesophases with strict pre-set ratios of volume or weight of components. Furthermore, platforms with integrated fluid handling capabilities are usually incompatible with advanced analytical techniques, including SAXS, due to signal attenuation caused by device materials.[40] On the other hand, although X-ray transparent microfluidic devices are available, they lack (with a single exception[41]) sophisticated architecture needed for mesophase formulation on-chip.

The microfluidic platform reported here combines active mixing capabilities and X-ray transparency for the analysis of the phase behavior of lipidic mesophases. The platform is specifically designed to assess the effect of detergent on the phase behavior and is capable of simultaneously preparing four mesophase samples with different compositions using less than a total of 200 nL of detergent solution and lipid, which represents a 300-fold reduction compared

to the standard method. To demonstrate the utility of this platform we mapped a section of a phase diagram for MO mixed with solutions of β-octylglucoside (βOG), a detergent commonly used in the isolation and purification of membrane proteins.[3,13]

3.2 Materials and methods

3.2.1 Device fabrication

Hybrid microfluidic chips consisted of a flat cyclic olefin copolymer (COC) top layer (4 mil, 5013 or 6013, TOPAS Advanced Polymers), a thin PDMS (RTV 650, Momentive Performance Adhesives) control layer, a thin PDMS fluid layer, and a flat COC bottom substrate (Section 3.3.1, Figure 3.1). The patterned PDMS layers were fabricated using standard soft lithographic procedures[42,43] as described below. Photoresist-on-silicon masters were created using SPR-220-7 photoresist (Shipley) for the fluid layer with the feature height of ~14 μm, and SU8-25 photoresist (Microchem) for the control layer with the feature height of ~25 μm. Positive photoresist was reflowed by heating at 120 °C for 2 min to ensure complete closure of channels upon valve actuation.[42,43] PDMS control layers were prepared by spin-coating PDMS with the monomer : cross-linker ratio of 12:1 followed by curing at 90 °C for 7-9 min to obtain a 45 μm-thick film. PDMS fluid layers were prepared by spin-coating PDMS with the monomer : cross-linker ratio of 5:1 followed by curing at 80 °C for 3 min to obtain a 25 μm-thick film.

COC sheets were flattened between glass slides at 177 °C and a load of 150-200 kg in a laminating press (Carver, Model 3851) prior to use to obtain sheets with smooth surface. A PDMS block with the thickness of 4-7 mm was bonded in the inlet area. PDMS-to-PDMS bonding was done using the standard multilayer soft lithography method[43] by placing layers of PDMS with different monomer : cross-linker ratios in conformal contact and heating them at 70 °C for 2 hrs. All PDMS-to-COC bonding was achieved using amine/epoxy chemistry as reported by Tang and Lee[44] using 3-aminopropyltrimethoxysilane (Sigma-Aldrich, >97%) and 3-glycidyloxypropyltrimethoxysilane (GPTMS, Sigma-Aldrich, 98%).

The chips were assembled as follows: (i) inlet holes were drilled in the thick PDMS block and in the top COC sheet using a 750 μm drill bit; (ii) the PDMS block was bonded to the top COC layer; (iii) the PDMS-COC assembly was bonded to the PDMS control layer; (iv) the resulting PDMS-COC-PDMS assembly was bonded to the PDMS fluid layer; and (v) the

assembled chip was bonded to the bottom COC substrate and kept at 70 °C for 1 hour to facilitate bonding. To prevent permanent closure of normally-closed valves in the final permanent bonding step, the corresponding control lines were actuated using a vacuum pump prior to bringing the two parts of the device in contact, and remained actuated at all times until the water-rinse step. After at least 3 hours, the fluid layer was filled with a solution of 1M TRIS buffer, pH 8.0, to neutralize remaining active epoxy groups of the GPTMS layer on the inner surface of fluid channels and chambers. After at least 1 hour the fluid layer was rinsed with deionised water and dried with nitrogen gas.

3.2.2 Device operation

During filling and mixing, microfluidic devices were monitored using an upright microscope (Leica MDG33) equipped with a macro lens and a digital camera (Leica DFC295).

Prior to filling and mixing operations, fluid-routing control lines (Chapter 3.3.1, Figure 3.1a) were filled with Fluorinert FC-40 (3M) to prevent gas leakage from the control layer through valve membranes to the fluid layer and subsequent bubble formation in the samples.

For pneumatic actuation we used a 32-line solenoid valve manifold (Fluidigm). The pressure in the manifold and the sequence of valve actuations were controlled by Genie V2 software (Fluidigm). The dead-ended fluid chambers were filled with samples by applying a pressure of 5.5 psi to the filling fluid to displace air from the chambers. Pressure of 22.5 psi was used to actuate fluid-routing valves. Pressure of 13-17 psi was used to actuate injection valves over the mixer chambers (Chapter 3.3.1, Figure 3.1a) during mixing steps. During mixing, an alternating series of forward and reverse sequences of lipidic mixer valve actuations[44] was used to avoid formation of stagnation zones in the chambers.

3.2.3 Chamber volume measurements

To determine the ratio of volumes for the aqueous and lipidic components of the mesophase, we measured the ratio of fluorescent intensities of the two small chambers and the large chamber of the lipidic mixer filled with the same solution of a fluorophore. The chambers were filled with a saturated solution of fluorescein (Acros Organics) in deionised water under the pressure of 5.5 psi, and the isolation valves were closed without releasing the pressure from the fluid lines. Inter-chamber isolation valves were closed during filling to simulate formulation

conditions of lipidic mesophases. Fluorescent images were collected with a Leica N PLAN 2.5× (0.07 NA) objective on a Leica DMI 4000B microscope equipped with a xenon lamp. All images were collected with a charge-coupled device camera (Hamamatsu ORCA-ER, Model C4742-80). Images were processed using the ImageJ program (v. 1.46i, Wayne Rasband, NIH, USA) by performing a background correction and a flatfield correction. The ratio of volumes of the lipid compartment and the aqueous solution compartment was calculated as the ratio of cumulative fluorescent intensities of respective chambers after corrections, resulting in the value of 55 (lipid) : 45 (aqueous solution) v/v. Because the illumination intensity in the original images was visibly non-uniform, we tested the accuracy of the intensity correction procedure by analyzing two photographs of the same mixer that differed with respect to the orientation of the mixer in the field of view (180° rotation in one image with respect to the other). After background and flatfield correction, the calculated ratio of intensities of the chambers in the two images differed by less than 0.5%, confirming the validity of our analysis.

3.2.4 Sample preparation

MO (Sigma Aldrich, 99%) was used as received. A 20% v/w βOG (Anatrace, Anagrade) solution in 25 mM NaH_2PO_4, pH 5.5 was diluted volumetrically with a detergent-fee solution of 25 mM NaH_2PO_4, pH 5.5, to obtain solutions with concentrations of 5% v/w and 10% v/w of βOG. NaH_2PO_4 was obtained from EMD Chemicals. Several drops of red food coloring solution (McCormick) were added to the 25 mM NaH_2PO_4, pH 5.5 buffer solution without detergent for visualization used for the preparation of on-chip samples. We established that addition of the food coloring did not affect the phase behavior of MO mesophases.

On-chip samples were prepared 1-4 days prior to the measurements. After preparation, the fluid layer inlets were sealed with Crystal Clear Tape (Hampton Research) and devices were stored at -80 °C to avoid water evaporation. Prior to measurements, the samples were defrosted, and held at data collection temperature (25 ± 0.5 °C) for at least 2 hours.

Samples prepared using coupled-syringe mixers were formulated gravimetrically for a total sample amount of 30-40 mg. Although samples on-chip were metered by volume, weight and volume compositions are nearly identical because densities of both MO and βOG solutions are very close to 1 g/mL.[45-47] Each sample was dispensed into four thin-walled 0.9 mm glass capillaries (Charles Supper), and sealed with CritoSeal (Leica Microsystems) and QuickSet

Epoxy (Henkel Co.). The capillaries were stored at -80 °C and allowed to equilibrate at data collection temperature (25 ± 0.5 °C) for at least 2 hours prior to measurements.

3.2.5 SAXS data collection

SAXS data collection was performed on protein crystallography beamline LS-CAT 21-ID-D at Advanced Photon Source (APS), Argonne National Lab. The beamline was equipped with a microdiffractometer (MAATEL MD2) consisting of a goniometer, XYZ micropositioner and an on-axis video microscope. For SAXS measurements, a vacuum flight tube and an adjustable beam stop with an incorporated pin-diode were installed between the sample and the CCD detector (Rayonix MX300). A detailed description of the setup is reported elsewhere.[24] The position of the sample in the X-ray beam was monitored using the video microscope; the microfluidic chip was translated relative to the beam using the XYZ micropositioner. The footprint of the X-ray beam was 20 μm. The beam energy was 8 keV. Attenuation of the incident X-ray beam and exposure time were optimized to achieve highest signal-to-noise ratio while avoiding radiation damage.[12,48]

Data were collected in a grid of points spaced approximately 250 μm apart, with 3 rows (along the long dimension of the chamber) of 8 points each in central chambers, and 2 rows of 6 points each in side chambers of each lipidic mixer.

3.2.6 SAXS data processing

Raw diffractograms were integrated in Fit2D software (v. 12.077, A. P. Hammersley, ESRF, 1994). Because the diffractograms for different points within a single sample chamber differed negligibly with respect to peak positions, indicating identical sample properties throughout the chamber, for further analysis we used a sum of all diffractograms corresponding to a given chamber to obtain a higher signal/noise ratio. Integrated diffractograms were processed in MATLAB (R2008a, v. 7.6.0.324, The MathWorks Inc., Natick, MA). Publicly available MATLAB code (findpeaks.m, T.C. O'Haver, v2, revised Oct 27, 2006) was used to locate peak center positions. A series of MATLAB scripts was developed for baseline correction, and phase assignment for integrated diffractograms. Accuracy of all phase assignments was verified manually. Mesophases were identified based on characteristic sets of reflections and lattice parameters were calculated using the peak position of the highest-intensity reflection for a

given mesophase (Appendix A). Relative amounts of mesophases were calculated based on the intensity of the highest-intensity reflection for each phase type (Chapter 3.2.7).

In calculating the average lattice parameters and relative amounts of each mesophase, the end points of each row of datapoints were excluded to avoid artifacts related to cross-talk between sample compartments and fluidic lines. We also noticed systematic differences within a given mixer (sample) between lattice parameters of samples in side chambers closest to the edges of the device and the other two chambers of the mixer. The lattice parameters of samples in outer chambers were smaller than the lattice parameters of central mixer chambers and side mixer chambers facing the center of the device, likely due to adsorption of water into PDMS. Thus, data points corresponding to outer chambers of mixers were also excluded in the averaging of lattice parameters and relative amounts of mesophases. We did not observe any systematic differences between the lattice parameters of samples in the central chamber of the mixer and the side chamber facing the center of the device in a given mixer.

3.2.7 Estimating relative amounts of mesophases

Amounts of mesophases in each sample were estimated based on the intensity of the most prominent reflection d_{max} of a given mesophase (d_1 for $L\alpha$, d_{111} for *Ia3d*, d_{110} for *Pn3m*). Raw diffractograms were integrated from θ = 0 to θ = 4° in 0.001333° increments for a total of 3000 points for each integrated diffractogram. The scattering vector q reported in Figures 3.4-3.7 is related to the scattering angle θ as $q = 4\pi \sin\theta / \lambda$.

The intensity corresponding to a given phase $I_{phase}^{\max}$ was read from the diffractogram based on the value of lattice parameter in the phase assignment:

$$\theta_{\max} = \operatorname{asin}\left(\frac{\lambda}{2a/\sqrt{h_{\max} + k_{\max} + l_{\max}}} \right) \qquad \text{Equation 3.1}$$

$$I_{phase}^{\max} = I^{corr}(\theta_{\max}) \qquad \text{Equation 3.2}$$

where a is the lattice parameter of a given phase, h_{max}, k_{max}, and l_{max} are the *hkl* indices of a highest-intensity reflection of a given phase, λ is the wavelength of the incident X-ray beam, I^{corr} is the intensity of the diffractogram after baseline correction to account for scattering around the beamstop, which is comparable in the intensity to the intensity of the sample (Chapter

3.3.5, Figures 3.4, 3.6, and 3.7).

Fluctuations of beam intensity during data collection, typical for synchrotron X-ray sources, could result in variations in signal intensity from otherwise identical samples. To crudely account for the fluctuations, we used the scattering intensity around the beamstop, free from *hkl* reflections, as a measure of beam intensity for each diffractogram:

$$I_{beam} = \frac{\sum_{n(\theta=0.15)}^{n(\theta=0.20)} I(n)}{n(\theta=0.20) - n(\theta=0.15)} - \frac{\sum_{n(\theta=2.5)}^{n(\theta=4.0)} I(n)}{n(\theta=4.0) - n(\theta=2.5)} \qquad \text{Equation 3.3}$$

where $n(\theta)$ is the number of data point in the diffraction angle – diffraction intensity array corresponding to a given value of θ. For the calculations of sample composition the beam intensity-adjusted value of sample intensity was used:

$$I_{phase}^{adj} = \frac{I_{phase}^{\max}}{I_{beam}} \qquad \text{Equation 3.4.}$$

A value of standard signal intensity I_{phase}^{std} was calculated for each mesophase type. This value corresponds to a sample containing a given phase type only, *i.e.*, 100% of *Pn3m*, *Ia3d*, or *Lα*. For *Ia3d* and *Lα* phases available data points containing a single mesophase type were used to estimate the average "unit" signal intensity corresponding to 100% of a given phase type in the sample

$$I_{phase}^{std} = \frac{\sum_{j} I_{phase}^{adj}(j)}{j_{phase\_only}} \qquad \text{Equation 3.5}$$

where j spans only diffractograms containing solely a given mesophase type and j_{phase_only} is the number of such diffractograms for a given phase type. For the *Pn3m* mesophase no such data were available because it was always observed together with at least one other phase. We used the model of Garstecki and Holyst[49,50] for scattering patterns of cubic phases to estimate the unit signal intensity for the *Pn3m* phase. In the model the intensity I_{hkl}^{mod} of a given *hkl* reflection of a mesophase is given by

$$I_{hkl}^{\mathrm{mod}} = M_{hkl}\left[F_{hkl}^{S*}\frac{\sin\left(\alpha_{hkl}\ \pi\left(h^2+k^2+l^2\right)^{1/2}\ L/a\right)}{\alpha_{hkl}\ 2\pi\left(h^2+k^2+l^2\right)^{1/2}}\right]^2 \qquad \text{Equation 3.6}$$

where L is the lipid bilayer thickness in the mesophase and parameters F_{hkl}^{S*}, α_{hkl}, and M_{hkl} are

constants for a given phase type and *hkl* reflection, given by Garstecki and Holyst.[50] Reflections *110* and *111* for *Pn3m* and *Ia3d* phases, respectively, were used to obtain diffraction signal intensity. Hence, the unit signal intensity for the *Pn3m* phase can be estimated as

$$I_{Pn3m}^{std} = \frac{I_{Ia3d}^{std}}{I_{111,Ia3d}^{\mathrm{mod}}} \cdot I_{110,Pn3m}^{\mathrm{mod}} \qquad \text{Equation 3.7}$$

In the calculations of I_{hkl}^{mod} the value of the bilayer thickness $L = 34.6$ Å was selected based on the correlation for MO/water mesophases by Briggs *et al.*;[10] the value does not change appreciably when detergent is added.[51] Values of lattice parameters used in the calculation were $a(Pn3m) = 148$ Å, $a(Ia3d) = 180$ Å.

Finally, for each lipidic mixer the average intensity of a given phase in the mixer is

$$I_{phase}^{mixer} = \frac{\sum_{j} I_{phase}^{adj}(j)}{j_{phase\_mixer}} \qquad \text{Equation 3.8}$$

where j spans the diffractograms in the mixer that contain a given mesophase type and j_{phase_mixer} is the number such diffractograms for a given mixer. The average amount of the mesophase v_{phase}^{mixer} in the mixer is then

$$v_{phase}^{mixer} = \frac{I_{phase}^{mixer}}{I_{phase}^{std}} \qquad \text{Equation 3.9.}$$

Ideally, the sum of values of v for different phases in the mixer must add up to unity. However, this was not the case here because certain parameters, such as the thickness of the sample and the beam intensity could not be controlled precisely during data collection. Therefore, the data were additionally rescaled:

$$\phi_{phase}^{mixer} = \frac{v_{phase}^{mixer}}{v_{Pn3m}^{mixer} + v_{Ia3d}^{mixer} + v_{L\alpha}^{mixer}} \cdot 100\% \qquad \text{Equation 3.10.}$$

If a certain phase type was absent in the mixer, the corresponding value of v was set to 0. Values of ϕ are reported in Figure 3.8 (Section 3.3.5). Based on the non-uniformity of signal intensities for $L\alpha$ phases we estimate the relative error of ±20% in the calculations of ϕ.

3.3 Results and discussion

The microfluidic platform developed here is capable of screening the phase behavior of lipidic mesophases by simultaneously preparing samples of different composition from only three stock solutions. The platform formulates mesophases by mixing a lipid with detergent solutions. For all on-chip samples the lipid/solution ratio is kept constant while the detergent concentration in solution is varied for different samples via automatic on-chip dilution. This situation where lipid/solution ratio is constant, but the detergent concentration varies is typical of membrane protein crystallization trials. These trials typically follow the same protocol for mesophase formulation, but have a poor control of the detergent concentration from one batch of protein solution to another.[3,15]

3.3.1 Chip fabrication

The microfluidic platform fabricated here met the two main requirements for the preparation and analysis of lipidic mesophases: (i) active mixing capabilities and (ii) X-ray transparency. The platform was fabricated using soft lithography methods with several modifications (see Section 3.2.1).

To retain mixing capabilities while ensuring X-ray transparency, only thin PDMS control and fluid layers were retained in the device. The PDMS layers were sandwiched between thin COC layers that provided rigidity and served as a barrier for water evaporation (Figure 3.1c). The overall thickness of the device was ~220 μm, significantly smaller compared to traditional PDMS-on-glass microfluidic devices. The nominal height of sample compartments was ~15 μm, and the cumulative thickness of PDMS and COC layers above and below sample compartment was 180 μm. All layers were irreversibly bonded to each other, as required for active mixing.

3.3.2 Chip design

The chip is designed to screen the effect of an additive such as detergent on the phase behavior of lipidic mesophases. The chip is capable of preparing several different samples from just three stock solutions. Due to space constraints during X-ray data collection the size of the sample area was limited to 8 x 4 mm, and the overall size of the chip to 12 x 30 mm. Up to *four* sample preparation units could be incorporated per chip under those limitations (Figure 3.1a, b).

The same design principles can be used to scale out the number of samples per chip.

The lipidic mixer was described in detail in our previous work.[25] Briefly, the mixer consists of three chambers that are filled with desired materials and are connected with each other via short, narrow channels. Each mesophase sample was prepared in its own lipidic mixer by combining a lipid with detergent solutions. The central chambers of the mixers were designated for lipid, and the side chambers for detergent solution (Figure 3.1b). The lipid : solution ratio was thus fixed at 55 : 45 v/v, but the detergent concentration in solutions could be varied using round dilution chambers adjacent to the side chambers of respective mixers (Figures 3.1b and 3.2a).

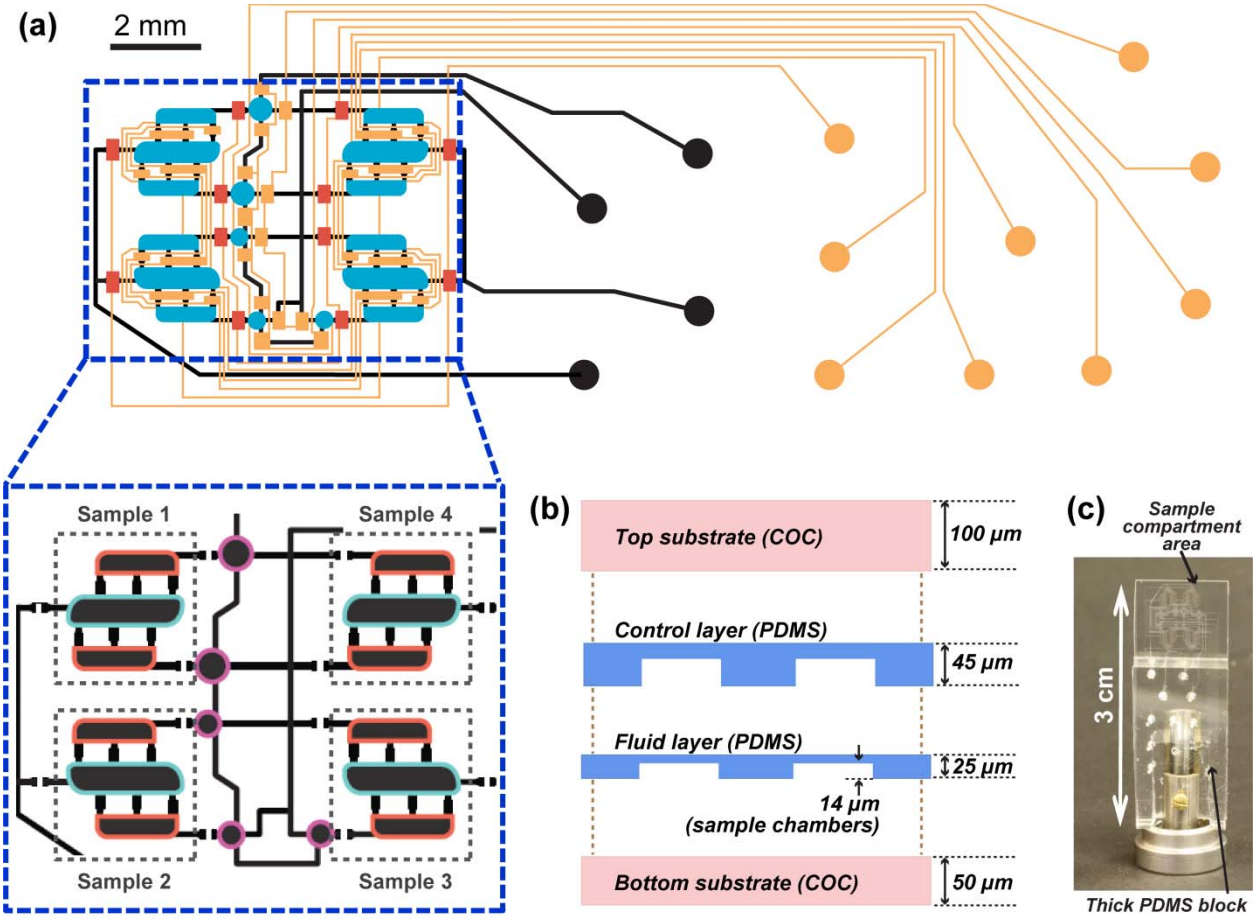

Figure 3.1. (a) Superimposed control (orange, blue, red) and fluid (black) layers of the microfluidic platform for screening of lipid phase behavior. Circles at ends of lines designate the locations of inlet ports. Control layer: orange, normally open routing valves; red, normally closed routing valves; blue, injection valves. The inset shows the layout of fluid layer with compartment designations for the three components required for filling the chip: lipid (blue outline), detergent solution (red outline), and diluent for detergent solution (purple outline). **(b)** Schematic of the layers that comprise the thin part of the chip. **(c)** Photograph of an assembled chip mounted for SAXS data collection. Sample compartments are located in the thin part of the chip, with the fluid and control layer inlets connected via the thick PDMS block.

For fluid routing during filling and mixing, the platform relied on normally open valves

that were controlled pneumatically. To minimize the number of control lines each set of valves performing identical functions was connected using a single control line (Figure 3.1a). Additionally, normally closed valves[52] were incorporated at the inlets of all lipidic mixer chambers to minimize cross-talk during X-ray data collection when pneumatic actuation was not possible.

3.3.3 Chip operation: filling and metering

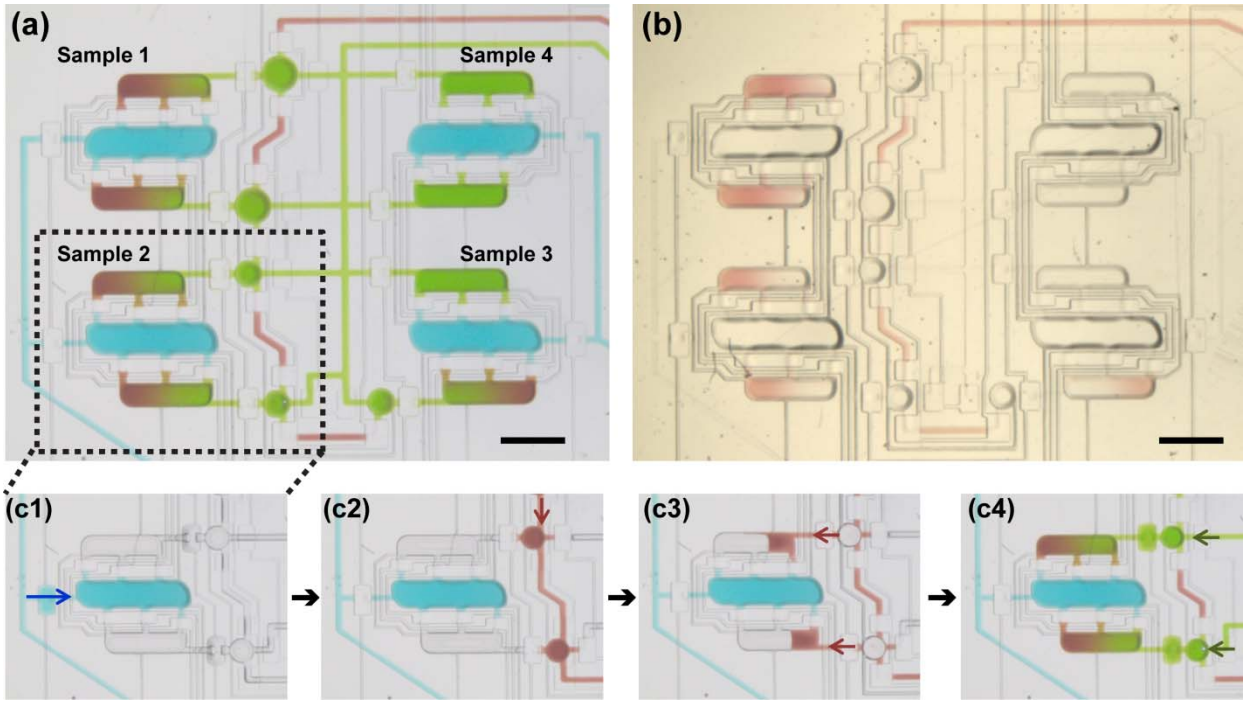

Figure 3.2. On-chip sample formulation. (a) Optical micrograph of a chip filled with solutions of food coloring to illustrate the composition of samples formulated on-chip. Blue color represents lipid; green, concentrated detergent solution; red, diluent for detergent solution. (b) Optical micrograph of a chip filled with components for mesophase preparation. Lipid: MO (colorless); concentrated detergent solution: 20% βOG in 25 mM NaH2PO4, pH 5.5 (colorless); diluent: 25 mM NaH2PO4, pH 5.5 (red). (c1-c4) Sample formulation protocol. Arrows indicate the direction of fluid movement. (c1) Central chamber of the mixer is filled with lipid (blue). (c2) Auxiliary round dilution chambers are filled with a diluent for detergent solution (red). (c3) Diluent is transferred into side chambers of the mixer by actuating injection valves on top of the round chambers. (c4) Side chambers are filled to volume with concentrated detergent solution (green). Scale bar: 1 mm.

The typical filling protocol is illustrated in Figure 3.2(c1)-2(c4). Central chambers of the mixer were filled with lipid, Figure 3.2(c1). To control the dilution of the detergent solution, the round chambers were filled with a diluent, Figure 3.2(c2) which was then transferred to adjacent chambers of lipidic mixers by actuating valve membranes on top of the round chambers, Figure 3.2(c3). The partially filled chambers of lipidic mixers were then filled to volume with a concentrated detergent solution through a separate fluid line, Figure 3.2(c4). In this step the

small amount of diluent remaining in the round chambers was also moved to the lipidic mixer chambers by the flow of the detergent solution.

All chambers, including round dilution chambers, were dead-ended and filling was carried out by pushing the filling fluid into the chambers and slowly displacing the air under the pressure of 5.5 psi. The inlet valves for each chamber of the mixer were closed without releasing the pressure from the fluidic lines. The applied pressure causes tenting of the valve membranes on top of each lipidic mixer chamber, thus altering the volume of each chamber from the originally specified design. The ratio of chamber volumes estimated from fluorescent intensity measurements was 55 (lipid) : 45 (solution) v/v, which deviated from the chamber footprint ratio of 1:1 v/v, presumably due to the tenting. We believe that releasing the pressure would have resulted in less accurate and reproducible metering due to uncontrollable sagging of valve membranes. The accuracy of our metering method is corroborated by the excellent agreement of SAXS data between different chips. The chip required a total volume of ~200 nL of each material (lipid, detergent solution, diluent) for filling, a 300-fold reduction compared to preparing four samples in coupled syringes.

The nominal chamber volume calculated based on the footprint of the chamber and the height of photoresist was 13.2 nL for lipid chambers and 13.7 nL for detergent solution chambers. However, the actual volume was probably larger due to the membrane tenting described above, but should not exceed 36.8 nL and 38.2 nL for lipid and detergent solution chambers, respectively, as estimated from the footprint of the chambers and the sum of heights of chambers in the fluid and the control layer.

3.3.4 Chip operation: mixing

Mixing was achieved by pneumatic actuation of injection valves located over each chamber. These valves drive the fluid from one chamber to another (Figure 3.1a). The valve actuation sequence used in this work was identical to that used for the original lipidic mixer as described previously[25] along with the mechanisms governing the mixing process. In the mixing tests here we established that solutions which resulted in lamellar phases were easily mixed and routed in the mixer. Cubic phases, however, could not be manipulated once formed, leading to partially mixed, non-uniform samples (Figure 3.3a). To circumvent this problem, we exploited the phase behavior of lipidic mesophases, which are known for their propensity to form lamellar

phases when cooled. Cooling was achieved by placing a piece of dry ice on the device to let the sample material freeze, inducing a cubic-to-lamellar phase transition. Active mixing was started as soon as the material thawed and was carried out for 1-2 min, after which the freeze-thaw-mixcycle was repeated. Because the chips were thin, freezing and thawing itself took under 1 min. Uniformly mixed lamellar samples were obtained after 5-7 cycles (Figure 3.3b). Although only tested for MO mesophases here, this strategy should be applicable to other monoacylglycerols, especially when mixed with detergent solutions, because formation of lamellar phases in a wide range of compositions at low temperatures is a general trend in their phase behavior.[13,14,53]

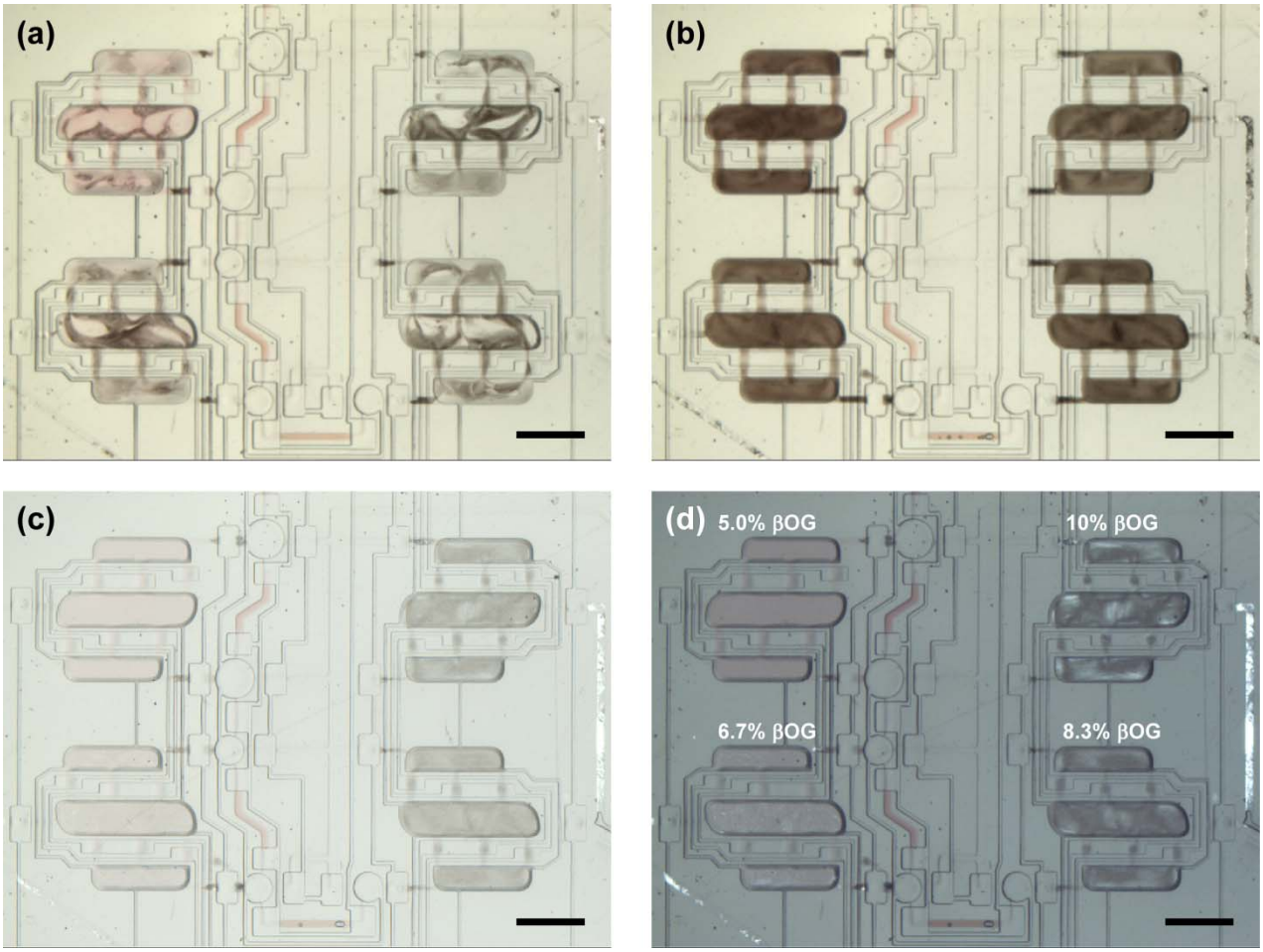

Figure 3.3. Optical micrographs of mesophase samples during mixing. **(a)** Non-uniform mixtures of cubic (light) and lamellar (dark) mesophases at ambient temperature. **(b)** Fully mixed mesophases after several freeze-thaw-mix cycles; the dark color indicates a predominantly lamellar state in all mixers. **(c)** Samples from **(b)** after 30 min at 23 °C. Changes in the appearance of the samples indicate a phase transition from a lamellar phase to cubic phases. **(d)** Same as panel **(c)**, under cross-polarized light. Numbers indicate initial βOG concentrations in aqueous compartments and are the same for all panels. Scale bar: 1 mm.

The uniformly lamellar state did not represent the equilibrium phase behavior of our

mesophase samples at ambient temperature. After letting the samples rest at room temperature, we observed changes in sample appearance indicative of phase transitions (Figure 3.3c, d). The mesophases samples with the two lowest detergent concentrations appeared predominantly cubic, and the ones with higher detergent concentrations appeared predominantly lamellar. Note that the occurrence of interspersed lamellar and cubic regions seen, for example, in the sample on the bottom left in Figure 3.3d does not suggest poor mixing of the samples. Regions of equilibrium phase coexistence are found in MO/water systems with[13,14] and without[10,11] detergent, depending on the composition.

Because SAXS analysis could not be carried out immediately after preparation, all chips were frozen using dry ice with all chamber inlet valves in an actuated state to minimize evaporation of water from the samples. Since the control lines were filled with a fluid, the samples remained sealed in their respective compartments during storage. The samples were transferred to a freezer without defrosting and were stored at -80 $^{\circ}$C for 1-3 days prior to the measurements.

Prior to SAXS analysis, the samples were allowed to equilibrate at the data collection temperature (25 ± 1 °C) for 2 hours. At first we observed chaotic fluid movement during defrosting of the sample that was sufficiently powerful to cause failure of normally closed valves at chamber inlets. To avoid this, the respective control lines were actuated at a pressure of 30 psi during sample defrosting and equilibration. The lines were disconnected from the pressure source immediately prior to measurements. This type of fluid motion did not take place upon freezing/defrosting during sample formulation, and the quality of the samples was not compromised in that step.

3.3.5 Analysis of the phase behavior of mesophases

A high-intensity X-ray source was required for the analysis of on-chip mesophase samples because of their small path length. SAXS data collection was performed at beamline 21-ID-D, of the Advanced Photon Source at Argonne National Lab. 48 locations were probed within each sample (lipidic mixer) using a 20 μm X-ray beam. An XY-positioner was used to move the chip in the X-ray beam; and exact beam position was monitored in an on-axis video microscope (Figure 3.4a). Although only a small part of the device was visible in the microscope, the beam position could be easily mapped to the location within the chip (Figure 3.4a).

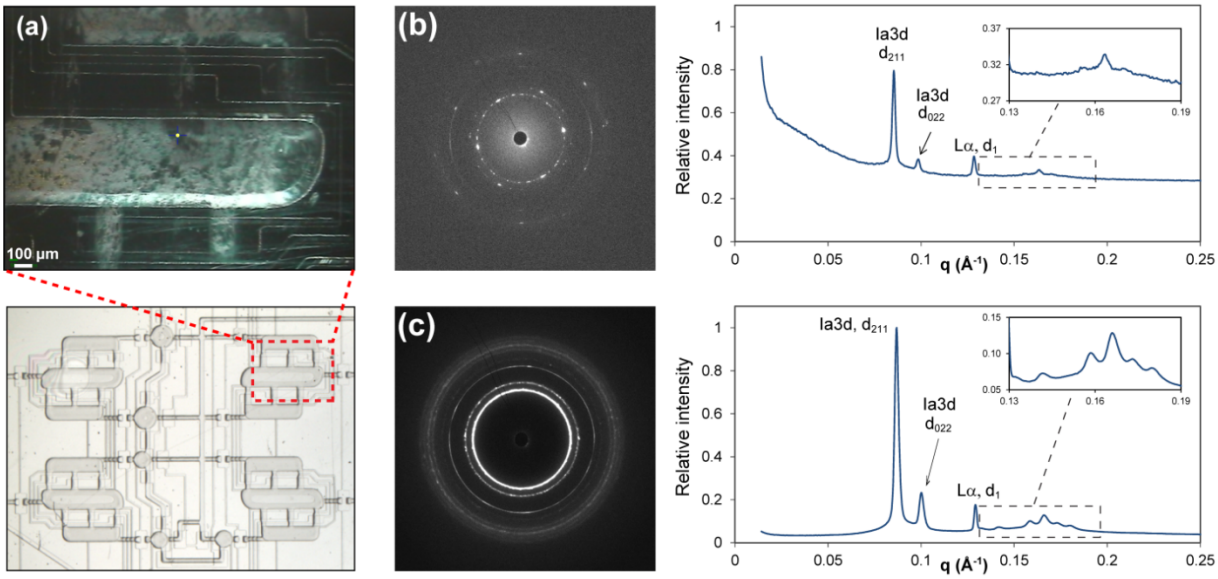

Figure 3.4. (a) Section of sample compartment seen in the on-axis video microscope during SAXS data collection (top) and the corresponding sample location (bottom). The bright dot in the center of the top image corresponds to the footprint of the X-ray beam, 20 µm. **(b, c)** Comparison of diffraction patterns for samples on-chip and in glass capillaries. Composition of both samples: MO/detergent solution ratio 55:45 v/v; detergent solution: 5% βOG in 25 mM NaH_2PO_4, pH 5.5. **(b)** Raw diffractogram of a 15-µm thick on-chip sample and a corresponding integrated diffractogram with peak assignments for prominent reflections. The inset shows a magnified view of higher-order *hkl* reflections from the *Ia3d* phase. Lattice parameters: *Ia3d*, 180 Å, and *Lα*, 48.9 Å. **(c)** Raw diffractogram of a ~0.9 mm-thick sample in a glass capillary and a corresponding integrated diffractogram with peak assignments for the most prominent reflections. The inset shows a magnified view of higher-order *hkl* reflections from the *Ia3d* phase. Lattice parameters: *Ia3d*, 177 Å, and *Lα*, 48.7 Å

Phase type identification. Comparison of data for samples prepared and analyzed on-chip to those prepared using the standard method (mixing in coupled syringes, analysis in glass capillaries) showed that the microfluidic platform reported here is suitable for the analysis of the nanostructure of lipidic mesophases (Figures 3.4b, c). Integrated diffraction patterns (Figure 3.4b, c) and, consequently, the structural characteristics, were very similar for the two samples that had near-identical compositions. The main differences between the two types of samples were the significant background in the on-chip data in the range of q values under ~0.06 $Å^{-1}$ and the higher signal/noise ratio for samples in capillaries than on-chip. We established that the background was predominantly due to scattering from PDMS present in array chips because the scattering from the COC films was comparable to that from air (Figure 3.5). The differences in signal/noise ratio are not unexpected given an up to 60-fold smaller sample path length on-chip and a significantly larger thickness, with 180 µm of PDMS and COC in the beam path, compared to X-ray glass capillaries with 10 µm-thick walls. The higher signal/noise ratio of samples in capillaries compared to on-chip samples is especially evident in the appearance of higher-*hkl* reflections of the *Ia3d* phase (insets in Figures 3.4b and 3.4c). However, signal intensity in the

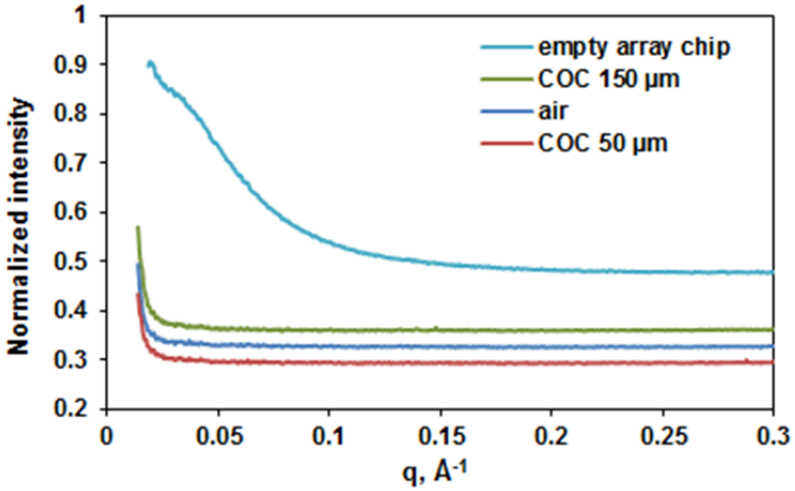

Figure 3.5. Normalized scattering intensity for COC films, an empty array chip, and air as a function of scattering vector *q*. The array chip consists of two COC films with respective thicknesses of 100 and 50 µm and two PDMS films with the combined thickness of 70 µm.

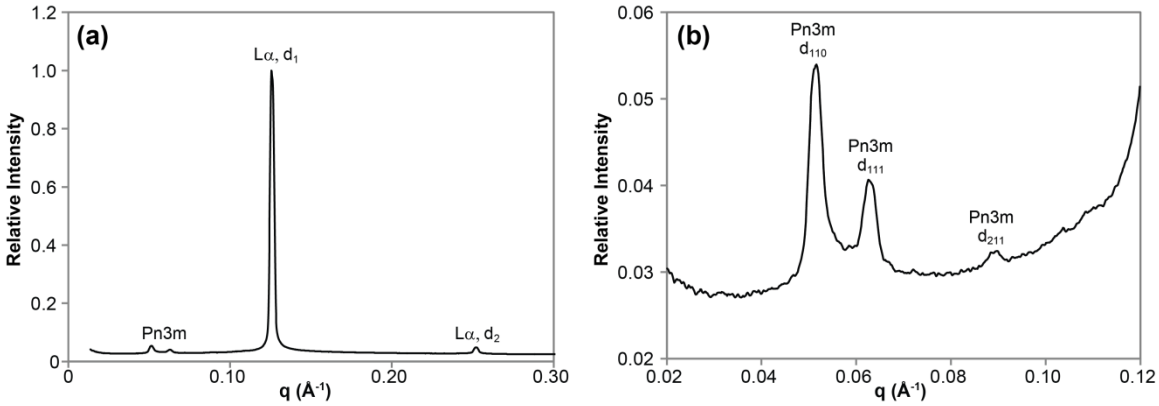

Figure 3.6. (a) A diffraction pattern of a sample containing *Pn3m* and *Lα* phases in a glass capillary collected after 2-hr equilibration at 25 °C and **(b)** a magnified view of *Pn3m* reflections. Sample composition: MO/detergent solution ratio 55:45 w/w; detergent solution: 10% βOG in 25 mM NaH_2PO_4, pH 5.5. Lattice parameters of mesophases: *Pn3m*, 174 Å; *Lα*, 50.1 Å.

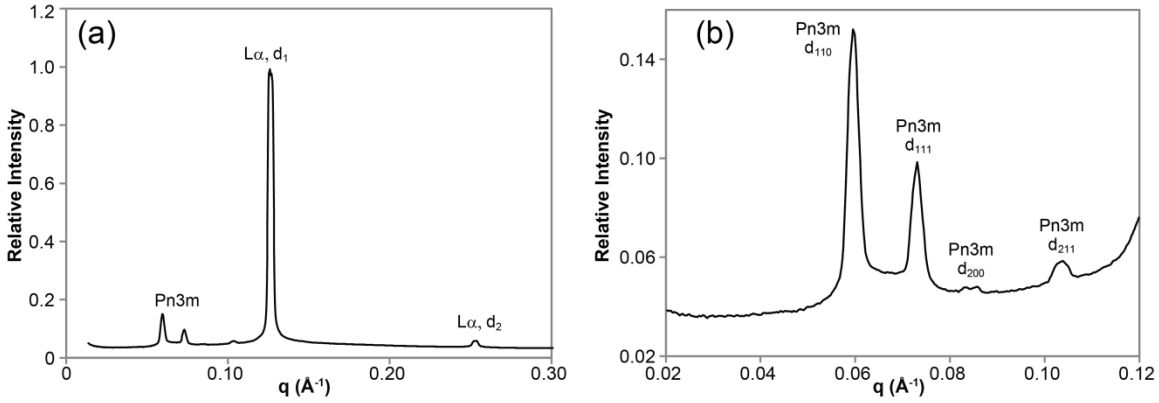

Figure 3.7. (a) A diffraction pattern of a sample containing *Pn3m* and *Lα* phases in a glass capillary collected after 24-hr equilibration at 25 °C and **(b)** magnified view of *Pn3m* reflections. Sample thickness ~0.9 mm. Sample composition: MO/detergent solution ratio 55:45 w/w; detergent solution: 10% βOG in 25 mM NaH_2PO_4, pH 5.5. Lattice parameters of mesophases: *Pn3m*, 150 Å; *Lα*, 50.0 Å.

on-chip data was sufficient for identifying the types of lipidic mesophases present in these samples. For example, both samples in Figure 3.4 contained a mixture of the *Ia3d* cubic phase and a lamellar *Lα* phase in equilibrium coexistence. Table 3.1 summarizes the phase assignments and lattice parameters of all on-chip samples tested in this work. Examples of diffractograms of samples containing mixtures of *Pn3m* and *Lα* phases are shown in Figures 3.6 and 3.7. Here the difference in background scattering between the capillaries appears not as pronounced as for diffractograms presented in Figure 3.4 due to the domination of the signal from the *Lα* phase in the diffractograms.

Another noticeable difference was the presence of spotty rings in the raw diffraction pattern of the on-chip samples (Figure 3.4b) compared to mostly uniform rings of the sample in a capillary (Figure 3.4c). The spottiness is the result of the path length of the on-chip sample being of comparable size to the monocrystalline domains of the mesophase (up to 50 μm for cubic phases).[12] The few monocrystalline domains in the X-ray beam path in a microfluidic device are insufficient to produce uniform diffraction rings, which require the presence of a large number of randomly oriented domains. Similar spotty patterns can also be observed for samples in capillaries if they are allowed to mature for several days.

Trends in phase behavior of lipidic mesophases. Figure 3.8 shows relative amounts of various phase types identified for identical samples in four different chips. The excellent reproducibility of the phase behavior data between different devices illustrates the robustness of the microfluidic platform reported here. The phase type, the lattice parameters, and the relative amount of phases agree well between different chips, indicating the accuracy of on-chip metering to formulate samples with identical compositions.

At the lowest βOG concentration tested in this work w predominantly *Ia3d* cubic phases were observed. As the amount of detergent increased the following was observed: (i) increasing amounts of the *Lα* phase; (ii) replacement of the *Ia3d* cubic phase with the *Pn3m* cubic phase; and (iii) increasing amount of *Lα* phase at the expense of the *Pn3m* cubic phase. These trends in phase behavior as a function of detergent concentration result from the flattening of lipid bilayers upon increasing the MO : detergent ratio due to the difference in their molecular shapes. The trends are in general agreement with those reported for samples prepared with the standard method.[13,14,54,55]

Table 3.1. Average lattice parameters and standard deviations (in Å) of mesophases at 25 ± 1 °C in samples prepared and analyzed on-chip and in samples prepared using coupled syringes and analyzed in glass capillaries. Chips A-D are the same as those in Figure 3.8.

	Sample composition											
	MO / 5% βOG 55:45 v/v			MO / 6.7% βOG 55:45 v/v			MO / 8.3% βOG 55:45 v/v			MO / 10% βOG 55:45 v/v		
	Detergent solutions and mesophases formulated on-chip [a]											
	Pn3m	***Ia3d***	***Lα*** [b]	***Pn3m***	***Ia3d***	***Lα*** [b]	***Pn3m***	***Ia3d***	***Lα*** [b]	***Pn3m***	***Ia3d***	***Lα*** [b]
Chip A		182 ± 2			185 ± 3	49.2	136 ± 1	215 ± 12	49.9	144 ± 3		49.8
Chip B		187 ± 3	49.1		183 ± 6	48.9	136 ± 1	190	49.7	146 ± 2		49.7
Chip C		181 ± 2	48.9		198 ± 1	49.5	143 ± 3	191	49.9	144 ± 2		49.7
Chip D		179 ± 1			193 ± 2	49.8	141 ± 2	215 ± 3	50.1	145 ± 2		50.0
	Detergent solutions formulated off-chip, mesophases formulated on-chip [c]											
Chip E		181 ± 2	48.6									
Chip F		182 ± 3	48.9									
Chip G										148 ± 3		49.8
Chip H										148 ± 8		49.7
	Samples prepared in coupled syringes and analyzed in glass capillaries											
CS-1		177 ± 2	48.4									
CS-2										173 ± 1		49.9

[a] Lattice parameters were averaged for each of the four samples on-chip

[b] Standard deviations of lattice parameters for Lα phases were <0.5 Å in all cases.

[c] Four identical samples were prepared on a single chip. The reported value is the average for the four samples.

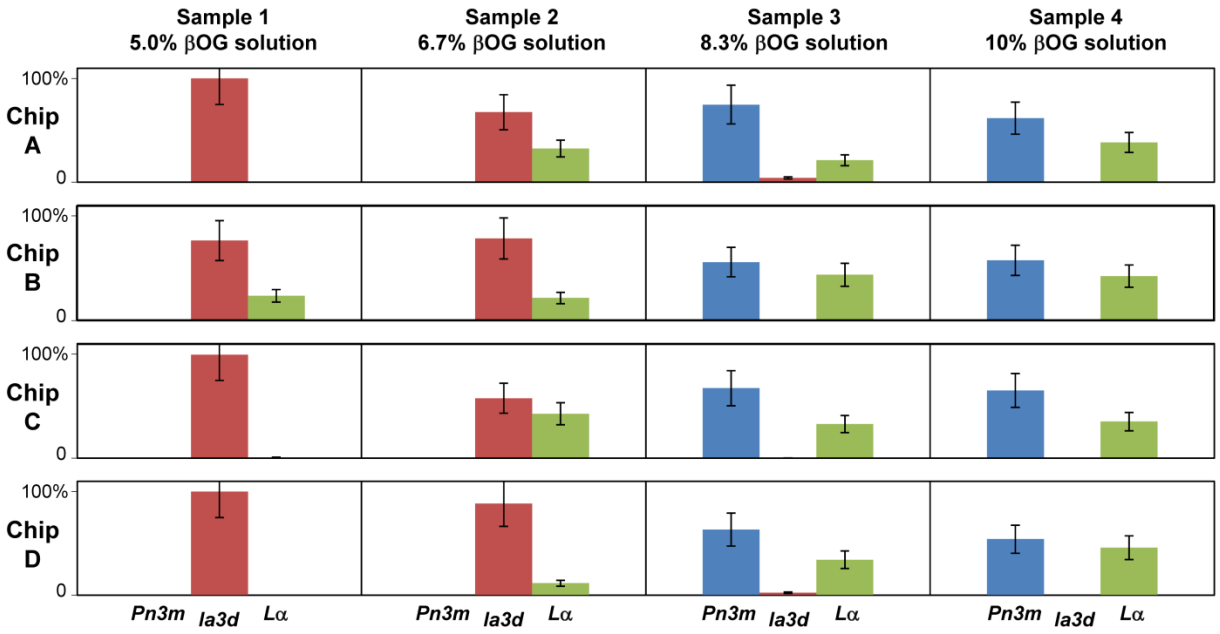

Figure 3.8. Relative amounts of different phases in samples prepared and analyzed on-chip using four different microfluidic devices at 25 ± 1 °C. The amount of each phase was estimated from intensities of corresponding reflections in SAXS diffractograms. Relative amounts were obtained by normalizing data for each sample to yield the combined amount of all phases of 100%.

Lattice parameters of mesophases. The lattice parameters of the lipidic mesophases established for samples on-chip and in capillaries are reported in Table 3.1. The lattice parameters of cubic phases are highly sensitive to their composition and are highly important for understanding the properties that govern phase transformations as well as for assessing the suitability of certain mesophases for applications such as membrane protein crystallization or drug delivery. To assess the accuracy of metering on-chip we prepared a set of samples where detergent solution was diluted off-chip on a milliliter scale, and then formulated samples on-chip without dilution, *i.e.*, skipping steps c2 and c3 in Figure 3.2. The results for samples prepared with 5% βOG solution and 10% βOG solution are also presented in Table 3.1. Lattice parameters of both *Pn3m* and *Ia3d* cubic phases are identical for samples prepared with and without on-chip dilutions, verifying the metering accuracy of the microfluidic platform and the filling method.

Lattice parameters: comparison of on-chip and the standard method. To benchmark data on mesophase microstructure obtained from on-chip samples, we prepared identical mesophase samples of MO mixed with 5% or 10% βOG solution (MO : solution ratio 55:45 w/w) using the standard method. The samples were prepared gravimetrically on a milligram (microliter) scale in a coupled-syringe mixer, followed by dispensing into 0.9 mm glass capillaries and SAXS data collection.

Table 3.1 shows phase assignments and corresponding lattice parameters obtained for samples in capillaries as well as from on-chip samples. Data of samples prepared with the 5% βOG solution are in excellent agreement with respect to phase types and lattice parameters. In the samples prepared with the 10% βOG solution, the phase types for the on-chip and macroscopic samples are the same, *Pn3m* and *Lα*, but the lattice parameters for the *Pn3m* phase are noticeably different, 144-148 Å on-chip vs. 173 Å off-chip. Here, the results likely illustrate the difficulty of reproducibly preparing and analyzing mesophase samples containing cubic phases with large lattice parameters observed previously. For example, Caffrey *et al*.[14] reported that samples with putatively identical compositions of MO : water 60:40 w/w may result in either *Pn3m* or *Ia3d* phases. Similar phenomena were also observed for detergent-containing samples.[14] Batch-to-batch variations in the lattice parameter of MO mesophases have also been reported.[13] We established that the discrepancy between on-chip and macroscopic sample behavior observed here did not result from potential inaccuracies in the ratio of volumes of chambers. At the same time, the value of 173 Å is at variance with previously reported lattice parameters of *Pn3m* cubic

phases of MO mixed with detergent solutions,[13,14,34] which typically do not exceed 135-145 Å under conditions similar to ours.

To further clarify the origin of mesophase behavior, observed here, we performed a new SAXS measurement of samples containing MO and 10% βOG solution in the 55 : 45 w/w ratio after 24 hrs of storage at 23 °C. We observed changes in the lattice parameters of the *Pn3m* phase in the four *sealed* capillaries that initially contained identical samples dispensed from the same coupled-syringe mixer. All samples contained the *Lα* phase (48.9 - 49.1 Å) coexisting with the *Pn3m* phase. The lattice parameters of the *Pn3m* phase varied significantly between capillaries, with one at the original value of 173 Å, one sample at 152 Å, and two samples at 144 Å. The likeliest cause of such changes is the minute loss of water from the samples in sealed capillaries, indicating a very strong dependence of the *Pn3m* lattice parameter on mesophase hydration. The latter may account for previous lack of observations of *Pn3m* phase with very large lattice parameters of over 170 Å, since consistent observations of such values require very fresh samples. Indeed, the values of lattice parameters in slightly dehydrated samples measured here, 144-152 Å, are much closer to those reported previously and to our on-chip data. Given the aforementioned difficulties, the excellent reproducibility of phase types and lattice parameters for the mesophase samples containing 10% βOG solution between different chips serves as a proof of the robustness of our platform and the validity of our results, even though the lattice parameters are only in qualitative agreement with the initial values for samples in capillaries. The good agreement between on-chip and macroscopic samples containing 5% βOG solution with respect to both phase types and lattice parameters also validates our approach.

3.4 Conclusions

The microfluidic platform presented here is, to our knowledge, the first example of a microfluidic device that combines metering and active mixing capabilities with X-ray transparency for on-chip SAXS analysis. The capabilities of the platform were demonstrated by mapping a section of the phase diagram of lipid MO mixed with solutions of detergent β-octylglucoside of different detergent concentrations, mimicking conditions of membrane protein crystallization trials. Four samples with different compositions were simultaneously prepared on-chip. Despite the very small thickness of the samples, 15-40 μm, the three phase types typical for

MO mesophases at ambient temperature could be distinguished from on-chip SAXS data. Analysis of SAXS data revealed excellent reproducibility of the phase types and lattice parameters of lipidic mesophases between different chips, confirming the high accuracy of sample formulation on-chip. Similarly, data from on-chip samples agree well with those for samples prepared using the standard method by mixing in coupled syringes.

The platform developed here is a viable alternative to the standard method of sample preparation. The platform reduces the amount of material required for sample formulation and analysis 300-fold, which makes it a valuable tool for analyzing the suitability of scarcely available novel lipids for membrane protein crystallization. Design principles used in this work can be used to scale out the number of samples per chip. With small modifications the platform could also be used to screen the phase behavior of lipidic mesophases in a wide range of lipid/solution ratios in order to gain understanding of driving forces behind phase transitions in liquid crystalline systems.

3.5 References

1 C. V. Kulkarni, W. Wachter, G. Iglesias-Salto, S. Engelskirchen and S. Ahualli. Monoolein: A magic lipid? *Phys. Chem. Chem. Phys.*, 2011, **13**, 3004-3021.

2 K. Larsson. Two cubic phases in monoolein-water system. *Nature*, 1983, **304**, 664-664.

3 M. Caffrey and V. Cherezov. Crystallizing membrane proteins using lipidic mesophases. *Nat. Protocols*, 2009, **4**, 706-731.

4 C. Guo, J. Wang, F. Cao, R. J. Lee and G. Zhai. Lyotropic liquid crystal systems in drug delivery. *Drug Discov. Today*, 2010, **15**, 1032-1040.

5 E. Nazaruk, R. Bilewicz, G. Lindblom and B. Lindholm-Sethson. Cubic phases in biosensing systems. *Anal. Bioanal. Chem.*, 2008, **391**, 1569-1578.

6 M. Caffrey. Crystallizing membrane proteins for structure–function studies using lipidic mesophases. *Biochem. Soc. Trans.*, 2011, **39**, 725-732.

7 V. Cherezov, D. M. Rosenbaum, M. A. Hanson, S. G. F. Rasmussen, F. S. Thian, T. S. Kobilka, H.-J. Choi, P. Kuhn, W. I. Weis, B. K. Kobilka and R. C. Stevens. High-resolution crystal structure of an engineered human β_2-adrenergic G-protein coupled receptor. *Science*, 2007, **318**, 1258-1265.

8 E. Y. T. Chien, W. Liu, Q. Zhao, V. Katritch, G. Won Han, M. A. Hanson, L. Shi, A. H. Newman, J. A. Javitch, V. Cherezov and R. C. Stevens. Structure of the human dopamine d3 receptor in complex with a d2/d3 selective antagonist. *Science*, 2010, **330**, 1091-1095.

9 H. Wu, D. Wacker, M. Mileni, V. Katritch, G. W. Han, E. Vardy, W. Liu, A. A. Thompson, X.-P. Huang, F. I. Carroll, S. W. Mascarella, R. B. Westkaemper, P. D. Mosier, B. L. Roth, V. Cherezov and R. C. Stevens. Structure of the human κ-opioid receptor in complex with JDTiC. *Nature*, 2012, **485**, 327-332.

10 J. Briggs, H. Chung and M. Caffrey. The temperature-composition phase diagram and

mesophase structure characterization of the monoolein/water system. *J. Phys. II*, 1996, 723-751.
11 H. Qiu and M. Caffrey. The phase diagram of the monoolein/water system: Metastability and equilibrium aspects. *Biomaterials*, 2000, **21**, 223-234.
12 V. Cherezov and M. Caffrey. Membrane protein crystallization in lipidic mesophases. A mechanism study using X-ray microdiffraction. *Faraday Discuss.*, 2007, **136**, 195-212.
13 Y. Misquitta and M. Caffrey. Detergents destabilize the cubic phase of monoolein: Implications for membrane protein crystallization. *Biophys. J.*, 2003, **85**, 3084-3096.
14 X. Ai and M. Caffrey. Membrane protein crystallization in lipidic mesophases: Detergent effects. *Biophys. J.*, 2000, **79**, 394-405.
15 P. Nollert, H. Qiu, M. Caffrey, J. P. Rosenbusch and E. M. Landau. Molecular mechanism for the crystallization of bacteriorhodopsin in lipidic cubic phases. *FEBS Lett.*, 2001, **504**, 179-186.
16 M. Caffrey. A lipid's eye view of membrane protein crystallization in mesophases. *Curr. Opin. Struct. Biol.*, 2000, **10**, 486-497.
17 W. Longley and T. J. McIntosh. A bicontinuous tetrahedral structure in a liquid-crystalline lipid. *Nature*, 1983, **303**, 612-614.
18 E. Sparr, P. Wadsten, V. Kocherbitov and S. Engstrom. The effect of bacteriorhodopsin, detergent and hydration on the cubic-to-lamellar phase transition in the monoolein distearoyl phosphatidyl glycerolwater system. *Biochim. Biophys. Acta*, 2004, **1665**, 156-166.
19 V. Cherezov, H. Fersi and M. Caffrey. Crystallization screens: Compatibility with the lipidic cubic phase for in meso crystallization of membrane proteins. *Biophys. J.*, 2001, **81**, 225-242.
20 B. Angelov, M. Ollivon and A. Angelova. X-ray diffraction study of the effect of the detergent octyl glucoside on the structure of lamellar and nonlamellar lipid/water phases of use for membrane protein reconstitution. *Langmuir*, 1999, **15**, 8225-8234.
21 R. Mezzenga, C. Meyer, C. Servais, A. I. Romoscanu, L. Sagalowicz and R. C. Hayward. Shear rheology of lyotropic liquid crystals: A case study. *Langmuir*, 2005, **21**, 3322-3333.
22 Y. Liang, F. Z. Yuan and C. Weidong. Efficient micromixing of a highly viscous biosample with water using orbital shaking and microchannels. *Review of Scientific Instruments - Rev. Sci. Instrum.*, 2010, **81**, 054301.
23 J. S. Joseph, W. Liu, J. Kunken, T. M. Weiss, H. Tsuruta and V. Cherezov. Characterization of lipid matrices for membrane protein crystallization by high-throughput small angle X-ray scattering. *Methods*, 2011, **55**, 342-349.
24 E. Kondrashkina, D. S. Khvostichenko, S. L. Perry, J. von Osinski, P. J. A. Kenis and K. Brister. Using macromolecular-crystallography beamline and microfluidic platform for small-angle diffraction studies of lipidic mesophases for membrane protein crystallization. *J. Phys. Conf. Ser.*, 2012, accepted.
25 S. L. Perry, G. W. Roberts, J. D. Tice, R. B. Gennis and P. J. A. Kenis. Microfluidic generation of lipidic mesophases for membrane protein crystallization. *Cryst. Growth Design*, 2009, **9**, 2566-2569.
26 F. Shi, Z. Han, J. Li, B. Zheng and C. Wu. Mapping polymer phase diagram in nanoliter droplets. *Macromolecules*, 2012, **44**, 686-689.
27 S. Park, P. A. L. Wijethunga, H. Moon and B. Han. On-chip characterization of

cryoprotective agent mixtures using an ewod-based digital microfluidic device. *Lab Chip*, 2011, **11**, 2212-2221.

28 P. Laval, N. Lisai, J.-B. Salmon and M. Joanicot. A microfluidic device based on droplet storage for screening solubility diagrams. *Lab Chip*, 2007, **7**, 829-834.

29 P. Moreau, J. Dehmoune, J. B. Salmon and J. Leng. Microevaporators with accumulators for the screening of phase diagrams of aqueous solutions. *Appl. Phys. Lett.*, 2009, **95**, 033108.

30 J.-B. Salmon and J. Leng. Microfluidics for kinetic inspection of phase diagrams. *Compt. Rend. Chim.*, 2009, **12**, 258-269.

31 J. Leng, M. Joanicot and A. Ajdari. Microfluidic exploration of the phase diagram of a surfactant/water binary system. *Langmuir*, 2007, **23**, 2315-2317.

32 J. Leng, B. Lonetti, P. Tabeling, M. Joanicot and A. Ajdari. Microevaporators for kinetic exploration of phase diagrams. *Phys. Rev. Lett.*, 2006, **96**, 084503.

33 X. Zhou, J. Li, C. Wu and B. Zheng. Constructing the phase diagram of an aqueous solution of poly(n-isopropyl acrylamide) by controlled microevaporation in a nanoliter microchamber. *Macromol. Rapid Comm.*, 2008, **29**, 1363-1367.

34 M. Sugiyama, D. Gasperino, J. J. Derby and V. H. Barocas. Protein-salt-water solution phase diagram determination by a combined experimental-computational scheme. *Cryst. Growth Design*, 2008, **8**, 4208-4214.

35 M. J. Anderson, C. L. Hansen and S. R. Quake. Phase knowledge enables rational screens for protein crystallization. *Proc. Natl. Acad. Sci. USA*, 2006, **103**, 16746-16751.

36 M. O. A. Sommer and S. Larsen. Crystallizing proteins on the basis of their precipitation diagram determined using a microfluidic formulator. *J. Synchrotron Rad.*, 2005, **12**, 779-785.

37 C. L. Hansen, M. O. A. Sommer and S. R. Quake. Systematic investigation of protein phase behavior with a microfluidic formulator. *Proc. Natl. Acad. Sci. USA*, 2004, **101**, 14431-14436.

38 J. U. Shim, G. Cristobal, D. R. Link, T. Thorsen, Y. W. Jia, K. Piattelli and S. Fraden. Control and measurement of the phase behavior of aqueous solutions using microfluidics. *J. Am. Chem. Soc.*, 2007, **129**, 8825-8835.

39 S. Selimovic, F. Gobeaux and S. Fraden. Mapping and manipulating temperature-concentration phase diagrams using microfluidics. *Lab Chip*, 2010, **10**, 1696-1699.

40 K. Dhouib, C. Khan Malek, W. Pfleging, B. Gauthier-Manuel, R. Duffait, G. Thuillier, R. Ferrigno, L. Jacquamet, J. Ohana, J.-L. Ferrer, A. Theobald-Dietrich, R. Giege, B. Lorber and C. Sauter. Microfluidic chips for the crystallization of biomacromolecules by counter-diffusion and on-chip crystal X-ray analysis. *Lab Chip*, 2009, **9**, 1412-1421.

41 S. L. Perry, S. Guha, A. S. Pawate, S. K. Nair and P. J. A. Kenis. Microfluidic array chips for de novo protein structure determination at room temperature. in preparation.

42 Y. Xia and G. M. Whitesides. Soft lithography. *Angew. Chem. Int. Ed.*, 1998, **37**, 550-575.

43 M. A. Unger, H.-P. Chou, T. Thorsen, A. Scherer and S. R. Quake. Monolithic microfabricated valves and pumps by multilayer soft lithography. *Science*, 2000, **288**, 113-116.

44 L. Tang and N. Y. Lee. A facile route for irreversible bonding of plastic-PDMS hybrid microdevices at room temperature. *Lab Chip*, 2010, **10**, 1274-1280.

45 M. L. Antonelli, M. G. Bonicelli, G. Ceccaroni, C. Mesa and B. Sesta. Solution

properties of octyl-β-d-glucoside. Part 2: Thermodynamics of micelle formation. *Colloid Polymer Sci.*, 1994, **272**, 704-711.

46 J. Kraineva, R. A. Narayanan, E. Kondrashkina, P. Thiyagarajan and R. Winter. Kinetics of lamellar-to-cubic and intercubic phase transitions of pure and cytochrome c containing monoolein dispersions monitored by time-resolved small-angle X-ray diffraction. *Langmuir*, 2005, **21**, 3559-3571.

47 H. Vacklin, B. J. Khoo, K. H. Madan, J. M. Seddon and R. H. Templer. The bending elasticity of 1-monoolein upon relief of packing stress. *Langmuir*, 2000, **16**, 4741-4748.

48 V. Cherezov, K. M. Riedl and M. Caffrey. Too hot to handle? Synchrotron X-ray damage of lipid membranes and mesophases. *J. Synchrotron Rad.*, 2002, **9**, 333-341.

49 P. Garstecki and R. Hołyst. Scattering patterns of self-assembled cubic phases. 2. Analysis of the experimental spectra. *Langmuir*, 2002, **18**, 2529-2537.

50 P. Garstecki and R. Hołyst. Scattering patterns of self-assembled cubic phases. 1. The model. *Langmuir*, 2002, **18**, 2519-2528.

51 B. Angelov, A. Angelova, M. Ollivon, C. Bourgaux and A. Campitelli. Diamond-type lipid cubic phase with large water channels. *J. Am. Chem. Soc.*, 2003, **125**, 7188-7189.

52 C.-C. Lee, G. Sui, A. Elizarov, C. J. Shu, Y.-S. Shin, A. N. Dooley, J. Huang, A. Daridon, P. Wyatt, D. Stout, H. C. Kolb, O. N. Witte, N. Satyamurthy, J. R. Heath, M. E. Phelps, S. R. Quake and H.-R. Tseng. Multistep synthesis of a radiolabeled imaging probe using integrated microfluidics. *Science*, 2005, **310**, 1793-1796.

53 Y. Misquitta, V. Cherezov, F. Havas, S. Patterson, J. M. Mohan, A. J. Wells, D. J. Hart and M. Caffrey. Rational design of lipid for membrane protein crystallization. *J. Struct. Biol.*, 2004, **148**, 169-175.

54 G. Persson, H. Edlund, H. Amenitsch, P. Laggner and G. Lindblom. The 1-monooleoyl-*rac*-glycerol/*n*-octyl-β-d-glucoside/water system. Phase diagram and phase structures determined by NMR and X-ray diffraction. *Langmuir*, 2003, **19**, 5813-5822.

55 G. Persson, H. Edlund and G. Lindblom. Phase behaviour of the 1-monooleoyl-*rac*-glycerol /*n*-octyl-β-d-glucoside/water system. *Progress in Colloid and Polymer Science*, 2004, **123**, 36-39.

Chapter 4.
X-ray transparent SlipChip for the studies of the phase behavior of lipidic mesophases

Abstract

This chapter describes an X-ray transparent SlipChip for the study of the phase behavior of lipidic mesophases in a wide range of hydration levels. The chip consists of two 150-250 μm-thick sheets of cyclic olefin co-polymer (COC). A novel lipid-filling strategy was developed to overcome unfavorable capillary effects that render the original SlipChip filling approach unsuitable for amphiphilic materials. The geometry of the chambers facilitates passive mixing between the lipid and the aqueous solution. The chip requires less than 100 nL of lipid to map out the phase behavior of mesophases containing 0-30 *or* 35-60 vol% of aqueous solutions in increments of 5%, a 600-fold reduction compared to the traditional macroscale methods. Six samples with different aqueous solution content could be prepared simultaneously on-chip. Preliminary studies showed that different types of lipidic mesophases can be identified from SAXS data collected on-chip. Furthermore, the previously reported sequence of phases in monoolein/water and monoolein/β-octylglucoside/water systems at increasing hydration levels could be successfully reproduced on-chip.

4.1 Introduction

Phase diagrams of lipidic mesophases are required to advance the understanding of fundamental principles that govern the self-assembly in natural and synthetic lipidic systems. In membrane protein crystallization, studies of phase behavior of novel lipids may facilitate discovery of new matrices for crystallization[1-4] and improve the success rate of crystallization trials. Studies of phase diagrams require the preparation and analysis of a large number of samples with systematic variations in the composition, and a number of microfluidic platforms that automate sample formulation and reduce the amount of material for phase behavior studies have been developed.[5-16] However, on-chip studies of lipidic mesophases present several challenges that are not addressed in reported platforms: (i) formulation of mesophases of well-defined pre-set compositions, (ii) manipulation of viscous mesophases in microfluidic channels, and (iii) on-chip small-angle X-ray analysis for the unequivocal identification of mesophase microstructure. Only one example of a microfluidic platform suitable for the studies of lipidic mesophases has been demonstrated (Chapter 3), with multilayer polydimethylsiloxane architecture, valve-based fluid routing strategies, and active mixing of the aqueous solution with the lipid to formulate a uniformly mixed mesophase. While the platform was successfully used to map a section of a phase diagram for a mixture of lipid monoolein, detergent β-octylglucoside (βOG), and a phosphate buffer solution, its fabrication was rather complicated, and the mixing strategy for mesophase formulation required special equipment and software.

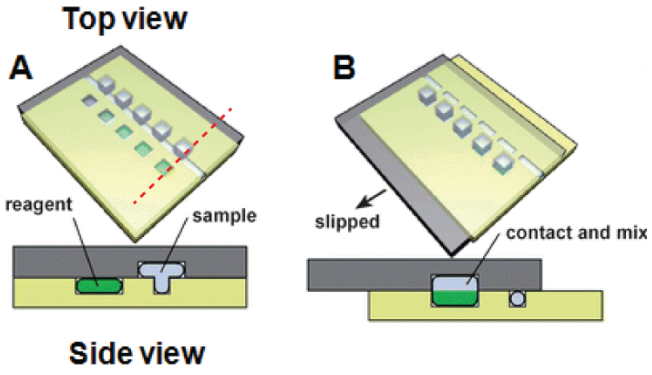

Figure 4.1. Schematic representation of the operation of a SlipChip. The side view corresponds to the cross-section of the chip along the red dotted line. (Reproduced from W. Du, L. Li, K. P. Nichols and R. F. Ismagilov. Lab on a Chip, 2009, 9, 2286-2292, with permission from the Royal Society of Chemistry.)

The elegant SlipChip approach demonstrated by Ismagilov *et al.*[17,18] (Figure 4.1) circumvents the complex fabrication procedure and mesophase formulation protocol required in

the lipidic mixer array chip. Briefly, the SlipChip consists of two rigid glass plates with reagent chambers and ducts etched into both plates so that they form continuous fluidic paths upon alignment. Once the separate sample compartments are filled, the plates are slipped relative to each other, bringing solutions from chambers in the top and the bottom plates in contact. The composition of the sample is controlled by the volume of the chambers. During slipping, solutions are held in their respective chambers by interfacial tension forces.[17-19] The interstitial space between the plates and the samples is typically filled with a fluorinated solvent to prevent cross-talk between the samples.[17-19] Even though mixing in the SlipChip occurs predominantly by mutual diffusion of components, the large interfacial area defined by the lateral dimensions of the sample chambers greatly facilitates mixing compared to traditional microfluidic designs with two large chambers connected via a narrow channel.[20-22] The SlipChip has been successfully used in a variety of applications, as crystallization of soluble proteins,[23] immunoassays,[24] and polymerase chain reaction.[25]

The SlipChip may provide an attractive route for the preparation of lipidic mesophases with a large range of hydration levels, which is not feasible with existing macroscale platforms for high-throughput phase behavior studies.[26,27] Compared to microfluidic chips with pneumatic valve actuation, the SlipChip is significantly easier to fabricate. Because of the passive mixing approach, mesophases do not need to be routed on-chip once formed, simplifying sample formulation protocol and avoiding the problem of manipulating cubic lipidic mesophases (Chapter 3.3.4). However, reported implementations of the SlipChip for various applications[17-19,24,25,28] rely on patterning of millimeter-thick glass slides and are incompatible with *in situ* X-ray analysis.

Here we present an X-ray transparent SlipChip for the analysis of the phase behavior of lipidic mesophases. For X-ray transparency the chip is fabricated by hot-embossing of 150-250 μm-thick sheets of cyclic olefin co-polymer. In Chapter 4.2 we describe fabrication methods, Chapters 4.3.1 and 4.3.2 describe chip design and sample formulation strategies, and Chapter 4.3.3 summarizes preliminary results of the analysis of the phase behavior of monoolein/water and monoolein/βOG/water mesophases in the SlipChip.

4.2 Materials and methods

4.2.1 SlipChip fabrication

Fabrication of photoresist-on-silicon masters. Photoresist-on-silicon masters were created with AZ50XT positive photoresist (AZ Electronic Materials) for patterns with 25-50 μm-tall rounded features and with SU8-25 negative photoresist for patterns with 25 μm-tall features with vertical walls. Patterned positive photoresist was reflowed at 115 °C for 45 s to achieve the rounded profile.[29] All photoresist-on-silicon masters were treated with (tridecafluoro-1,1,2,2-tetrahydrooctyl) trichlorosilane (Gelest, Inc.) in a vacuum chamber for 4 hours for easy release of PDMS replicas.[30]

Fabrication of patterned cyclic olefin co-polymer (COC) components. Patterned COC sheets (6013, TOPAS Advanced Polymers) were fabricated by hot embossing using high-temperature epoxy molds (Conapoxy FR 1080) in a laminating press (Carver Inc., Model 3851) under the load of 150-200 kg. The thicknesses of the sheets used to pattern lipid and aqueous solution chambers were 6 mil and 4 mil, respectively. For high-fidelity pattern transfer, a stack of (i) 7-10 mm PDMS slab, (ii) an epoxy mold, (iii) a COC sheet, and (iv) a 7.5 × 5 cm microscope glass slide was placed between the platens of the press. The temperature of the assembly was brought to 350 °F (177 °C) and then to below 250 °F (121 °C) before removing the patterned layer. Holding at 177 °C for an extended period of time was not required for accurate pattern transfer.

The SlipChip relies on capillary effects[18,19] and requires a smooth flat surface of patterned COC sheets for successful filling and slipping. Because epoxy softens at the temperature required for hot-embossing, COC sheets larger than in size than the epoxy molds were used to avoid the imprints of sheet edges in the epoxy and compromising the smoothness of the surface of the mold.

Holes were drilled in COC sheets with patterned solution chambers using a 750 μm drill bit (McMaster-Carr). Burrs around the holes were removed very carefully with a razor blade without scraping the rest of the surface of the chip.

Fabrication of epoxy molds for hot-embossing of COC films. The epoxy molds were fabricated using the procedure developed by Guha *et al.*[21] with minor modifications to ensure flat surface of resulting epoxy molds as required for SlipChip operation. Briefly, PDMS with 10:1

monomer : crosslinker ratio was used to fabricate a thick inverse master of the photoresist-on-silicon master. Here we used exclusively positive photoresist masters with reflowed features to facilitate lift-off of COC films from epoxy molds in the hot embossing step. For flatness, two 1/4"-thick polymethylmetacrylate (PMMA) spacers were placed on a 4-inch wafer with patterned photoresist and a 1/8"-thick 3" × 3" flat PMMA plate was placed on the spacers. PDMS was poured into the space between the wafer and the PMMA plate to completely fill the space without air bubbles (Figure 4.2). The assembly was baked for 2 hours at 75 °C on a hotplate or in an oven to cure PDMS. After curing, the top PMMA plate was removed and the inverse PDMS master of largest possible dimensions was cut out and peeled off the wafer.

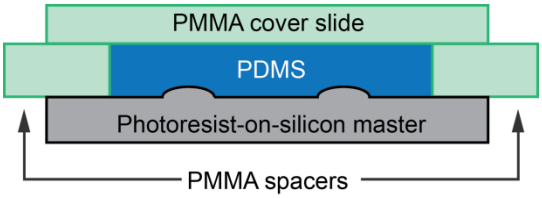

Figure 4.2. Schematic representation of the assembly for the fabrication of inverse PDMS molds.

An epoxy master (Conapoxy FR 1080) for use in hot-embossing was then molded off the PDMS master. The epoxy components (83:100 hardener:epoxy, by mass) were mixed using a planetary centrifugal mixer (Thinky USA Inc.) for 15 min at 2000 rpm with rotation and then de-foamed for 12 min at 2200 rpm. The inverse PDMS master was used for epoxy patterning. Again, precautions were taken to ensure that the epoxy mold with a smooth flat surface is obtained. The PDMS mold was placed on a 3-inch silanized silicon wafer without a pattern and a ~1 cm-thick PDMS frame was placed on the mold to create a walled compartment for uncured liquid epoxy. To prevent evolution of gas bubbles from the PDMS master during epoxy curing, the assembly was degassed for ~10 min. After degassing, the assembly was placed on a level hotplate held at 120 °C, PDMS was thoroughly cleaned with Scotch Tape (3M), and epoxy was poured into the mold and cured for 4 hrs at 120 °C. To prevent buckling of PDMS, a 400 g aluminum block was kept on the assembly throughout the curing process. Although inverse PDMS molds remained flat throughout curing due to stiction with wafer surface and the weight placed on the assembly, the molds buckled upon removal from the wafer after epoxy curing, and were not re-used.

Fabrication of thick PDMS assemblies for lipid filling. PDMS control layers of 5-10 mm in thickness were prepared by pouring a mixture with the monomer : cross-linker ratio of 5:1

on the photoresist-on-silicon master followed by curing at 90 °C for 5-10 min. For the fluid layers we spin-coated photoresist-on-silicon masters using PDMS with the monomer: cross-linker ratio of 15:1 to obtain a 45 μm-thick film. Fluid layers were cured at 90 °C for 7-9 min. Here we used photoresist-on-silicon masters with 25 μm-tall features fabricated in SU8-25 (Microchem) for control and fluid layers.

The chips were assembled as follows: (i) inlet ports were punched in the control layer using a 20 AWG needle with a thin wire plunger, (ii) control layers were irreversibly bonded to fluid layers by placing the two layers in conformal contact and heating at 70 °C for 2 hrs,[29] and (iii) the thin membrane connecting the control and the fluid line (Chapter 4.3.2, Figure 4.6) was removed carefully with sharp tweezers.

For lipid filling the control/fluid layer assembly was placed on a patterned COC substrate, and a reversible bond between the PDMS fluid layer and the COC substrate formed spontaneously.[21]

4.2.2 Lipid filling strategy

Lipid filling and mesophase properties on-chip were monitored using an upright microscope (Leica MDG33) equipped with a macro lens and a digital camera (Leica DFC295).

Lipid chambers were filled into the patterned COC substrate using the thick PDMS assembly that was aligned with the substrate to form a continuous fluidic line. A piece of 30 AWG PTFE tubing (Cole-Parmer) filled with ~0.5-cm-long plug of molten monoolein or monoolein/βOG mixture was inserted into the corresponding the inlet port of the auxiliary thick PDMS assembly. Applying negative pressure (vacuum) caused pressure gradient to form in the fluid line/patterned chambers due to air permeability of PDMS and drew monoolein into the device. Prior to removing the preliminary PDMS assembly from the lipid-filled COC substrate, the lipid was frozen by placing a piece of dry ice on the device. Monoolein remained on COC in locations under patterned PDMS channels and was carefully removed with toothpicks and Scotch Tape (3M) as much as possible. Monoolein remaining outside of chambers was very carefully wiped using a Kimwipe (SCIENCE brand, Kimberly-Clark) slightly moistened in isopropanol so as not to dissolve monoolein in COC chambers. Using a vacuum pump to draw lipid into the fluid line caused the thin PDMS layer under the control line to lift off the substrate and monoolein to creep under the line. Hence, only house vacuum was used for lipid filling.

Monoolein (Sigma-Aldrich, 99%) was used as received. The monoolein/βOG mixture with a βOG/MO ratio of 0.033 w/w was prepared gravimetrically as follows. Desired amounts of monoolein and βOG (Anatrace, Anagrade) were weighed in a glass vial and dissolved in chloroform (Sigma Aldrich, ≥99.8%). The solvent was removed under a stream on nitrogen gas. Solid samples were dried in a desiccator under vacuum at room temperature (21-23 °C) overnight.

4.2.3 Solution filling strategy

Prior to assembly, monoolein-filled COC sheets and empty COC sheets with chambers for aqueous solutions were spin-coated with Novec 1700 (3M) at 1200 rpm to form a ~0.25-0.3 µm layer of a fluoropolymer on the surface of the sheets for higher hydrophobicity (Figure 4.3). Coating with the fluoropolymer was necessary to make sure that the aqueous solution did not spread beyond fluidic ducts and chambers upon filling and slipping.

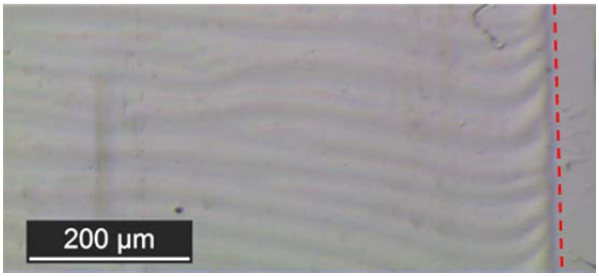

Figure 4.3. The surface of a COC sheet after spin-coating with Novec 1700. The dashed red line separates the coated region (left) from the non-coated region (right).

Clamping the two patterned COC sheets together was found necessary for filling, similarly to the original glass-based SlipChip that is held together with binder clips. The thin COC sheets used in this work required a more complex assembly (Figure 4.4) that consisted of (top-to-bottom): a 1/4"-thick 2"×3" PMMA slide, a ~ 5-mm thick PDMS gasket, a 12.5 µm-thick Teflon film (FEP 50A, American Durafilm), and a 1/4"-thick 2"×3" PMMA frame (edge width 1 cm). The gasket was required to ensure even pressure on the COC sheets and the Teflon sheet served to avoid adhesion between COC and PDMS, which caused problems during disassembly. The assembly was held together with four clamping screws with corresponding holes drilled in the corners of the acrylic slide/frame. Access holes for fluid inlets were drilled using a 750 µm drill bit in the acrylic slide and punched in the PDMS gasket using a 20 AWG needle. A small opening was cut out in the Teflon sheet in the area around the inlet ports for access.

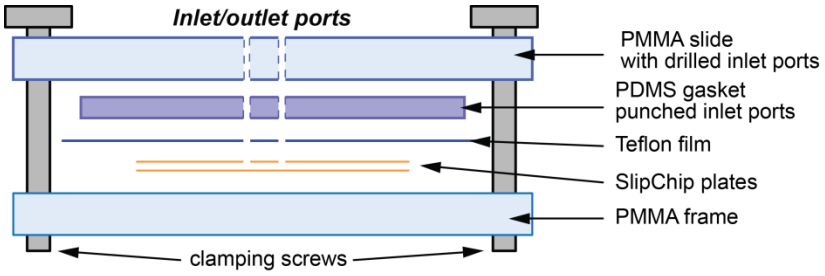

Figure 4.4. Schematic representation of the clamping assembly used in the filling of the COC SlipChip with aqueous solutions.

The assembly process was as follows: the acrylic slide, the PDMS gasket, the Teflon film, and the monoolein-filled COC sheet were aligned so that inlet ports in the four pieces overlapped. Several drops of Fluorinert FC-40 (3M) were placed on the COC sheet and the other COC plate was aligned with the assembly to match the pattern in the monoolein-filled sheet. The acrylic frame was carefully placed on the assembly without disturbing the alignment of the COC sheets and clamping screws were tightened.

To remove air pockets remaining in the aqueous line, the line was flushed with Fluorinert FC-40 using a 1 mL syringe with a 27 AWG needle connected to 30 AWG PTFE tubing (Cole-Parmer). The line was then filled with a saturated solution of fluorescein (Acros Organics) in deionized water.

An inverted Leica DMI 4000B microscope equipped with a xenon lamp, a Leica N PLAN 2.5× (0.07 NA) objective, and a charge-coupled device camera (Hamamatsu ORCA-ER, Model C4742-80) was used to monitor filling of aqueous solutions into the chip. The amount of aqueous phase in chambers was estimated as the ratio of the area occupied by the fluorescent aqueous phase to the total area of the chamber. Calculations were done using the ImageJ program (v. 1.45s, Wayne Rasband, NIH, USA).

After filling, the assembly was carefully taken apart, and the plates were carefully slipped in order to bring the chambers with aqueous solution and monoolein in contact. The sheets were sealed at long edges with Crystal Clear Tape (Hampton Research), and at short edges with QuickSet Epoxy (Henkel). Prior to sealing, FC-40 was added between the plates if air bubbles were visible. Inlet ports were also sealed with Crystal Clear tape. The chips were placed under FC-40 and stored at room temperature for ~24 hours for mixing between monoolein and the aqueous solution. Afterwards the chips were kept at -12 °C to reduce evaporation of water from the samples. Prior to SAXS data collection the chips were defrosted and kept under FC-40 for at least 2 hours for equilibration.

4.2.4 SAXS data collection

SAXS data were collected on protein crystallography beamline LS-CAT 21-ID-D at the Advanced Photon Source (APS), Argonne National Lab. A detailed description of the setup is available elsewhere.[31] For SAXS measurements, a vacuum flight tube and an adjustable beam stop with an incorporated pin-diode were installed between the sample and the CCD detector (Rayonix MX300). The beamline was equipped with a microdiffractometer (MAATEL MD2) consisting of a goniometer, XYZ micropositioner and an on-axis video microscope. The latter was used to monitor the position of the sample in the X-ray beam. The footprint of the X-ray beam was 20 μm. The beam energy was 8 keV. Attenuation of the incident X-ray beam and exposure time were adjusted to avoid radiation damage.[32]

Data for each 500 x 500 μm^2 chamber of a given SlipChip were collected on a grid of points spaced 150-180 μm apart along both dimensions of the chamber, for a total of 9 points per chamber (*i.e.*, per mesophase composition).

Raw diffractograms were integrated in Fit2D software (v. 12.077, A.P. Hammersley, ESRF, 1994). Because the diffractograms for different points within a single sample chamber differed negligibly with respect to peak positions, indicating identical sample properties throughout the chamber, for further analysis we used a sum of all diffractograms corresponding to a given chamber to obtain a higher signal/noise ratio. Integrated diffractograms were processed in MATLAB (R2008a, v. 7.6.0.324, The MathWorks Inc., Natick, MA). Publicly available MATLAB code (findpeaks.m, T.C. O'Haver, v2, revised Oct 27, 2006) was used to locate peak center positions. No baseline correction was required due to the very low background scatter of COC films. For phase assignment, diffraction angles were converted into *d*-spacings using Bragg's law.[33] Mesophases were identified based on characteristic sets of reflections and lattice parameters were calculated using the peak position of the highest-intensity reflection for a given mesophase (Appendix A).

4.3 Results

4.3.1 Design of the SlipChip

The SlipChip described in this section was designed for mapping the phase diagram of lipidic mesophases in the interval of compositions of 0-60 vol% of the aqueous solution in 5

vol% increments. The volume of lipid required for each composition was 12.5 nL, and the volume of aqueous solution varied in the range of 1.4 - 18.8 nL to match the target composition of the sample. Because of the space constraints during SAXS data collection that limited the overall size of the chip, two chips with six sample chambers per chip (SlipChip30 for 0-30 vol% of solution and SlipChip60 for 35-60 vol% of solution) were required, as shown in Figure 4.5.

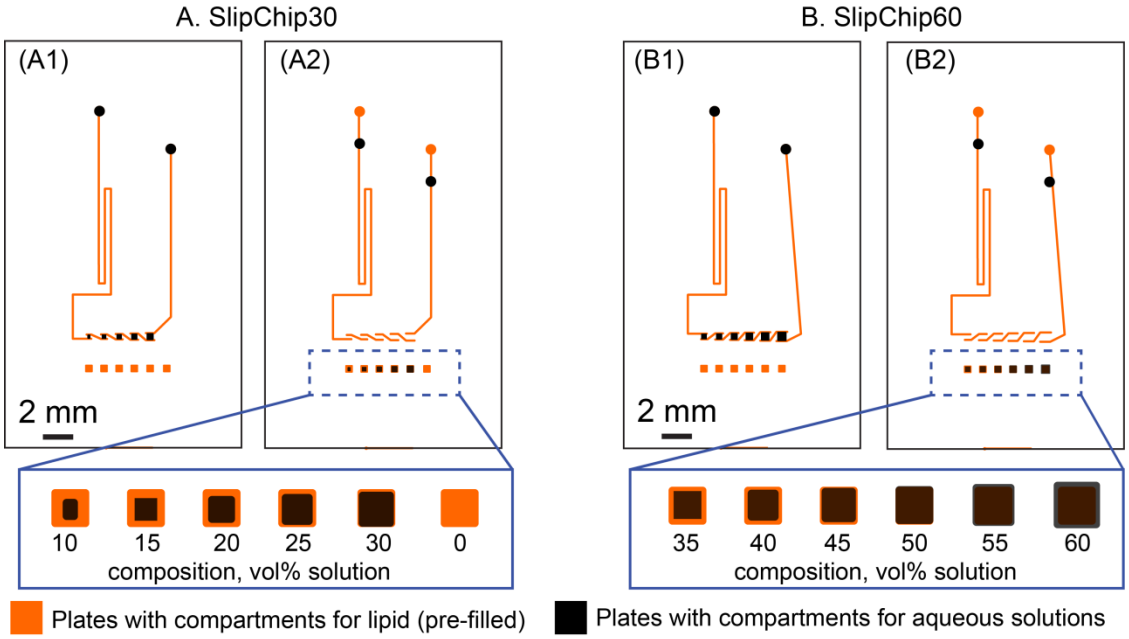

Figure 4.5. The layouts of lipid chambers and ducts for the aqueous solution (orange) and the chambers for aqueous solutions (black) patterned in the two plates of the SlipChips for the formulation of mesophases containing **(A)** 0-30 vol% of the aqueous solution and **(B)** 35-60 vol% of the aqueous solution. (A1) and (B1) represent alignment of the SlipChip plates in the solution filling step with overlapping ducts (orange) and solution chambers (black), and (A2) and (B2) represent alignment of the SlipChip plates after slipping for mesophase formulation. The insets show an enlarged view of the mesophase chambers with labeled mesophase composition. The size of lipid chambers (orange) is 500 × 500 μm^2, and the size of aqueous solution chambers (black) varies to achieve the target composition. SlipChip30 is designed for different depths of lipid and solution chambers ($depth_{solution}$ = 1/2 $depth_{lipid}$) in order to achieve target mesophase compositions; SlipChip60 is designed for identical depths of lipid and solution chambers.

SlipChip30 was designed for different depths of lipid and solution chambers ($depth_{solution}$ = 1/2 $depth_{lipid}$) to achieve target mesophase compositions. Thus, chambers for aqueous solutions with very small lateral dimensions that would present challenges in the solution filling step were avoided. For the same reason SlipChip30 omitted the composition with 5 vol% solution. This chip also contained a lipid chamber without a matching solution chamber in order to assess the possibility of accidental cross-talk between sample chambers and/or fluidic ducts after slipping. The cross-talk would cause changes in the well-defined diffraction pattern of the solid lipid. SlipChip60 was designed for identical depths of lipid and solution chambers. The total volume of lipid required to fill each chip (6 compositions) was under 100 nL, whereas ~100 µL of solution

was required due to the dead volume of the syringe and the clamping assembly.

4.3.2 Lipid filling

The original glass SlipChip relies on capillary properties of liquids: even though the two rigid glass slides are likely separated with a very narrow gap, the samples are confined in sample chambers and ducts by ensuring that the liquids used to fill the chip do not wet its surface.[18,19] Thus, pressure required to push the liquids beyond the chambers is significantly higher than the pressure required to drive the fluids through the chambers for filling due to capillary effects:

$$\Delta p_{cap} = -\gamma\left(\frac{1}{w}+\frac{1}{h}\right)\cos\theta \qquad \text{Equation 4.1}$$

where Δp_{cap} is the capillary pressure require to drive the fluid through an opening of width w and height h, θ is the contact angle between the solution and the chip surface, and γ is the interfacial tension between the solution and the fluorinated solvent typically used to fill the interstitial space between the plates.[19] For fluidic chambers and ducts w and h represent height and width of the channels, whereas for non-patterned areas of the chip $w \sim \infty$ and h is the gap between the plates, which is significantly smaller than the height of the channels. Ismagilov *et al.* established that for accurate filling the contact angle must be at least 130°.[18] Monoolein, being amphiphilic, wets hydrophobic as well as hydrophilic surfaces (θ ~0° on either), and can be expected to spontaneously spread between the plates, which was indeed observed upon filling SlipChips fabricated in COC with molten monoolein.

To overcome the challenge of reliable lipid metering in the SlipChip, a two-step filling strategy was devised. In the first step monoolein was filled into the chambers of the corresponding COC plate using and auxiliary PDMS assembly with channels patterned to overlap with the sample chambers similarly to the original SlipChip (Figure 4.6). Because PDMS is elastomeric and sticky, it reversibly adhered to the COC plate, conforming to the imperfectly smooth COC surface and preventing the lipid from spreading during filling. The lipid was drawn into the chambers by the pressure gradient that was created by applying negative pressure (vacuum) to the control line passing over sample chambers and separated from them with a thin PDMS membrane. Once the lipid filled the chambers, it was solidified by cooling with dry ice and remained solid at room temperature (T_{melt} = 37 °C) and remained in the plate upon removal of the PDMS assembly (Figure 4.6B-D), allowing for easy manipulation of lipid-filled COC

sheets.

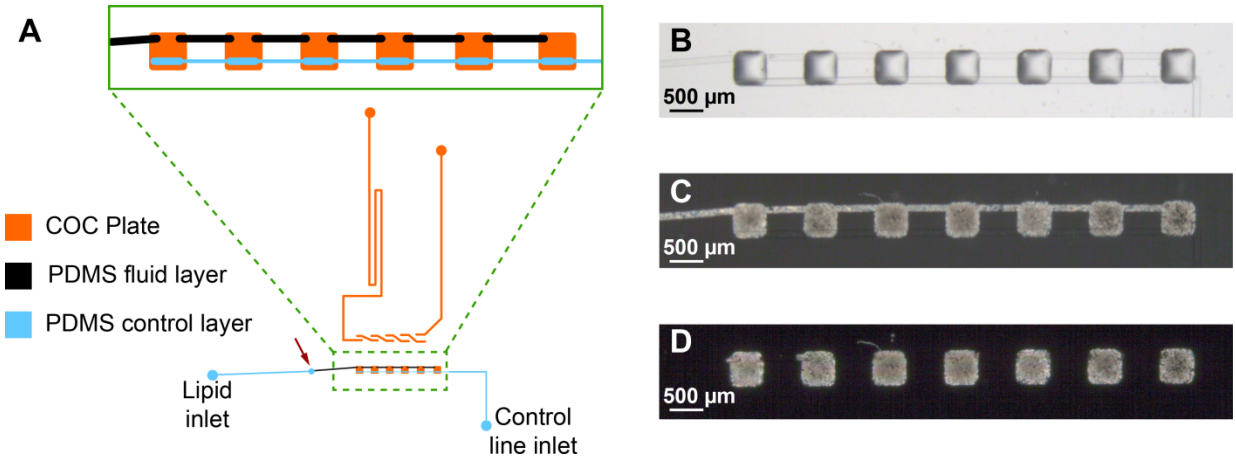

Figure 4.6. Filling the SlipChip with a lipid. **(A)** Design of the assembly used for filling respective compartments of the SlipChip with the lipid with the compartments hot-embossed in the COC plate (orange), and the auxiliary PDMS assembly (black, fluid layer, and blue, control layer). The thin PDMS membrane separating the two layers is removed in the location indicated with an arrow to connect the two parts of the fluidic line fabricated in different layers of the PDMS assembly. The inset shows a magnified view of the area with the lipid chambers. The size of the lipid chambers is 500 × 500 µm. **(B-D)** Optical micrographs of the assembly at different stages of the filling process: (B) the PDMS assembly with control and fluid lines aligned with the patterned COC sheet; **(C)** monoolein filled into the chambers and frozen prior to the removal of the PDMS assembly and **(D)** after removal of the PDMS assembly. Monoolein in interconnecting lines between the chambers remained on the COC plate and was carefully removed to retain monoolein in sample chambers only. Images in (C) and (D) were taken with crossed polarizers, making birefringent monoolein appear bright on a black non-birefringent background.

4.3.3 Solution filling and mesophase formulation

COC plates pre-filled with lipid were aligned with the plates patterned with aqueous chambers, the interstitial space between the plates was filled with a fluorinated solvent (Fluorinert FC-40), and respective sample compartments were filled with solution following the original SlipChip protocol[18] with some modifications to ensure reliable contact between the COC plates (Chapter 4.2.3, Figure 4.4). Although some of the chambers were not completely filled (Figure 4.7), the volume of solution in the chamber could be quantified by measuring the area occupied with the solution relative to the total area of the chamber. A more precise quantification could be done based on the cumulative fluorescence intensity of the solution in the chamber as was done for the lipidic mixer array chip (Chapter 3). After slipping (Figure 4.7 B1-C2) the chips were sealed, stored under FC-40 at room temperature for 24 hours to allow for passive mixing (Figure 4.7 D, E), and then kept at -12 °C until SAXS data collection. Prior to SAXS analysis the chips were defrosted and kept under FC-40 for at least 2 hours at the data collection temperature (25 ± 1 °C).

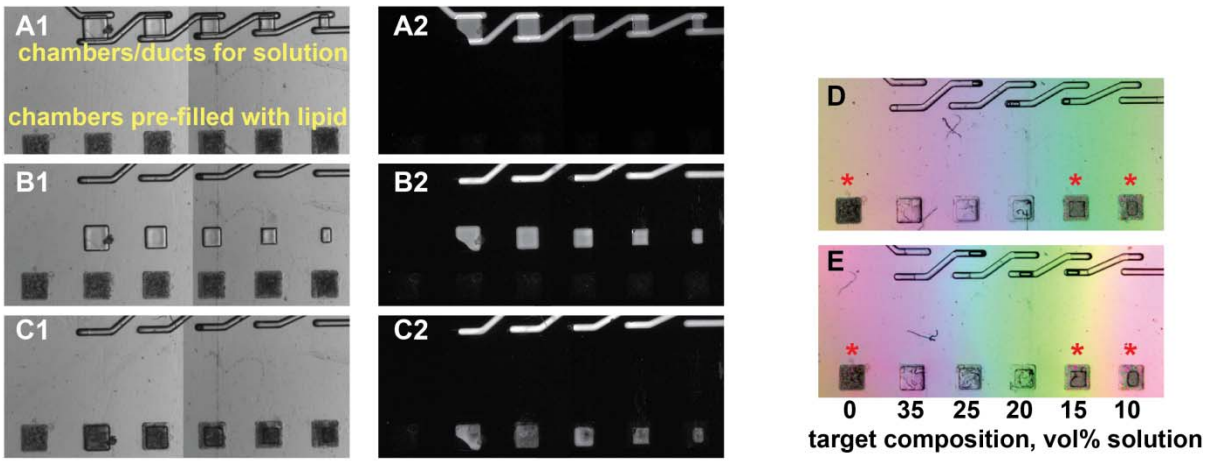

Figure 4.7. Micrographs of a SlipChip30 during **(A1, A2)** solution filling, **(B1, B2)** intermediate slipping step, **(C1, C2)** solution/lipid contact, and **(D)** after 2 hrs. and **(E)** 24 hrs. of incubation at room temperature. (A-C) Pairs of brightfield (1) and fluorescence (2) images at each step are shown, illustrating clean filling and slipping of the fluorescent aqueous solution. The solid lipid in respective chambers remained non-fluorescent until (C) coming in contact with the solution. Due to the small field of view each image in (A-C) was obtained by stitching together two micrographs, resulting in the appearance with non-uniform illumination intensity in the brightfield images. (D, E). Mesophases remained in respective chambers during prolonged storage and the appearance changes little between 2 and 24 hrs, suggesting that mixing occurred in less than 2 hrs. The rainbow background is due to birefringence of the polystyrene Petri dish used for chip storage. Birefringent lipidic mesophases, such as *Lc* and *Lα* appear dark and are additionally labeled with red asterisks, and non-birefringent cubic mesophases appear light. The size of lipid chambers is 500 × 500 μm^2.

Two sets of chips were fabricated with a 1.5-month interval and used for mesophase formulation. Although fabrication procedures for the two sets were identical, the devices behaved differently with respect to filling and slipping. Devices from set #1 could be filled and slipped cleanly, with solution confined to the ducts and chambers in both steps (Figure 4.7 A1-C2). Devices from set #2 presented multiple problems, with solutions leaking out of fluidic ducts upon de-clamping (Chapter 4.2.3) and especially slipping. Upon closer inspection we established that a small area immediately adjacent to sample chambers in the COC plate designated for aqueous solutions was not coated with the fluoropolymer used to enhance the hydrophobicity of COC (Chapter 4.2.3). Additional dip-coating of the plates with the fluoropolymer improved the success rate of sample formulation. However, out of 11 chips with the target composition of 0-30% in set #2, four had to be discarded immediately after slipping, and one more device was discarded after SAXS data collection. The origin of the disparate behavior of the two sets of devices is being investigated. We note that even in chips discarded on the basis of SAXS analysis, the dry lipid material remained intact in its designated chamber in 6 out of 7 cases. Therefore, we conclude that the quality of on-chip samples is typically compromised at the sample formulation stage rather than during storage, and the fluorinated solvent filling the space

between the plates and the samples provides an adequate barrier against transport of water between samples of different compositions.

4.3.4 SAXS data collection in a SlipChip

SAXS data collection was performed at beamline 21-ID-D of the Advanced Photon Source at Argonne National Lab using a setup that combined excellent visualization with small-angle X-ray diffraction capabilities.[31] A total of 9 locations were probed within each 500 × 500 μm^2 sample chamber using a 20 μm X-ray beam. An XY-positioner was used to move the chip in the X-ray beam, and exact beam position was monitored in an on-axis video microscope. Although only a single sample chamber was typically visible in the microscope, its location within the chip, and, consequently, the nominal sample composition, could be easily established by translating the chip in the field of view.

In comparison with the lipidic mixer array chip (Chapter 3), the SlipChip produced SAXS data of higher quality (Figure 4.8): (i) signal-to-noise ratio for samples in the SlipChip was consistently higher, presumably to the larger sample thickness (75-100 μm in the SlipChip vs. 15-40 μm in the lipidic mixer array, and (ii) the noticeable background scattering below q = 0.06 $Å^{-1}$ was absent in samples in the SlipChip, in agreement with scattering properties of materials (Chapter 3, Figure 3.5). Furthermore, the quality of samples themselves in the SlipChip was higher than in the lipidic mixer array chip. The lattice parameters at different locations within a given chamber in the SlipChip were found to be identical in most cases, indicating the uniformity of the sample and lending support to the passive mixing procedure for mesophase formulation. In the array chip, on the other hand, the points closest to chamber inlets were often found to differ from the rest of the sample in a given mixer, possibly due to the cross-talk with fluidic lines, and had to be excluded during data processing. The differences in the quality of the samples are illustrated in Figure 4.8. In the cumulative diffractogram for a given sample (Figure 4.6B) higher-order reflections of the cubic phase remain as well-resolved as in the diffractogram for an individual datapoint (Figure 4.8A) in the sample formulated in the SlipChip. In the PDMS/COC array chip the higher-order reflections in the cumulative diffractogram form a wide band without resolving into individual peaks (Figure 4.8D), unlike in the diffractogram for an individual point in the same sample (Figure 4.8C), due to the variation in the lattice parameters between individual datapoints.

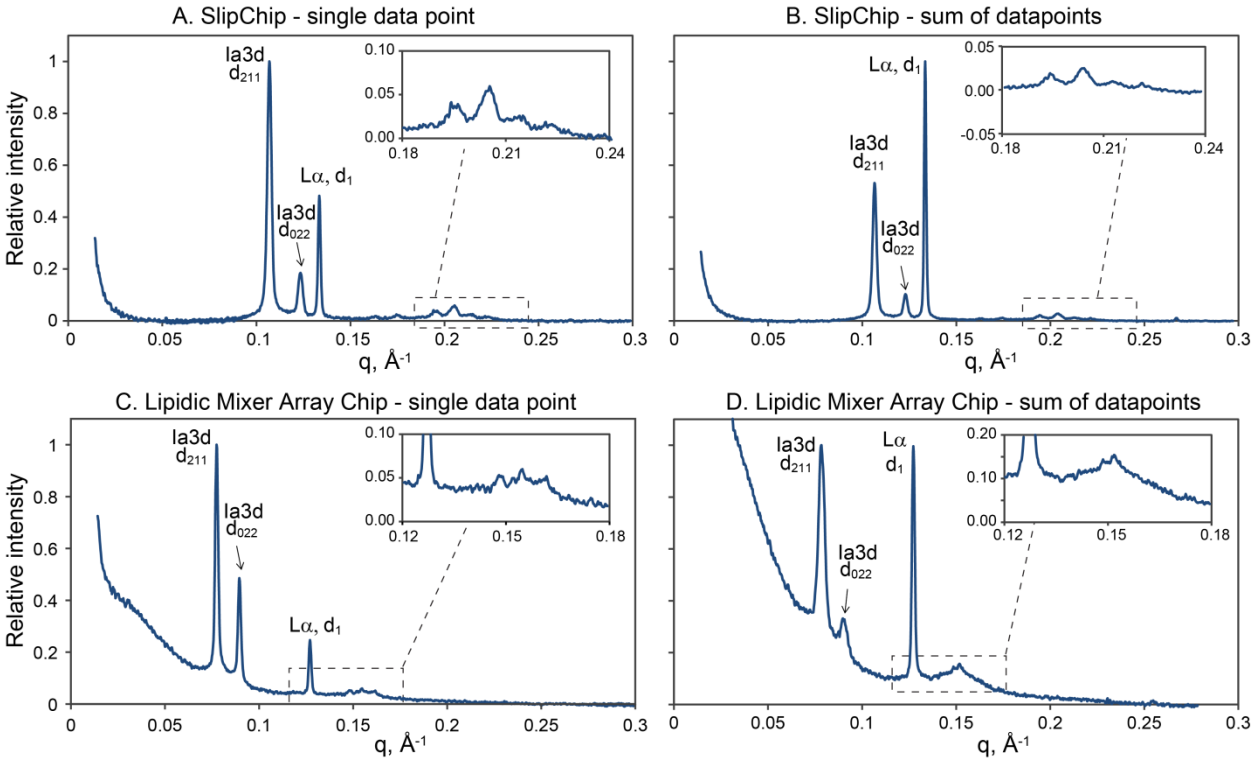

Figure 4.8. (A,B) Integrated SAXS diffractograms of lipidic mesophases formulated and analyzed in a SlipChip: **(A)** a single location within the sample chamber and **(B)** the sum of 9 diffractograms collected for the same chamber. Nominal sample composition: 25 vol% water, 75 vol% βOG/monoolein mixture (βOG/monoolein ratio 0.033 w/w); phase assignment: *Ia3d*, 145 Å, and *Lα*, 47.1 Å. **(C, D)** Integrated SAXS diffractograms of lipidic mesophases formulated and analyzed in a PDMS/COC lipidic mixer array chip described in Chapter 3: **(C)** a single location within the mixing unit and **(D)** the sum of 48 diffractograms collected for the same mixing unit. Sample composition: 55 vol% of βOG in 25 mM NaH_2PO_4, pH 5.5 (βOG concentration 5% w/v), 45 vol% of monoolein; phase assignment: *Ia3d*, 199 Å, and *Lα*, 49.5 Å. A baseline correction was performed in each diffractogram prior to normalizing intensities. Peak assignments for prominent reflections are indicated in each panel. The insets in each panel show a magnified view of higher-order *hkl* reflections from the *Ia3d* phase for respective diffractograms.

4.3.5 Phase behavior of lipidic mesophases

The results of the SAXS analysis for two types of samples, (i) monoolein/water mesophases and (ii) monoolein/βOG/water mesophases, are discussed below. Monoolein/water mesophases were prepared in both sets of SlipChips (Chapter 4.3.3), whereas the latter were prepared only as a part of set #2. SlipChip30 produced a diverse range of phase types and lattice parameters, providing a route to assess the accuracy of metering in the SlipChip based on existing data for monoolein/water mesophases. In agreement with properties of monoolein which is known to form a fully hydrated *Pn3m* mesophase at ~43 vol% of water,[34,35] SlipChip60 produced mostly water-saturated monoolein mesophases with no variation in the lattice parameter, with the exception of the samples with the lowest water content of the mesophase (nominal 35 vol%). All mesophases of monoolein/βOG/water formulated in the SlipChip60 were

of the *Pn3m* type and their lattice parameters showed relatively little variation.

Table 4.1. Types and lattice parameters of monoolein/water mesophases identified in five SlipChips as a function of nominal sample composition.

Nominal sample composition, vol% water	Types of mesophases	Chip A[a]	Chip B[a]	Chip C[a]	Chip D[a]	Chip E[a]
0	***Lc***	49.6	49.6	49.6	49.6	49.6
10	***Pn3m***					
	Ia3d					
	Lα	39.0	39.2	39.2		43.2
15	***Pn3m***					
	Ia3d				114	
	Lα	43.2	42.9	43.6	46.3	42.1
20	***Pn3m***					
	Ia3d	116	125	123	115	114
	Lα	44.0				46.3
25	***Pn3m***					
	Ia3d	144	139	138	133	135
	Lα					
30	***Pn3m***	102				103
	Ia3d		138	155	148	
	Lα					

[a] Numbers are lattice parameters of respective mesophases in angstroms. Several phases listed for a given sample compositions indicate equilibrium phase coexistence.

Table 4.1 lists the types and lattice parameters of monoolein/water mesophases identified in five independently set up SlipChips with the target composition range of 0-30 vol% water for devices from set #1 (A-C) and set #2 (D, E). The results were in agreement with the properties of monoolein/water mesophases:[34,35] as the amount of water in the sample increased, the *Lα – Ia3d – Pn3m* sequence of phases was observed, including several instances of coexisting *Lα* and *Ia3d* phases. The lattice parameters of mesophases increased with increasing content of water in the sample.[34,35] Chip B in Table 4.1 is the one photographed in Figure 4.5, and SAXS data are in excellent agreement with the appearance of the samples: samples identified as lamellar by SAXS are birefringent in the photographs, and samples identified as cubic are non-birefringent. These results validate our storage and equilibration procedure. However, in several instances either different types of phases or identical mesophases with different lattice parameters were observed at the same nominal sample composition in different chips. These differences indicate the variation between actual sample compositions in the different chips, and could be partially traced to the incomplete filling of sample chambers.

Table 4.2. Types and lattice parameters of monoolein/βOG/water mesophases identified in three SlipChips as a function of nominal sample composition. The βOG/monoolein ratio was fixed at 0.033 w/w, while the amount of water in the samples was varied.

Nominal sample composition, vol% water	Types of mesophases	Chip F[a]	Chip G[a]	Chip H[a]
0	***Lc***	36.1[b]	49.6, 35.6	49.6, 36.1
10	***Pn3m***			
	Ia3d			
	Lα	43.1	38.0	39.6
15	***Pn3m***			
	Ia3d			
	Lα	43.1	42.7	44.1
20	***Pn3m***			
	Ia3d		140	
	Lα	43.3	46.7	46.0
25	***Pn3m***			
	Ia3d	147	145	148
	Lα	47.1	47.1	47.2
30	***Pn3m***			
	Ia3d	149	154	159
	Lα	47.3		

[a] Numbers are lattice parameters of respective mesophases in angstroms. Several phases listed for a given sample compositions indicate equilibrium phase coexistence.
[b] This sample likely represents a lamellar *Lα* phase that formed due to cross-talk with solution-containing chambers

To formulate monoolein/βOG/water mesophases, we used a mixture of monoolein and βOG with a fixed ratio of components (βOG/monoolein 0.033 w/w) to fill the lipid chambers, followed by mixing with different amounts of water as defined by the volume of the chambers in the SlipChip. The mesophases formulated and analyzed on-chip (Table 4.2) showed expected differences from the monoolein/water mesophases:[36-38] the sequence of phases as a function of water content in the samples with detergent remained the same, but introduction of detergent caused the lattice parameters of the *Ia3d* phases to increase relative to mesophases without detergent (Table 4.1). Furthermore, based on the results for samples formulated in SlipChip60, in the fully hydrated *Pn3m* phase the lattice parameter increased to 120 Å upon addition of detergent compared to the 103 Å established for the fully hydrated monoolein/water *Pn3m* phase. Both values are in quantitative agreement with previously reported lattice parameters.[34,38] The solid mixed monoolein/βOG phase remained intact in most cases, and a peak at 35.6 Å appeared in addition to the peak at 49.6 Å observed for pure solid monoolein. Variation in sample compositions between nominally identical samples in different chips was observed (Table 4.2), similarly to our findings for monoolein/water mesophases.

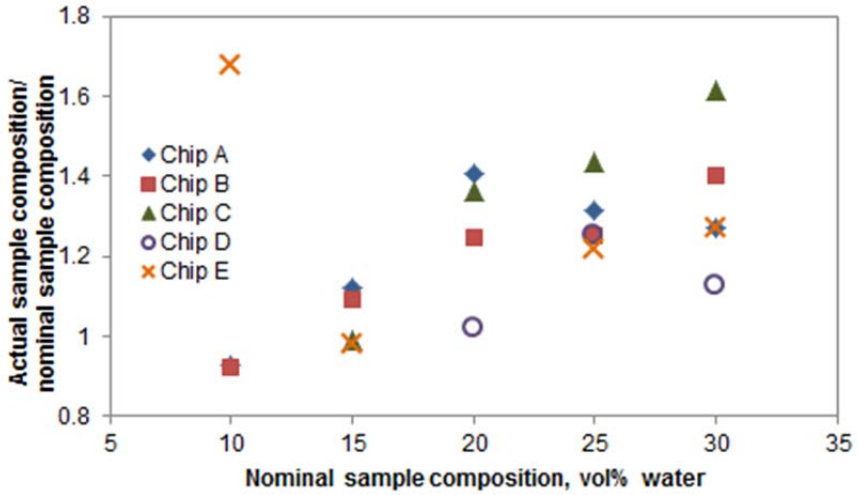

Figure 4.9. The ratio between actual and nominal sample compositions (in vol% water) as a function of the nominal sample composition in five SlipChips. Nominal sample compositions used to calculate the ratios were adjusted based on the area of the fluorescent part of each chamber to account for incompletely filled chambers. Chip notations A-D correspond to those in Table 4.1. Points with coexisting *Lα* and *Ia3d* mesophases are excluded due to the ambiguity in the sample compositions.

To assess the accuracy of metering in the SlipChip, actual sample compositions were estimated based on the lattice parameter dependence of monoolein mesophases on the water content of the samples[34] (Figure 4.9). The difference between nominal sample compositions and actual sample compositions appeared to increase systematically from the chamber with the lowest content of water (10 vol%) to the chamber with the highest content of water (30 vol%) in all SlipChips. The nominal amount of water in the sample could be exceeded by a factor of 1.3-1.4x. For example, the sample with the target composition of 30 vol% water was found to contain 38 vol% water. Because all devices tested here were fabricated using a single photoresist-on-silicon master, this result may indicate that the height of the sample chamber varied due to the uneven thickness of the photoresist. Achieving highly uniform coating thickness with thick (> 25 μm) positive photoresists is difficult, yet highly precise sample formulation is required for the studies of the phase behavior of lipidic mesophases because of the possibility of several phase transitions within a very narrow range of compositions (Chapter 1, Figure 1.12). We note that even the etched-glass SlipChip that produced compositions within 0.9 - 1.1x of the target[18] may not be sufficiently accurate for such studies without additional calibration of sample volumes. Our findings suggest that precise calibration of chamber volumes and measurement of the volumes of samples in each chip is required for mapping of the phase behavior of lipidic mesophases.

4.4 Conclusions

The X-ray transparent SlipChip demonstrated in this chapter is a viable concept for the studies of the phase behavior of lipidic mesophases, as illustrated by formulating and analyzing mesophases of monoolein/water or monoolein/βOG/water of different compositions using 12.5 nL per composition. The advantages of the all-COC SlipChip compared to hybrid PDMS/COC devices are the higher signal-to-noise ratio of SAXS data, lower background scatter from chip materials, and the higher degree of uniformity of samples within a given sample chamber. The three major mesophase types (*Pn3m*, *Ia3d*, *Lα*), and a solid crystalline phase *Lc* typical for monoolein mesophases under ambient conditions[34,35] were successfully identified in the SlipChip. The sequence of phases and the values of lattice parameters established for both types of samples are in agreement with previously reported data. However, for highly accurate estimates of mesophase composition as required in the studies of the phase behavior, calibration of the exact volume of samples in the chambers is highly desirable and will need to be addressed in future work.

4.5 References

1 Y. Misquitta, V. Cherezov, F. Havas, S. Patterson, J. M. Mohan, A. J. Wells, D. J. Hart and M. Caffrey. Rational design of lipid for membrane protein crystallization. *J. Struct. Biol.*, 2004, **148**, 169-175.

2 J. Yamashita, M. Shiono and M. Hato. New lipid family that forms inverted cubic phases in equilibrium with excess water: Molecular structure − aqueous phase structure relationship for lipids with 5,9,13,17-tetramethyloctadecyl and 5,9,13,17-tetramethyloctadecanoyl chains. *J. Phys. Chem. B*, 2008, **112**, 12286-12296.

3 V. Borshchevskiy, E. Moiseeva, A. Kuklin, G. Büldt, M. Hato and V. Gordeliy. Isoprenoid-chained lipid β-xyloc16+4—a novel molecule for *in meso* membrane protein crystallization. *J. Gryst. Growth*, 2010, **312**, 3326-3330.

4 D. Li, J. Lee and M. Caffrey. Crystallizing membrane proteins in lipidic mesophases. A host lipid screen. *Cryst. Growth Design*, 2011, **11**, 530-537.

5 F. Shi, Z. Han, J. Li, B. Zheng and C. Wu. Mapping polymer phase diagram in nanoliter droplets. *Macromolecules*, 2012, **44**, 686-689.

6 S. Park, P. A. L. Wijethunga, H. Moon and B. Han. On-chip characterization of cryoprotective agent mixtures using an EWOD-based digital microfluidic device. *Lab Chip*, 2011, **11**, 2212-2221.

7 J. U. Shim, G. Cristobal, D. R. Link, T. Thorsen, Y. W. Jia, K. Piattelli and S. Fraden. Control and measurement of the phase behavior of aqueous solutions using microfluidics. *J. Am. Chem. Soc.*, 2007, **129**, 8825-8835.

8 M. J. Anderson, C. L. Hansen and S. R. Quake. Phase knowledge enables rational screens for protein crystallization. *Proc. Natl. Acad. Sci. USA*, 2006, **103**, 16746-16751.
9 M. O. A. Sommer and S. Larsen. Crystallizing proteins on the basis of their precipitation diagram determined using a microfluidic formulator. *J. Synchrotron Rad.*, 2005, **12**, 779-785.
10 C. L. Hansen, M. O. A. Sommer and S. R. Quake. Systematic investigation of protein phase behavior with a microfluidic formulator. *Proc. Natl. Acad. Sci. USA*, 2004, **101**, 14431-14436.
11 P. Moreau, J. Dehmoune, J. B. Salmon and J. Leng. Microevaporators with accumulators for the screening of phase diagrams of aqueous solutions. *Appl. Phys. Lett.*, 2009, **95**, 033108.
12 J.-B. Salmon and J. Leng. Microfluidics for kinetic inspection of phase diagrams. *Compt. Rend. Chim.*, 2009, **12**, 258-269.
13 J. Leng, M. Joanicot and A. Ajdari. Microfluidic exploration of the phase diagram of a surfactant/water binary system. *Langmuir*, 2007, **23**, 2315-2317.
14 J. Leng, B. Lonetti, P. Tabeling, M. Joanicot and A. Ajdari. Microevaporators for kinetic exploration of phase diagrams. *Phys. Rev. Lett.*, 2006, **96**, 084503.
15 X. Zhou, J. Li, C. Wu and B. Zheng. Constructing the phase diagram of an aqueous solution of poly(n-isopropyl acrylamide) by controlled microevaporation in a nanoliter microchamber. *Macromol. Rapid Comm.*, 2008, **29**, 1363-1367.
16 S. Selimovic, F. Gobeaux and S. Fraden. Mapping and manipulating temperature-concentration phase diagrams using microfluidics. *Lab Chip*, 2010, **10**, 1696-1699.
17 W. Du, L. Li, K. P. Nichols and R. F. Ismagilov. SlipChip. *Lab Chip*, 2009, **9**, 2286-2292.
18 L. Li, W. Du and R. Ismagilov. User-loaded SlipChip for equipment-free multiplexed nanoliter-scale experiments. *J. Am. Chem. Soc.*, 2009, **132**, 106-111.
19 L. Li, M. A. Karymov, K. P. Nichols and R. F. Ismagilov. Dead-end filling of SlipChip evaluated theoretically and experimentally as a function of the surface chemistry and the gap size between the plates for lubricated and dry slipchips. *Langmuir*, 2010, **26**, 12465-12471.
20 C. L. Hansen, S. Classen, J. M. Berger and S. R. Quake. A microfluidic device for kinetic optimization of protein crystallization and in situ structure determination. *J. Am. Chem. Soc.*, 2006, **128**, 3142-3143.
21 S. Guha, S. L. Perry, A. S. Pawate and P. J. A. Kenis. Fabrication of X-ray compatible microfluidic platforms for protein crystallization. *Sensors Actuators B*, 2012, **174**, 1-9.
22 M. R. Thorson, S. Goyal, Y. Gong, G. G. Z. Zhang and P. J. A. Kenis. Microfluidic approach to polymorph screening through antisolvent crystallization. *CrystEngComm*, 2012, **14**, 2404-2412.
23 L. Li and R. F. Ismagilov. Protein crystallization using microfluidic technologies based on valves, droplets, and SlipChip. *Annu. Rev. Biophys.*, 2010, **39**, 139-158.
24 W. Liu, D. Chen, W. Du, K. P. Nichols and R. F. Ismagilov. SlipChip for immunoassays in nanoliter volumes. *Anal. Chem.*, 2010, **82**, 3276-3282.
25 F. Shen, W. Du, J. E. Kreutz, A. Fok and R. F. Ismagilov. Digital pcr on a SlipChip. *Lab Chip*, 2010, **10**, 2666-2672.
26 J. S. Joseph, W. Liu, J. Kunken, T. M. Weiss, H. Tsuruta and V. Cherezov. Characterization of lipid matrices for membrane protein crystallization by high-

throughput small angle X-ray scattering. *Methods*, 2011, **55**, 342-349.
27 C. E. Conn, C. Darmanin, X. Mulet, S. Le Cann, N. Kirby and C. J. Drummond. High-throughput analysis of the structural evolution of the monoolein cubic phase *in situ* under crystallogenesis conditions. *Soft Matter*, 2012, **8**, 2310-2321.
28 L. Li, W. Du and R. F. Ismagilov. Multiparameter screening on SlipChip used for nanoliter protein crystallization combining free interface diffusion and microbatch methods. *J. Am. Chem. Soc.*, 2009, **132**, 112-119.
29 M. A. Unger, H.-P. Chou, T. Thorsen, A. Scherer and S. R. Quake. Monolithic microfabricated valves and pumps by multilayer soft lithography. *Science*, 2000, **288**, 113-116.
30 Y. Xia and G. M. Whitesides. Soft lithography. *Angew. Chem. Int. Ed.*, 1998, **37**, 550-575.
31 E. Kondrashkina, D. S. Khvostichenko, S. L. Perry, J. von Osinski, P. J. A. Kenis and K. Brister. Using macromolecular-crystallography beamline and microfluidic platform for small-angle diffraction studies of lipidic mesophases for membrane protein crystallization. *J. Phys. Conf. Ser.*, 2012, accepted.
32 V. Cherezov, K. M. Riedl and M. Caffrey. Too hot to handle? Synchrotron X-ray damage of lipid membranes and mesophases. *J. Synchrotron Rad.*, 2002, **9**, 333-341.
33 D. E. Sands, *Introduction to crystallography*, W.A. Benjamin, Inc., New York, NY, 1969.
34 J. Briggs, H. Chung and M. Caffrey. The temperature-composition phase diagram and mesophase structure characterization of the monoolein/water system. *J. Phys. II*, 1996, 723-751.
35 H. Qiu and M. Caffrey. The phase diagram of the monoolein/water system: Metastability and equilibrium aspects. *Biomaterials*, 2000, **21**, 223-234.
36 G. Persson, H. Edlund, H. Amenitsch, P. Laggner and G. Lindblom. The 1-monooleoyl-*rac*-glycerol/*n*-octyl-β-d-glucoside/water system. Phase diagram and phase structures determined by NMR and X-ray diffraction. *Langmuir*, 2003, **19**, 5813-5822.
37 G. Persson, H. Edlund and G. Lindblom. Phase behaviour of the 1-monooleoyl-*rac*-glycerol /*n*-octyl-β-d-glucoside/water system. *Progr. Colloid Polym. Sci.*, 2004, **123**, 36-39.
38 Y. Misquitta and M. Caffrey. Detergents destabilize the cubic phase of monoolein: Implications for membrane protein crystallization. *Biophys. J.*, 2003, **85**, 3084-3096.

Chapter 5.
X-ray compatible microfluidic platform for *in meso* crystallization of membrane proteins

Abstract

In this chapter an X-ray compatible microfluidic platform for *in meso* crystallization of membrane proteins is reported. The platform was designed specifically to facilitate passive mixing between the protein solution and the lipid for the formation of protein-loaded mesophases, and to avoid on-chip routing of protein-loaded mesophases. The 12-well cyclic olefin co-polymer/polydimethylsiloxane chip described in this chapter is under 210 μm thick, and requires respectively 25, 40-65, and 215-300 nL of the lipid, protein solution, and precipitant per well. The approach was validated by crystallizing the membrane protein photosynthetic reaction center from *R. Sphaeroides* and successfully solving its structure at a resolution of 3.33 Å using crystal X-ray diffraction data collected from multiple crystals on-chip.

5.1 Introduction

Despite the biochemical importance of membrane proteins and recent advances in crystallization, detailed spatial structures of membrane proteins remain a somewhat elusive target of structural biology. Membrane proteins represent approximately 1% of all protein crystal structures available.[1] The differences in the numbers of crystal structures available for soluble and membrane proteins presumably illustrate the respective combined difficulties of expression, purification, and crystallization, the latter being an important bottleneck. In large-scale screening efforts, only ~1% of crystallization trials for soluble proteins resulted in crystallogenesis, and only ~30% of soluble proteins could be crystallized.[2] The success rate for membrane proteins is likely significantly lower.

Crystallization of membrane proteins in lipidic mesophases[3] (usually termed LCP or *in meso*) is a proven powerful alternative to the traditional crystallization approach from detergent-stabilized solutions and has been used to crystallize a number of biologically and pharmacologically important proteins, such as human G-protein coupled receptors.[4,5] Nevertheless, the penetration of the *in meso* method in the wider structural biology community has been slow, likely due to the difficulties of handling of the toothpaste-like mesophases and substantial deviations of the *in meso* crystallization procedure from the traditional crystallization from solutions. Although relatively user-friendly alternatives appeared recently,[6,7] the most common variant of the *in meso* method requires specialized tools in every step of the crystallization protocol:[3,8] (i) a coupled-syringe mixer for mixing of lipid (typically monoolein) and the protein solution in the preparation of protein-loaded mesophases, (ii) a ratchet dispenser for dispensing the mesophase into crystallization well, and (iii) special glass sandwich well plates for crystal visualization due to the non-uniform optical properties of the mesophase. The glass sandwich plates make crystal harvesting especially cumbersome,[4] and the problem is compounded by the typical small size of (often transparent) membrane protein crystals, 5-50 μm, and the viscosity of mesophases. While trial formulation can be automated with robotic systems,[8,9] crystal harvesting from well plates is necessarily manual and the fragile crystals may get damaged due to shear and dehydration, compromising the quality of X-ray diffraction data.

Inexpensive microfluidic systems have been successfully used to automate sample formulation and to reduce the amount of material per crystallization trial for protein

crystallization from solutions.[10] Importantly, a number of X-ray transparent platforms for *in situ* crystal diffraction data collection have been demonstrated to eliminate the manual crystal harvesting step.[11-21] These approaches would be highly desirable for working with scarcely available membrane proteins that form small fragile crystals, but only two microfluidic systems have been developed for *in meso* crystallization[22,23] (Chapter 1.2.5). While an X-ray transparent variant for one of them, the lipidic mixer, has been demonstrated (Chapter 3), it is not suitable for the formulation of protein-loaded mesophases due to the requirement for cooling during mesophase mixing.

Here microfluidic platforms are described for *in meso* crystallization that rely on passive mixing between lipid and protein solution for the formulation of protein-loaded mesophases, similar to the recently demonstrated macroscale methods.[6,7] Chapter 5.2.1 and 5.2.2 describe the fabrication and operation of the chips. Sample formulation strategies in preliminary design concepts are outlined in Chapter 5.3. Chapter 5.4 describes a successful X-ray transparent array chip for *in meso* crystallization, with operation and sample formulation principles summarized in Chapter 5.4.1 and 5.4.2. The chip has been validated by crystallizing a membrane protein photosynthetic reaction center (RC) from *R. Sphaeroides* (Chapter 5.4.3) and collecting X-ray diffraction data *in situ* for crystal structure solution at the resolution of 3 Å (Chapter 5.4.4).

5.2 Materials and methods

5.2.1 Device fabrication

Fabrication of photoresist-on-silicon masters. Depending on the desired feature height and profile, photoresist-on-silicon masters were created with SU8-2050 photoresist (Microchem) for 40-65 μm-tall vertical features, SU8-25 (Microchem) for the patterns with the 25 μm-tall vertical features, SPR-220-7 (Shipley) for 14 μm-tall rounded features, and AZ50XT (AZ Electronic Materials) for 50 μm-tall rounded features. SPR-220-7 masters were reflowed after patterning by heating at 120 °C for 2 min, and AZ50XT masters were reflowed at 115 °C for 45 s to achieve the rounded profile.[24] Specific feature heights are listed for all tested device types in respective sections. All photoresist-on-silicon masters were treated with (tridecafluoro-1,1,2,2-tetrahydrooctyl) trichlorosilane (Gelest, Inc.) in a vacuum chamber for 4 hours for easy release of PDMS replicas.[25]

Fabrication of cyclic olefin co-polymer (COC) substrates. Patterned COC substrates (2 mil, 6013, TOPAS Advanced Polymers Inc.) were fabricated by hot embossing using high-temperature epoxy molds (Conapoxy FR 1080) in a laminating press (Carver Inc., Model 3851) under the load of 150-200 kg. For high-fidelity pattern transfer, a stack of (i) 7-10 mm PDMS slab, (ii) an epoxy mold, (iii) a COC sheet, and (iv) a 7.5 × 5 cm microscope glass slide was placed between the platens of the press. The temperature of the assembly was brought to 350 °F (177 °C) and then to below 250 °F (121 °C) before removing the patterned layer. Holding at 177 °C for an extended period of time was not required for accurate pattern transfer. The epoxy molds were fabricated using the procedure developed by Guha *et al*.[21] Briefly, PDMS with 10:1 monomer : crosslinker ratio was used to fabricate a thick inverse master of the photoresist-on-silicon master. PDMS was baked for 2 hrs at 75 °C. An epoxy master (Conapoxy FR 1080) for use in hot-embossing was then molded off the PDMS master. The epoxy components (83:100 hardener:epoxy, by mass) were mixed using a planetary centrifugal mixer (Thinky USA) for 15 min at 2000 rpm with rotation and then de-foamed for 12 min at 2200 rpm. The epoxy mixture was poured into the inverse PDMS master and cured on a level hot plate at 120 °C for 4 hours. To prevent evolution of gas bubbles from the PDMS master during epoxy curing, the mold was either degassed for ~10 min under vacuum or heated on the hot-plate at 120 °C for 20 min prior to filling it with epoxy. The PDMS master could be re-used several times for epoxy molding.

The non-patterned 2 mil-thick COC sheets were flattened between glass slides at 177 °C and a load of 150-200 kg in a laminating press prior to use to obtain sheets with smooth surface.

Fabrication of thick PDMS devices. Thick PDMS devices (Chapter 5.3, Figures 5.1 and 5.2) were fabricated for initial testing of designs with normally open and normally closed valves (Chapter 1.2.5) and for lipid filling into the patterned COC substrate (Chapter 5.4.1, Figure 5.3). The PDMS control layers of 5-10 mm in thickness were prepared by pouring a mixture with the monomer : cross-linker ratio of 5:1 on the photoresist-on-silicon master followed by curing at 90 °C for 5-10 min. For the fluid layers photoresist-on-silicon masters were spin-coated using PDMS with the monomer: cross-linker ratio of 15:1 to obtain films of ~10 μm thicker than the height of the photoresist features. Fluid layers were cured at 90 °C for 7-9 min. Non-patterned PDMS films were fabricated in the same way as the fluid layers by spin-coating plain silane-treated silicon wafers to obtain ~20 μm-thick films.

The chips were assembled as follows: (i) inlet ports were punched in the control layers using a 20 AWG needle with a thin wire plunger, (ii) control layers were irreversibly bonded to fluid layers by placing the two layers in conformal contact and heating at 70 °C for 2 hrs,[24] and (iii) inlet ports for the fluid layer were punched. For preliminary device tests described in Chapter 5.3, the control/fluid layer assembly was permanently bonded to a microscope glass slide by activating the surfaces using atmospheric plasma treatment[26] in the plasma cleaner (Harrick, Model PDC-001) for 1 min at 500-700 mTorr. To prevent permanent closure of normally-closed valves in this step, the corresponding control lines were actuated using a vacuum pump prior to bringing the two parts of the device in contact, and remained actuated for at least 3 hours.

For filling the COC substrates with lipid the parts of thin membranes to be located over the lipid chambers were removed carefully with sharp tweezers (Chapter 5.4.1, Figure 5.3). The control/fluid layer assembly was then placed a patterned COC substrate, and a reversible bond between the PDMS fluid layer and the COC substrate formed spontaneously.[21]

Fabrication of thin hybrid PDMS/COC devices. Hybrid microfluidic chips consisted of a 2 mil-thick flat cyclic olefin copolymer (COC) top layer (2 mil, 6013, TOPAS Advanced Polymers), a thin PDMS (RTV 650, Momentive Performance Adhesives) control layer, a thin PDMS fluid layer, and a patterned 2 mil-thick COC bottom substrate (Chapter 5.4.1, Figure 5.4). The PDMS layers were fabricated using standard replica molding procedures[24,25] by spin-coating the photoresist-on-silicon masters to obtain a PDMS film height ~10 μm thicker than the corresponding photoresist feature height. For the fluid layer we used PDMS with the monomer : cross-linker ratio of 15:1 followed by curing at 90 °C for 7-9 min. For the control layer we used PDMS with the monomer : cross-linker ratio of 5:1 followed by curing at 80 °C for 3 min.

The chips were assembled as follows: (i) a flat COC sheet was irreversibly bonded to the PDMS control layer, and (ii) the resulting COC-PDMS assembly was irreversibly bonded to the PDMS fluid layer. Permanent COC-PDMS bonding in step (i) was achieved by activating the surfaces using atmospheric plasma treatment[26] in a plasma cleaner (Harrick, Model PDC-001) for 1 min at 500-700 mTorr. Permanent PDMS-PDMS bonding in step (ii) was done using the standard multilayer soft lithography method[24] by placing layers of PDMS with different monomer : cross-linker ratios in conformal contact and heating them at 70 °C for 2 hours. Inlet holes for the control and the fluid layer were drilled in the COC-PDMS-PDMS assembly using a

750 μm drill bit (McMaster-Carr). The assembly was then placed on a patterned COC substrate pre-filled with lipid, and a reversible bond between the PDMS fluid layer and the COC substrate formed spontaneously.[21]

5.2.2 Device operation

During filling and mixing, microfluidic devices were monitored using an upright microscope (Leica MDG33) equipped with a macro lens and a digital camera (Leica DFC295).

Thick devices with normally open valves. Prior to filling and mixing operations, fluid-routing control lines (Section 5.3.1, Figure 5.1) were filled with Fluorinert FC-40 (3M) to prevent gas leakage from the control layer through valve membranes to the fluid layer and subsequent bubble formation in sample chambers. For pneumatic actuation we used a 32-line solenoid valve manifold (Fluidigm). The pressure in the manifold and the sequence of valve actuations were controlled by Genie V2 software (Fluidigm). The dead-ended fluid chambers were filled with samples by applying a pressure of 5.5 psi to the filling fluid to displace air from the chambers. Pressure of 22.5 psi was used to actuate fluid-routing valves. This pressure was the highest achievable with the Fluidigm solenoid valve manifold.

Thick devices with normally closed valves. The dead-ended fluid chambers were filled with samples by applying a pressure of 5.5 psi to the filling fluid to displace air from the chambers. Valves were actuated using a vacuum pump (GAST, Model DOA-P704-AA).

Thin hybrid PDMS/COC devices. For fluid routing and metering these chips rely on normally closed valves. Fluid chambers were filled by placing several microliters of solution onto fluid layer inlet ports and applying negative pressure (vacuum) to valve lines and auxiliary control lines (Chapter 5.3.2, Figure 5.2). A pressure gradient formed in the fluid layer due to the air permeability of PDMS, resulting in the solutions being pulled into the device. The solutions eventually replaced all air pockets in the sample chambers. Various chamber geometries were tested, as discussed in Chapter 5.4.2. The same strategy was applied for filling the lipid into the chambers patterned in the COC substrate (Chapter 5.4.1). The lipid used in this work (monoolein, Sigma Aldrich, 99%) melts at 37 °C and was heated with a hair dryer for filling. Prior to removing the preliminary PDMS assembly from the lipid-filled COC substrate, the lipid was frozen by placing a piece of dry ice on the device.

5.2.3 Sample preparation

Monoolein (Sigma Aldrich, 99%) was used as received. 5% v/w and 10% v/w solutions of βOG (Anatrace, Anagrade) were prepared by dilution from a 20% v/w βOG solution in 25 mM NaH_2PO_4, pH 5.5. NaH_2PO_4 was obtained from EMD Chemicals.

Rhodobacter Sphaeroides photosynthetic reaction center (RC) in 10mM Tris pH 7.8, 280 mM NaCl, 0.05% LDAO was a gift from Dr. Philip Laible, Argonne National Lab. The RC solution at an initial concentration of 6 mg/mL was concentrated in a Microcon centrifugal filter device (Millipore corp.) with a 10,000 Da cut-off by spinning in a microcentrifuge at 10,000 g in a cold room maintained at 4 °C. The volume of the concentrate was measured after every 5-min spin and the centrifugation was stopped when the final volume reached ¼ of the initial volume, yielding a solution with a calculated final concentration of 24 mg/mL. The filtrate was used to dilute this solution to obtain samples with RC concentration of 10-24 mg/mL. The solutions were either used immediately for crystallization trials or separated into 2-3 µL aliquots and kept in the freezer at -12 °C before using.

Precipitants for protein crystallization trials were formulated by first preparing an aqueous solution of 1M HEPES (Sigma) and 1.15 M $(NH_4)_2SO_4$ (Fisher) and adjusting the pH to 7.5. Jeffamine M-600 (Hampton Research) was then mixed with the aqueous solution to obtain mixtures containing 11, 12, 13, and 14% w/v of Jeffamine.

5.2.4 Crystallization of photosynthetic reaction center in well plates

Protein crystallization in 96-well flat bottom microplates (Corning Crystal*EX* 3785) replicated the PLI[6] protocol (Chapter 1.2.4) and the crystallization conditions established in the original report. Dry monoolein was used instead of preparing the lipid mesophase with water. Monoolein was dispensed into the well plate (0.2 µL/well) using a ratchet dispenser (Hampton Research), covered with Crystal Clear Sealing Film (Hampton Research) and cooled to -12 °C for freezing. Sealed monoolein-filled well plates were stored in the freezer for up to 3 weeks. Prior to use, the plates were brought to room temperature before removing the tape.

For crystallization, 0.4 µL of the RC protein solution was added on top of dry monoolein in the wells, sealed, and incubated for 4-14 hrs at 20 °C. Afterwards, 2 µL of the precipitant solution was added to the crystallization well and 5-10 µL of the same solution was added to the

reservoir well. The plates were sealed and incubated at 20 °C. Protein crystals of 5-60 μm in size formed in 24-48 hrs.

5.2.5 On-chip crystallization of photosynthetic reaction center

Protein crystallization on-chip was carried out with the same materials and incubation times as used in the crystallization in well plates. Solution volumes were set by the volume of the chambers of the chip. Chip operation and metering strategies are described in detail in Chapter 5.4.1 and 5.4.2 (Figures 5.3 - 5.6).

5.2.6 Crystal X-ray diffraction data collection

Protein crystal X-ray diffraction data were collected at macromolecular crystallography beamlines 21-ID-F and 21-ID-D of the Life Sciences Collaborative Access Team (LS-CAT), Advanced Photon Source, Argonne National Lab. Both beamlines are equipped with microdiffractometers (MAATEL MD2) consisting of a goniometer, XYZ micropositioner and an on-axis video microscope. Beamline 21-ID-F operates at a fixed wavelength (λ = 0.979 Å, 12.7 keV) and has a MarMosaic 225 detector (Rayonix). Beamline 21-ID-D is fully tunable and has a MX-300 detector (MarResearch). Here beam energy was kept at 12.7 keV for data collection to match that of the 21-ID-F station. Beam-defining apertures of 20 or 50 μm in diameter were used to control the footprint of the beam.

Protein crystals grown in well plates were harvested using microloops (Hampton Research), flash-frozen in liquid nitrogen without the addition of cryoprotectant,[3,27] and kept under a cryostream during data collection. Up to 400 data frames could be collected per crystal without noticeable deterioration in data quality.

On-chip data collection was done at room temperature. The chip was trimmed to a size of ~2×2.5 cm to conform to spatial requirements of the goniometer and mounted using a modified goniometer mount with magnetic base (Chapter 5.4.4, Figure 5.9). The position of the chip relative to the X-ray beam was monitored using the video microscope; the microfluidic chip was translated using the XYZ micropositioner to target different protein crystals within the chip. In a typical data collection protocol, frames were collected using 1° oscillation and 1 s exposure time per frame with beam attenuation of 70-80%. Depending on the crystal, 5-15 frames could be collected before radiation damage to the crystal became critical.

5.2.7 Analysis of crystal X-ray diffraction data

Analysis of X-ray diffraction data collected at the synchrotron was performed using HKL2000 software for indexing, refinement, integration, and scaling (HKL Research Inc.).[28] The resolution range of the data was established based on the resolution shell at which I/σ fell below 2.3 provided that R_{sym} was also less than 0.50. Subsequent processing of crystallography datasets was done using the Phenix suite of programs.[29] Molecular replacement[30] was done in Phaser using PDB structure 2UWW as a model.[31] Model refinement was performed using phenix.refine. Electron density maps were displayed using Coot.[32]

5.3 Preliminary diffusion-based platforms for mesophase formulation

In the course of developing an X-ray transparent lipidic mixer (Chapter 3), we established that even though this design was previously used for crystalizing membrane proteins on-chip,[22] it was not optimal for high-throughput crystallization efforts and for X-ray transparency. Many of the problems associated with the mixer stemmed from the active mixing approach, which required normally open valves and permanent bonding between all layers of the device. Normally open valves require high actuation pressures for isolating tall channels,[33] ultimately limiting the height of the sample compartments and, consequently, the maximal vertical dimension of protein crystals that can be grown on-chip. This parameter is extremely important because crystal size correlates with the quality of crystal X-ray diffraction data.[21,34] The requirement for permanent bonding between all device layers led to an extremely laborious fabrication procedure with a relatively low success rate compared to the traditional multilayer soft lithography[24-26] and the fabrication methods for X-ray transparent devices that use passive mixing.[21] Most importantly, we found that true cubic phases could not be manipulated once formed, and the cooling procedure used to overcome this problem in the formulation of mesophases for phase behavior studies is unsuitable for protein-containing mesophases. Therefore, our subsequent efforts on developing X-ray transparent platforms for *in meso* crystallization focused on passive mixing strategies similar to the PLI[6] and CIMP[7] macroscale crystallization protocols (Chapter 1.2.4) and on sample formulation strategies that would not require mesophase routing on-chip.

Initially we attempted to optimize diffusion-based platforms for mesophase formulation based on the standard microfluidic architecture[35,36] with compartments for lipid and aqueous solution fabricated in a fluid layer and connected through channels isolated with normally closed[24,25] or normally open[37-40] valves for metering. These approaches were found suboptimal for a variety of reasons as described in Chapters 5.3.1 and 5.3.2. The design finally used for *in meso* crystallization relied on multi-level sample compartments patterned in the fluid layer and in the substrate and is described in Chapter 5.4.

5.3.1 Microfluidic devices with normally open valves

To maximize the contact area between the lipid and the protein solution chambers and facilitate diffusion between the two materials, we tested a design where a single large chamber in the fluid layer was divided into compartments by actuating normally open valves[24,25] spanning the entire width of the chamber (Figure 5.1). Here we used thick PDMS devices with 25 μm-tall control layer features and 14 μm-tall rounded fluid layer features as prototypes. The PDMS assembly was permanently bonded to a glass slide. The valves were kept closed during the chamber filling step and released for mixing. The mixing tests were carried out with monoolein and solutions of 5-20% βOG in 25 mM NaH_2PO_4. Although some degree of mixing between the two materials could be achieved (Figure 5.1C), we established that the size of the valves made reliable actuation and compartment isolation difficult even when using small chamber heights (14 μm). We decided to not pursue this approach any further, in lieu of the alternative approaches described below.

5.3.2 Microfluidic devices with normally closed valves

Next we tested a design with the lipid and solution compartments connected via multiple channels isolated with normally closed valves[37-40] (Figure 5.2) to avoid positive pressure actuation. As prototypes, we used thick PDMS devices permanently bonded to a glass slide with 25 μm-tall control layer features and 50 μm-tall fluid layer features with vertical walls. The tests were carried out with monoolein and solutions of 10% βOG in 25 mM NaH_2PO_4 or with detergent-free 25 mM NaH_2PO_4. Although the fluid layer compartments could be filled with the respective materials, the mixing step was unsuccessful. Application of vacuum for opening of the

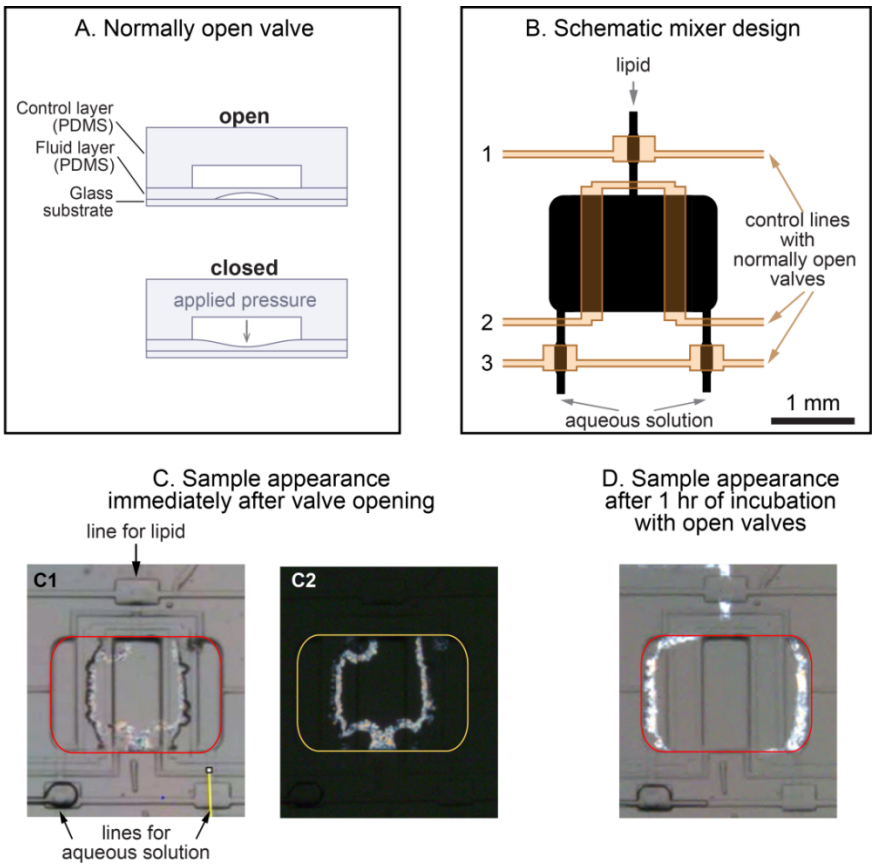

Figure 5.1. (A) Schematic cross-section of a normally open pneumatic valve fabricated in PDMS. Open and closed states are shown. **(B)** Schematic design of a diffusion-based mixer with normally open valves with superimposed control (brown) and fluid (black) layer features and **(C, D)** optical micrographs of the mixing process between monoolein and a solution of 5% βOG in 25 mM NaH_2PO_4, pH 5.5. For clarity, the boundary of the combined sample chamber in optical micrographs is indicated with a red or yellow line. **(B)** During device filling, valve line 2 is actuated to separate the large sample chamber into compartments for lipid (center) and aqueous solution (sides). Valve lines 1 and 3 are open in the filling step, and are closed once filling is complete. The control layer design is simplified to show only the lines used in the sample filling step. **(C)** Partially (C1) and fully (C2) cross-polarized micrographs of the filled device immediately after opening of valve line 2. Formation of the lamellar phase, appearing bright under cross-polarized light, is immediately visible at the original lipid/solution/boundary due to the fast diffusion of water into lipid. **(D)** After 1 hr of incubation time the sample in the central part of the chamber has converted into a non-birefringent phase, whereas the sides of the chamber that initially contained βOG solution remain birefringent. We speculate that the difference in diffusion rates of water and detergent leads to the formation of a water-rich cubic phase (dark) in the central part of the chamber, and a detergent-rich lamellar phase (bright) at edges. Overall, the appearance of the uniformly mixed sample obtained after 1 hour of diffusion is different from the appearance in the lipidic mixer at the identical sample composition (Chapter 3.3.4, Figure 3.3).

mixing valve resulted in withdrawal of water from the fluid layer through the thin PDMS membrane in the valve seat area due to permeability of PDMS. Evaporation of water from the sample was faster than diffusion of water into the mesophase, rendering this approach unsuitable for the formulation of protein-loaded mesophases. This mixing strategy was successfully employed for aqueous solutions in soluble protein crystallization,[21] highlighting the difficulties of applying the methods developed for low-viscosity solutions of small solutes to *in meso*

crystallization.

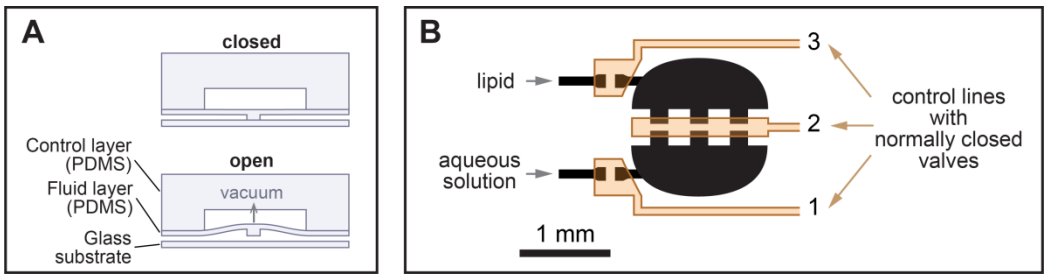

Figure 5.2. (A) Schematic cross-section of a normally closed pneumatic valve fabricated in PDMS. Open and closed states are shown. **(B)** Schematic design of a diffusion-based mixer with normally closed valves with superimposed control (brown) and fluid (black) layer features. Valves 1 and 3 at chamber inlets are open by applying negative pressure (vacuum) to respective control lines and are closed once lipid and aqueous solution fill dedicated chambers. For mixing, valve 2 separating the two fluid layer compartments is opened by applying negative pressure to the line.

5.4 X-ray transparent array chip for *in meso* protein crystallization

The successful strategy developed for *in meso* crystallization on-chip combined the metering and fluid routing capabilities of multilayer PDMS devices with the architecture of the SlipChip[41-43] (Chapter 4). The microfluidic platform described here is under 210 μm in thickness and implements the PLI method[6] described in Chapter 1.2.5: the protein-loaded mesophase is prepared by incubating the protein solution with monoolein for several hours, followed by the addition of precipitant to induce protein crystallization. The platform contains 12 crystallization wells. The amount of monoolein per well was kept constant at 25 nL, whereas the amount of protein solution and precipitant varied between 40-65 and 215-300 nL, respectively, depending on the compartment height of the crystallization layer (Figure 5.4B). Thus, the total amount of material needed was reduced at least 6-fold compared to the macroscopic PLI approach.[6] The device architecture (Figure 5.4-C1) maximizes the contact area between the monoolein and the protein solution for the formulation of the protein-loaded mesophases. The approach outlined below relies on the favorable combination of thermodynamic properties of the lipid and the dynamic properties of lipidic mesophases and eliminates the need for prolonged valve actuation during sample formulation.

5.4.1 Sample formulation strategy

The formulation strategy relied on two distinct fluid-routing assemblies (Figures 5.3 and

5.4), one of which was less than 200 µm thick (Figure 5.4) as required for X-ray transparency.[16,21] The first auxiliary PDMS assembly (Figure 5.3) was used to fill molten monoolein into the respective 25 µm-deep chambers of the COC substrate (Figure 5.3C). Monoolein was then frozen using dry ice and the auxiliary PDMS assembly was removed. Because monoolein is solid at room temperature, the lipid-filled substrates could be easily manipulated in subsequent steps, unlike volatile and mobile aqueous solutions that require special precautions.[44]

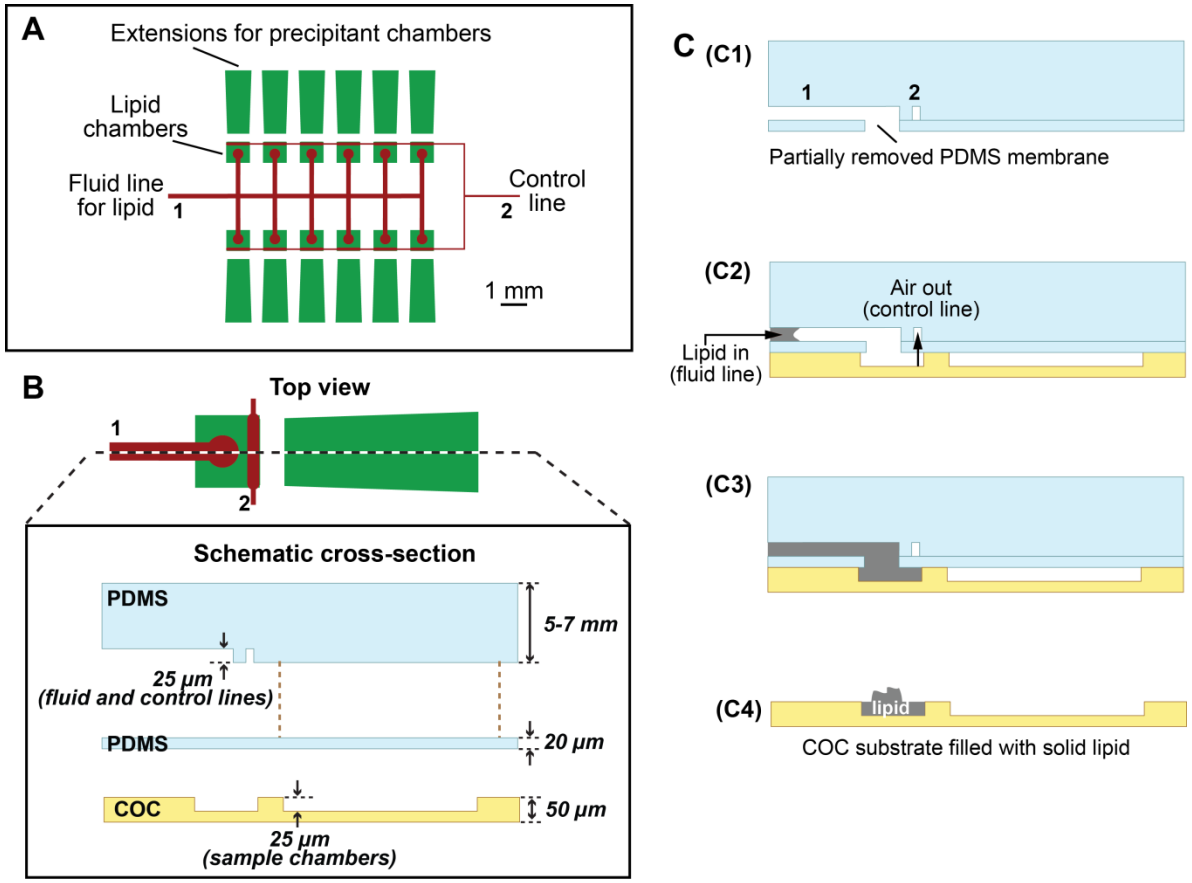

Figure 5.3. Device architecture and the sequence of operations in the lipid filling step. **(A)** Superimposed patterns in the hot-embossed COC substrate (green) and in the auxiliary thick PDMS layer (red) of the 12-well microfluidic platform for *in meso* crystallization. **(B)** A magnified top view of a single well and the cross-section schematic of the PDMS assembly aligned with the patterned COC layer. Features in the top PDMS layer correspond to lines 1 and 2. **(C1-C4)** The sequence of steps for the lipid-filling protocol. (C1) The part of the thin PDMS membrane corresponding to the circular end of line 1 in (A) is removed. (C2) The PDMS layer is placed on the COC substrate and upon application of negative pressure (vacuum) to line 2 air is withdrawn from line 1 due to air permeability of PDMS. This draws molten lipid into the chamber through line 1, (C3) eventually filling the entire chamber. (C4) After filling, the lipid is frozen and remains solid at room temperature. The auxiliary PDMS layer is removed. The lipid-filled COC layer is ready for the crystallization step (Figure 5.4).

The auxiliary PDMS layer for lipid filling contained two sets of channels patterned in the thick PDMS layers and was sealed by bonding a thin PDMS layer to the thick layer (Figure

5.3B). One set was used as a fluidic line and consisted of branched channels that terminated above the patterned chambers in the COC substrate (Figure 5.3A). The thin PDMS membranes were selectively removed at the ends of the channels to form a continuous fluidic path between the inlet port and the chambers patterned in COC (Figure 5.3-C1 and C2). The other set of channels passed over the patterned chambers and was connected to the vacuum source. Although the control line was separated from the chambers with the thin PDMS membrane, a pressure gradient between the chambers and the inlet port of the fluidic line arose due to the air permeability of PDMS, and monoolein was drawn into the chambers through the fluidic line (Figure 5.3-C2). This approach, while slightly sacrificing the accuracy of monoolein metering in the chambers due to lipid protrusions above the chamber height upon removal of the PDMS layer (Figure 5.3-C4), ensured that monoolein only remained in the COC chambers once the PDMS layer was removed as the fluidic lines themselves were sealed from contact with the substrate. Lipid protrusions may be minimized by optimizing the PDMS membrane removal procedure to handle membranes of small lateral dimensions.

In the second step, a hybrid COC/PDMS/PDMS assembly of 135-160 μm in thickness with patterned control and fluid layers was aligned over the 50 μm-thick monoolein-filled COC substrate (Figure 5.4). The normally closed monolithic microvalves of this assembly were used for fluid routing on-chip as usual.[37-40] Protein solution was drawn through a dedicated fluidic line on top of the lipid by applying vacuum to respective control lines, and then incubated for several hours to form the mesophase (Figure 5.4-C2). Strategies for protein solution metering are discussed in Chapter 5.4.2. The geometry of the protein solution/lipid contact is similar to the SlipChip[43] (Chapter 4) and is optimal for passive mixing due to the large contact area between the samples and the small length scale required for diffusion (Figure 5.4-C2). The mesophase formed in the incubation step remained immobile in the compartment due to is viscoelastic properties (Figure 5.4-C3), enabling the valve-less geometry of the combined mesophase/precipitant chamber (the crystallization well). Once the mesophase had formed, a precipitant solution was used to fill the mesophase/precipitant chamber to volume through a dedicated fluidic line (Figure 5.4-C4) and the device was incubated for crystal growth for up to several days.

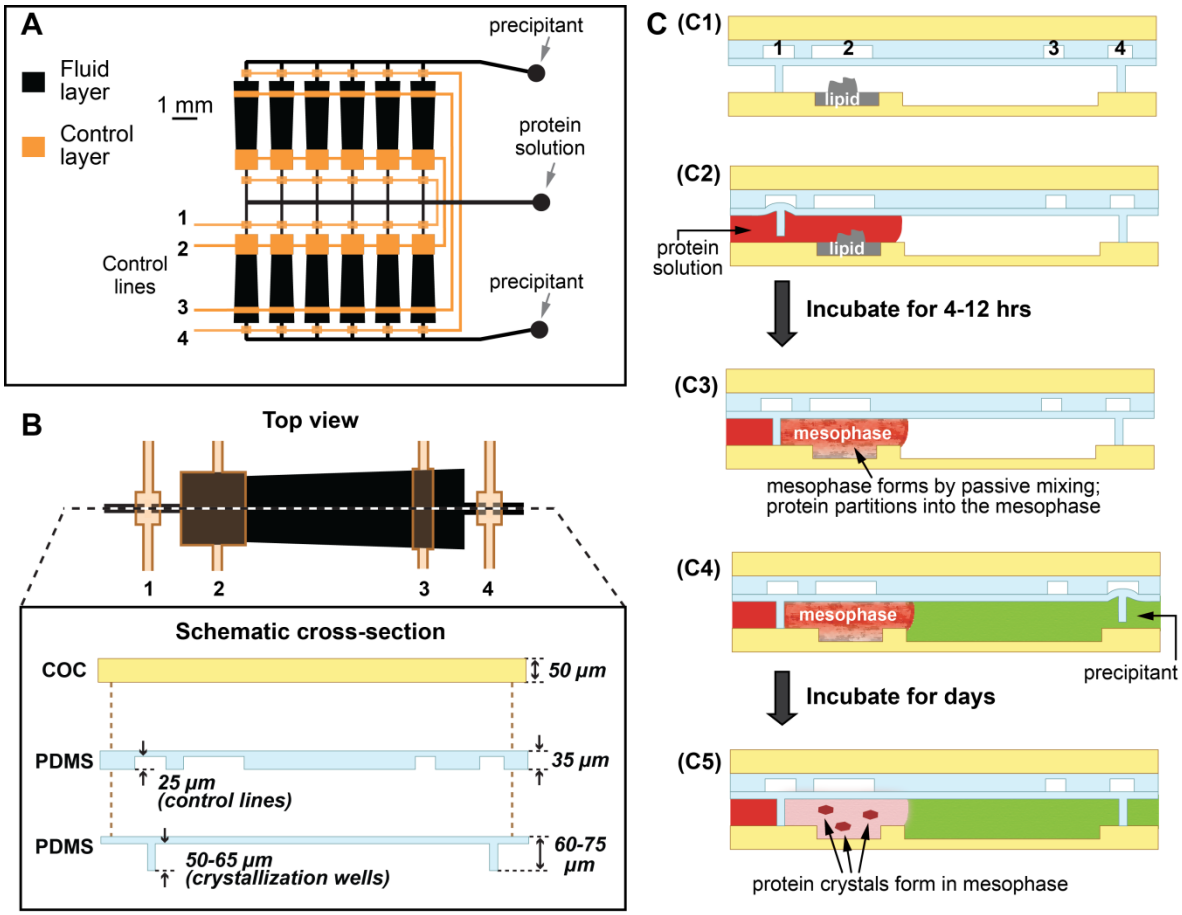

Figure 5.4. Device architecture and the sequence of operations in the protein crystallization step. **(A)** Superimposed patterns of the control (orange) and fluid (black) layer of the 12-well microfluidic platform for *in meso* crystallization. **(B)** A magnified top view of a single crystallization well and the corresponding cross-section of the COC/PDMS/PDMS assembly for fluid routing. **(C1-C5)** The sequence of steps for the protein crystallization protocol. **(C1)** The hybrid COC/PDMS/PDMS assembly is placed on a patterned COC substrate previously filled with the lipid. **(C2)** Protein solution is drawn on top of the lipid through the corresponding fluid line by applying negative pressure (vacuum) to control lines 1 and 2. Line 2 serves to increase the rate of air withdrawal from the chamber. **(C3)** Protein-loaded mesophase forms spontaneously upon incubation.[6,7] **(C4)** Precipitant is filled through the corresponding fluid line by applying negative pressure to lines 3 and 4. Line 3 serves to increase the rate of air withdrawal from the chamber. **(C5)** Protein crystals form in the mesophase after incubation.

5.4.2 Protein metering strategies

The valve-less architecture of the crystallization well is a highly desirable feature as it eliminates prolonged valve actuation that would otherwise be necessary either in the protein solution metering step or during incubation with the precipitant. However, this architecture presents challenges for protein solution metering because the volume of solution is not rigidly defined by the volume of the corresponding chamber, as typical for multilayer PDMS microfluidic devices. Therefore, several strategies and geometries of the protein/mesophase chamber were tested for protein solution metering (Figures 5.5. and 5.6).

One of the approaches to the protein solution metering involved filling of auxiliary metering chambers connected to the crystallization well via a channel isolated with normally closed valves (Figure 5.5A). After metering into the auxiliary chambers, the protein solution was transferred onto the lipid by opening the normally closed valve and briefly actuating the membrane on top of the chambers (Figure 5.5B). Several geometries of the channels connecting the metering chamber with the crystallization well were tested (Figure 5.5A).

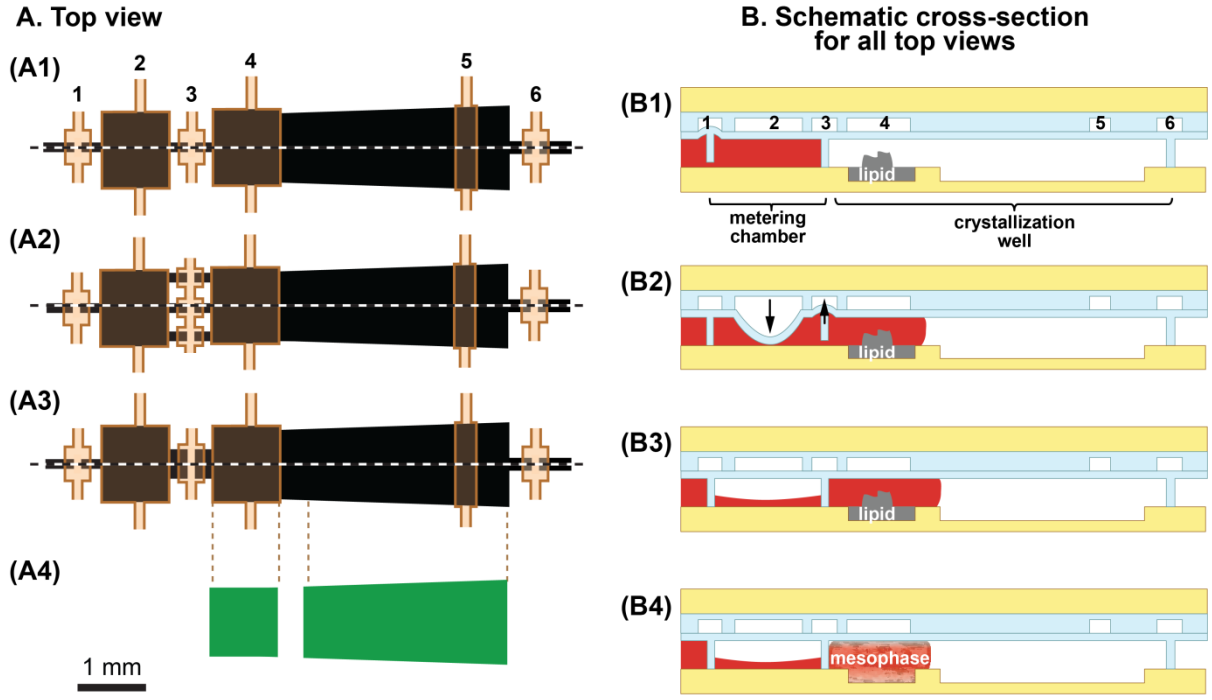

Figure 5.5. Different approaches to protein solution metering with positive/negative pressure actuation. **(A)** Top view of crystallization wells with (A1-3) various types of channel geometries connecting the protein metering chamber and the crystallization well with superimposed patterns of the control (brown) and fluid (black) layers. The compartments patterned in PDMS (brown and black) are shown side-by-side with the (A4) compartments patterned in COC substrate (green), alignment of the patterns is shown with the dotted lines. **(B)** Cross-section of the crystallization wells corresponding to the dashed lines for all geometries in (A). **(B1-B5)** The sequence of steps in the protein metering protocol. **(B1)** Protein solution is drawn into the metering chamber through the corresponding fluid line by applying negative pressure (vacuum) to control lines 1 and 2. Line 2 serves to increase the rate of air withdrawal from the chamber. **(B2)** The solution is transferred into the crystallization well by applying negative pressure to line 3 to open the valve, and positive pressure to line 2 to push the solution out. **(B3)** Positive/negative pressure actuation is stopped and **(B4)** protein loaded-mesophase forms after incubation.

This approach ensured a well-defined protein solution volume in the metering step, but accurate solution transfer from the metering chamber into the crystallization well could not be achieved. A variable amount of solution stayed in the metering chambers after transfer, and back-flow from the crystallization wells into the metering chamber was observed once pressure was released from the membranes on top of the metering chambers. Valve-less metering strategies for the protein solution were also tested. In the crystallization trials of RC on-chip

described below we employed a modified device geometry with valve-less metering (Figure 5.6), achieved by offsetting the position of the hybrid COC/PDMS/PDMS crystallization layer (Figure 5.4) relative to lipid chambers patterned in COC (Figure 5.3). This type of geometry provided a way of sampling various strategies of incorporating the protein solution into the mesophase in a single device and of creating samples with gradients of protein concentrations within the mesophase for testing a wider area of the crystallization phase space.

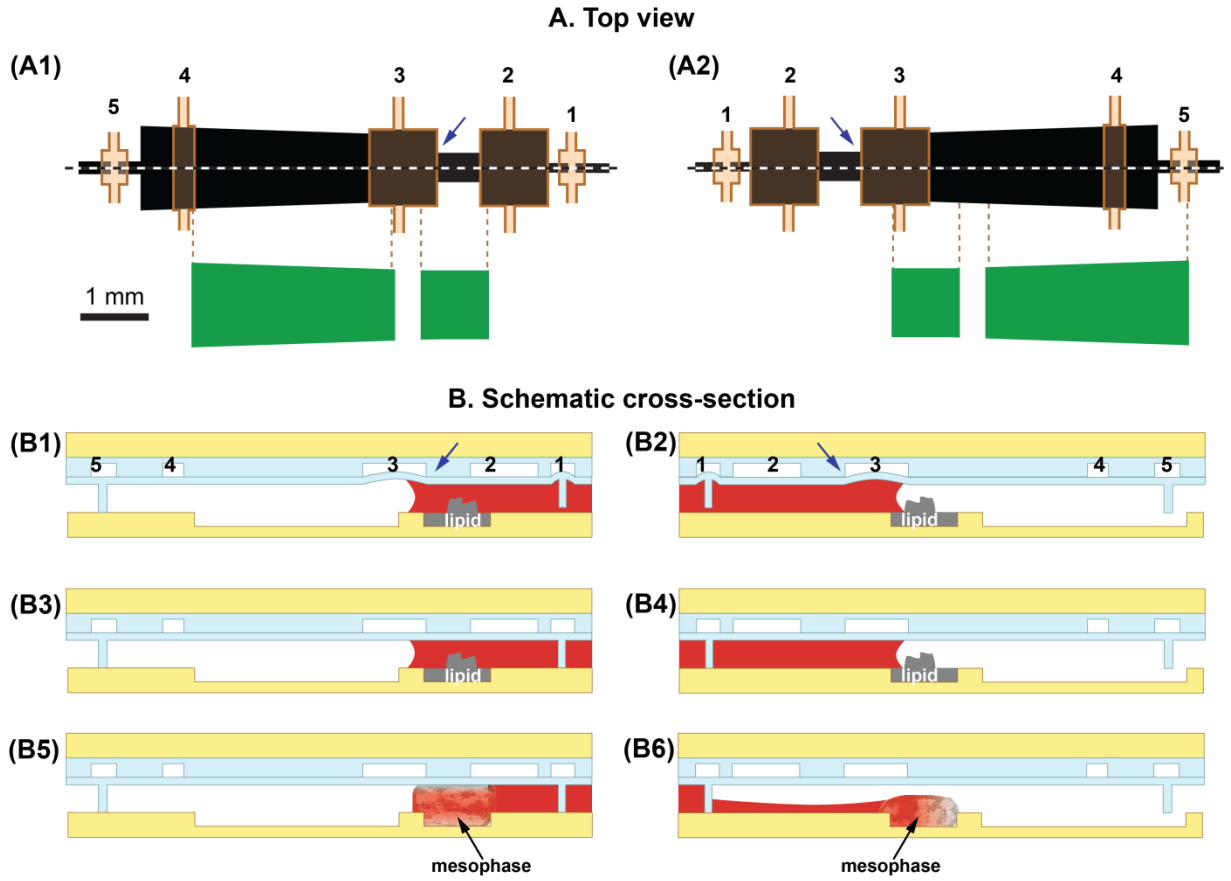

Figure 5.6. Valve-less protein solution metering for mesophase formulation with offset crystallization layers and COC substrates. **(A1, A2)** Top view of crystallization wells in the two 6-well rows of a single 12-well device with superimposed patterns of the control (orange) and fluid (black) layers. The compartments patterned in PDMS (brown and black) are shown side-by-side with the (A4) compartments patterned in COC substrate (green), alignment of the patterns is shown with brown dotted lines. The COC/PDMS/PDMS layer is offset relative to the lipid-filled COC substrate to achieve different configurations of the wells on the two sides of the device. Control layer features with identical numbers belong to the same control line and operate simultaneously. Arrows indicate channel expansion points that acts as capillary valves for advancing protein solution. **(B)** Cross-section of the crystallization wells corresponding to the dashed lines in (A). **(B1-B6)** The sequence of steps for protein metering. The steps take place simultaneously on both sides of the device. **(B1, B2**) Protein solution is drawn into the metering chamber through the corresponding fluid line by applying negative pressure (vacuum) to control lines 1 and 2. Line 2 serves to increase the rate of air withdrawal from the chamber and draw the protein solution past the channel expansion area that serves as a capillary valve (indicated with arrows). **(B3, B4)** After drawing a desired volume of the protein solution into crystallization wells **(B5, B6)** protein loaded-mesophase forms after incubation.

Work is currently in progress to further optimize protein solution metering strategies to

improve consistency of protein solution metering by incorporating capillary valves of different geometries[45] in the device.

5.4.3 Results: crystallization of photosynthetic reaction center on-chip and in well plates

All protein solution metering strategies produced crystals on-chip after the incubation and precipitant addition step with a variety of protein and precipitant concentrations and incubation times allowed for mesophase formation. Figure 5.7 shows samples at different stages of the crystallization protocol. Examples of crystals grown on-chip are shown in Figure 5.8.

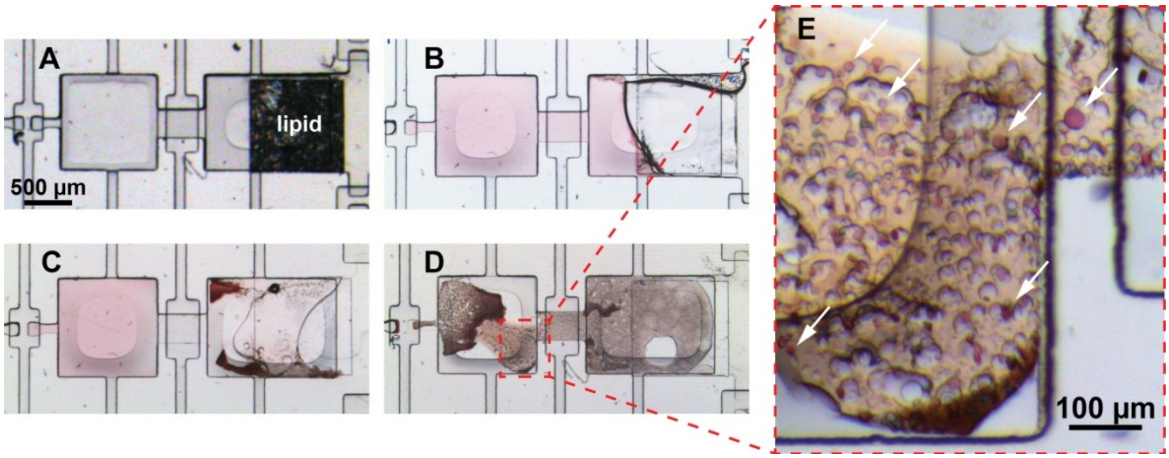

Figure 5.7. Appearance of crystallization wells at different stages of the crystallization protocol. The design shown corresponds to panel A2 in Figure 5.6. A view of a crystallization well with: **(A)** dry monoolein prior to filling the protein solution in the chambers; **(B)** the protein solution prior to incubation to form **(C)** protein-loaded mesophase after 12 hrs of incubation; **(D)** protein crystals in the mesophase after 2 days of incubation with **(E)** the inset showing a magnified view of the section containing crystals. Some of the protein crystals are indicated with white arrows. The mesophase converts into a fluid sponge phase[35,46,47] and is pushed away from the original location of monoolein. Crystallization conditions: RC, 10 mg/mL in 10mM Tris pH 7.8, 280 mM NaCl, 0.05% LDAO; precipitant: 1.15 M $(NH_4)_2SO_4$, 14% Jeffamine, 1 M HEPES, pH 7.5.

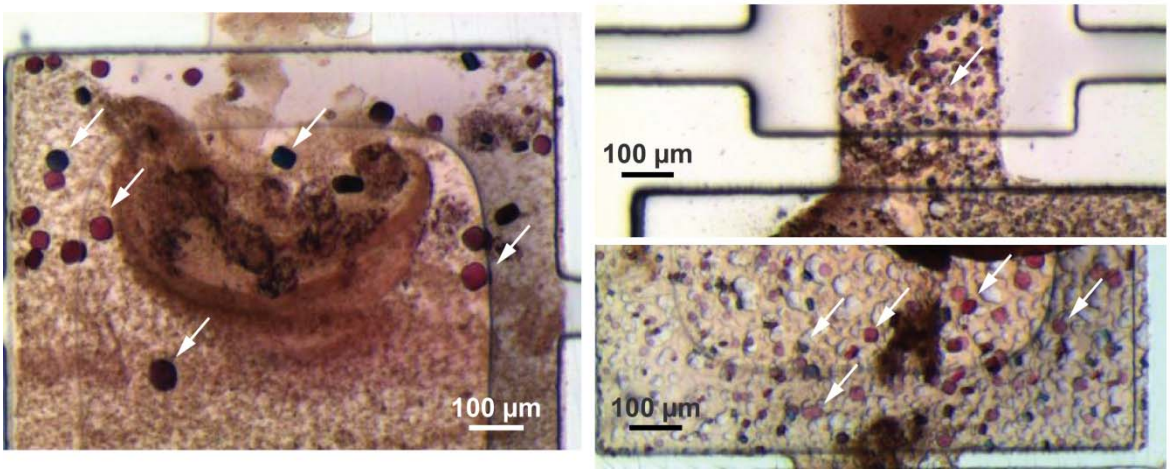

Figure 5.8. Examples of crystals of RC grown on-chip. Some of the crystals are indicated with white arrows. Crystallization conditions: RC, 10-24 mg/mL in 10mM Tris pH 7.8, 280 mM NaCl, 0.05% LDAO; precipitant: 1.15 M $(NH_4)_2SO_4$, 14% Jeffamine, 1 M HEPES, pH 7.5.

A systematic study of RC crystallization on-chip was carried out to investigate the effects of the (i) incubation time for mesophase formulation (4, 8, and 12 hrs) and (ii) the protein concentration in solution (10, 15, 20, and 24 mg/mL). Two 12-well crystallization devices were set up for each combination of parameters. A single precipitant formulation that produced best results in prior wellplate trials was used (1M HEPES, 1.15 M $(NH_4)_2SO_4$, pH 7.5, 14% w/v Jeffamine M-600). All chips were set up using valve-less metering with offset crystallization / lipid layers (Figure 5.6). For comparison, well-plate trials were also set up at the same time using the same batches of the protein solutions with incubation times identical to on-chip samples (4, 8, and 12 hrs) for protein solutions with the concentrations of 15 and 24 mg/mL (4 wells per each incubation time/concentration combination). While many on-chip crystallization trials produced small crystals or showers of crystals with little dependence on the incubation time or protein concentration, a single device (12 hr incubation, RC 24 mg/mL) produced large, well-separated crystals in several wells that were used for crystal X-ray diffraction data collection. Similar results were obtained with crystallization trials in well plates, where well-separated crystals or showers of crystals formed in different wells set up for the same condition.

Overall, these results suggest lack of reproducibility in the protein incorporation into the mesophase in the first incubation step both on-chip and off-chip. Efforts are underway to optimize the design of crystallization wells on-chip to improve consistency of protein incorporation into the mesophase. Here microfluidic chips provide an advantage over well plates, where precise control of mass transport may not be possible.

5.4.4 Results: crystal X-ray diffraction and protein structure solution

On-chip crystal X-ray diffraction data were collected on-chip at room temperature at beamlines 21-ID-F and 21-ID-D, of LS-CAT, Advanced Photon Source, Argonne National Lab. The microfluidic chips were fully compatible with existing beamline infrastructure and could be mounted directly on the goniometer using the standard magnetic base (Figure 5.9A). An XY-positioner was used to move the chip in the X-ray beam to target different crystals within the chip, and exact beam position was monitored in an on-axis video microscope (Figure 5.9B). Compared to the standard cryogenic technique, the advantage of room-temperature data collection is a potentially higher quality of some metrics of diffraction data (for example, mosaicity), and the lack of ice formation on the protein crystals during data collection, which

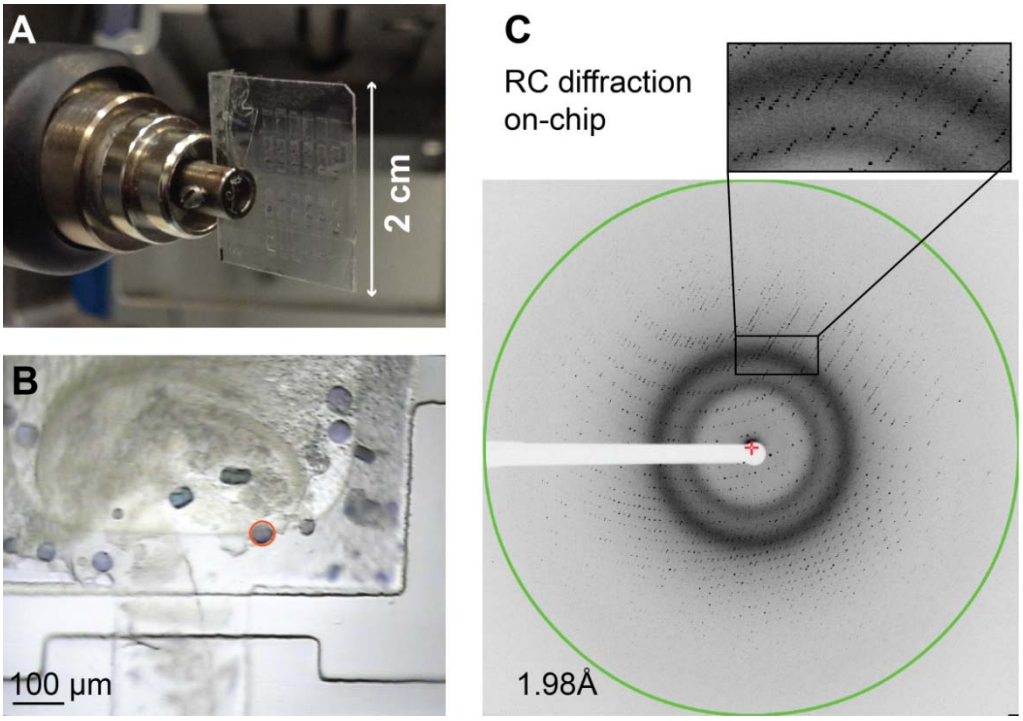

Figure 5.9. (A) The 12-well chip mounted on the goniometer for crystal X-ray diffraction data collection at beamline 21-ID-F. **(B)** Section of a crystallization well as with several crystals of RC as seen in the on-axis video microscope during data collection. The red circle represents the footprint and the location of the X-ray beam. **(C)** A diffraction pattern of an RC crystal grown and analyzed on-chip. The green ring indicates the resolution of 1.98 Å. The inset shows the clearly resolved diffraction spots from the crystal on top of the background noise (dark rings) coming from the chip materials.

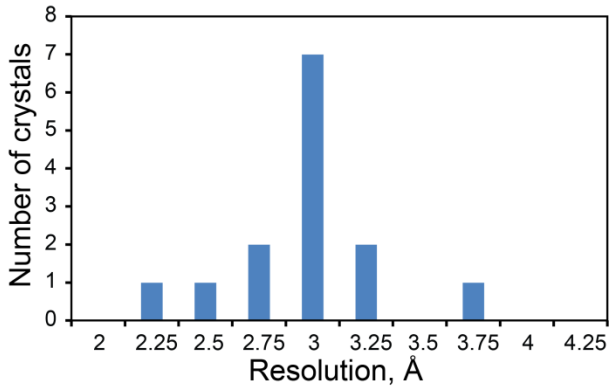

Figure 5.10. Distribution of resolution of partial crystal X-ray diffraction datasets for RC crystals grown and analyzed on-chip and used for structure solution (Table 5.1).

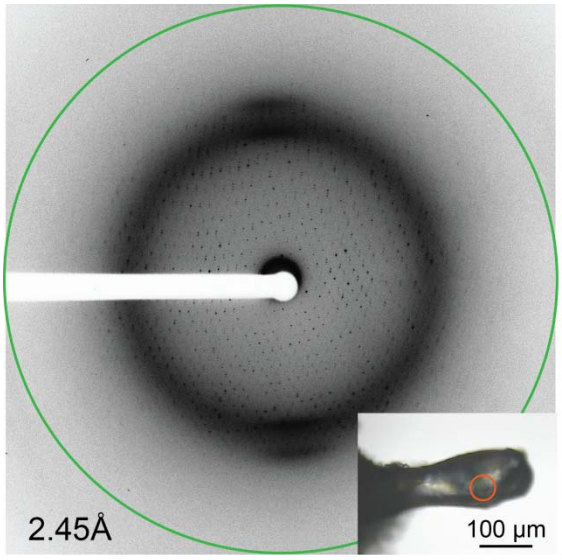

Figure 5.11. A diffraction pattern of an RC crystal grown in a well plate, mounted in a crystal loop and analyzed under cryogenic conditions. The green ring indicates the resolution of 2.45 Å. The inset shows the mounted crystal as seen in the on-axis video microscope during data collection. The protein crystal is poorly visible in the mesophase and is within the red circle representing the footprint and the location of the X-ray beam.

contributes to the diffraction pattern and compromises resolution.[48] However, because of radiation damage only an incomplete data set can be obtained from each crystal at room temperature. To overcome this problem, we used the previously established strategy of collecting small wedges of diffraction data from a number of crystals and then merging the datasets.[21,34] This approach is relatively straightforward in the on-chip data collection because multiple crystals can be grown and analyzed in a single chip and the cumbersome manual harvesting is not required for each crystal. Furthermore, locating the crystals in the chip during data collection is often easier than in standard loop mounts (Figures 5.9B and inset in Figure 5.11) due to the favorable optical properties of the chips.

RC crystals grown on-chip diffracted to 1.98 Å (Figure 5.9C), which is a significant improvement compared to the previously reported diffraction limit of 2.5 Å reported for crystals of the same protein in a plug-based microfluidic system.[23] Using the data collection strategy outlined above, we were able to obtain a complete dataset for RC crystals on-chip and solve the structure at the resolution of 3.33 Å (Table 5.1) using data from 14 best-diffracting crystals out of the 54 crystals that were probed. Space group type and lattice parameters were in agreement with previously published data for RC.[27,47] Although the background scatter from device materials was clearly visible in the diffractograms as diffuse rings in the *d*-spacing ranges of 4.7-5.7 and 6.9-8.7 Å (Figure 5.9C), it did not interfere with indexing of X-ray diffraction data. Figure 5.10 shows the distribution of resolution limits of diffraction data for on-chip crystals used for the final dataset as assessed visually from the X-ray diffraction data. The majority of crystals diffracted to ~3 Å, slightly better the final resolution of the structure. The resolution deteriorated consistently with each frame collected for a given crystal.

Contrary to the findings for soluble protein structure determination,[34] we were able to obtain higher-resolution data on-chip than for crystals grown and analyzed following the traditional cryogenic data collection protocol (Table 5.1). Nine RC crystals grown in well-plates were harvested, flash-frozen, and analyzed under cryogenic conditions. Although a complete dataset could be obtained from a single crystal, the crystals only diffracted to 3.3-3.8 Å and produced a structure with the resolution of 3.93 Å. These results are in agreement with the 3.6 Å resolution of diffraction data reported for the RC crystals grown previously in well plates using the PLI approach with dry monoolein.[6] Additionally, background scattering similar in the intensity to that seen from the chip materials was observed in the 3.6-4.9Å range of *d*-spacings

(Figure 5.11), which may be attributed amorphous ice, a vitrified monoolein- or Jeffamine-containing phase, or noise from the nylon loop. Data collected both on-chip and off-chip were of poorer quality than the highest-resolution structure of RC reported so far (solved to 2.2 Å).[47]

Table 5.1 Summary of crystallographic data for RC crystals grown and analyzed on-chip and in the traditional cryogenic data collection for crystals grown in well-plates.

Parameter	**On-chip**	**Traditional (cryogenic)**
	Crystal quality	
# of crystals probed	54	9
# of indexable crystals	22	5
# of crystals used for structure solution	14	1
# of frames for structure solution	85	120
	Crystallographic data[a,b]	
Space group	$P4_22_12$	$P4_22_12$
Unit cell dimensions	*a, b* =102.5 Å, *c* = 240.1 Å	*a, b* =100 Å, *c* = 232.8 Å
Resolution	**24 - 3.33 Å**	**24 - 3.93 Å**
R_{sym}	0.5	0.5
Mosaicity	**0.16°**	**1.2°**
Redundancy	3	4.5
Completeness	98%	99.9%
I/σ	2	2
	Refinement	
R (R_{free})	0.2237 (0.2988)	0.2817 (0.3672)
	Ramachandran statistics[c]	
Most favored	91.9%	83.8%
Allowed	6.4%	12.0%
Disallowed	1.7%	4.3%

[a] On-chip structure solution: merging of small datasets from "multiple crystals" analyzed on-chip within a 24-well device at room temperature. [b]The "traditional" sample was grown using the PLI technique[6] in a well plate and mounted using a standard crystal mount for cryogenic data collection. [c]Ramachandran statistics is reported without manual optimization. Reported values are for all hkls. R-factor = $\Sigma(|F_{obs}|-k|F_{calc}|)/\Sigma|F_{obs}|$ and R_{free} is the R value for a test set of reflections consisting of a random 5% of the diffraction data not used in refinement.[49] $R_{sym} = \Sigma|I_i - \langle I_i \rangle| / \Sigma I_i$ where I_i = intensity of the i^{th} reflection and $\langle I_i \rangle$ = mean intensity.

Anecdotal evidence suggests that several hundred crystals may be probed in order to find one that diffracts to high resolution, and the limited number of crystals tested here does not allow for rigorous statistical analysis. However, the quality of X-ray diffraction data for all crystals mounted in loops as assessed visually was relatively poor, with diffuse diffraction spots and significant background noise, although a larger fraction of well-plate crystals (~55%) produced

indexable diffraction data than in on-chip crystals (~40%). We speculate that the quality of the well-plate crystals may have been compromised due to manual harvesting and flash-freezing, highlighting the crucial nature of those steps and further suggesting that strategies that obviate those steps may provide a pathway to higher-resolution structure data for membrane proteins.

5.5 Conclusions

To our knowledge, the microfluidic chip described in this chapter the first example of an X-ray transparent microfluidic platform for *in meso* crystallization of membrane proteins. Successful crystallization of a membrane protein photosynthetic reaction center (R. Sphaeroides) followed by resolving its structure at a resolution of 3Å using crystal X-ray diffraction on-chip validates our approach.

The 12-well crystallization platform developed here reduces the amount of material for trial formulation at least 7-fold compared to comparable methods of protein crystallization in well plates. The X-ray transparency of the platform obviates the manual crystal harvesting and freezing steps that often compromise the quality of crystals and thus the resolution of diffraction data. The X-ray transparent platform can be used for *in situ* crystal X-ray data collection without additional modifications to beamline infrastructure. Furthermore, it can be easily used to test different lipids as crystallization matrices. These features make it a highly valuable tool for the crystallization of scarcely available membrane proteins that typically form only small fragile crystals.

The chip automates metering required for sample formulation and only requires a vacuum pump for the operation, in contrast to expensive and complex crystallization robots. Because the architecture of the chip is optimized for passive mixing between protein solution and solid lipid for the formulation of protein-loaded mesophases, the chip can be easily pre-filled with the lipid before supplying it to biochemists for protein crystallization. Elimination of lipid handling, which is perceived as difficult by the users, may facilitate the wider penetration of the method in the structural biology community.

5.6 References

1 H. M. Berman, J. Westbrook, Z. Feng, G. Gilliland, T. N. Bhat, H. Weissig, I. N. Shindyalov and P. E. Bourne. The protein data bank. *Nucleic Acids Res.*, 2000, **28**, 235-242. http://www.pdb.org.

2 J. R. Luft, G. T. DeTitta, R. M. Nagel and E. H. Snell, presented in part at the 14 Intl. Conference on the Crystallization of Biological Macromolecules, September 23-28, Huntsville, AL, 2012.

3 M. Caffrey and V. Cherezov. Crystallizing membrane proteins using lipidic mesophases. *Nat. Protocols*, 2009, **4**, 706-731.

4 V. Cherezov, E. Abola and R. C. Stevens. Recent progress in the structure determination of GPCRs, a membrane protein family with high potential as pharmaceutical targets. *Methods Mol. Biol.*, 2010, **654**, 141-168.

5 V. Katritch, V. Cherezov and R. C. Stevens. Diversity and modularity of G protein-coupled receptor structures. *Trends in Pharmacological Sciences*, 2012, **33**, 17-27.

6 E. Wallace, D. Dranow, P. D. Laible, J. Christensen and P. Nollert. Monoolein lipid phases as incorporation and enrichment materials for membrane protein crystallization. *PLoS ONE*, 2011, **6**, e24488.

7 J. Kubicek, R. Schlesinger, C. Baeken, G. Büldt, F. Schäfer and J. Labahn. Controlled *in meso* phase crystallization – a method for the structural investigation of membrane proteins. *PLoS ONE*, 2012, **7**, e35458.

8 V. Cherezov. Lipidic cubic phase technologies for membrane protein structural studies. *Curr. Opin. Struct. Biol.*, 2011, **21**, 559-566.

9 V. Cherezov, A. Peddi, L. Muthusubramaniam, Y. F. Zheng and M. Caffrey. A robotic system for crystallizing membrane and soluble proteins in lipidic mesophases. *Acta Crystallogr. D*, 2004, **60**, 1795-1807.

10 L. Li and R. F. Ismagilov. Protein crystallization using microfluidic technologies based on valves, droplets, and SlipChip. *Annu. Rev. Biophys.*, 2010, **39**, 139-158.

11 G. Kisselman, W. Qiu, V. Romanov, C. M. Thompson, R. Lam, K. P. Battaile, E. F. Pai and N. Y. Chirgadze. X-chip: An integrated platform for high-throughput protein crystallization and on-the-chip X-ray diffraction data collection. *Acta Crystallogr. D*, 2011, **67**, 533-539.

12 B. Zheng, J. D. Tice, L. S. Roach and R. F. Ismagilov. A droplet-based, composite PDMS/glass capillary microfluidic system for evaluating protein crystallization conditions by microbatch and vapor-diffusion methods with on-chip X-ray diffraction. *Angew. Chem. Int. Ed.*, 2004, **43**, 2508-2511.

13 C. J. Gerdts, M. Elliott, S. Lovell, M. B. Mixon, A. J. Napuli, B. L. Staker, P. Nollert and L. Stewart. The plug-based nanovolume microcapillary protein crystallization system (mpcs). *Acta Crystallogr. D*, 2008, **64**, 1116-1122.

14 C. P. Steinert, J. Mueller-Dieckmann, M. Weiss, M. Roessle, R. Zengerle and P. Koltay, Miniaturized and highly parallel protein crystallization on a microfluidic disc, 20th IEEE Intl. Conf. on Micro Electro Mechanical Systems (MEMS 2007), Hyogo, Japan, 2007.

15 J. D. Ng, P. J. Clark, R. C. Stevens and P. Kuhn. *In situ* X-ray analysis of protein crystals in low-birefringent and X-ray transmissive plastic microchannels. *Acta Crystallogr. D*, 2008, **64**, 189-197.

16 K. Dhouib, C. Khan Malek, W. Pfleging, B. Gauthier-Manuel, R. Duffait, G. Thuillier, R.

Ferrigno, L. Jacquamet, J. Ohana, J.-L. Ferrer, A. Theobald-Dietrich, R. Giege, B. Lorber and C. Sauter. Microfluidic chips for the crystallization of biomacromolecules by counter-diffusion and on-chip crystal X-ray analysis. *Lab Chip*, 2009, **9**, 1412-1421.

17 C. L. Hansen, S. Classen, J. M. Berger and S. R. Quake. A microfluidic device for kinetic optimization of protein crystallization and in situ structure determination. *J. Am. Chem. Soc.*, 2006, **128**, 3142-3143.

18 C. Sauter, K. Dhouib and B. Lorber. From macrofluidics to microfluidics for the crystallization of biological macromolecules. *Cryst. Growth Design*, 2007, **7**, 2247-2250.

19 E. D. Greaves and A. Manz. Toward on-chip X-ray analysis. *Lab Chip*, 2005, **5**, 382-391.

20 R. Barrett, M. Faucon, J. Lopez, G. Cristobal, F. Destremaut, A. Dodge, P. Guillot, P. Laval, C. Masselon and J.-B. Salmon. X-ray microfocussing combined with microfluidics for on-chip X-ray scattering measurements. *Lab Chip*, 2006, **6**, 494-499.

21 S. Guha, S. L. Perry, A. S. Pawate and P. J. A. Kenis. Fabrication of X-ray compatible microfluidic platforms for protein crystallization. *Sensors Actuators B*, 2012, **174**, 1-9.

22 S. L. Perry, G. W. Roberts, J. D. Tice, R. B. Gennis and P. J. A. Kenis. Microfluidic generation of lipidic mesophases for membrane protein crystallization. *Cryst. Growth Design*, 2009, **9**, 2566-2569.

23 L. Li, Q. Fu, C. Kors, L. Stewart, P. Nollert, P. Laible and R. Ismagilov. A plug-based microfluidic system for dispensing lipidic cubic phase (LCP) material validated by crystallizing membrane proteins in lipidic mesophases. *Microfluidics Nanofluidics*, 2010, **8**, 789-798.

24 M. A. Unger, H.-P. Chou, T. Thorsen, A. Scherer and S. R. Quake. Monolithic microfabricated valves and pumps by multilayer soft lithography. *Science*, 2000, **288**, 113-116.

25 Y. Xia and G. M. Whitesides. Soft lithography. *Angew. Chem. Int. Ed.*, 1998, **37**, 550-575.

26 D. C. Duffy, J. C. McDonald, O. J. A. Schueller and G. M. Whitesides. Rapid prototyping of microfluidic systems in poly(dimethylsiloxane). *Anal. Chem.*, 1998, **70**, 4974-4984.

27 G. Katona, U. Andréasson, E. M. Landau, L.-E. Andréasson and R. Neutze. Lipidic cubic phase crystal structure of the photosynthetic reaction centre from rhodobacter sphaeroides at 2.35 Å resolution. *J. Mol. Biol.*, 2003, **331**, 681-692.

28 Z. Otwinowski and W. Minor, in *Methods in enzymology*, ed. Charles W. Carter, Jr., Academic Press, 1997, vol. Volume 276, pp. 307-326.

29 P. D. Adams, P. V. Afonine, G. Bunkoczi, V. B. Chen, I. W. Davis, N. Echols, J. J. Headd, L.-W. Hung, G. J. Kapral, R. W. Grosse-Kunstleve, A. J. McCoy, N. W. Moriarty, R. Oeffner, R. J. Read, D. C. Richardson, J. S. Richardson, T. C. Terwilliger and P. H. Zwart. Phenix: A comprehensive python-based system for macromolecular structure solution. *Acta Crystallogr. D*, 2010, **66**, 213-221.

30 P. Evans and A. McCoy. An introduction to molecular replacement. *Acta Crystallogr. D*, 2008, **64**, 1-10.

31 J. Koepke, E.-M. Krammer, A. R. Klingen, P. Sebban, G. M. Ullmann and G. Fritzsch. pH modulates the quinone position in the photosynthetic reaction center from *Rhodobacter Sphaeroides* in the neutral and charge separated states. *J. Mol. Biol.*, 2007, **371**, 396-409.

32 P. Emsley and K. Cowtan. *Coot*: Model-building tools for molecular graphics. *Acta*

Crystallogr. D, 2004, **60**, 2126-2132.
33 E. P. Kartalov, A. Scherer, S. R. Quake, C. R. Taylor and W. F. Anderson. Experimentally validated quantitative linear model for the device physics of elastomeric microfluidic valves. *J. Appl. Phys.*, 2007, **101**, 064505.
34 S. L. Perry, S. Guha, A. S. Pawate, V. Agarwal, S. N. Nair and P. J. A. Kenis. Microfluidic array chips for *de novo* protein structure determination at room temperature. *submitted*, 2012.
35 V. Cherezov, J. Clogston, M. Z. Papiz and M. Caffrey. Room to move: Crystallizing membrane proteins in swollen lipidic mesophases. *J. Mol. Biol.*, 2006, **357**, 1605-1618.
36 M. R. Thorson, S. Goyal, Y. Gong, G. G. Z. Zhang and P. J. A. Kenis. Microfluidic approach to polymorph screening through antisolvent crystallization. *CrystEngComm*, 2012, **14**, 2404-2412.
37 K. Hosokawa and R. Maeda. A pneumatically-actuated three-way microvalve fabricated with polydimethylsiloxane using the membrane transfer technique. *J. Micromech. Microeng.*, 2000, **10**, 415.
38 G. A. Cooksey, C. G. Sip and A. Folch. A multi-purpose microfluidic perfusion system with combinatorial choice of inputs, mixtures, gradient patterns, and flow rates. *Lab Chip*, 2009, **9**, 417-426.
39 B. R. Schudel, M. Tanyeri, A. Mukherjee, C. M. Schroeder and P. J. A. Kenis. Multiplexed detection of nucleic acids in a combinatorial screening chip. *Lab Chip*, 2011, **11**, 1916-1923.
40 R. Mohan, B. R. Schudel, A. V. Desai, J. D. Yearsley, C. A. Apblett and P. J. A. Kenis. Design considerations for elastomeric normally closed microfluidic valves. *Sensors Actuators B*, 2011, **160**, 1216-1223.
41 W. Du, L. Li, K. P. Nichols and R. F. Ismagilov. SlipChip. *Lab Chip*, 2009, **9**, 2286-2292.
42 L. Li, W. Du and R. F. Ismagilov. Multiparameter screening on SlipChip used for nanoliter protein crystallization combining free interface diffusion and microbatch methods. *J. Am. Chem. Soc.*, 2009, **132**, 112-119.
43 L. Li, W. Du and R. Ismagilov. User-loaded SlipChip for equipment-free multiplexed nanoliter-scale experiments. *J. Am. Chem. Soc.*, 2009, **132**, 106-111.
44 X. Zhou, L. Lau, W. W. L. Lam, S. W. N. Au and B. Zheng. Nanoliter dispensing method by degassed poly(dimethylsiloxane) microchannels and its application in protein crystallization. *Anal. Chem.*, 2007, **79**, 4924-4930.
45 J. Moore, A. McCuiston, I. Mittendorf, R. Ottway and R. Johnson. Behavior of capillary valves in centrifugal microfluidic devices prepared by three-dimensional printing. *Microfluidics Nanofluidics*, 2011, **10**, 877-888.
46 A. B. Wohri, L. C. Johansson, P. Wadsten-Hindrichsen, W. Y. Wahlgren, G. Fischer, R. Horsefield, G. Katona, M. Nyblom, F. Oberg, G. Young, R. J. Cogdell, N. J. Fraser, S. Engstrom and R. Neutze. A lipidic-sponge phase screen for membrane protein crystallization. *Structure*, 2008, **16**, 1003-1009.
47 P. Wadsten, A. B. Wöhri, A. Snijder, G. Katona, A. T. Gardiner, R. J. Cogdell, R. Neutze and S. Engström. Lipidic sponge phase crystallization of membrane proteins. *J. Mol. Biol.*, 2006, **364**, 44-53.
48 M. S. Chapman and T. Somasundaram. De-icing: Recovery of diffraction intensities in the presence of ice rings. *Acta Crystallogr. D*, 2010, **66**, 741-744.

49 A. T. Brunger. Free R value: A novel statistical quantity for assessing the accuracy of crystal structures. *Nature*, 1992, **355**, 472-475.

Appendix A.

Small-angle X-ray scattering analysis of lipidic mesophases

The microstructure of lipidic mesophases is deduced from diffraction patterns obtained in small-angle X-ray scattering (SAXS) experiments. In direct analogy with atomic, ionic, or small-molecule crystals, the ordered arrangement of bilayers is characterized by the lattice type and the lattice parameter, *i.e.,* the dimensions of the smallest repeating unit. Mesophases produce diffraction patterns similar to those of powder crystalline samples, and their analysis relies on well-established crystallographic principles. Below the important aspects of crystallography relevant for SAXS analysis of the microstructure of lipidic mesophases are outlined. Detailed information on principles of crystal X-ray diffraction analysis, concepts used in the description of crystal symmetry and diffraction patterns (for example, *hkl* planes and Miller indices), and on types of crystal structures can be found in standard texts on X-ray crystallography.[1]

Raw diffraction patterns of lipidic mesophases consist of sets of concentric rings, similar to those of powdered crystalline samples. Diffractograms of various types of lipidic mesophases are shown at the end of this section (Figures A1-A5). The small-angle range arises due to the values of lattice parameters of lipidic mesophases that typically lie in the range of 40-200 Å, significantly larger than those of atomic, ionic or small-molecule crystals. Large lattice parameters result in small scattering angles because of the inverse relationship between the two as postulated by Bragg's law:[1]

$$\lambda = 2d_{hkl} \sin \theta_{hkl} \qquad \text{Equation A1}$$

where λ is the wavelength of the incident X-ray beam, d_{hkl} is the lattice spacing of a family of periodically spaced crystal planes with Miller indices h, k, and l, and θ_{hkl} is the scattering angle corresponding to this family of planes. The values of d_{hkl} are related to lattice parameters, as described below for relevant types of phases.

Integration of diffraction patterns produces plots of intensity I vs. scattering angle 2θ with a series of peaks. (Care must be taken when processing data as the original SAXS patterns produce plots of I vs. 2θ, rather than I vs. θ, which must be taken into account in subsequent calculations based on Equation A1.) Each peak in the diffractogram corresponds to a family of periodically spaced *hkl* crystal planes. The symmetry of the unit cell determines the combinations of values of h, k, and l for reflections with non-zero intensities, and these

combinations have been summarized for all possible crystallographic unit cells in reference sources.[2] For uniform representation of data obtained at different X-ray wavelengths, intensity may be plotted as a function of scattering vector q related to the scattering angle θ as

$$q = \frac{4\pi \sin\theta}{\lambda} \qquad \text{Equation A2.}$$

Depending on the shape of the unit cell, up to three length parameters and three angles may be required for its description. The unit cells of cubic mesophases belong to cubic symmetry and require a single parameter (cell edge length) to fully characterize the unit cell. Hexagonal and lamellar mesophases differ from small molecule crystals because they are only periodic in one (lamellar) or two (hexagonal) dimensions. Conveniently, each of these phases can also be described with a single parameter, which is easily obtained from SAXS data.

Below we describe phase assignment and lattice parameter calculation procedures for each type of mesophases. All procedures relied on the conversion of the positions of peaks (reflections) observed in the diffractogram into corresponding *d*-spacings via Bragg's law (Equation A1), followed by the calculation of ratios between inverse *d*-spacings, *i.e.*, d^{-1}, to establish the mesophase type. Lattice parameters were calculated based on the *d*-spacing corresponding to the highest-intensity reflection of a given mesophase type as indicated in respective subsections.

Lamellar phases. The lamellar $L\alpha$ phase is comprised of stacks of flat lipid bilayers separated with layers of water (Chapter 1, Figure 1.10). This phase has a single periodic repeat distance, that between midplanes of bilayers, and possible *hkl* indices of *h00*. In diffractograms it appears as a set of rings with the ratio of inverse *d*-spacings 1:2:3:etc. (Figure A1). The highest-intensity reflection of the $L\alpha$ phase is *100*, and the lattice parameter of a lamellar phase reported in Chapters 2-4 is simply

$$a_{L\alpha} = d_{100} \qquad \text{Equation A3}$$

which is obtained directly from SAXS data via Bragg's law (Equation A1).

Hexagonal phases. The inverse hexagonal lipidic mesophase (H_{II}) consists of infinitely long cylindrical inverse micelles packed on a hexagonal lattice (Chapter 1, Figure 1.10). This arrangement can be thought of as the P6 phase (space group 168) with one of the dimensions of the unit cell being infinitely long. Because of symmetry, a single parameter corresponding to the distance between the centers of the cylinders is sufficient to unequivocally describe the H_{II}

phase. For small-molecule hexagonal crystals with finite unit cell dimensions the equation relating *hkl* spacings and the lattice parameters in the hexagonal phase is

$$d_{hkl} = \left[\frac{4}{3a^2} \left(h^2 + hk + k^2 + \frac{l^2}{c^2} \right) \right]^{-1/2} \qquad \text{Equation A4}$$

where a and c are, respectively, the center-to-center distance between the cylinders and the length of the cylinders. The length of the cylinder for H_{II} mesophases is infinitely large ($c = \infty$), resulting in the only allowed value of $l = 0$. Hence, Equation A4 reduces to

$$d_{hk0} = \left[\frac{4}{3a^2} \left(h^2 + hk + k^2 \right) \right]^{-1/2} \qquad \text{Equation A5.}$$

Equation A5 indicates that the H_{II} phase produces patterns with the ratios of inverse *d*-spacings of $1 : \sqrt{3} : 2, etc.$ corresponding to the *hkl* reflections *100/010*, *210/120*, *220, etc*. The highest-intensity reflection of the H_{II} mesophase is d_{100}/d_{010}, and, consequently, the lattice parameter of the H_{II} mesophase in Chapter 2 was calculated as

$$a(H_{II}) = \frac{d_{100}\sqrt{3}}{2} \qquad \text{Equation A6.}$$

Cubic phases. Conveniently, IPMS of G, P, and D types correspond to crystallographic cubic space groups *Ia3d* (Q^{230}), *Im3m* (Q^{229}), and *Pn3m* (Q^{224}). The unit cell of any cubic phase is a cube and requires a single lattice parameter a (the length of the edge of the cube) to fully describe its dimensions, which is related to *d*-spacings simply as

$$a_{cubic} = d_{hkl}\sqrt{h^2 + k^2 + l^2} \qquad \text{Equation A7.}$$

Due to the high symmetry of cubic phases, only certain combinations of *hkl* values produce reflections with non-zero intensity,[2] as listed below along with corresponding ratios of d_{hkl} for the first several peaks of each cubic mesophase:

Phase type	**Allowed *hkl* combinations**	**Ratios of inverse *d*-spacings**
Pn3m	*110*, *111*, *200*, *211*, *220*, *221*, *310*, *311*, *222*, *321*, *322*	$\sqrt{2} : \sqrt{3} : \sqrt{4} : \sqrt{6} : \sqrt{8} : \sqrt{9} : \sqrt{10} : \sqrt{11} : \sqrt{12} : \sqrt{14} : \sqrt{17}$
Ia3d	*211*, *220*, *321*, *400*, *042/332*, *422*, *431*, *440*	$\sqrt{6} : \sqrt{8} : \sqrt{14} : \sqrt{16} : \sqrt{20} : \sqrt{22} : \sqrt{26}$
Im3m	*110*, *200*, *211*, *220*, *310*, *222*, *321*	$\sqrt{2} : \sqrt{3} : \sqrt{4} : \sqrt{6} : \sqrt{8} : \sqrt{10} : \sqrt{12}$

Cubic mesophases tend to produce low-intensity reflections starting at the peak corresponding to the third- or fourth-highest value of *d* (Figures A2 and A3). Depending on the sample composition and the X-ray source, only a few reflections of cubic phases may be visible in the

diffractogram, appearing in the low range of q values (Figure A4). *Im3m* phases are not typical for monoolein systems and have not been observed in this work. Lattice parameters of *Pn3m* and *Ia3d* phases in Chapters 2-4 were calculated based on respective highest-intensity reflections, d_{110} and d_{211}, respectively, and Equation A7.

Differences between cubic and lamellar phases. Cubic and lamellar mesophases often produce diffraction patterns with marked differences in the appearance of the rings (Figures A4 and A5), which may be helpful in the preliminary assessment of diffractograms of samples with coexisting mesophases. Diffraction patterns of cubic phases may appear as spotty rings, owing to the tendency of cubic phases to form relatively large (up to 50 μm) monocrystalline domains[3] (Figure A4). On the contrary, lamellar phases typically produce uniform diffraction rings (Figures A1 and A4) or rings with smooth variations in intensity along the radial direction of the ring (Figure A5). Here intensity variations are caused by the preferred orientation of lamellar sheets in the sample.

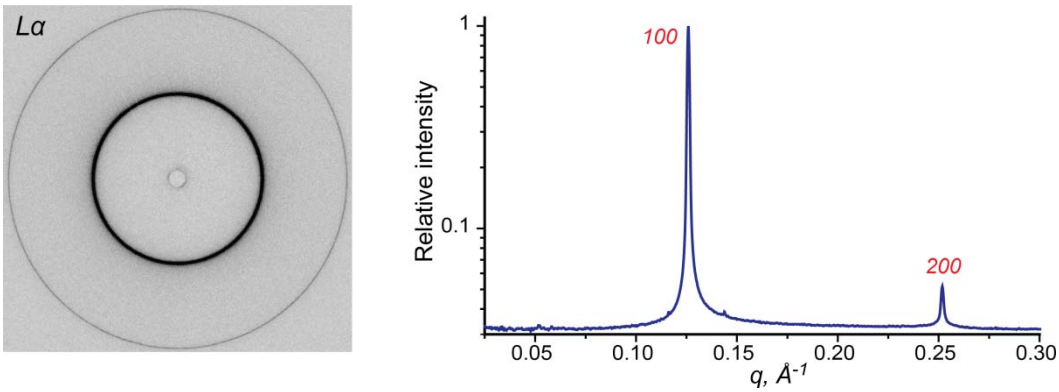

Figure A1. Raw diffractogram of a lamellar *Lα* phase with the lattice parameter of 50.5 Å (right) and a corresponding integrated diffractogram (left) with *hkl* peak assignments. Sample composition: 50 wt% of monoolein, 50 wt% of solution of 10% w/v β-octylclucosige in 25 mM NaH_2PO_4, pH 5.5.

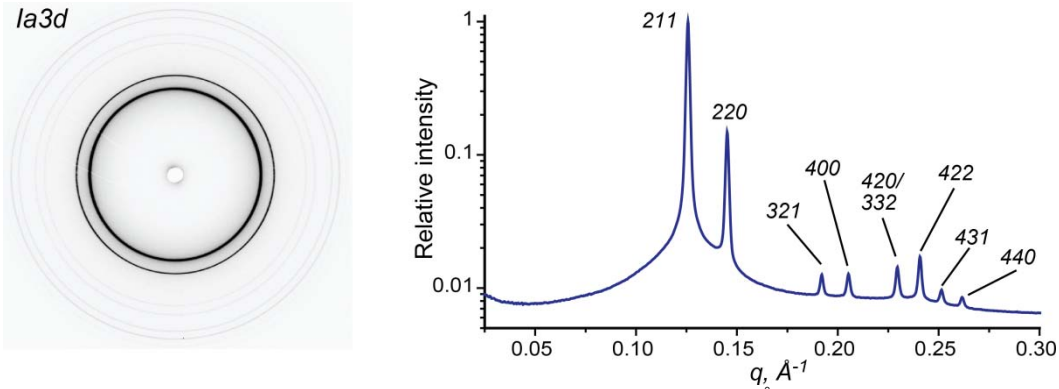

Figure A2. Raw diffractogram of a cubic *Ia3d* phase with the lattice parameter of 123 Å (right) and a corresponding integrated diffractogram (left) with *hkl* peak assignments. Sample composition: 30 wt% of aqueous solution of 1.0M KH_2PO_4, pH 5.5, 70 wt% of mixture of monoolein and β-octylglucoside (β-octylglucoside/monoolein ratio of 0.066 w/w).

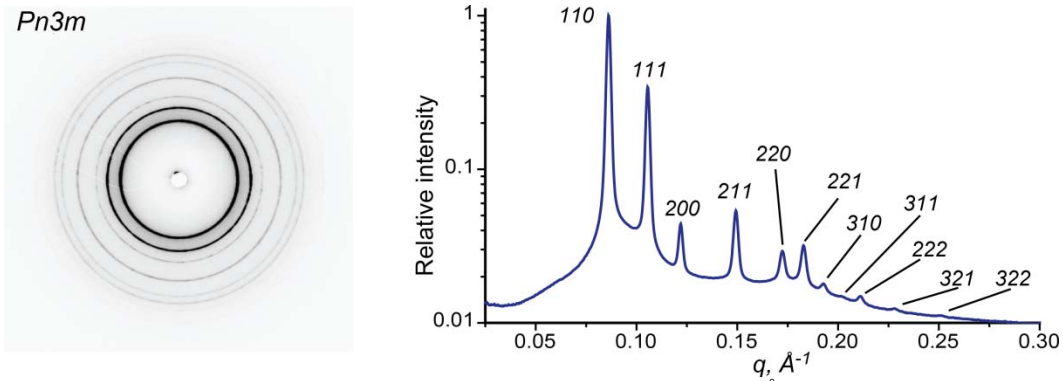

Figure A3. Raw diffractogram of a cubic *Pn3m* phase with the lattice parameter of 102 Å (right) and a corresponding integrated diffractogram (left) with *hkl* peak assignments. Sample composition: 30 wt% of aqueous solution of 1.0M KH_2PO_4, pH 5.5, and 70 wt% of mixture of monoolein and β-octylglucoside (β-octylglucoside/monoolein ratio of 0.066 w/w).

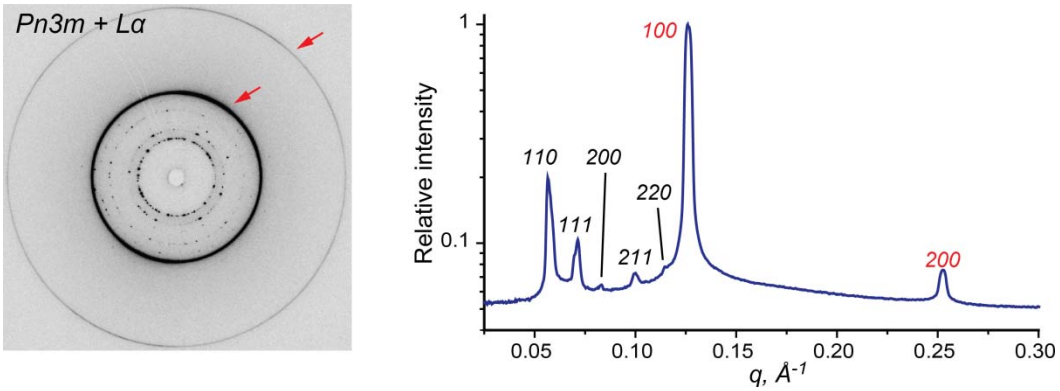

Figure A4. Raw diffractogram (right) of a mixture of a cubic *Pn3m* mesophase with a lamellar *Lα* phase. Reflections corresponding to the *Lα* phase are indicated with red arrows and have a smooth texture, unlike the spotty rings corresponding to the cubic *Pn3m* phase. Corresponding integrated diffractogram (left) with *hkl* assignments for *Pn3m* and *Lα* phases shown in respectively in black and red. Because of the low content of the *Pn3m* phase in the sample, only reflections up to *220* are visible. Sample composition: 55 wt% of monoolein, 45 wt% of solution of 10% w/v β-octylclucosige in 25 mM NaH_2PO_4, pH 5.5. Lattice parameters: *Pn3m*, 175 Å, *Lα*, 50.1 Å.

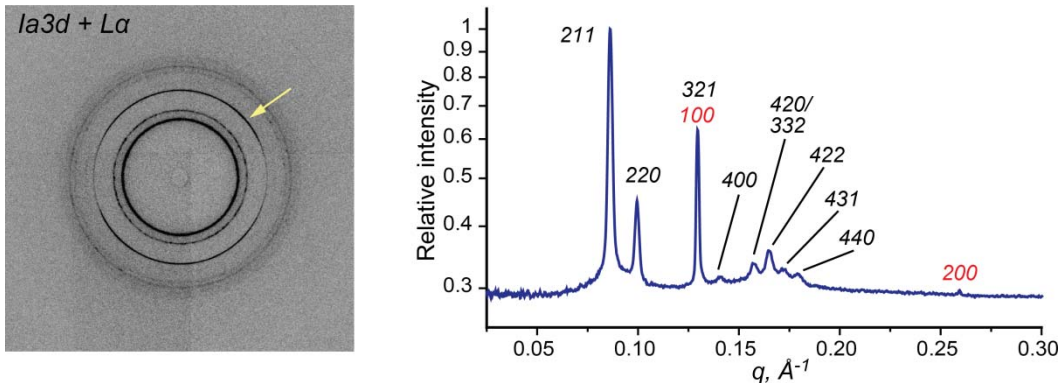

Figure A5. Raw diffractogram (right) of a mixture of a cubic *Ia3d* mesophase with a lamellar *Lα* phase. The intensity of the *100* reflection of the *Lα* phase (indicated with a yellow arrow) varies smoothly in the radial direction. Corresponding integrated diffractogram (left) with *hkl* assignments for *Ia3d* and *Lα* phases shown in respectively in black and red. The *321* reflection of the *Ia3d* phase overlaps with the *100* reflection of the *Lα* phase. Sample composition: 56 wt% of monoolein, 44 wt% of solution of 5% w/v β-octylclucosige in 25 mM NaH_2PO_4, pH 5.5. Lattice parameters: *Ia3d*, 178 Å, *Lα*, 48.7 Å.

References

1 D. E. Sands, *Introduction to crystallography*, W.A. Benjamin, Inc., New York, NY, 1969.

2 T. Hahn, ed., *International tables for crystallography, vol. A - space-group symmetry*, D Reidel Publishing Co., Dordrecht: Holland; Boston: USA, 1983.

3 V. Cherezov and M. Caffrey. Membrane protein crystallization in lipidic mesophases. A mechanism study using X-ray microdiffraction. *Faraday Discuss.*, 2007, **136**, 195-212.

Appendix B.

Effect of phosphate salts and β-octylglucoside on lattice parameters of lipidic mesophases

Quantitative effects of detergent β-octylglucoside (βOG) and phosphate salts on the lattice parameter of fully hydrated quaternary mesophases of lipid monoolein (MO) reported in Chapter 2 were estimated as described below.

MO/βOG/ salt solution samples with KH_2PO_4. Various datasets used for the calculations of regression coefficients in samples prepared with KH_2PO_4 and resulting values of regression coefficients are shown in Table B1.

Table B1. Lattice parameters and regression coefficients for MO/βOG/salt solution mixtures prepared with KH_2PO_4.

		a_{Pn3m}, Å			
$R_{\beta OG/MO}$	c_{salt}, M	Set A*	Set B*	Set C*	Set D*
0.033	0.7	112.1	112.1	115.1	115.1
0.066	0.7	131.7	131.7	138.9	131.7
0.099	0.7	156.1	156.1	162.4	156.1
0.033	1.0	102.4	97.8	102.4	106.0
0.066	1.0	122.0	122.0	128.5	128.5
0.099	1.0	141.4	141.4	154.4	141.4
0.033	1.3	96.2	93.7	96.2	99.2
0.066	1.3	114.6	114.6	118.0	118.0
0.099	1.3	134.6	134.6	137.7	134.6
		Regression coefficients**			
		Set A	**Set B**	**Set C**	**Set D**
Intercept, Å		113 ± 8	112 ± 9	117 ± 9	117 ± 10
$\partial a_{Pn3m}/\partial R_{\beta OG/MO}$		6.1 ± 0.6	6.5 ± 0.7	7.1 ± 0.7	5.6 ±0.8
$\partial a_{Pn3m}/\partial c_{salt}$		-3.0 ± 0.7	-3.2 ± 0.8	-3.6 ± 0.7	-2.8 ± 0.8

*__Set A:__ at each $R_{\beta OG/MO}$ and c_{salt}, lattice parameter at lowest w_{aq} resulting in excess aqueous phase formation.

*__Set B:__ at each $R_{\beta OG/MO}$ and c_{salt}, lattice parameter at lowest w_{aq} producing the *Pn3m* mesophase without other mesophase types present (may be above or below the hydration boundary depending on the sample).

*__Set C:__ at each $R_{\beta OG/MO}$ and c_{salt}, lattice parameter at second-lowest w_{aq} producing the *Pn3m* mesophase without other mesophase types present (*i.e.*, w_{aq} is 10% larger for each sample than in set B).

*__Set D:__ lattice parameters at w_{aq} = 60 wt% for all values of $R_{\beta OG/MO}$ and c_{salt}.

**Values for the 95% confidence interval are shown.

For each set of data shown in Table B1 coefficients were calculated in Matlab (R2012a, v. 7.14.0.739, The MathWorks Inc., Natick, MA) via multilinear regression and scaled to correspond to the unit of 0.01 for βOG/MO ratio and to the unit of 0.1M for the salt

concentration, respectively, for ease of numerical comparison between the two additives. For example, the projected lattice parameter of the *Pn3m* phase a_{Pn3m} at $R_{\beta OG/MO}$ = 0.033 and KH_2PO_4 concentration of 0.7 M based on the coefficients for Set A in Table B1 is calculated as

$$a_{Pn3m} = 113.2 + 6.13 \cdot 3.3 + (-3.0) \cdot 7.$$

Mixtures with NaH_2PO_4. Perusal of data for samples prepared with NaH_2PO_4 revealed that under otherwise identical conditions the change in the lattice parameters upon transition from $R_{\beta OG/MO}$ = 0.033 to $R_{\beta OG/MO}$ = 0.066 was noticeably smaller than upon transition from 0.066 to 0.099 in fully hydrated *Pn3m* mesophase. This disparity led to very large standard deviations if a single set of parameters was used in the regression. In contrast, in mixtures with KH_2PO_4 the lattice parameters changed uniformly in the entire range of conditions studied in this work. Because of those differences, a modified protocol was adopted for the calculations in mixtures with NaH_2PO_4. Lattice parameters of *Pn3m* phases did not vary appreciably above the hydration boundary in samples with NaH_2PO_4, and all data points where *Pn3m*-only mesophase was observed at both NaH_2PO_4 concentrations at a given w_{aq} were used in the regression (Table B2). Regression coefficients were calculated separately for the $R_{\beta OG/MO}$ range 0.033 - 0.066 (data in rows 1-20 in Table B2) and 0.066 - 0.099 (data in rows 11-28 in Table B2). Regression coefficients reported in Table B2 have been scaled in the same way as those in Table B1 to correspond to the unit of 0.01 for βOG/MO ratio and to the unit of 0.1M for the salt concentration.

Table B2. Lattice parameters and regression coefficients for MO/βOG/salt solution mixtures prepared with NaH_2PO_4.

Row #	$R_{\beta OG/MO}$	w_{aq}, wt%	c_{salt}, M	a_{Pn3m}, Å
1	0.033	40.1	1.3	94.2
2	0.033	50.1	1.3	96.5
3	0.033	59.9	1.3	97.9
4	0.033	69.8	1.3	99.0
5	0.033	80.0	1.3	100.4
6	0.033	39.9	2.0	76.1
7	0.033	49.8	2.0	80.7
8	0.033	59.9	2.0	82.7
9	0.033	70.0	2.0	81.9
10	0.033	79.9	2.0	86.4
11	0.066	40.0	1.3	98.1
12	0.066	50.0	1.3	105.8
13	0.066	59.9	1.3	104.9
14	0.066	69.9	1.3	111.6
15	0.066	80.0	1.3	113.3
16	0.066	40.1	2.0	88.2
17	0.066	49.9	2.0	93.2
18	0.066	60.0	2.0	96.5
19	0.066	70.0	2.0	96.6
20	0.066	79.9	2.0	98.2
21	0.099	50.0	1.3	118.8
22	0.099	59.8	1.3	132.1
23	0.099	69.9	1.3	133.2
24	0.099	80.1	1.3	131.9
25	0.099	50.0	2.0	103.8
26	0.099	59.9	2.0	105.1
27	0.099	69.9	2.0	108.5
28	0.099	80.0	2.0	109.8
Regression coefficients,* $R_{\beta OG/MO}$ = 0.033 - 0.066, rows 1 - 20				
Intercept, Å			111.8 ± 11.3	
$\partial a_{Pn3m}/\partial R_{\beta OG/MO}$			3.4 ± 1.2	
$\partial a_{Pn3m}/\partial c_{salt}$			-2.0 ± 0.6	
Regression coefficients,* $R_{\beta OG/MO}$ = 0.066 - 0.099, rows 11 - 28				
Intercept, Å			105.4 ± 19.6	
$\partial a_{Pn3m}/\partial R_{\beta OG/MO}$			5.2 ± 1.7	
$\partial a_{Pn3m}/\partial c_{salt}$			-2.4 ± 0.8	
*Values for the 95% confidence interval are shown.				